COMENIUS UNIVERSITY BRATISLAVA
FACULTY OF MATHEMATICS, PHYSICS AND INFORMATICS

Spectrometer and Kinematic Studies for New Physics Searches in Rare $K^+ \to \pi^+ \nu\bar{\nu}$ Decay at NA62 Experiment at CERN

Dissertation thesis

Study programme:	Nuclear and Subnuclear Physics
Branch of study:	1124 Nuclear and Subnuclear Physics
Department:	Department of Theoretical Physics
Supervisor:	doc. RNDr. Tomáš Blažek, PhD.
Consultant:	Mgr. Michal Kovaľ, PhD.

Bratislava, 2020 **Mgr. Zuzana Kučerová**

Univerzita Komenského v Bratislave
Fakulta matematiky, fyziky a informatiky

ZADANIE ZÁVEREČNEJ PRÁCE

Meno a priezvisko študenta: Mgr. Zuzana Kučerová
Študijný program: jadrová a subjadrová fyzika (Jednoodborové štúdium, doktorandské III. st., denná forma)
Študijný odbor: fyzika
Typ záverečnej práce: dizertačná
Jazyk záverečnej práce: anglický
Sekundárny jazyk: slovenský

Názov: Spectrometer and Kinematic Studies for New Physics Searches in Rare K+ to Pi+ Nu Nubar Decay at NA62 Experiment at CERN
Štúdie spektrometra a kinematiky zamerané na hľadanie novej fyziky v zriedkavom rozpade K+ na pí+ ní anti-ní v NA62 Experimente v CERN-e

Anotácia: Študent sa oboznámi so štandardným modelom
a základnými princípmi experimentálej časticovej fyziky a analýzy dát.
Cieľom práce je zamerať sa na niektorý zo zriedkavých procesov v súčasnosti študovaných v NA62 Experimente v laboratóriu CERN.
Navrhujeme, že študent si počas štúdia nájde svoju parketu
pri analýze a simulačnej práci pre subdetektor STRAW s dôrazom
na zriedkavý kaónový rozpad K+ na pí+ ní anti-ní, ktorý má dobrý potenciál testovať štandardný model a nájsť signály novej fyziky.
Práca si môže vyžadovať opakovaný pobyt v laboratóriu CERN alebo partnerských
inštitúciách (University of Birmingham a iné).

Cieľ: Prispieť do NA62 Experimentu štúdiom zriedkavého kaónového rozpadu K^+ \to \pi^+ \nu \nu v rámci pracovnej skupiny STRAW subdetektora.

Literatúra:
Halzen, F. and Martin, A.D. :
Kvarky a leptóny: Úvodný kurz modernej časticovej teoretickej fyziky,
v anglickom jazyku,
New York: Wiley, 1984.

Peskin, M.E. a Schroeder, V.:
Úvod do kvantovej teórie poľa,
v anglickom jazyku,
Addison-Wesley, 1995

Kľúčové slová: kvarky, leptóny, K mezóny, štandardný model, elementárne častice, zriedkavé časticové rozpady

Školiteľ: doc. RNDr. Tomáš Blažek, PhD.
Konzultant: Mgr. Michal Kovaľ, PhD.
Katedra: FMFI.KTF - Katedra teoretickej fyziky
Vedúci katedry: doc. RNDr. Tomáš Blažek, PhD.

Spôsob sprístupnenia elektronickej verzie práce:
bez obmedzenia

Univerzita Komenského v Bratislave
Fakulta matematiky, fyziky a informatiky

Dátum zadania: 23.02.2015

Dátum schválenia: 24.02.2015

prof. RNDr. Jozef Masarik, DrSc.
garant študijného programu

.....

študent

.....

školiteľ

Comenius University in Bratislava
Faculty of Mathematics, Physics and Informatics

13085318

THESIS ASSIGNMENT

Name and Surname:	Mgr. Zuzana Kučerová
Study programme:	Nuclear and Subnuclear Physics (Single degree study, Ph.D. III. deg., full time form)
Field of Study:	Physics
Type of Thesis:	Dissertation thesis
Language of Thesis:	English
Secondary language:	Slovak

Title: Spectrometer and Kinematic Studies for New Physics Searches in Rare K+ to Pi+ Nu Nubar Decay at NA62 Experiment at CERN

Annotation: The student will first learn the Standard Model physics and get to know basic principles of experimental particle physics and data analysis.
The goal of the thesis is to focus on a rare process currently under investigation at the NA62 Experiment at CERN.
We propose that the student will find his/her place in the analysis or simulation work
for the STRAW subdetector group, with emphasis on the rare K+ to Pi+ Nu Nubar kaon decay which has excellent potential for probing the Standard Model and finding signals of new physics.
The work on this project may require repeated stays at CERN or our partner institutions (University of Birmingham and others).

Aim: Contribute to the NA62 Experiment by studying rare kaon decay K^+ \to \pi^+ \nu \nu within the STRAW subdetector group

Literature: Halzen, F. and Martin, A.D. :
Quarks and Leptons: An Introductory Course in Modern Particle Theory Physics,
New York: Wiley, 1984.

Peskin, M.E. and Schroeder, V.:
An Introduction to Quantum Field Theory,
Addison-Wesley, 1995

Keywords: quarks, leptons, kaons, Standard Model, elementary particles, rare particle decays

Tutor:	doc. RNDr. Tomáš Blažek, PhD.
Consultant:	Mgr. Michal Kovaľ, PhD.
Department:	FMFI.KTF - Department of Theoretical Physics
Head of department:	doc. RNDr. Tomáš Blažek, PhD.
Assigned:	23.02.2015
Approved:	24.02.2015

prof. RNDr. Jozef Masarik, DrSc.
Guarantor of Study Programme

Comenius University in Bratislava
Faculty of Mathematics, Physics and Informatics

....

Student Tutor

Acknowledgement

I would like to thank my supervisor doc. RNDr. Tomáš Blažek, PhD. for the opportunity to work at NA62. Furthermore, I wish to express my gratitude to my consultant Mgr. Michal Kovaľ, PhD. for his guidance and valuable advice and Mgr. Ľuboš Bičian, PhD. for his time and support.

I also thank my family and friends for their care and patience.

Dedicated to the memory of my beloved grandfather.

Abstract

The LHC experiments have already reached their energy limitations and are starting high luminosity programs to continue direct searches for new physics signals. At the same time the importance of low energy experiments in the field of experimental particle physics is rising, as they offer a wide range of possibilities to challenge the Standard Model of particle physics and to look for indirect signs of new physics in quantum corrections and forbidden processes.

The NA62 experiment at CERN is one of the most active particle experiments in the kaon physics today. It was designed specifically to study the ultra-rare "golden decay" $K^+ \to \pi^+\nu\overline{\nu}$ ($K_{\pi\nu\nu}$). A new result with the most precise measurement of the $K_{\pi\nu\nu}$ branching fraction obtained from the full NA62 data set recorded in 2016–2018, has been recently presented at the ICHEP 2020 conference. The same data is used in multiple other analyses of rare kaon decays and searches for new particles from the hidden sector, also producing world leading results.

NA62 is preparing for the new run expected to start in 2021. Analysis of the available data set showed that the NA62 has potential to reach the precision of the Standard Model $K_{\pi\nu\nu}$ branching fraction prediction. Additionally, it revealed several drawbacks of the current experimental setup and indicated data analysis methods and algorithms that need improvement before the new run.

This work details the author's contribution towards the $K_{\pi\nu\nu}$ decay measurement at the NA62. The contribution is twofold, which is reflected in the organization of the presented thesis.

First the analysis of the STRAW spectrometer reconstruction efficiency for single track events is presented. The efficiency is measured for π^+, μ^+ and e^+ tracks from selected $K^+ \to \pi^+\pi^0$, $K^+ \to \pi^0\mu^+\nu_\mu$ and $K^+ \to \pi^0 e^+\nu_e$ events, respectively. The track reconstruction efficiency for all three types of charged tracks is measured to be above 95 % in 2016 and above 98 % in 2017 and 2018 data sets when all reconstructed candidates are considered. The efficiency for tracks reconstructed using hits from all four STRAW chambers is above 92 % in 2016 and above 94 % in 2017 and 2018. The reconstruction efficiency measured on π^+ tracks was used in the $K_{\pi\nu\nu}$ analysis of 2017 and 2018 data sets.

Secondly, one of the critical parts of the $K_{\pi\nu\nu}$ analysis – the matching between the kaon and pion tracks – is studied. A new matching algorithm based on hypothesis testing using likelihood is proposed. Performance of the algorithm is studied with fully reconstructed $K^+ \to \pi^+\pi^+\pi^-$ event candidates and decrease in mismatch rate of up to 80 % is observed. Additionally, a part of the main $K_{\pi\nu\nu}$ analysis was implemented independently in this work to study the effect of the proposed

matching algorithm on the reconstruction tails of the two dominant kaon decay background sources, $K^+ \to \pi^+\pi^0$ and $K^+ \to \mu^+\nu$, in the 2017 data. The new algorithm significantly improves the resolution tails of the kinematic variable m^2_{miss} and thus reduces the $K^+ \to \pi^+\pi^0$ background by up to 30 %, leading to an increased signal-over-background ratio with a single event sensitivity comparable to the main analysis. After the planned upgrade of the NA62 detector system, the new matching algorithm is intended to be used in the main $K_{\pi\nu\nu}$ analysis in the next run.

Keywords: NA62 experiment, rare kaon decays, reconstruction efficiency, likelihood

Abstrakt

Časticové experimenty na LHC už dosiahli najvššie možné energie a pokračujú v hľadaní priamych signálov novej fyziky pomocou zvyšovania luminozity. V súčasnosti sa však stávajú rovnako dôležitými aj experimenty pracujúce pri nižších energiách, nakoľko ponúkajú široké spektrum možností na testovanie predpovedí Štandardného modelu a na hľadanie nepriamych signálov novej fyziky v kvantových korekciách a v zakázaných procesoch.

Experiment NA62 v laboratóriu CERN je dnes jedným z najaktívnejších experimentov v kaónovej fyzike. Bol navrhnutý špeciálne za účelom študovania zriedkavého "zlatého" rozpadu $K^+ \to \pi^+ \nu\overline{\nu}$ ($K_{\pi\nu\nu}$). Kolaborácia NA62 prezentovala na nedávnej konferencii ICHEP 2020 nový výsledok s doposiaľ najpresnejším meraním vetviaceho pomeru rozpadu $K_{\pi\nu\nu}$. Na meranie boli použité všetky dostupné dáta zaznamenané v období rokov 2016–2018. Tie isté dáta používajú aj ďalšie analýzy zriedkavých rozpadov kaónu prebiehajúce na experimente NA62, ktoré v súčasnosti tiež produkujú najpresnejšie výsledky na svete.

NA62 sa pripravuje na opätovné spustenie prevádzky v roku 2021. Analýza doposiaľ zaznamenaných dát ukázala, že experiment má potenciál dosiahnuť presnosť, s ktorou Štandardný model predpovedá vetviaci pomer rozpadu $K_{\pi\nu\nu}$. Okrem toho sa však prejavili aj nedostatky použitej experimentálnej zostavy a niektorých analytických metód a algoritmov, ktoré je potrebné vylepšiť skôr, než NA62 začne naberať nové dáta.

Táto práca zaznamenáva dva autorkine príspevky k meraniu rozpadu $K_{\pi\nu\nu}$ na experimente NA62.

Prvým príspevkom je meranie efektivity spektrometra STRAW, s ktorou sme schopní v rozpadoch kaónu s jednou nabitou časticou v koncovom stave zrekonštruovať jej trajektóriu a hybnosť. Efektivitu sme merali osobitne pre častice π^+, μ^+ a e^+ pochádzajúce z rozpadov $K^+ \to \pi^+\pi^0$, $K^+ \to \pi^0\mu^+\nu_\mu$ a $K^+ \to \pi^0 e^+\nu_e$. Berúc do úvahy kandidátov zrekonštruovaných zo signálu v štyroch STRAW komorách, pre všetky tri typy častíc sme namerali efektivitu ich rekonštrukcie presahujúcu 92 % v dátach z roku 2016 a 94 % v dátach z rokov 2017 a 2018. V prípade, že uvažujeme všetkých zrekonštruovaných kandidátov, nameraná efektivita narastie na vyše 95 % v dátach z roku 2016 a 98 % v dátach z rokov 2017 a 2018. Nami odmeraná efektivita rekonštrukcie π^+ kandidátov bola použitá v hlavnej $K_{\pi\nu\nu}$ analýze dát z rokov 2017 a 2018.

Druhý príspevok sa týka jednej z kritických častí analýzy rozpadu $K_{\pi\nu\nu}$, ktorou je párovanie piónových a kaónových kandidátov. V práci navrhujeme nový párovací algoritmus založený na testovaní hypotéz pomocou likelihood-u. Prostredníctvom

úplne zrekonštruovaných $K^+ \to \pi^+\pi^+\pi^-$ rozpadov sme zistili, že s novým algoritmom vidíme až o 80 % menej prípadov nesprávneho spárovania. V našej práci sme navyše nezávisle zreprodukovali časť hlavnej $K_{\pi\nu\nu}$ analýzy za účelom testovania efektu navrhovaného párovacieho algoritmu na rozdelenia rozpadov $K^+ \to \pi^+\pi^0$ and $K^+ \to \mu^+\nu$. Tieto tvoria hlavnú časť pozadia od kaónových rozpadov v $K_{\pi\nu\nu}$ analýze dát z roku 2017. S novým algoritmom dosahujeme výrazné zlepšenie rozlíšenia v kinematickej premennej m^2_{miss} a tým aj zníženie pozadia od rozpadu $K^+ \to \pi^+\pi^0$, a to až o 30 %. To vedie na zvýšenie pomeru signálu k pozadiu pri citlivosti na jeden $K_{\pi\nu\nu}$ rozpad porovnateľnej s hlavnou $K_{\pi\nu\nu}$ analýzou. Cieľom je použiť nový párovací algoritmus v hlavnej $K_{\pi\nu\nu}$ analýze dát, ktoré experiment NA62 začne naberať po ukončení plánovaných prác na detektore.

Kľúčové slová: Experiment NA62, zriedkavé rozpady kaónu, efektivita rekonštrukcie, likelihood

Contents

Introduction

The Standard Model of particle physics (SM) [1, 2, 3, 4], completed in 1970s, has proven to be a great success not only in describing new phenomena observed throughout the 20th century, but also in predicting existence of new particles, such as the top quark (discovered in 1995 [5, 6]), tau neutrino (discovered in 2000 [7]) and lastly the Higgs boson, discovered in 2012 [8, 9]. Additionally, it predicted the existence of the W and Z bosons [10, 11] and the gluon [12, 13].

On the other hand, we have already observed new phenomena that are not described by the SM. Among the best established ones are the gravity, the obvious predominance of matter over anti-matter in our Universe, the existence of dark matter observed in cosmology by means of galactic rotation curves [14] (among other methods), or neutrino masses required in neutrino oscillations (already recognized by Nobel Prize in 2015 [15, 16, 17, 18]). Moreover, the SM comes with several free parameters (such as Yukawa couplings determining lepton and quark masses, Higgs vacuum expectation value, CP-violating phase, etc.) that have to be measured experimentally, it employs mechanisms with unclear origin (such as CP violation, color confinement), there is no clear reason for the existence of three quark and lepton families, and others.

Current theoretical efforts are twofold. First is improving the precision of the SM calculations of both the predictions as well as subsidiary parameters or functions that are needed to evaluate variables of interest once the corresponding experimental result is available. These include mainly QCD computations. Second is the development of models of new physics based on all available evidence, addressing the new phenomena and giving predictions for observables that can be tested experimentally.

The experimental particle physics focuses on improving our understanding of the already observed phenomena as well as on searching for evidence for the ones predicted by the SM or by the new physics models. One possible approach is to detect and examine naturally occurring processes and particles. This method is typically adopted by experiments in the cosmic frontier such as the AMS [19], IceCube [20] or Super-Kamiokande [21], seeking to reveal the origin of the Universe, dark matter and dark energy.

Another approach is to artificially create conditions at which the examined events would occur (e.g. experiment ALICE [22] at CERN [23] designed to study quark-gluon plasma in heavy-ion collisions). Experiments in the energy frontier aim to directly probe high energy scales in the hope of discovering new heavy particles by increasing the centre-of-mass energy in particle collisions. This approach lead to the discovery of the Higgs boson by the ATLAS [24] and CMS [25] experiments, which was observed as a resonance in an invariant mass distribution. Alternatively, new physics can manifest itself as a missing transverse momentum, charge or angular asymmetries, etc. Conversely, experiments in the precision frontier utilise much lower initial particle energies. They aim to measure quantities predicted by the SM with competitive precision. Therefore, if significant discrepancies are observed, they could indicate a presence of new physics. The precision experiments are also able to reach phenomena at high energy scales, typically via production of heavy particles in loop diagrams. These occur mainly in very rare processes governed by flavor-changing neutral currents with the loops dominated by top-quark contribution, or potentially by a new heavy particle. Since the precision experiments probe mostly parts of the SM concerning weak interactions of quarks and leptons, they typically study decays of D, B and K mesons and baryons, for which the theoretical predictions often suffer from hadronic uncertainties. In some cases this could be overcome by providing ratios of similar observables measured in different processes. The experiments at precision frontier are currently closely watched as they provide a vast range of opportunities to study the fundamental properties of the SM as well as to look for new physics signals.

Our work focuses on decays of the charged K meson, in particular the rare decay $K^+ \to \pi^+ \nu\overline{\nu}$ ($K_{\pi\nu\nu}$) studied by the NA62 experiment at CERN [26, 27]. From the theoretical point of view, this decay has a very clean theoretical character and is potentially sensitive to new physics. On the other hand, due to a gap of about ten orders of magnitude between branching fractions of the common kaon decays and the $K_{\pi\nu\nu}$ [28], it is experimentally very challenging.

This thesis is divided into four chapters. In the first chapter a brief introduction to kaon physics is given. Furthermore, the role of the $K \to \pi\nu\nu$ decay in both experimental and theoretical particle physics fields is explained. The current experimental status as well as the implications of the branching fraction measurement are summarized. Finally, the most recent results from NA62 are reported.

The second chapter contains description of the NA62 beamline and detector, with the emphasis on the sub-detectors most relevant for this work. Moreover, the Monte Carlo simulation, reconstruction and the analysis part of the NA62 framework are explained.

The last two chapters contain a full description of two analyses carried out by

the author. In the third chapter, the Spectrometer track reconstruction efficiency measurement using 2016, 2017, 2018 data and Monte Carlo (MC) samples is presented. The efficiency is evaluated separately for three different types of charged tracks produced in kaon decays in the NA62 experiment: π^+, μ^+ and e^+. For this purpose, three kaon decay event selections were developed and are described in detail.

The fourth chapter focuses on the $K^+ \to \pi^+\nu\overline{\nu}$ analysis of the 2017 data set. Event selections of kaon decays relevant for this thesis are summarized. Detailed description of a new proposed algorithm for matching kaon and pion tracks is given. The results of the comparison with the standard algorithm used in the main $K^+ \to \pi^+\nu\overline{\nu}$ analysis are reported.

1 Kaon physics

Kaons played an important role in the construction of the Standard Model of particle physics (SM) by giving rise to flavour quantum numbers, revealing P and CP violation in weak interactions, meson–anti-meson mixing as well as the GIM mechanism [29]. Kaon decays allow us to indirectly probe high energy scales, help improve our understanding of weak interactions, give us a possibility to test the SM, and overall provide a window of opportunity to search for Beyond Standard Model physics signals.

In this chapter we briefly summarize the rich history of kaon physics emphasizing the details which motivate the experimental efforts in kaon physics today. Ultrarare $golden$ kaon decays $K \to \pi\nu\nu$ are then discussed further, explaining the profits of the measurement of the branching fractions $\mathcal{B}(K \to \pi\nu\nu)$. Finally, the experimental status of both neutral and charged modes is summarized, naturally focusing on the $K^+ \to \pi^+\nu\overline{\nu}$ measurement at NA62.

1.1 History

History of kaon physics began in 1947, when the first events of V^0 and V^+ particle decays into $\pi^+\pi^-$ and $\mu^+\nu$, respectively, were reported by G. Rochester and C. Butler [30]. The events were observed in a cloud chamber and were associated with a cosmic radiation shower penetrating the Earth's atmosphere. Although these two events were observed in the Manchester laboratory at the ground level, cosmic radiation physicists would often move the cloud chambers and special photographic emulsion detectors to high altitudes in order to catch the cosmic radiation particles with enough energy to be detected. The first example of a $\tau^+ \to \pi^+\pi^+\pi^-$ decay[1] was observed in 1948 by the Bristol group from an exposure of a new electron-sensitive emulsion to cosmic radiation in Swiss Alps [31].

In early 1950s' the detectors became more advanced and the collection of cosmic radiation data with unstable particles increased rapidly. Several new particles and

[1]Newly discovered mesons were labeled by letters of greek alphabet. Today, τ^+ is the heaviest lepton in the SM, and it is believed that the observed process was, in fact, the decay $K^+ \to \pi^+\pi^+\pi^-$.

decay modes emerged in multiple laboratories around the world, each using their own naming system. It was not until the International Cosmic Ray Conference in France in 1953 where it became clear that the laboratories were observing, measuring and identifying the same particles with masses in the range $(500 \pm 200)\,\mathrm{MeV}/c^2$ [32]. A new name $K\text{-}meson$ was adopted for these particles.

In 1956, a new era of studying kaon decays in accelerator experiments began. Theoretical attempts to organize the new particles and explain the rates of the various decay modes lead to the creation of several new quantum numbers (e.g. strangeness introduced by Gell-Mann, Pais and Nishijima [33, 34, 35, 36]). Although conserved in strong interactions producing the hadrons, some quantum numbers were not conserved in weak interactions by which the hadrons decayed, leading to introduction of new selection rules explaining observed long lifetimes of decaying particles (of the order of 10^{-8} s). It is important to notice that two neutral kaons, K^0 and $\overline{K}^0$, with definite but opposite values of strangeness were required.

Reviewing the experimental results, a new paradox emerged: two mesons (then called θ^+ and τ^+) with the same masses within several MeV/c^2 and lifetimes equal within the experimental errors were observed, each decaying to the final states ($(\pi^+\pi^0)$ and $(\pi^+\pi^+\pi^-)$, respectively) with opposite parity (P). In 1956, theoretical physicists T. D. Lee and C. N. Yang proposed a solution to this τ-θ paradox [37] claiming that the parity conservation, valid for strong interactions, does not hold in weak interactions, leading to different strong and weak eigenstates of the same particle. The puzzle was settled when in 1957 C. S. Wu reported parity violation in beta decay of polarized cobalt nuclei[2] [38], followed shortly by two other experiments observing it in pion decay to muon [39]. Confirmation of P violation in weak processes lead to a new understanding of τ^+ and θ^+ particles as one charged kaon K^+ decaying weakly into states with opposite parities. Since the combined CPT invariance of all physics laws was and still is assumed, and violation of T-symmetry was seen as unacceptable, a CP invariance was expected in all, even weak, processes.

The situation was similar for neutral kaons as both (being states with definite parity) were observed to decay to two and three pion states (with different parities). Consequently, two new CP eigenstates, believed then to be observed in the weak neutral kaon decays, were created as linear combinations of K^0 and $\overline{K}^0$:

$$K_1 = \frac{1}{\sqrt{2}}(K^0 - \overline{K}^0) \quad CP\,|K_1\rangle = |K_1\rangle \tag{1.1.1}$$

$$K_2 = \frac{1}{\sqrt{2}}(K^0 + \overline{K}^0) \quad CP\,|K_2\rangle = -\,|K_2\rangle\,. \tag{1.1.2}$$

Such combinations distinguish between K_1 decaying predominantly via the two-π mode with a mean lifetime almost three orders of magnitude smaller than K_2

[2] According to Lee and Yang, the experiment also indicated violation of charge conjugation.

decaying via the three-π mode. Different lifetimes are related to different phase space volumes as well as to non-degenerate masses (as opposed to K^0 and $\overline{K}^0$ in terms of strong interactions alone). An example of a phenomenon supporting the K^0-$\overline{K}^0$ mixing idea is the process of regeneration [40]. A K^0 beam produced in hadronic interactions and containing equally K_1 and K_2 is first observed to lose the short-lived K_1 part, leaving a pure K_2 beam. Impinging on an absorptive barrier, the $\overline{K}^0$ component of K_2 is absorbed due to higher interaction cross-section with nucleons in the material, leaving again only a pure K^0 beam, however with the intensity reduced by a factor of 1/4.

The understanding of weak interactions changed again in 1964, when the experiment of J. H. Christenson, J. W. Cronin, V. L. Fitch and R. Turlay [41] observed the long-lived neutral kaon K_2 to decay to two pions suggesting that CP symmetry, and consequently T symmetry, are broken in weak interactions. The CP violation can occur in the mass mixing matrix of neutral kaons, or directly in the decay amplitudes of both neutral and charged kaons [42]. Under consideration that the CP violation in the K^0-$\overline{K}^0$ mixing is small, it can be accommodated by a complex parameter $\bar{\varepsilon}$ defining two new states:

$$K_S = \frac{K_1 + \bar{\varepsilon} K_2}{\sqrt{1 + |\bar{\varepsilon}|^2}}, \tag{1.1.3}$$

$$K_L = \frac{\bar{\varepsilon} K_1 + K_2}{\sqrt{1 + |\bar{\varepsilon}|^2}}, \tag{1.1.4}$$

where S (L) stands for short (long) and reflects their lifetime given mostly by the dominant contribution from K_1 (K_2). CP violation of this type is referred to as *indirect* as it is caused by a mixture of CP eigenstates with different eigenvalues rather than by explicit CP symmetry breaking in the interaction. The measure of indirect CP violation is ε and is related to $\bar{\varepsilon}$ from the K^0-$\overline{K}^0$ mixing.

The second type of CP violation, realized via a *direct* transition between two CP eigenstates with opposite CP parities, is quantified by the parameter ε'. Charged kaons can only experience direct CP violation, while neutral kaons are usually affected by both direct and indirect CP violation, possibly with very different strengths. Experimentally accessible is often the ratio of the two, ε'/ε. In 1988, the first evidence for direct CP violation was observed by NA31 experiment at CERN [43]. Discovery of the direct CP violation is attributed to the NA48 experiment (CERN) [44] with the result confirmed by the KTeV collaboration (Fermilab) [45, 46]. Both experiments measured non-zero value of $\mathrm{Re}\left(\frac{\varepsilon'}{\varepsilon}\right)$ in the neutral kaon decays to two pions.

In the SM, all CP-violating effects are accommodated in a single phase in the Cabibbo-Kobayashi-Maskawa (CKM) matrix [47, 48, 49]. The CKM matrix is a 3×3

unitary matrix (Equation (1.1.5)) remaining in the Yukawa interaction part of the SM lagrangian after diagonalization of quark mass matrices and is responsible for connecting weak quark eigenstates to mass eigenstates. Considering redefinition of five quark fields, the CKM matrix can be parametrized by four real parameters, one of them being the CP-violating phase [50]. Alternatively, the Wolfenstein parametrization [51, 52, 53], which takes into account the experimentally observed hierarchy between three elements of the CKM matrix, is more suited for relating various experimental results. The parametrization is given by four real numbers: A, $\bar{\rho}$, $\bar{\eta}$ and a small parameter λ (Equation (1.1.5), Equation (1.1.6) [42]), in which the matrix terms can be expanded while retaining the matrix unitarity.

$$V_{CKM} = \begin{pmatrix} V_{ud} & V_{us} & V_{ub} \\ V_{cd} & V_{cs} & V_{cb} \\ V_{td} & V_{ts} & V_{tb} \end{pmatrix} = \begin{pmatrix} 1-\lambda^2/2 & \lambda & A\lambda^3(\rho - i\eta) \\ -\lambda & 1-\lambda^2/2 & A\lambda^2 \\ A\lambda^3(1-\rho-i\eta) & -A\lambda^2 & 1 \end{pmatrix} + \mathcal{O}(\lambda^4) \tag{1.1.5}$$

$$\begin{aligned} \lambda &= \frac{|V_{us}|}{\sqrt{|V_{ud}|^2 + |V_{us}|^2}} & A\lambda &= \left|\frac{V_{cb}}{V_{us}}\right| \\ V_{ub}^* = A\lambda^3(\rho + i\eta) &= \frac{A\lambda^3(\bar{\rho} + i\bar{\eta})\sqrt{1 - A^2\lambda^4}}{\sqrt{1-\lambda^2}\left[1 - A^2\lambda^4(\bar{\rho} + i\bar{\eta})\right]} & \bar{\rho} + i\bar{\eta} &= -\frac{(V_{ud}V_{ub}^*)}{(V_{cd}V_{vb}^*)} \end{aligned} \tag{1.1.6}$$

The CKM matrix elements are fundamental constants of the SM and thus have to be determined experimentally. Moreover, since multiple flavor physics experiments are sensitive to the same parameters, not only can the parameters be measured very precisely, they can also become over-constrained and thus reveal indirect signs of new physics.

Conditions of the CKM matrix unitarity, namely for the columns (and rows) to form an orthonormal basis in $\mathbb{C}^n$, results in equalities

$$\begin{aligned} \sum_{i \in \{u,c,t\}} V_{ij}V_{ik}^* &= \delta_{jk} & j,k &\in \{d,s,b\}, \\ \sum_{j \in \{d,s,b\}} V_{ij}V_{kj}^* &= \delta_{ik} & i,k &\in \{u,c,t\}. \end{aligned} \tag{1.1.7}$$

Considering one of the vanishing equations and definition of $\bar{\rho} + i\bar{\eta}$ in Equation (1.1.6), one obtains a new relation

$$\bar{\rho} + i\bar{\eta} = 1 + \frac{V_{td}V_{tb}^*}{V_{cd}V_{cb}^*}. \tag{1.1.8}$$

Once displayed in the complex plane, a triangle with vertices (0,0), (0,1), ($\bar{\rho}$,$\bar{\eta}$) and two sides corresponding to $\left|\frac{(V_{ud}V_{ub}^*)}{(V_{cd}V_{vb}^*)}\right|$ and $\left|\frac{V_{td}V_{tb}^*}{V_{cd}V_{cb}^*}\right|$ can be recognised [42]. Three

angles α, β and γ can be related to the CKM matrix elements and if determined experimentally, they provide additional constraints on the shape of the unitarity triangle.

1.2 $K \to \pi\nu\nu$ decays

Decays of both charged and neutral kaons to a pion and a neutrino-antineutrino pair are two of the most promising processes to challenge the Standard Model predictions. Being flavor-changing neutral-current (FCNC) processes, they occur in the SM only beyond the tree level in box and penguin diagrams. The transitions are dominated by CP-violating top quark contribution with non-negligible charm quark contribution in the charged mode [42]. This results in branching fractions at the level of 10^{-11} [28]. The short-distance domination implies that the low energy hadronic matrix elements corresponding to quark currents between hadron states can be extracted from well measured $K \to \pi l \nu_l$ decays. Both branching fractions can be predicted very accurately with the largest uncertainties coming from features inherent to perturbative QCD.

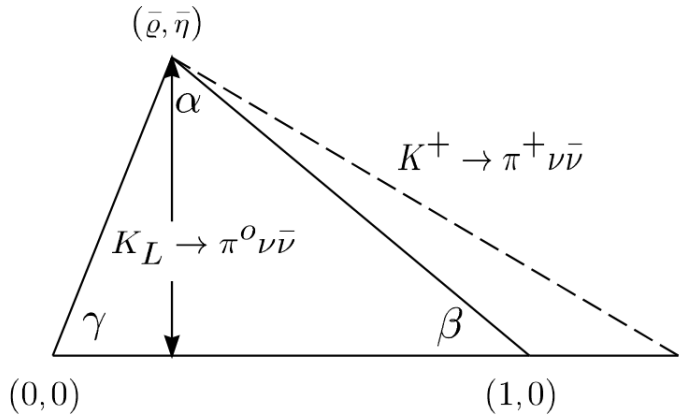

Figure 1.2.1: The CKM unitarity triangle and $K \to \pi\nu\nu$ decays [42].

As depicted in Figure 1.2.1 and explained in [42], simultaneous measurement of both branching fractions is enough to determine the full CKM unitarity triangle, provided that the top quark mass m_t and element V_{cb} are known. Additionally, combining both branching fractions allows us to eliminate multiple sources of uncertainty (even m_t and V_{cb} to a very good approximation) and provides a measurement of $\sin(2\beta)$ (where β is one of the angles in the unitarity triangle) free from all hadronic uncertainties. Finally, as pointed out in [54], branching fractions of the charged and neutral modes are related in a model-independent way as $\mathcal{B}(K_L \to \pi^0 \nu\nu) \lesssim 4.4 \mathcal{B}(K^+ \to \pi^+ \nu\bar{\nu})$ (Grossman-Nir bound).

While awaiting the measurements of $K \to \pi\nu\nu$ branching fractions accurate enough to be competitive with the SM prediction, updated computations of the expected branching fractions in several new physics models were reported in the past few years. New physics is expected to manifest itself mostly in the loops of the box and penguin diagrams, although some models allow also tree level contributions, albeit rather small. Here we mention just a few new physics models expecting significant deviations of the branching fraction with respect to the SM prediction in either charged or neutral decay mode. In two leptoquark models [55] designed to address possible lepton flavor universality violation (LFUV) in B-meson decays (hints observed by LHCb [56, 57, 58]), correlated loop effects of new physics in $K \to \pi\nu\nu$ and $B \to K^{(*)}\mu^+\mu^-$ decays were studied. As reported, up to 30 % suppression of $\mathcal{B}(K^+ \to \pi^+\nu\overline{\nu})$ with respect to the SM is expected. Another group adopting effective field theory approach to relate B-physics anomalies to kaon decays [59] investigated possible effects of LFUV on the $K^+ \to \pi^+\nu\overline{\nu}$ decay and expected correlations between $K^+ \to \pi^+\nu\overline{\nu}$, $B \to K^{(*)}\nu\overline{\nu}$ and R_{D^*} anomaly[3]. They expect a sizeable deviation from the SM as well, admitting a possibility of significant suppression. Taking into account the latest theoretical and experimental information available, the allowed departure of rare kaon and B-meson decay branching fractions computed in the Littlest Higgs model with T-parity [60] were updated. The results show a significant suppression in the neutral decay mode while allowing only a small disagreement with respect to the SM in the charged mode. Studies of $K \to \pi\nu\nu$ decays and ε'/ε in the simplified Z, Z′ models with minimal flavor violation [61] showed that, as opposed to other new physics models, a simultaneous enhancement of ε'/ε and the branching fraction of $K_L \to \pi^0\nu\bar{\nu}$ can be accommodated within this model, as well as significant enhancement of the charged decay mode. Finally, computation of the branching fraction of the charged decay mode in the minimal supersymmetric model with large $\tan\beta$ was reported in [62]. It was suggested that up to 10 % deviation from the SM prediction can be interpreted within the studied model.

1.2.1 Neutral mode $K_L \to \pi^0\nu\overline{\nu}$

The neutral decay mode in the SM is affected by both direct and indirect CP violation. However, as shown in [42] the dominant contribution is from the direct CP violation, while the indirect and CP-conserving contributions can be neglected. Transitions proceed mainly via top quark loop. Uncertainty of the SM prediction

[3] $R_{D^*} = \mathcal{B}(\overline{B} \to D^*\tau\overline{\nu}_\tau)/\mathcal{B}(\overline{B} \to D^* l\overline{\nu}_l)$

[63] comes mostly from CKM parameters:

$$\mathcal{B}(K_L \to \pi^0 \nu\overline{\nu})(\text{SM}) = (3.00 \pm 0.30) \times 10^{-11}. \tag{1.2.1}$$

As already shown, the branching fraction of the $K_L \to \pi^0 \nu\overline{\nu}$ decay is proportional to the height of the unitarity triangle.

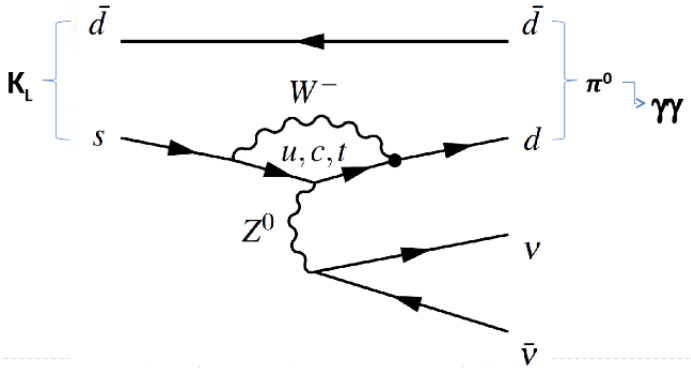

Figure 1.2.2: Standard Model diagram of $K_L \to \pi^0 \nu\nu$ [64].

Experimental detection of $K_L \to \pi^0 \nu\overline{\nu}$ is very challenging due to the lack of a charged particle in the final state. Two signal detection techniques were employed throughout the years. The first one searched for the Dalitz decay of the neutral pion, $\pi^0 \to e^+e^-\gamma$ (so called Dalitz mode), while the other – a more popular one – looked for π^0 decays to two photons (2γ mode). In the years 1992 - 2000, Fermilab experiments reported multiple results in both search modes, always looking at 50 GeV/c or 70 GeV/c kaons decaying in flight [65, 66, 67]. The analyses relied on an extensive set of photon detectors and, depending on the search mode, a spectrometer or an electromagnetic calorimeter, both placed downstream of the decay volume. They did not observe any events and set the best upper limit on the branching fraction $\mathcal{B}(K_L \to \pi^0 \nu\overline{\nu}) < 5.9 \times 10^{-7}$ at 90 % CL from the Dalitz search mode.

The first dedicated search for the decay $K_L \to \pi^0 \nu\overline{\nu}$ was carried out by the E391a experiment at the KEK proton synchrotron in Japan [68]. The experiment used an unseparated neutral beam with the K_L mean momentum of about 2 GeV/c. Due to the signature of the 2γ search mode employed in this measurement, any charged particles or additional photons would correspond to a background event. Therefore, the experiment strongly relied on an electromagnetic calorimeter for the photon detection and a variety of plastic scintillators and lead-scintillator components for the detection of charged particles originating in background events. One signal region was identified in the $Z_{vtx}p_T$-plane (p_T is the transverse momentum of the reconstructed π^0). Since no events were observed in the full (2004-2005) data set, an upper limit on the branching fraction was computed: $\mathcal{B}(K_L \to \pi^0 \nu\overline{\nu}) < 2.6 \times 10^{-8}$ at 90 % CL.

The latest results on the $K_L \to \pi^0 \nu\overline{\nu}$ branching fraction measurement come from the KOTO experiment in Japan [69]. A similar detector layout and composition as

in the KEK experiment was chosen, with several improvements in the photon veto and charged particle veto counters. Looking for a signal in the 2γ search mode, a CsI calorimeter was used to measure the photon energies and the veto counters surrounding the decay region ensured that no other detectable particles were present. One signal region was defined in the $Z_{vtx}p_T$-plane. The dominant background in the 2015 data analysis was caused by neutron-induced hadronic showers in the CsI calorimeter, mimicking the clusters from $\pi^0 \to \gamma\gamma$. The KOTO was able to reach a single event sensitivity of $\left(1.3 \pm 0.01_{\text{stat.}} \pm 0.14_{\text{syst.}}\right) \times 10^{-9}$, thus improving their first preliminary result from the 2013 data by almost an order of magnitude. In the 2015 data set, KOTO did not observe any signal candidate events leading to an upper limit on the branching fraction $\mathcal{B}(K_L \to \pi^0\nu\overline{\nu}) < 3.0 \times 10^{-9}$ at 90 % CL [70]. The analysis of a large data set collected in the years 2016 to 2018 is still ongoing, as while expecting 0.05 ± 0.02 Standard Model signal events in the signal region, four events were observed [64] (see Figure 1.2.3). The latest report at the ICHEP 2020 conference [71] suggests that one of the four events was not rejected by mistake, while the other events might be caused by a new unexpected background source.

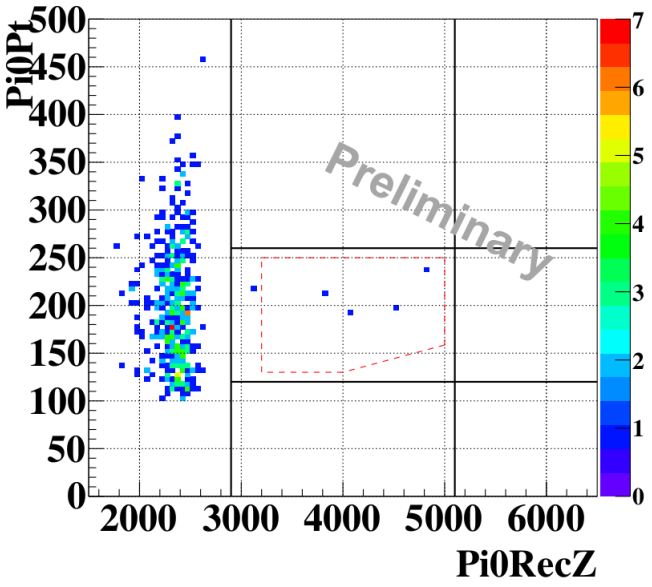

Figure 1.2.3: Preliminary result from KOTO experiment in search for the $K_L \to \pi^0\nu\overline{\nu}$ with 2016-2018 data set [64].

1.2.2 Charged mode $K^+ \to \pi^+\nu\overline{\nu}$

Leading contributions to the $K^+ \to \pi^+\nu\overline{\nu}$ amplitude in the SM are governed by one-loop electroweak processes [27], as shown in Figure 1.2.4.

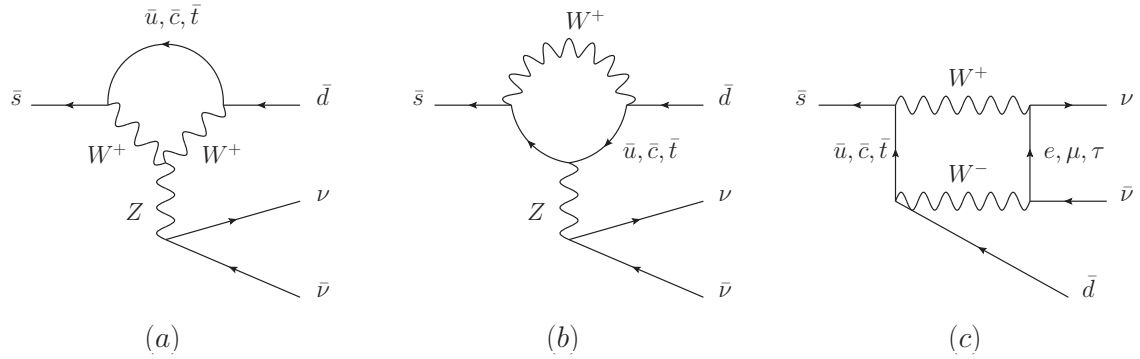

Figure 1.2.4: Feynman diagrams for $K^+ \to \pi^+ \nu\overline{\nu}$ leading contributions [72].

Due to the large top mass, the amplitude is dominated by the top quark loops, but receives also sizeable contribution from the charm transitions.

The latest SM prediction reads [63]

$$\mathcal{B}\left(K^+ \to \pi^+ \nu\overline{\nu}\right)(\text{SM}) = (8.4 \pm 1.0) \times 10^{-11}. \tag{1.2.2}$$

The experimental study of the $K_{\pi\nu\nu}$ decay began over 50 years ago with experiments observing K^+ decays at rest. A bubble chamber experiment at Argonne National laboratory in Illinois [73, 74] and a counter-spark chamber experiment at Berkeley [75] observed zero $K_{\pi\nu\nu}$ candidate events and set an upper limit on the $K_{\pi\nu\nu}$ branching fraction at the level of 5×10^{-7}. The limit was improved by the KEK experiment in Japan in 1981 to 1.4×10^{-7} [76].

The first measurement of the branching fraction $\mathcal{B}(K^+ \to \pi^+ \nu\overline{\nu})$ was performed by the E787 experiment at Brookhaven National Laboratory [77] and its successor, E949 [78]. Both experiments employed the same technique: the incoming kaons were first identified in a Cherenkov counter and two proportional wire chambers, then slowed down by a set of active and passive degraders, registered in the beam hodoscope, and finally stopped in a scintillating fiber target. Momenta and directions of the outgoing pions were measured in a drift chamber followed by a stack of plastic scintillator layers facilitating measurement of the pion range R_π and energy E_π. The whole spectrometer was surrounded by a solenoid providing a magnetic field of 1 T. A hermetic photon veto system covered 4π solid angle around the K^+ decay vertex. The background to the $K_{\pi\nu\nu}$ measurement consisted of the abundant kaon decays with misidentified muons, undetected photons and misreconstructed kinematics due to scattering in the detector material, as well as beam-related background from early kaon decays, misidentification of beam pions, and kaon decays in the target to K_L then decaying semi-leptonicaly. The $K_{\pi\nu\nu}$ was measured in two signal regions defined in the pion range versus E_π plane around the $K^+ \to \pi^+\pi^0$ peak. Both experiments adopted a blind analysis method, in which the signal regions were masked until the full event selection and background estimation were completed.

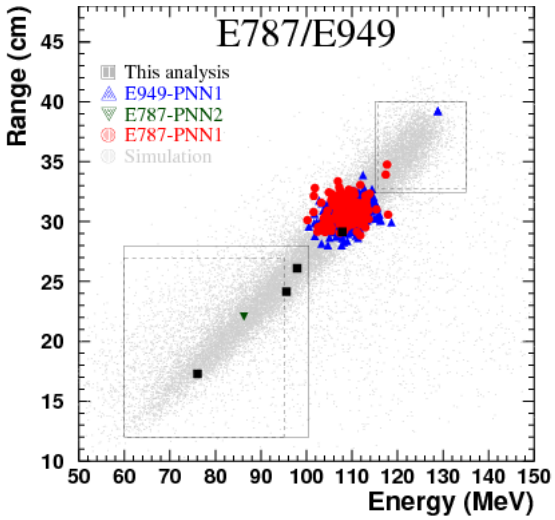

Figure 1.2.5: Seven $K^+ \to \pi^+ \nu\bar{\nu}$ candidates observed by the E949 and E787 experiments [79].

The combined result from data collected by the E787 and E949 experiments in both signal regions led to the branching fraction [79]

$$\mathcal{B}\left(K^+ \to \pi^+ \nu\bar{\nu}\right)(\text{EXP}) = (1.73^{+1.15}_{-1.05}) \times 10^{-10}, \tag{1.2.3}$$

obtained from seven signal event candidates. The result is consistent with the Standard Model prediction, however due to the limited precision it doesn't challenge the prediction.

1.2.2.1 Measurement at NA62

The NA62 Experiment at CERN exploits a different approach for the $K^+ \to \pi^+ \nu\bar{\nu}$ measurement with a high momentum (75 GeV/c) unseparated hadron beam with the kaon component decaying in flight [27]. Description of the NA62 detector is given in Chapter 2 of this thesis. The overall goal of NA62 is to measure the branching fraction of the $K_{\pi\nu\nu}$ decay at 10 % precision level.

The experimental signature of a $K_{\pi\nu\nu}$ event is one incoming kaon decaying into a single positively charged pion and missing energy carried away by neutrinos. Two signal regions with minimal contamination from the common kaon decays are defined using the kinematic variable squared missing mass

$$m^2_{miss} = \left(P_{K^+} - P_{\pi^+}\right)^2, \tag{1.2.4}$$

where P_{K^+} is the four-momentum of the detected upstream beam particle identified as a kaon and P_{π^+} is the four-momentum of the charged particle detected downstream, identified as a pion. The choice of the signal regions shown in Figure 1.2.6 provides 90 % kinematic rejection of other K^+ decays, listed in Table 1.2.1.

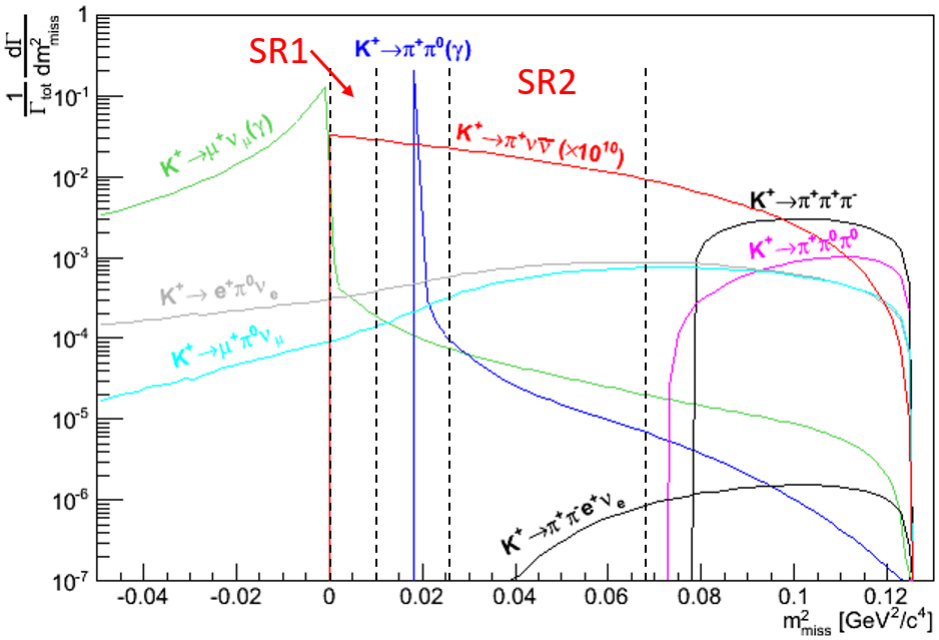

Figure 1.2.6: Differential branching fraction as a function of the kinematic variable m^2_{miss} (Equation (1.2.4)). Two signal regions are indicated by dashed lines. Signal region 1 (SR1) is defined between the $K_{\mu 2}$ and $K_{2\pi}$ peaks, signal region 2 (SR2) is defined between the $K_{2\pi}$ peak and the $K^+ \to \pi^+\pi^+\pi^-$ threshold.

The NA62 Experiment collected three data sets for the $K_{\pi\nu\nu}$ decay measurement, denoted by the year of data taking. Separate blind analyses were adopted in each recorded data set. The 2017 $K_{\pi\nu\nu}$ analysis is of great importance for the presented thesis. Specifically, the matching between the kaon and pion tracks, crucial for the reconstruction of signal events and suppression of background contribution to the $K_{\pi\nu\nu}$ signal regions, is studied on the 2017 data and discussed in Chapter 4. Optimization of the matching algorithm, addressed in Section 4.2, is desired for the future $K_{\pi\nu\nu}$ analysis to lower the background from the $K_{2\pi}$ and $K_{\mu 2}$ reconstruction tails and potentially also from upstream events (Appendix A).

The data sample of 2016 contained 1.21×10^{11} K^+ decays, and with a 4 % signal acceptance resulted in a single event sensitivity at the level of 3.15×10^{-10} [80]. One $K_{\pi\nu\nu}$ event candidate (see Figure 1.2.8a) was observed in signal region 2 leading to an upper limit $\mathcal{B}(K^+ \to \pi^+\nu\bar{\nu}) < 14 \times 10^{-10}$ at 95 % CL. Even though the result was not competitive with the previous measurements, it established the new decay-in-flight technique and showed that with more statistics and improved signal selection, the sensitivity of the Standard Model prediction can be reached.

Final state	Abbreviation	Branching fraction
$\mu^+\nu_\mu$	$K_{\mu 2}$	$63.56 \pm 0.11\%$
$\pi^+\pi^0$	$K_{2\pi}$	$20.67 \pm 0.08\%$
$\pi^+\pi^+\pi^-$	$K_{3\pi}$	$5.58 \pm 0.02\%$
$\pi^0 e^+\nu_e$	K_{e3}	$5.07 \pm 0.04\%$
$\pi^0\mu^+\nu_\mu$	$K_{\mu 3}$	$3.35 \pm 0.03\%$
$\pi^+\pi^0\pi^0$	$K_{3\pi^0}$	$1.76 \pm 0.02\%$
$\pi^+\pi^- e^+\nu_e$	K_{e4}	$(4.25 \pm 0.02) \times 10^{-5}$
$\pi^+\gamma\gamma$		$(1.01 \pm 0.06) \times 10^{-6}$
$\pi^+\nu\overline{\nu}$	$K_{\pi\nu\nu}$	$(8.4 \pm 1.0) \times 10^{-11}$

Table 1.2.1: K^+ decay modes relevant for this thesis. Standard abbreviations and branching fractions [28] are listed. SM prediction for the $K_{\pi\nu\nu}$ branching fraction is quoted [63].

Process	Events expected
$K^+ \to \pi^+\nu\bar{\nu}$ (SM)	$2.16 \pm 0.13_{\text{syst}} \pm 0.26_{\text{ext}}$
$K^+ \to \pi^+\pi^0(\gamma)$	$0.29 \pm 0.03_{\text{stat}} \pm 0.03_{\text{syst}}$
$K^+ \to \mu^+\nu(\gamma)$	$0.15 \pm 0.02_{\text{stat}} \pm 0.04_{\text{syst}}$
$K^+ \to \pi^+\pi^- e^+\nu$	$0.12 \pm 0.05_{\text{stat}} \pm 0.06_{\text{syst}}$
$K^+ \to \pi^+\pi^+\pi^-$	$0.008 \pm 0.008_{\text{syst}}$
$K^+ \to \pi^+\gamma\gamma$	$0.005 \pm 0.005_{\text{syst}}$
$K^+ \to \pi^0\ell^+\nu$ $(\ell = \mu, e)$	< 0.001
Upstream background	$0.89 \pm 0.24_{\text{stat}} \pm 0.20_{\text{syst}}$
Total background	$1.46 \pm 0.25_{\text{stat}} \pm 0.21_{\text{syst}}$

(a)

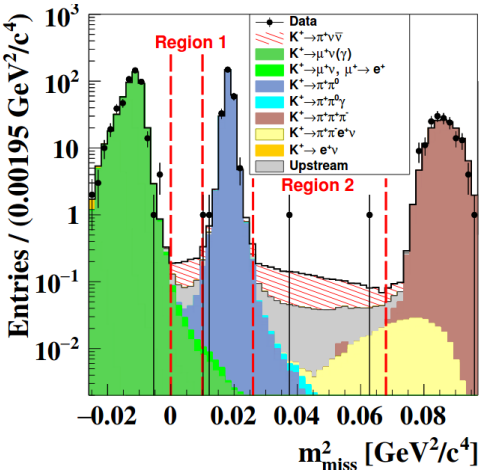

(b)

Figure 1.2.7: (a): Summary of the expected numbers of the $K_{\pi\nu\nu}$ decays and background events in the $K_{\pi\nu\nu}$ signal regions in the 2017 data set. The upstream, $K_{2\pi}$, $K_{\mu 2}$ and $K^+ \to \pi^+\pi^+\pi^-$ contributions were estimated from data, the rest was estimated from simulation. (b) Reconstructed m^2_{miss} (Equation (1.2.4)) distribution of data events passing the $K_{\pi\nu\nu}$ event selection from the 2017 data set. The expected background and SM $K_{\pi\nu\nu}$ event contributions are superimposed as stacked histograms. The distributions of the $K_{2\pi}$, $K_{\mu 2}$ and $K^+ \to \pi^+\pi^+\pi^-$ decays and of the upstream events are extracted from data. The other contributions are obtained from simulations [81].

The 2017 data sample contained 2×10^{12} K^+ decays [81]. The single event sensitivity, measured to be $(0.389 \pm 0.021) \times 10^{-10}$, constituted an improvement with respect to the 2016 result by one order of magnitude, thus reaching the world's best

value in the $K^+ \to \pi^+\nu\overline{\nu}$ decay channel. The expected number of Standard Model $K_{\pi\nu\nu}$ events and the background contribution to the $K_{\pi\nu\nu}$ signal regions are summarized in Figure 1.2.7a. The background is dominated by upstream decays in the beam line and interactions between the beam particles and upstream detectors (see Appendix A), with significant contribution from $K_{2\pi}$ and $K^+ \to \mu^+\nu$ ($K_{\mu 2}$) kinematic tails, as shown in Figure 1.2.7b.

Two $K_{\pi\nu\nu}$ candidate events were observed in the 2017 data set. Combined with one event from the 2016 data sample, the most stringent upper limit on the branching fraction $\mathcal{B}(K^+ \to \pi^+\nu\overline{\nu}) < 1.78 \times 10^{-10}$ at 90 % CL was set, corresponding to the branching fraction $\mathcal{B}(K^+ \to \pi^+\nu\overline{\nu}) = 0.48^{+0.72}_{-0.48} \times 10^{-10}$.

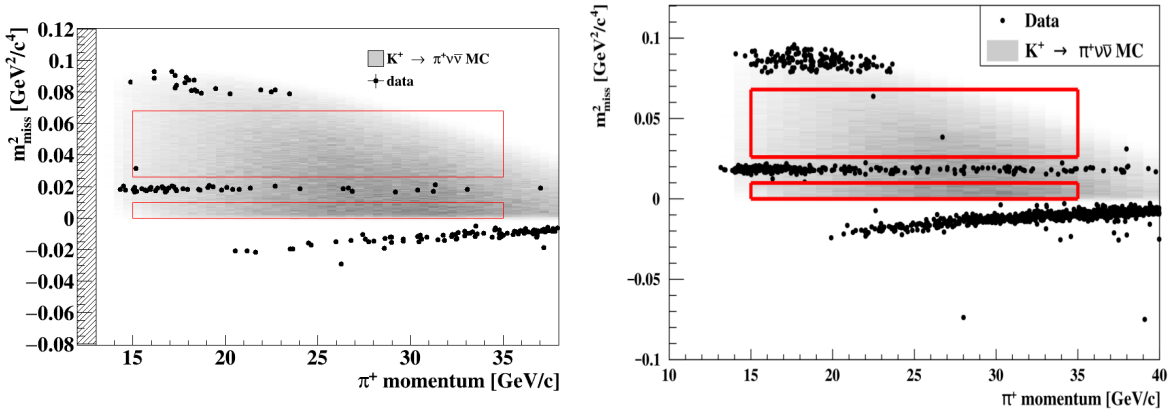

(a) 2016 [80]

(b) 2017 [81]

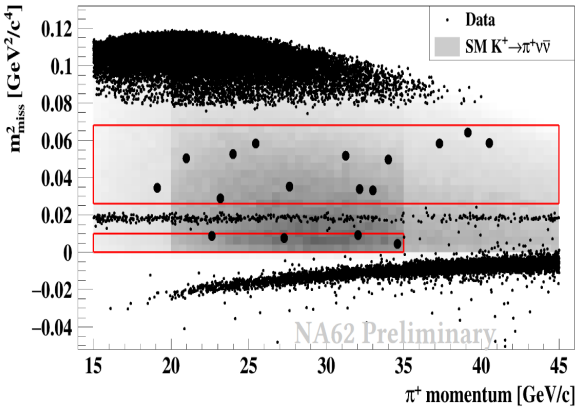

(c) 2018 [82]

Figure 1.2.8: NA62 results of the $K_{\pi\nu\nu}$ measurement from the first three years of data taking. Red rectangles correspond to the $K_{\pi\nu\nu}$ signal regions. Signal event candidates in the 2018 plot are enlarged for better visibility.

The results from the analysis of the last data set (2018), containing almost 4×10^{12} K^+ decays, have recently been presented at the ICHEP 2020 conference [82]. The single event sensitivity, measured at 1.11×10^{-11}, shows a factor-three improvement with respect to the 2017 analysis. To increase the signal acceptance, the $K_{\pi\nu\nu}$ signal region 2 was extended to higher π^+ momenta (see Figure 1.2.8c). In the 2018 data

set, 17 $K_{\pi\nu\nu}$ candidate events were observed in total, while 5.3 background and 7.6 SM signal events were expected.

Combination of the results obtained from all three NA62 data sets leads to the total of ∼10 expected SM signal events and ∼7 expected background events, while observing 20 events. This results in the new measurement of the $K_{\pi\nu\nu}$ branching fraction (Figure 1.2.9):

$$\mathcal{B}(K^+ \to \pi^+ \nu\bar{\nu}) = \left(11.0^{+4.0}_{-3.5}\big|_{\text{stat.}} \pm 0.3_{\text{syst.}}\right) \times 10^{-11}. \tag{1.2.5}$$

The analysis of the full NA62 data set (especially 2017 and 2018 samples, see subsection 1.2.2.1) showed that a significant improvement of the upstream background suppression and increase of the $K_{\pi\nu\nu}$ signal acceptance are needed. With the aim of achieving this, the NA62 collaboration plans to install an additional station to the beam spectrometer and a new upstream veto counter before resuming the data taking in 2021. Subsequently, certain cuts used to suppress upstream background in the current analysis are going to be relaxed.

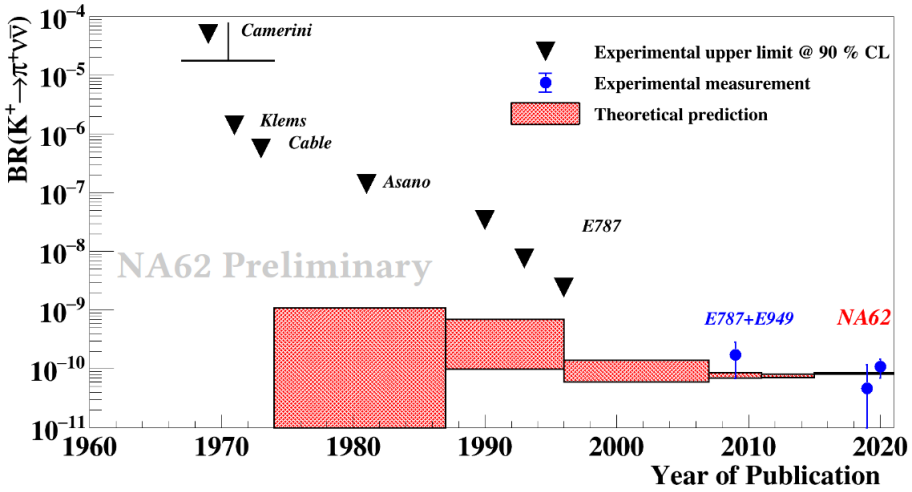

Figure 1.2.9: Historical overview of the $K_{\pi\nu\nu}$ decay measurements [82]. The first NA62 measurement corresponds to the combined 2016 and 2017 results. The second measurement corresponds to the full NA62 data set (2016-2018).

2 NA62

Measurement of such a rare kaon decay as $K^+ \to \pi^+\nu\overline{\nu}$ using the novel decay-in-flight technique poses many challenges for the beam line and detector design. Assuming the SM branching fraction of $K_{\pi\nu\nu}$ (Equation (1.2.2)) and a signal acceptance of a few percent, $\mathcal{O}(10^{13})$ kaon decays are needed to be produced in the fiducial volume to collect $\mathcal{O}(10)$ signal events. Additionally, considering $\sim$10 orders of magnitude difference between the signal and background branching fractions [28], suppression of other kaon decay modes by a factor of $\sim 10^{12}$ is also necessary, which leads to exceptional requirements on the precision of time measurement, spatial and angular resolution, as well as efficient particle identification (especially to distinguish pions and muons) and hermetic photon veto systems.

The NA62 experiment is situated in the CERN North Area located inside of the LHC ring. Simplified experimental setup of the detector is shown in Figure 2.0.1.

The design of the $\sim$300 m long NA62 beam line and the detector is in full detail described in the NA62 Technical Design Document [83], while the updated detector description and performance achieved in the first two years after the detector was commissioned, is reported in [84]. In this section, we summarize the most relevant details about the NA62 beam and detector, trigger system and software used in the presented work.

The detector design and the measurement strategy used by the NA62 benefits the suppression of the dominant background kaon decays ($K_{2\pi}$ and $K_{\mu 2}$) by efficient particle identification and photon rejection. The high momentum (75 GeV/c) of beam kaons and the signal selection of π^+ with momentum less than 35 GeV/c leaves at least 40 GeV of missing energy to be detected by calorimeters with high efficiency. Additionally, the Ring Imaging Cherenkov detector (RICH, subsection 2.1.6) exhibits improved particle separation and identification at lower momenta. Finally, the long design of the NA62 detector allows for the use of a hermetic photon veto system covering angles up to 50 mrad with respect to the beam axis and efficiently detecting photons with energies above 1 GeV.

The NA62 tracking system consists of upstream (GTK, subsection 2.1.2) and downstream (STRAW, subsection 2.1.5) spectrometers separated by $\sim$75 m long vacuum decay region. The location of the upstream spectrometer immediately before

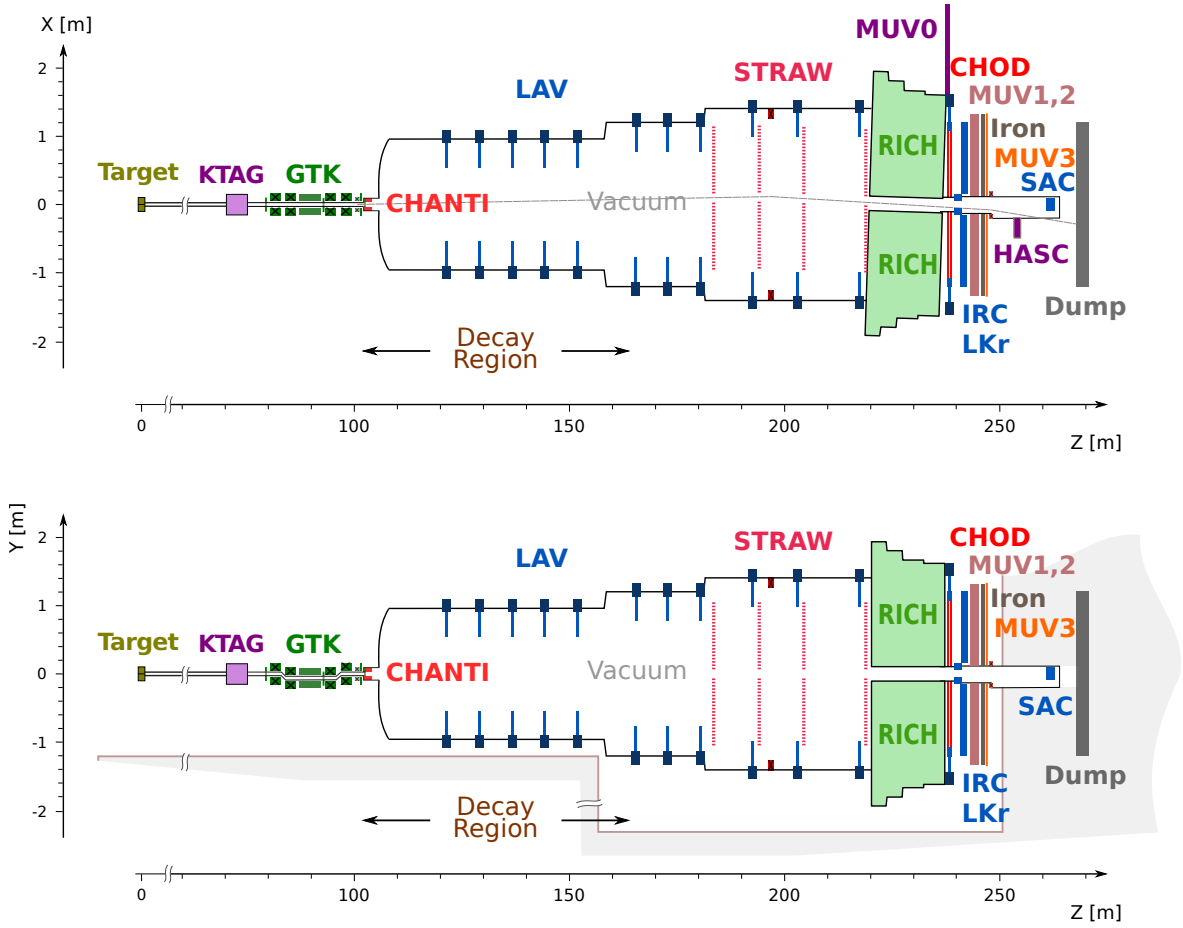

Figure 2.0.1: Schematic layout of the NA62 experiment in XZ-view (top) and YZ-view (bottom) [83]. In the experimental cavern, the Z-axis points downstream, the Y-axis points upwards and the positive X-axis is oriented such that the final coordinate system is right-handed. Beam enters from the left.

the decay region allows for precise measurement of the momentum vector, position and time of all beam particles. Similarly, the downstream spectrometer located right after the decay region provides momentum and position measurement of charged decay products. Time measurement of the charged particles downstream of the decay region is provided by two hodoscopes (NA48-CHOD, CHOD (subsection 2.1.7)) and RICH.

Located at the beginning of the experiment, a Cherenkov sub-detector (KTAG (subsection 2.1.1)) with time resolution of 70 ps is used to identify kaons in the beam. Reconstruction of the kaon component of the beam entering the decay region is achieved by combining the information from KTAG with the momentum and position measured by the GTK.

In the downstream part of the experiment, placed immediately after the STRAW spectrometer, the RICH sub-detector is designed to distinguish pions with momentum above 13 GeV/c from positrons and muons. Additionally, an electromag-

netic calorimeter (LKr (subsection 2.1.8)), a pair of hadronic calorimeters (MUV1, MUV2 (subsection 2.1.10)) and a fast muon veto (MUV3) contribute to the pion identification and suppression of events with positrons and muons. The photon veto sub-detectors (LAV, IRC, SAC (subsection 2.1.9) and LKr) are located along the decay region and further downstream to achieve full geometrical coverage for photons occurring in beam kaon decays.

2.1 Beamline and sub-detectors

A 400 GeV/c proton beam extracted from the CERN SPS accelerator is directed towards a fixed beryllium target in the form of a 40 cm long rod with 2 mm diameter. The secondary particles (mainly protons, pions and kaons), as well as the remaining primary protons then pass through a set of collimators reducing the lateral spread of the secondary beam. Several sets of quadrupole and dipole magnets are used to select the beam with mean momentum of 75 GeV/c and spread of about 1 %. Two collimator modules composed of copper-iron blocks are placed in-between the magnets to absorb the unwanted particles.

The positrons are caused to lose their energy via bremsstrahlung, forcing them to separate from the beam and get absorbed in a collimator. The muons surrounding the hadron beam are separated and swept away by three dipole magnets. Finally, the beam is focused and aligned parallel to the axis of the KTAG by two quadrupole magnets and two collimators. At this point the beam content is mostly protons (23 %) and pions (70 %) with about 6 % of kaons.

2.1.1 KTAG

Due to the high rate in the upstream detectors measuring kaon properties, it is of great importance to positively identify kaons within the hadron beam before they enter the decay region. Placed right after the steering and sweeping magnets at the end of the beamline from the target to the experimental hall, the KTAG sub-detector is used for tagging kaons in the secondary hadron beam. It consists of two parts: a 6 m long radiator volume (CEDAR) filled with nitrogen gas and a circular frame with eight light boxes (also referred to as sectors). The CEDAR is operated at room temperature at 1.75 bar. The pressure is chosen in a way which ensures that only Cherenkov light produced by kaons passing through the gas reaches eight windows surrounding the beam pipe at the end of the vessel. The gas together with CEDAR windows represent a total of 3.5 % X_0 of material in the beam path. The light passing through the windows is focused onto eight spherical mirrors and then radially reflected outwards into the light boxes. Every light box is equipped with 48 conical

light guides, each connected to a photomultiplier placed on the outermost surface of the circular frame. Clear discrimination between kaons and other beam particles is obtained by requiring signal coincidence in at least five KTAG sectors. This setting leads to 70 ps kaon time resolution and 98 % kaon identification efficiency.

2.1.2 GigaTracker

The momentum, direction and time of the beam particles is measured by the beam spectrometer GigaTracker (GTK). It is located inside a vacuum pipe and composed of three similar stations (GTK1, GTK2, GTK3) installed around four dipole magnets arranged in pairs. Particle displacement in the second station due to the horizontal magnetic field allows for the measurement of the beam momentum and direction. Each GTK station is a silicon pixel detector with a total area of $(62.8 \times 27)\,\mathrm{mm}^2$ covered by 18000 pixels with area of $(300 \times 300)\,\mu\mathrm{m}^2$ each. Every station is equipped with ten readout chips organized in two rows and kept at approximately $-15\,^{\circ}\mathrm{C}$ by a single cooling plate. The cooling liquid flowing through micro-channels inside the plate is supplied by an external cooling plant common to the three GTK stations. The total material budget per station including cooling plates does not exceed $0.5\,\%X_0$. This reduces multiple Coulomb scattering and hadronic interactions with the detector, which in turn improves the angular resolution. While most of the products of such interactions in the first two stations are deflected by the magnetic field and absorbed in the final cleaning collimator placed after the last dipole magnet, the inelastic interactions in the last station (GTK3) contribute to the upstream background to the $K^+ \to \pi^+\nu\bar{\nu}$ decay (see Appendix A).

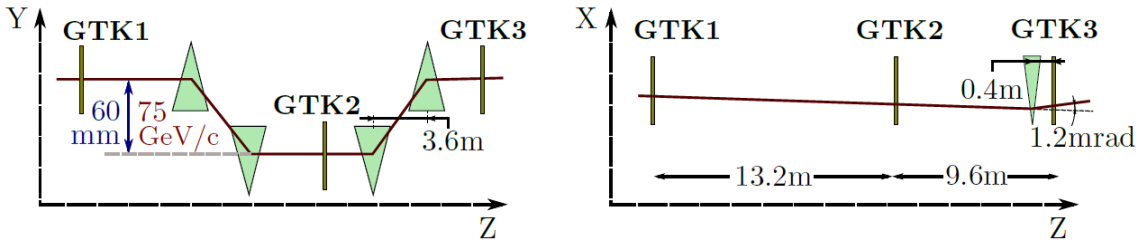

Figure 2.1.1: Scheme of the YZ and XZ-view of GTK stations, four dipole magnets (left) and horizontal steering magnet TRIM5 (right) [84].

At the nominal intensity, the detector is operated at 750 MHz beam rate with up to $1.5\,\mathrm{MHz/mm}^2$ around the station centre. It is expected to sustain such conditions without significant degradation of performance for at least 100 consecutive days. Even in such extreme conditions, time resolution of less than 200 ps, required for a successful association of a beam particle with kaon decay products, has been achieved. The pixel dimensions and station separation allows to measure beam mo-

mentum with 0.2 % precision and direction with 16 µrad precision.

A horizontal steering magnet TRIM5 placed before the last GTK station is used to deflect the beam by 1.2 mrad towards positive X. The angle is adjusted such that a subsequent deflection by 3.6 mrad in negative X direction in the MNP33 magnet in the STRAW spectrometer directs the beam through the central aperture of the LKr calorimeter.

During the 2017 and 2018 data taking, two new passive components were installed in the area of the GTK sub-detector to suppress pions produced before the decay volume causing upstream background to $K_{\pi\nu\nu}$ (discussed in Appendix A). In 2017, a copper plug was inserted in the upper part of the aperture of the last dipole magnet. Additionally, the original final cleaning collimator was replaced with a larger one in 2018.

2.1.3 CHANTI

Inelastic interactions of the beam in the last GTK station produce particles which can enter the decay region and geometrical acceptance of the downstream detectors creating background for the $K_{\pi\nu\nu}$. Similarly, muon halo surrounding the beam and charged particles generated upstream of the GTK3, which are not swept away by magnets between the GTK stations, contribute to the background as well. The Charged Anti-Coincidence detector (CHANTI) consists of six squared hodoscope stations installed between the GTK3 and the decay volume and provides time measurement of the charged particles coming from the upstream part of the NA62 detector.

Each station covers area of $(300 \times 300)\,\mathrm{mm}^2$ with a $(95 \times 65)\,\mathrm{mm}^2$ hole in the center to allow free passage of the beam. The first station is placed 28 mm downstream of GTK3 and the distance between each two successive stations approximately doubles to cover angles between 49 mrad and 1.34 rad for particles generated in GTK3. The stations are made of two planes, one with horizontally and one with vertically oriented scintillator bars of triangular cross section arranged alternately in each plane. Every station consists of 48 bars connected to silicon photomultipliers. The CHANTI is operated in a vacuum.

2.1.4 Vacuum vessel

The vacuum vessel consists of cylinders of various diameters intercepted by 11 LAV stations and four STRAW stations with MNP33 magnet. Pressure inside this evacuated region with total length of about 116.5 m is kept below 10^{-6} mbar to minimise interactions with the residual gas. The first cylinder is placed immediately after the

last CHANTI station. The vessel is closed off after the last STRAW station by a thin aluminium window separating it from the gas in the RICH sub-detector. However, the vacuum is extended via an aluminium beam pipe which follows the trajectory of the beam and allows it to pass freely through the downstream detectors. After MUV3, the beam is deflected by 13.6 mrad towards negative X by a dipole magnet (BEND) and finally absorbed in an iron-concrete block.

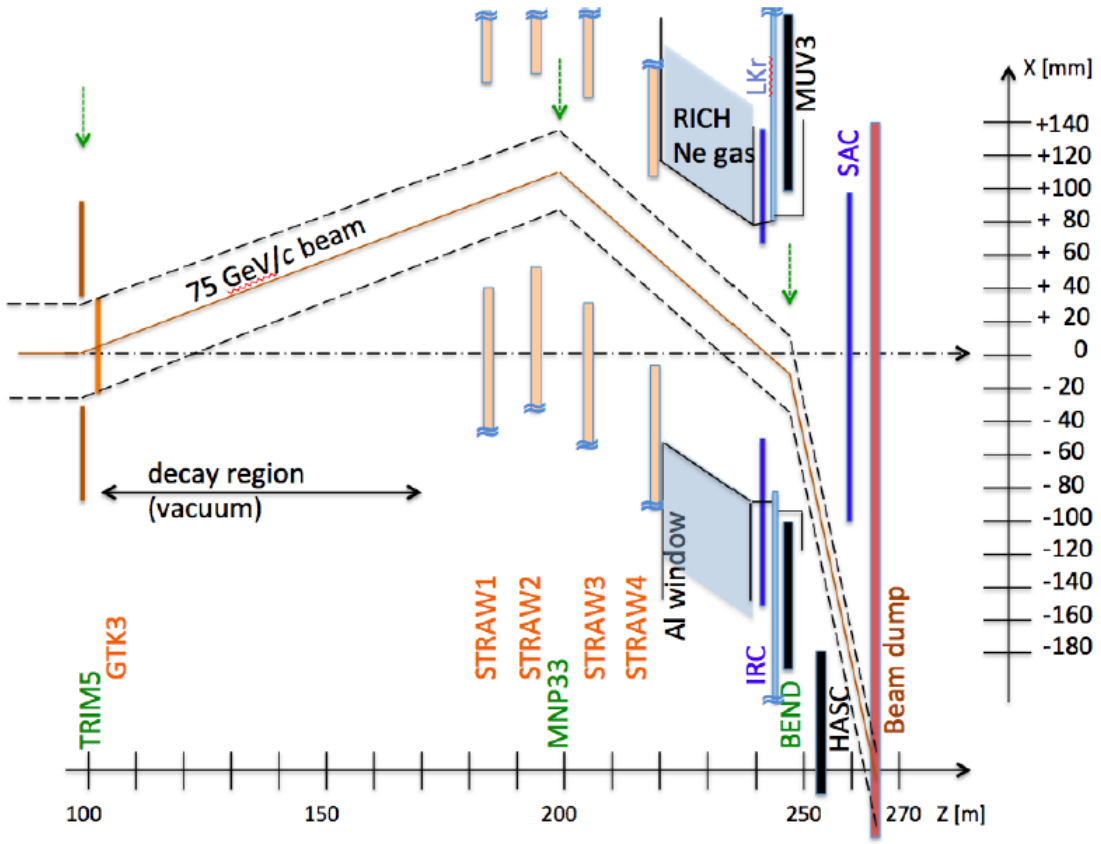

Figure 2.1.2: Schematic view of the NA62 beam line after the GTK3 station in XZ-view [84].

The part of the vessel between the last GTK station and the first STRAW spectrometer chamber is referred to as the Blue Tube. In this region, the trajectories of charged particles are affected by the magnetic field (so called Blue Tube field) with two sources: the Earth and the metallic material of the tube. A field map has been measured before the data taking and its effect has to be taken into account in the offline analysis when charged particle trajectories are extrapolated from the spectrometers to the decay region.

A fiducial decay region is contained in the first 60 m of the vacuum vessel. In this region about 10 % of beam kaons decay and the decay products are registered in the downstream sub-detectors.

2.1.5 STRAW spectrometer

The purpose of the STRAW spectrometer is to measure the direction, momentum and position of the charged particles downstream of the decay region. The STRAW sub-detector, spanning over 35 m inside the vacuum vessel, consists of four similar chambers with a high aperture dipole magnet MNP33 located in the middle. The magnet provides a vertical magnetic field of 0.36 T, which results in deflection of the beam passing through holes in the STRAW chambers towards the center of the aperture of the LKr sub-detector.

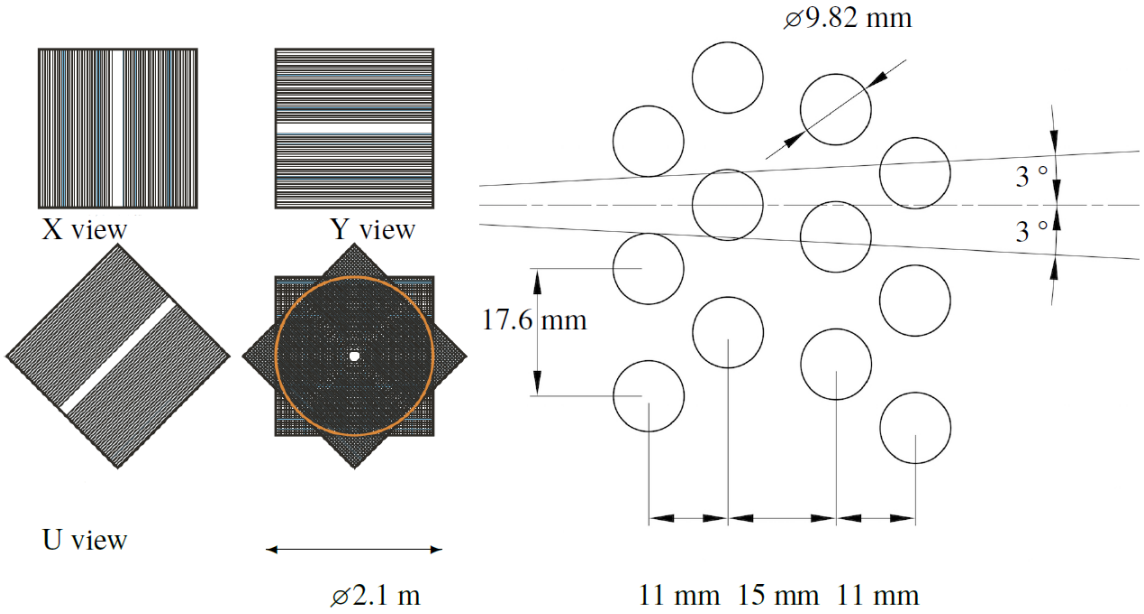

Figure 2.1.3: Example of individual STRAW views X, Y, U and combination of four STRAW views in one chamber (left). Schematic drawing of straws and spaces between them in four layers of one view (right). [84]

Each STRAW chamber consists of 16 layers of parallel drift tubes (straws) divided into four views - X, U, Y and V - rotated from the vertical position by 0°, 45°, 90° and 135° around the beam axis, respectively. Every view is formed by four planes of 112 straws. The planes are slightly shifted in the direction perpendicular to the orientation of the straws to guarantee at least two hits in a view per particle. Each view has a gap with missing straws near the center to allow for beam passage. Considering the full chamber, this results into several regions covered by only 1, 2 or 3 views and an octagonal hole with 6 cm apothem near the center of the chamber. The position of the gaps in the views, and subsequently the position of the hole, is specific to a chamber and is adjusted to accommodate the beam trajectory deflected by TRIM5 and MNP33 magnets.

The straws are 2.1 m long and 9.8 mm in diameter, and are made of a 36 µm thick PET foil coated on the inside with a 0.05 µm layer of copper and 0.02 µm layer of gold

to provide electrical conductance on the cathode. The anode wire stretched through the center of each tube is made out of gold-plated tungsten with total diameter of 30 µm. The straws are filled with a gas mixture of 30 % CO_2 and 70 % argon at the atmospheric pressure. The total amount of material in the STRAW corresponds to 1.8 % X_0.

The design of the STRAW spectrometer allows to achieve the level of kinematic rejection of background from the most abundant kaon decays required by the analyses at the NA62 experiment. The arrangement of the straws into layers, views and chambers is optimised to provide redundancy of space points for the momentum measurement, resulting into following track momentum resolution:

$$\frac{\sigma_p}{p} = 0.300\,\% \oplus 0.005\,\% \cdot \frac{p}{\mathrm{GeV}/c}. \tag{2.1.1}$$

Track angular resolution improves for larger track momenta: from 60 µrad at 10 GeV/c to 20 µrad at 50 GeV/c. Time resolution of the reconstructed tracks is about 6 ns and thus several times larger that time resolution of most of the sub-detectors in NA62. This is caused by poor ($\sim$30 ns) trailing time resolution of individual hits.

2.1.6 RICH

The RICH detector, or Ring Imaging Cherenkov counter, consists of a 17.5 m long cylindrical vessel filled with neon gas at atmospheric pressure and room temperature. These parameters are optimised to provide the best possible pion–muon separation for charged particles with momenta between 15 GeV/c and 35 GeV/c.

Particles traversing the neon gas emit Cherenkov radiation at angles larger for high velocity particles. The downstream end of the vessel is equipped with a mosaic of 18 hexagonal and two semi-hexagonal spherical mirrors with the focal length of 17 m. The Cherenkov cones are reflected as rings on two arrays embedded into the upstream end of the RICH vessel outside of the RICH active area, each consisting of 976 photomultipliers. The diameter of each array is about 0.7 m. Due to this requirement the vessel diameter has to be extended to 4.2 m at the upstream end, while the diameter of the vessel element with mirrors is only 3.2 m. The active area of the RICH increases from 1.1 m radius at the entrance to 1.4 m radius at the exit window. A lightweight aluminium beam pipe is placed at the RICH axis and is connected to the vacuum vessel.

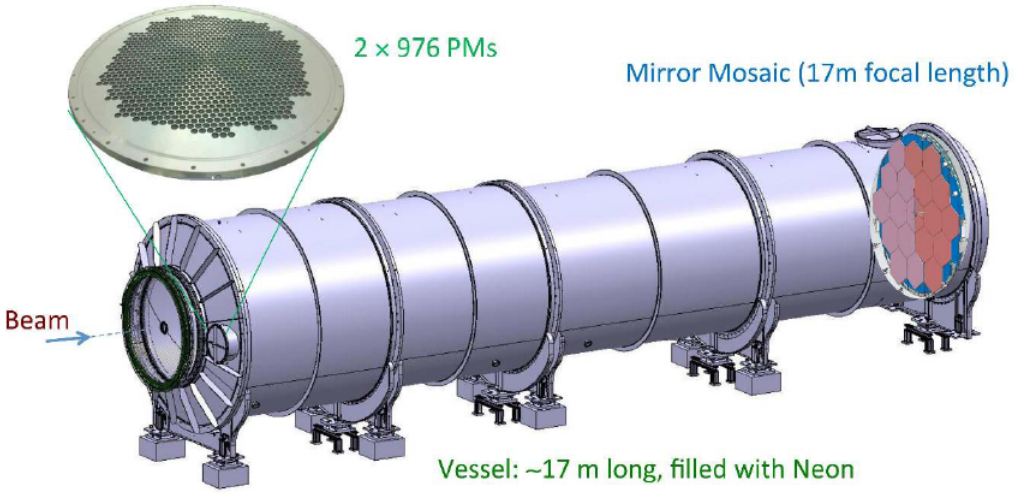

Figure 2.1.4: RICH vessel with mosaic of mirrors at the downstream end and closer look at one of the two arrays with photomultipliers [84]. The beam enters from the left.

The ring radius seen by the photomultipliers depends on the particle momentum and type and is used to distinguish pions from positrons and muons. The time resolution of a RICH ring is better than 100 ps.

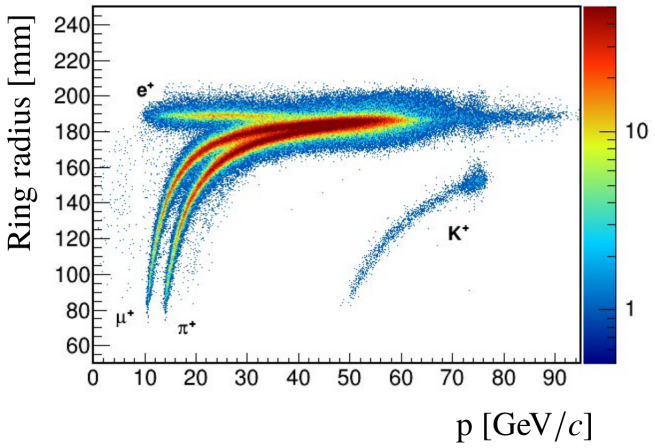

Figure 2.1.5: Cherenkov ring radius in the RICH as a function of particle momentum [84].

2.1.7 Charged particles hodoscope system

The NA62 setup includes two independent charged particle hodoscopes operated simultaneously. They are placed between the RICH and the LKr calorimeter, about 70 cm apart, and are exposed to a nominal rate of 30 MHz and 45 MHz of charged particles with about 13 MHz coming from beam kaon decays and the rest caused by high multiplicity events from interactions in the material upstream of the hodoscopes. Apart from time and position measurement, they also provide reference

times for events with charged particles in the final state.

NA48-CHOD

The NA48-CHOD, located before the LKr calorimeter, was previously used in a former kaon experiment NA48, and is reused in NA62 to provide an input for the minimum bias trigger (subsection 2.2.2) and to detect possible photo-nuclear interactions in the RICH mirror plane. It consists of two consecutive octagonal planes of 64 horizontal and vertical scintillating slabs arranged in four quadrants, with a central hole of 128 mm radius for the beam pipe. The slabs width varies from 65 mm in the central part, where finer granularity is required due to a higher particle flux, to 99 mm in the outer parts. Each slab is connected to a photomultiplier via a light guide. The time measurement is performed independently in both planes and a time coincidence in the same quadrant is required, thus improving the time resolution to ∼200 ps, while the spatial resolution is given by the slab widths.

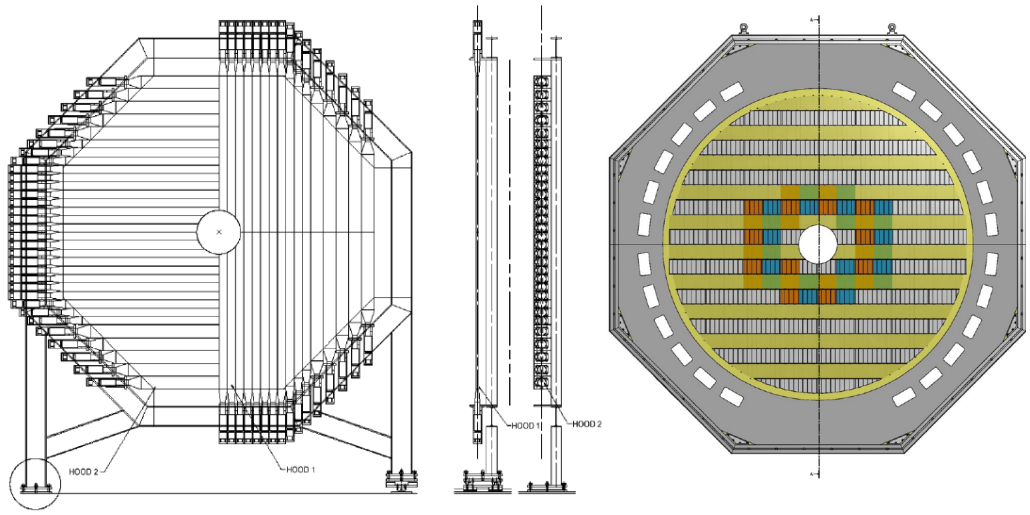

Figure 2.1.6: Drawing of the vertical and horizontal layers of NA48-CHOD slabs (left, center). In reality each layer covers full area of the octagon. Front view of CHOD tiles (right). [84]

CHOD

The CHOD sub-detector, optimised specifically for the high intensity conditions at NA62, is placed immediately after the RICH. It consists of a circular array of 152 rectangular plastic scintillator tiles covering an area of 1070 mm radius with a central hole (280 mm in diameter) for the beam pipe. The 30 mm thick tiles are arranged in horizontal stripes 108 mm high. Width of the tiles varies from 134 mm in the central part around the beam pipe to 268 mm in the rest of the active area. The scintillation light from each tile is collected and transmitted by optical fibers and detected by a pair of silicon photomultipliers placed outside of the detector active region. Time

resolution of the CHOD is ∼1 ns.

2.1.8 LKr

The LKr electromagnetic calorimeter was previously used in the NA48 experiment and after several upgrades, it is reused by NA62 as a part of the photon veto system and to provide energy measurement for photons and charged decay products. Besides a vacuum beam pipe of 16 mm in diameter passing through the center, the volume of 127 cm long tank with 128 cm radius is filled with about 9000 litres of liquid krypton at the temperature of 120 K maintained by a cryostat holding the tank. The sensitive area of this ionization chamber is divided by Cu-Be electrode ribbons into 13248 longitudinal cells with approximate cross-section of $(2 \times 2)\,\mathrm{cm}^2$.

The electrodes are directly attached to preamplifiers located inside the cryostat, which collect the signal from showers produced by particles crossing the LKr. The old readout system was upgraded to be able to operate in high rate environment and to satisfy the requirements for an excellent photon detection efficiency above 35 GeV and to provide trigger signals based on the deposited energy. The relative energy resolution of the LKr is

$$\frac{\sigma_E}{E} = \frac{4.8\,\%}{\sqrt{E}} \oplus \frac{11\,\%}{E} \oplus 0.9\,\%, \tag{2.1.2}$$

where the energy is given in GeV.

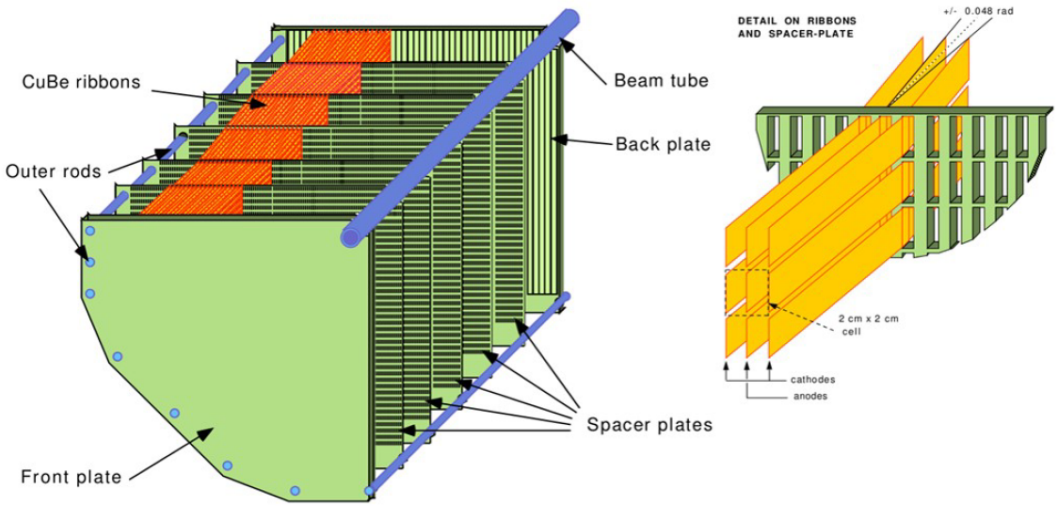

Figure 2.1.7: Lower left quadrant of the LKr vessel with spacer plates supporting electrodes (left). Example of the electrode ribbons (right). [84]

2.1.9 Photon veto system

The photon veto system of the NA62 detector consists of 12 stations of Large-Angle Veto (LAV), the LKr, the Intermediate Ring Calorimeter (IRC) and the Small-Angle

Calorimeter (SAC) sub-detectors. It is used mainly to eliminate photon background, such as the one from $K^+ \to \pi^+\pi^0$ ($\pi^0 \to \gamma\gamma$), and is able to register photons coming from the decay region at angles between 0 mrad and 50 mrad with respect to the beam axis. The angular acceptance in the intermediate range between 1 mrad and 8.5 mrad is covered by the LKr.

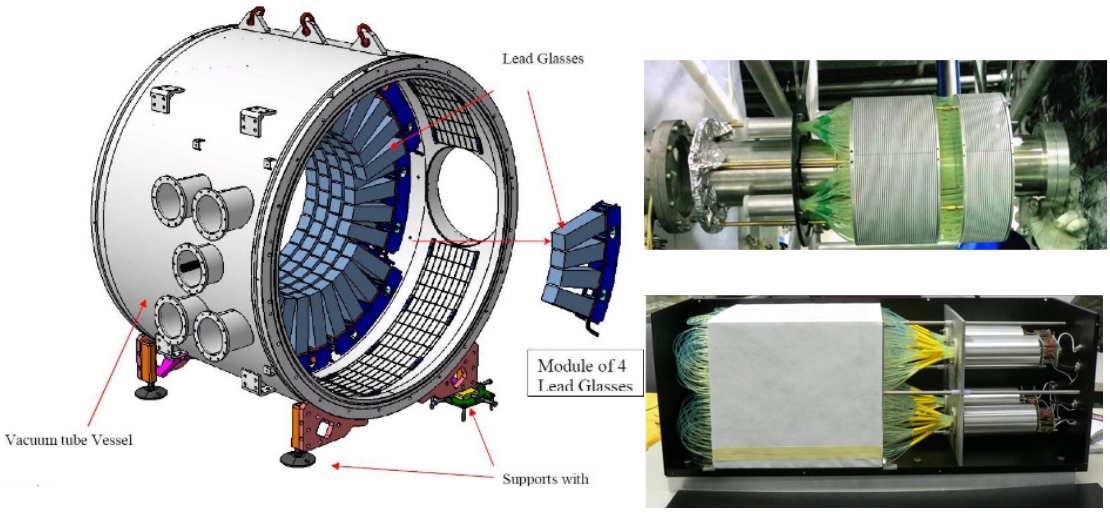

Figure 2.1.8: A section of the vacuum vessel with one LAV station (left) [83]. Picture of IRC sub-detector during installation, the beam enters from right (top right). Picture of SAC sub-detector during testing (bottom right). After installation into the vacuum tube, the detected particles are incident from the left. [84]

LAV

The LAV system consists of 12 similar ring-shaped stations, the first eleven of which are part of the vacuum vessel, while the last station is placed between CHOD and NA48-CHOD and is operated in air. The stations with outer diameter varying from about 2200 mm (LAV1-5) up to 3300 mm (LAV12) are distributed in such a way so that they provide full geometrical coverage for photons emitted from the decay region at angles between 8 mrad and 50 mrad.

The basic building blocks are 37 cm long lead-glass crystals mounted radially in four or five rows around the inner perimeter of a ring-shaped support structure. Each block is read out by a photomultiplier attached to the back face with an area of $(11 \times 11)\,\mathrm{cm}^2$. The electromagnetic showers produced by photons crossing the lead-glass blocks are detected via Cherenkov light.

The LAV system provides measurement of time with resolution of about 1 ns,

and of energy with about 10 % accuracy, which fulfills the requirements for application of photon veto conditions in offline analysis, and also facilitates the use of LAV veto condition in online triggers.

SAV

The small-angle veto system consists of two sub-detectors, IRC and SAC, with combined angular acceptance in range (0, 1) mrad.

The IRC sub-detector is a shashlyk calorimeter in the cylindrical shape with outer diameter of 290 mm surrounding the vacuum beam pipe. It is divided into two subsequent modules spaced by 40 mm gap. The modules consist of ring-shaped 1.5 mm thick lead absorber layers alternated with 1.5mm thick scintillator plates. The scintillation light produced by photons is collected by optical fibers traversing both modules through a mesh of 570 holes. At the downstream end of the IRC, the optical fibers are bundled into four sections each connected to a photomultiplier. The detector is enclosed in a black cover ensuring light tightness.

The SAC sub-detector consists of 70 plates of lead alternated by 70 plates of plastic scintillator. The plates are 1.5 mm thick and have square cross section with dimensions $(205 \times 205)\,\mathrm{mm}^2$. Optical fibers are threaded through the module in a rectangular grid of 484 holes. Each fiber traverses the module twice, thus keeping both ends of the fiber at the back face of the SAC, where the fibers are grouped into four bundles, each connected to a photomultiplier. The SAC is installed inside a tube extending the beam vacuum behind the final magnet deflecting the beam towards the beam-dump.

2.1.10 Muon veto system

The muon veto system consists of two hadronic sampling calorimeters MUV1 and MUV2 and a fast muon veto MUV3. It provides complementary discrimination between pions and muons as well as input to online L0 trigger (only MUV3, see subsection 2.2.2).

MUV1

The MUV1 module is made of 24 layers of iron and 23 layers of vertically or horizontally oriented 60 mm wide scintillator strips. The module has a rectangular cross section with dimensions $(2700 \times 2600)\,\mathrm{mm}^2$. The strips are connected via optical fibers to a total of 176 photomultipliers.

MUV2

The MUV2 module was previously used as a part of the NA48 hadronic calorimeter.

It consists of 24 iron plates each followed by a layer of horizontally or vertically oriented 119 mm wide plastic scintillator strips. The module is read out by 88 photomultipliers connected to scintillator strips by Plexiglass light guides. Both modules have similar dimensions with a vacuum beam pipe passing through the center and are placed immediately after the LKr.

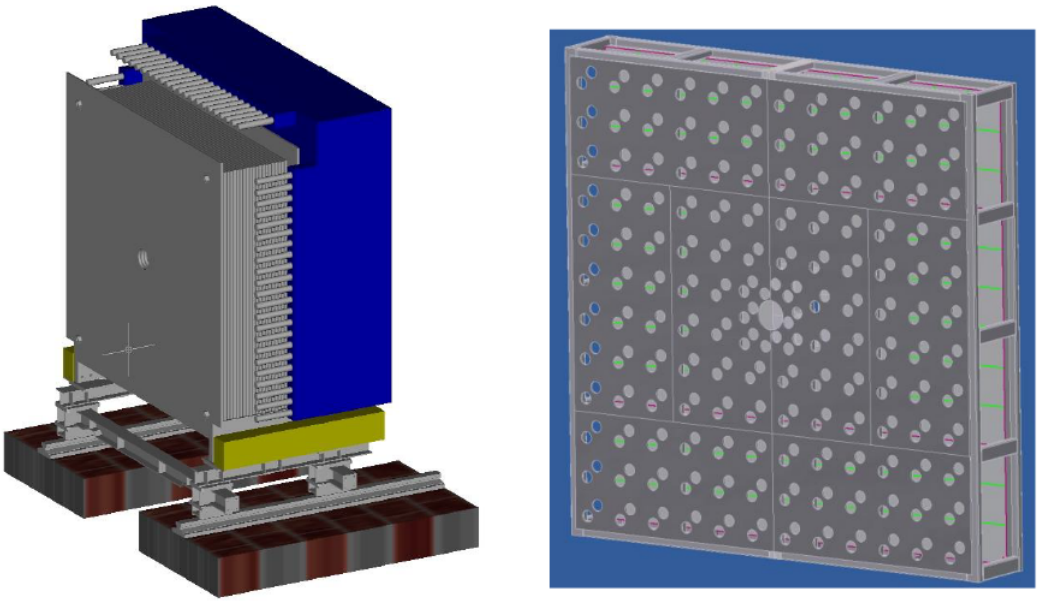

Figure 2.1.9: View of MUV1 (grey) and MUV2 (blue) modules (left), the beam is incident from the left. Layout of the MUV3 module (right). The holes indicate positions of photomultipliers. [83]

MUV3

The MUV3 sub-detector is located behind an 80 cm thick iron wall separating it from the MUV1 and MUV2 modules and serving as a filter for muons. Both the iron wall and the MUV3 have a circular opening in the center to accommodate the beam pipe. The MUV3 is a square shaped module with dimensions of $(2640 \times 2640)\,\mathrm{mm}^2$ divided into 148 mostly rectangular scintillator tiles with smaller dimensions in the areas adjacent to the beam pipe. The tiles are divided by aluminized PET foil and at the back each connected via light-tight boxes to two photomultipliers. The MUV3 is exposed to a total rate of 13 MHz of muons at nominal beam intensity.

The MUV3 muon identification efficiency exceeds 99.5 % for muon momenta above 15 GeV/c and the signal time resolution of individual channels is about 0.5 ns.

2.1.11 Additional veto detectors

Two complementary veto detectors, MUV0 and HASC, are used to detect pions from $K_{3\pi}$ decays outside of the STRAW geometrical acceptance.

MUV0

The MUV0 is designed to detect negative pions with momenta below 10 GeV/c produced in $K_{3\pi}$ decays. Passing through the STRAW, they are deflected by the MNP33 magnet towards positive X (as opposed to the positive particles and the beam deflected towards negative X), causing them to escape the geometrical acceptance of the RICH. The MUV0 is a scintillator hodoscope placed in the first quadrant (+X, +Y) downstream of the RICH. It covers an area of $(1.4 \times 1.4)\,\mathrm{m}^2$ and consists of two layers of 48 plastic scintillator tiles. Both layers are divided into nine super-tiles, each connected to a photomultiplier via optical fibres.

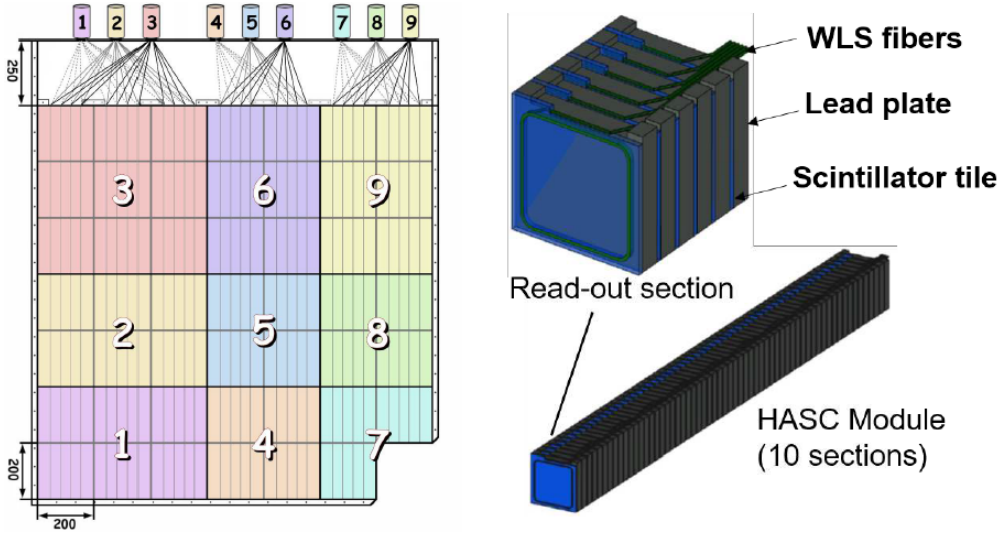

Figure 2.1.10: Shcematic view of MUV0 subdetector (left) with nine super-tiles connected to photomultipliers at the top. One HASC section with layers of lead and scintillator (top right) and a full HASC module (bottom right). [84]

HASC

The hadronic sampling calorimeter, HASC, is designed to detect positive pions with momenta above 50 GeV/c originating in $K_{3\pi}$ decays, that escaped the STRAW acceptance through the beam holes. Such pions are separated from the beam by the last bending magnet and are deflected towards a specific area at negative X. The HASC is constructed of nine modules arranged in three rows with total cross section of $(100 \times 100)\,\mathrm{mm}^2$. A HASC module consists of 60 plates of lead, each followed by a scintillator layer, and is divided into 10 consecutive sections. Every section is connected via optical fibers to a photomultiplier placed behind the module.

2.2 Data taking

The NA62 Experiment was commissioned in 2014 and started taking data in 2015, however without fully equipped GTK sub-detector. The first physics run took place

in 2016-2018, in which the NA62 collected data for the $K_{\pi\nu\nu}$ measurement as well as for other physics analyses. During the current LHC shutdown (LS2), the NA62 detector is undergoing an upgrade and will resume collecting physics data in 2021.

2.2.1 Data taking conditions

The NA62 beam provided by the SPS is delivered in spills lasting about 6 s (3 s effective) separated by ∼10 s breaks. A burst corresponds to data recorded in an individual spill, while a set of $\mathcal{O}(1000)$ consecutive bursts sharing the same experimental conditions represents a run.

All runs collected by NA62 in years 2016, 2017 and 2018 are divided into periods which differ by essential changes in data-taking conditions or are naturally defined by planned or unplanned breaks in data-taking. The periods are referred to by year in which the data was collected and a capital letter: 2016(A,B), 2017(A-D), 2018(A-H). Some of the changes considered relevant for the presented work are summarized in Table 2.2.1 together with corresponding data-taking periods affected by that change.

Two shielding components against upstream background events were installed before the decay region during the first physics run. A copper insert was placed in the gap inside the last GTK magnet above the beam. Additionally, a 1 m long collimator was installed between the last two GTK stations to absorb particles from upstream kaon decays.

Beam intensity 350 MHz	2016
Beam intensity 450 MHz	2017, 2018(A-G)
High intensity test (750 MHz)	2018H
Copper insert installed in the last GTK magnet	2017A, 2018
Collimator installed immediately before TRIM5	2018(D-H)

Table 2.2.1: Summary of data taking conditions relevant for this work and affected data sets.

2.2.2 Trigger conditions

In order to efficiently utilise disk space by storing only the relevant data, one hardware (L0) and two levels of online software triggers (L1, L2) are implemented in NA62 (L2 is currently not used). The L0 trigger decision is based on the output of basic signal clustering algorithms specific to each sub-detector involved in the L0 trigger scheme. The information is issued in the form of trigger primitives and is

collected by L0 trigger processor. While the L0 trigger decision is being evaluated, data from all sub-detectors is stored in buffers.

After a positive L0 trigger decision is made, the data associated with the L0 trigger timestamp is moved to a PC-farm where L1 trigger algorithms are evaluated. All data corresponding to an event which passed the selected trigger stream is saved on tape, the rest of the data is discarded.

Multiple trigger schemes suited for physics analysis and detector calibration are designed and used in parallel. In this work, the data collected with minimum bias (also referred to as control) and PNN trigger streams is used.

Control trigger

The control trigger stream contains a single condition in L0 and does not employ any L1 trigger algorithm. The L0 condition requires time coincidence of signals from at least one pair of horizontal and vertical NA48-CHOD slabs. If this event passed a L0 RICH condition (see below), a trigger time is defined by the RICH, otherwise the NA48-CHOD time is used. Due to high rate of data passing this condition, the control trigger is downscaled by a factor of 400. In the presented analysis, data collected with control trigger is used to measure STRAW track reconstruction efficiency (Section 3.2) and to estimate backgrounds and kaon flux in the $K_{\pi\nu\nu}$ analysis (Chapter 4).

PNN trigger

The PNN trigger stream is developed specifically for the $K_{\pi\nu\nu}$ measurement and consists of RICH, CHOD, MUV3 and LKr conditions at L0 and KTAG, LAV and STRAW algorithms at L1. The L0 RICH condition is fulfilled if a cluster in the RICH consisting of at least two hits within 6.25 ns is found. Time of the cluster defines the event trigger time used as a reference for time coincidences with other L0 primitives as well as in the offline analysis. The L0 RICH condition is meant to select events with at least one charged particle. The L0 CHOD condition requires time coincidence between hits in one to four CHOD tiles, but rejects events with time coincidence between hits in tiles located in opposing CHOD quadrants, aiming to suppress the $K_{3\pi}$ decays. Similarly, the L0 MUV3 condition is meant to suppress $K_{\mu 2}$ events by asking for no signal in the MUV3 in coincidence with the trigger time. Finally, to reject $K_{2\pi}$ events, the L0 LKr condition requires that no more than one cluster is found and less than 30 GeV of energy is deposited in the LKr.

The L1 trigger algorithms evaluate sub-detector information obtained from simplified online event reconstruction. The algorithms are executed in a specific order given by their complexity and processing time. The L1 KTAG algorithm is executed first and requires a kaon candidate reconstructed from hits in more than four KTAG

sectors to be in time with the trigger time. It is followed by the L1 LAV algorithm checking that in each LAV station, hits in at most two LAV blocks are in time with the trigger. Finally, the L1 STRAW algorithm looks for a STRAW track with momentum less than 50 GeV/c forming a vertex with the nominal beam axis upstream of the first STRAW station.

2.3 NA62 framework

The NA62 software framework [85] consists of three parts: Monte Carlo (MC) event simulation in the NA62 detector, event reconstruction and data analysis. The software is developed mostly in C++ using ROOT library [86].

2.3.1 Detector and event simulation

The NA62 MC package used to produce Monte Carlo samples of various kaon decays is developed within the NA62 collaboration with the use of external tools mentioned in the following paragraphs.

Simulation of the kaon beam component starts at 69.2 m. A computer program for simulating charged particle beams, Decay TURTLE [87], is used to propagate the kaon beam through the beam optics up to the KTAG. From this point onwards, propagation of kaons and their decay products through the detector, interactions with the material, as well as full simulation of the NA62 detector is handled by Geant4 toolkit [88, 89, 90]. Decay generators developed at NA62 are used to produce kinematics of particle decays according to theoretical (usually Standard Model) computations and pass the generated particle properties to Geant4.

Simulated detector response is saved in MC hits containing true information about position, energy, time or other variables relevant for a given sub-detector.

The beam position and momentum, as well as other MC parameters are tuned to match data taking conditions of reference runs selected in data.

The output consisting of the simulated detector response and true information about particles obtained from Geant4 is stored in ROOT files.

2.3.2 Reconstruction

The NA62 reconstruction package consists of two modules. The first module, used for digitization of MC hits, produces MC output equivalent to the stored data. The second module performs event reconstruction and consists of reconstruction algorithms specific to each sub-detector. It is executed identically on data and MC

output from the first module, and produces reconstructed *hits* containing information about reconstructed signal properties relevant for a given sub-detector. Reconstruction algorithms for most of the sub-detectors use the hits to produce *candidates*, which ideally contain single particle properties measured by a given sub-detector. The GTK and STRAW reconstruction algorithms are summarized in the following paragraphs, as they play an important role in this work.

The GTK reconstruction algorithm starts by selecting hits in the GTK stations within a set time window with respect to a reference and combining them into triplets. Three χ^2 variables, testing compatibility of hit times with their weighted mean and the hit positions in XZ and YZ-planes, are computed for each triplet and then summed to be used as a test of a GTK candidate reconstruction quality. Considering the XZ-plane, hit positions in the first two GTK stations are corrected for the effect of the TRIM5 magnet and fitted with a straight-line using a χ^2 fit. On the other hand, the beam trajectory in the YZ-plane is affected by two pairs of dipole magnets allowing the beam momentum measurement. In this case, a χ^2 variable is built to test the compatibility of hit Y-positions in each two consecutive GTK stations. Finally, the hit-triplet momentum is computed from the Y hit positions in GTK stations, taking into account the magnetic field of the bending magnets. The momentum slope in the XZ-plane is obtained from the straight-line fit and the slope in YZ-plane is computed from the Y hit positions in the first and the last GTK stations. The obtained momentum and slopes are checked for consistency with the nominal NA62 beam parameters. Triplets that pass the conditions form GTK candidates containing information about hit times and positions, particle momentum, χ^2, etc.

The STRAW candidate reconstruction procedure consists of multiple stages and uses the trailing and leading times of the hit signal to define hit time and distance from the straw wire, respectively. Firstly, hits within each view are grouped into view-clusters, solving the ambiguity in hit position with respect to the wire by considering the wire distance and cluster slope, if possible. The current STRAW sub-detector design, specifically the straw staggering in each view, ensures that a charged particle produced in the decay region passes through two or three straws in a view. However, due to detection inefficiency close to the straw wall, it is expected to reconstruct view-clusters with one, two or three hits corresponding to a three-straw path, and one or two hits corresponding to a two-straw path. Since the central part of each view is not occupied with straws to allow for the beam passage, the four rotated views forming a chamber create areas covered by one, two, three and four views. If possible, the view-clusters in each chamber are grouped into quad-

ruplets or triplets forming chamber-clusters. Pattern recognition algorithm employing the Hough transform [91] in the YZ-plane (not affected by the MNP33 magnet) and simple extrapolation in the XZ-plane is then used, testing all combinations of chamber clusters. First estimation of the track parameters (momentum, slopes) is obtained from the calculations in the XZ-plane. Finally, Kalman filter [92] is used to fit the STRAW track and provide precise computation of the STRAW candidate momentum, slopes and positions in each STRAW chamber. A STRAW track can be reconstructed from clusters in three or four chambers.

2.3.3 Analysis

The NA62 analysis package comprises analyzers used for event selection and filtering (including selections described in Section 3.1, Section 3.3, Section 3.4 and Section 3.5), for monitoring of data quality (including `SpectrometerEfficiency` analyzer described in Section 3.2), algorithms used for association of hit clusters or candidates between sub-detectors (including association tools referenced in subsection 4.1.1.2, as well as matching algorithms defined in subsection 4.2.1, subsection 4.2.2.1 and subsection 4.2.2.2) and other tools used in physics analyses (such as `StrawSegmentAlgorithm` summarized in subsection 4.1.2.6). Additionally, STRAW and GTK candidate reconstruction algorithms implemented in subsection 2.3.2 are made accessible from this package and can be used within any analysis. This is to give the user an opportunity to use custom settings and reference times to build the candidates.

A special category of tools, referred to as pre-analyzers, are to be applied prior to the standard analyzers. Five pre-analyzers are used in the presented work and are referenced correspondingly.

The `UpstreamPileupGenerator` is applied on MC events to reproduce the accidental activity in the GTK by injecting GTK hits based on the beam intensity spectrum measured in the reference run. Additionally, a constant 4 % GTK hit reconstruction inefficiency is simulated by removing randomly chosen GTK hits by the `GigaTrackerInefficiency`. The `DownstreamPileupGenerator` is used to inject accidental hits to multiple downstream sub-detectors (STRAW, CHOD, LKr, MUV3, LAV, IRC, SAC) to emulate the pile-up caused by products of overlapping beam particle decays, muon halo surrounding the beam, or unwanted interactions with the detector material. Both pile-up–generating pre-analyzers are used in this work in the STRAW efficiency analysis (Section 3.2), while only the `UpstreamPileupGenerator` and `GigaTrackerInefficiency` are used in the $K^+ \to \pi^+ \nu\overline{\nu}$ decay analysis (Chapter 4).

The `SpectrometerTrackCorrections` pre-analyzer is in the presented work

applied on both data and MC in the $K_{\pi\nu\nu}$ decay analysis. When applied on data, it is used to correct the momenta magnitudes of the reconstructed STRAW candidates for the variations in the MNP33 magnetic field integral and for the residual misalignment of the STRAW stations. Applied on MC, it corrects for residual differences between the MNP33 field map integrals in the MC and in the reconstruction. Contrary to data, the MC corrections do not reflect any physical changes in the STRAW sub-detector. The `LKrClusterCorrections` pre-analyzer, applied on data and MC in $K_{\pi\nu\nu}$ decay analysis and the STRAW track reconstruction efficiency evaluation, is used to fine-tune the reconstructed LKr cluster energies and positions. In the default mode (used in both presented analyses), the energy of LKr clusters is corrected to fix the $\pi^0 \to \gamma\gamma$ reconstructed mass to the PDG [28] value of the neutral pion mass.

3 STRAW track reconstruction efficiency

In this chapter, the measurement of the reconstruction efficiency of π^+, μ^+ and e^+ tracks in the STRAW spectrometer (subsection 2.1.5) is described. Reconstruction of the STRAW tracks is based on hit clustering. For a track to be reconstructed, clusters of hits have to be found in at least three STRAW chambers (Section 2.3).

The STRAW track reconstruction efficiency affects the acceptance of signal and normalization selections in the $K_{\pi\nu\nu}$ analysis and thus enters the evaluation of the single event sensitivity of the $K_{\pi\nu\nu}$ measurement (subsection 4.1.8). The efficiency measurement carried out by the author and presented in this chapter uses control data samples obtained in 2016, 2017 and 2018 runs.

The efficiency is measured separately using three different kaon decay modes: $K_{2\pi}$, $K_{\mu 3}$ and K_{e3} (subsection 1.2.2). Each measurement begins with a strict event selection allowing to obtain a very pure event sample of the desired kaon decay. Information from any sub-detector but the STRAW is allowed to be used in the selection. For each selected event a charged particle pointer is created. The pointer is compared to the reconstructed STRAW candidates available in the event. Based on the position and momentum difference between the pointer and a candidate, decision about event being efficient or inefficient is made.

In the next two sections, a π^0 selection, used for reconstruction of a π^0 candidate produced by a kaon decay in the fiducial decay region, and the method of the STRAW track reconstruction efficiency evaluation are described. Both of these algorithms are common for all three track reconstruction efficiency measurements. Sections 3.3 to 3.5 contain detailed descriptions of the $K_{2\pi}$, $K_{\mu 3}$ and K_{e3} event selections and results of the efficiency measurement. These were also summarized in an internal note [93].

3.1 π^0 selection

A neutral pion decays almost immediately after its production ($\tau = (8.52 \pm 0.18) \times 10^{-17}$ s [28]), which translates to a mean free path of only few micrometers in the NA62 laboratory frame. The branching fraction of the dominant decay mode into two photons is $\mathcal{B}(\pi^0 \to \gamma\gamma) = 98.823(34)\,\%$ [28]. Our selection of $\pi^0 \to \gamma\gamma$ candidates starts with an identification of cluster pairs in the electromagnetic calorimeter (LKr). A reconstructed kaon candidate in KTAG, matched in time with the π^0 candidate, is then required and used to find a good quality GigaTracker (GTK) K^+ track candidate. Alternatively, run-dependent mean beam kaon momentum can be used. Assuming the positions of K^+ and π^0 decay vertices are identical, the neutral pion production vertex is found and its momentum is then computed from the LKr cluster positions and energies.

The procedure of selecting π^0 candidate and finding the neutral vertex position, which is described in the following paragraphs, is to its full extent implemented in an analyzer `Pi0Selection` (subsection 2.3.3). Various optional cuts are prepared in the analyzer and can be turned on via separate parameters by any user according to the needs of a given analysis. Output of this analyzer consists of a boolean variable indicating if at least one π^0 has been reconstructed, vector of all LKr clusters identified by the conditions described in Table 3.1.1, which are saved in a form of objects of the class `EnergyCluster`, as well as a vector of reconstructed π^0 candidates saved in a form of structure `Pi0SelectionOutput` defined in the header file of the `Pi0Selection` analyzer.

3.1.1 Cluster Selection

The pre-analyzer `LKrClusterCorrections` (subsection 2.3.3) is used to apply fine energy corrections for LKr clusters. Only events with at least two LKr clusters are taken into account. For each event, a set of good LKr clusters is chosen satisfying the following conditions: close in time (20 ns) with the trigger time and at least 20 mm away from any dead cell. The energy of a good cluster is required to be greater than 3 GeV, to reject minimum ionising particles (MIPs) and to be in the validity region of the LKr energy corrections.

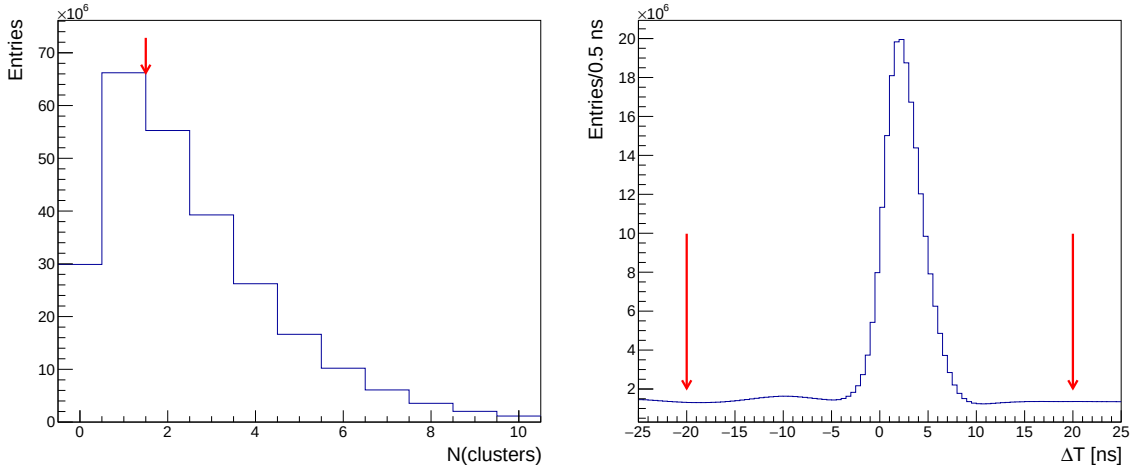

(a) (b)

Figure 3.1.1: (a) Number of LKr clusters. (b) Difference between time of a LKr cluster and the event trigger time. Data sample: 2017A, control trigger. Red arrows indicate the cut values used in the selection.

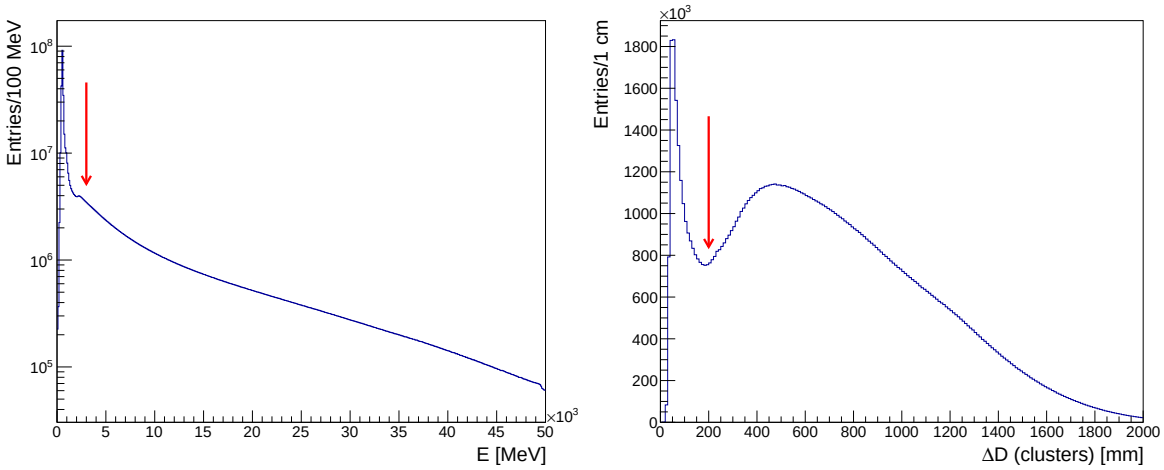

(a) (b)

Figure 3.1.2: (a) Cluster energy. (b) Cluster separation. Data sample: 2017A, control trigger. Red arrows indicate the cut values used in the π^0 candidate selection.

Three additional conditions are available and are used in the $K_{2\pi}$ event selection for $K_{\pi\nu\nu}$ kinematic background studies in Chapter 4. First, a requirement can be made for the LKr clusters to be inside LKr geometrical acceptance defined as regular octagon with apothem of 1130 mm and a hole with radius 150 mm in the center. Second, a set of conditions selecting electromagnetic, rather than hadronic cluster can be imposed. Depending on the cluster energy E, number of LKr hits N_{hits} forming the cluster and the energy of the seed E_{seed} (cluster hit with highest energy), conditions in Equation (3.1.1) define an electromagnetic cluster. Lastly, the cluster could be required to be isolated.

$$(0.00093 \cdot E + 2.21) < N_{hits} < (0.002046 \cdot E + 2.21)$$
$$0.2 < \frac{E_{seed}}{E} < 0.44 \tag{3.1.1}$$

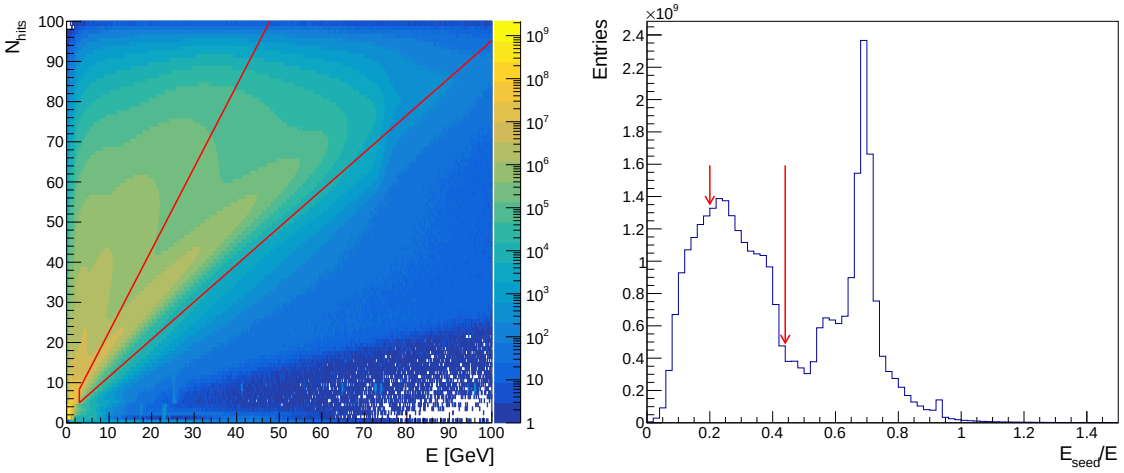

(a) (b)

Figure 3.1.3: Electromagnetic cluster: (a) Number of LKr hits corresponding to a cluster as a function of the cluster energy. Red lines indicate the cut selecting electromagnetic clusters. Vertical line corresponds to the cut on cluster energy (Figure 3.1.2a). (b) Ratio of the seed energy to the total cluster energy. Red arrows indicate the cut values used in the selection. Data sample: 2017, control trigger.

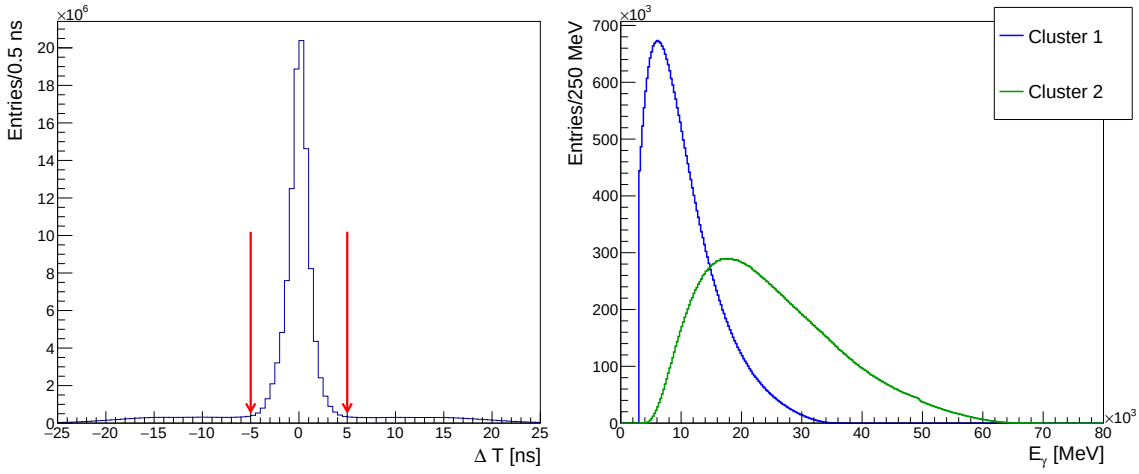

(a) (b)

Figure 3.1.4: Good cluster pairs: (a) Time difference between the two clusters. Red arrows indicate the cut used in the π^0 candidate selection. (b) Energy of the two clusters, Cluster 1 is the cluster with the lower energy. Data sample: 2017A, control trigger.

Events with at least two good clusters are considered in the next step of the selection. The following requirements have to be met by a pair of good clusters in order to be considered as a $\pi^0 \to \gamma\gamma$ decay candidate: clusters are required to be close in time (within 5 ns), they have to be separated by at least 20 cm, and their total energy has to be between 6 GeV and 75 GeV.

3.1.2 π^0 reconstruction

For each pair of selected clusters identified in subsection 3.1.1, a $\pi^0 \to \gamma\gamma$ vertex is reconstructed using the constraint on the invariant mass of the two photon candidates and the (X, Y) position of the vertex, which is given by the beam (kaon) path. The mathematical formulation of the problem is given in Appendix C. The resolution of the reconstructed Z coordinate of the vertex is given by the LKr energy resolution and by resolution of the beam kaon position in the XY-plane. The usual approach is to use the nominal beam path, however the π^0 vertex resolution can be improved by matching the cluster pair to a reconstructed upstream kaon track. In this selection, this is done using timing information provided by KTAG and GTK sub-detectors. The neutral pion time is defined as the average of the two cluster times. A good quality KTAG candidate ($N(\text{sectors}) > 4$) closest in time with respect to the π^0 time is identified. Then, a GTK candidate closest in time to the KTAG candidate is selected from all GTK candidates with $\chi^2 \leq 50$ and $\Delta T(\text{KTAG}, \text{GTK}) < 0.7$ ns. If no such GTK candidate is available, the average kaon beam momentum and direction are used for the π^0 vertex reconstruction. The average beam momentum is monitored on a run-by-run basis using fully reconstructed $K_{3\pi}$ decays.

If a GTK candidate is selected, the π^0 decay vertex is found using a formula derived in Appendix C:

$$m^2(\pi^0) = 2 \cdot E_1 \cdot E_2 \cdot \left[1 - \frac{(\vec{r_1} - \vec{r_v}) \cdot (\vec{r_2} - \vec{r_v})}{|\vec{r_1} - \vec{r_v}||\vec{r_2} - \vec{r_v}|}\right], \tag{3.1.2}$$

where E_1 and E_2 are the energies of the two clusters and $\vec{r_1}$ and $\vec{r_2}$ are their positions at Z_{LKr}. The reconstructed vertex position $\vec{r_v}$ is found by solving the Equation (3.1.2) numerically. Tested vertex positions in the numerical procedure are obtained by propagating the kaon from its reconstructed position in the last GTK station to any $Z < 180$ m (corrections due to Blue Tube field are applied).

If no GTK candidate is matched to the cluster pair, the (run dependent) average kaon momentum and position at $Z = 102.4\,\text{m}$ are used and Z position of the vertex is calculated in the same manner as in the case with a GTK candidate.

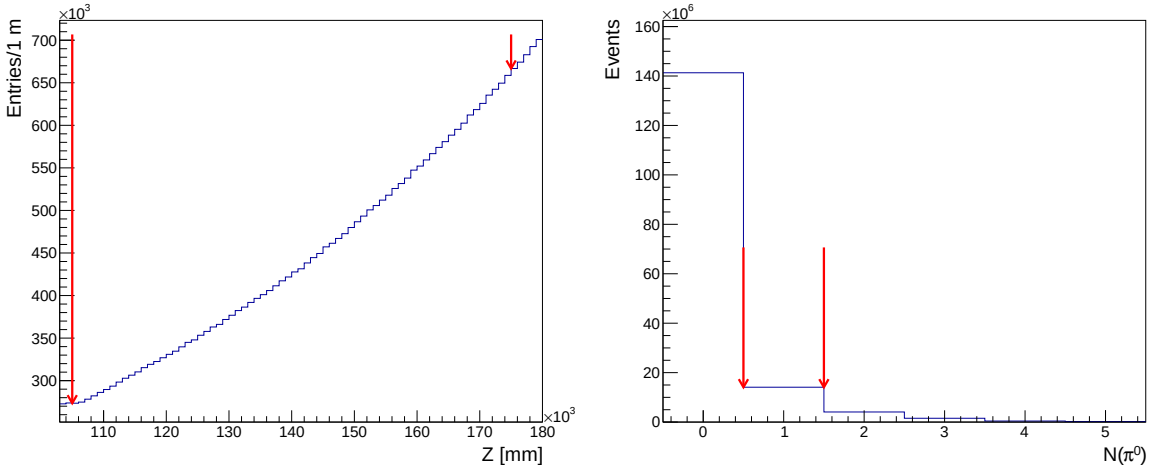

(a) (b)

Figure 3.1.5: (a) Z position of the neutral vertex. (b) Number of π^0 candidates. Exactly one reconstructed π^0 candidate is required in $K_{2\pi}$ and $K_{\ell 3}$ selections. Data sample: 2017A, control trigger.

Finally, the reconstructed vertex position is required to be in the range $Z \in (105,\, 175)\,\mathrm{m}$ to select the cluster pair as a π^0 candidate. In the 2017A data sample, about 85 % of events with a single π^0 selected have a GTK candidate matched to the π^0. Given the cluster energies, their positions in the LKr and the reconstructed vertex position, the π^0 four-momentum is calculated as the sum of the four-momenta of the two photon candidates. Since the vertex reconstruction is performed for each cluster pair, there can be multiple $\pi^0 \to \gamma\gamma$ decay candidates reconstructed in the same event.

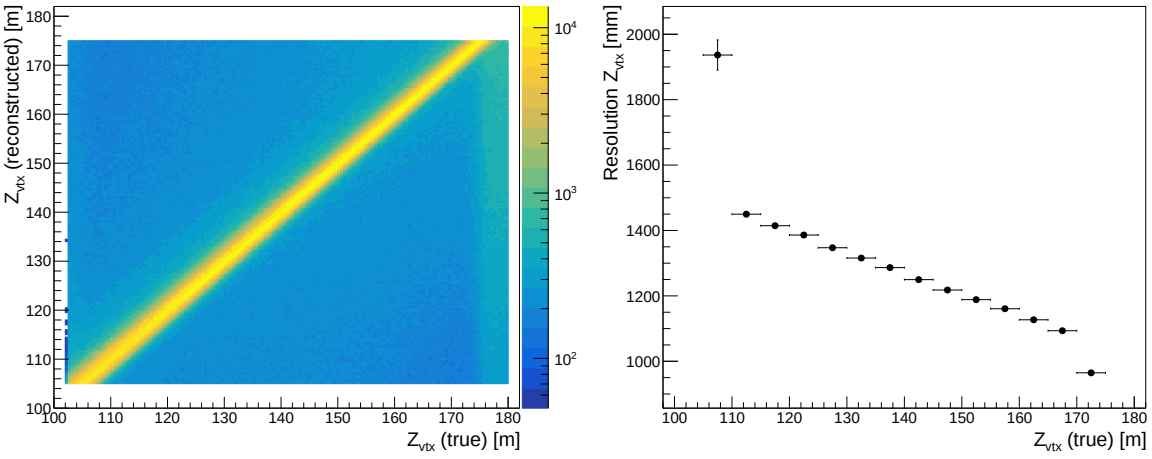

(a) (b)

Figure 3.1.6: Events with a single π^0 selected. (a) Z position of the reconstructed vs. the true vertex. (b) Resolution of the vertex Z position in bins of true vertex Z. Data sample: $K_{2\pi}$ MC.

Condition	Spectrometer efficiency	$K_{\pi\nu\nu}$ analysis
LKr clusters	≥ 2	≥ 2
In time with the trigger time	< 20 ns	not used
Distance from a dead cell	> 20 mm	> 20 mm
Cluster energy	> 3000 MeV	> 3000 MeV
Cluster in LKr acceptance	not used	octagon (A=1130 mm), central hole (R=150 mm)
Electromagnetic cluster	not used	Equation (3.1.1)
Isolated from other LKr candidates	not used	> 150 mm
Clusters close in time	< 5 ns	< 3 ns
Clusters separated in space	> 200 mm	> 150 mm
Total energy of two clusters	(6, 75) GeV	(6, 75) GeV
π^0 time	$t_{\pi^0} = (t_{cl1} + t_{cl2})/2$	$t_{\pi^0} = (t_{cl1} + t_{cl2})/2$
KTAG candidate quality	> 4 sectors	not used
KTAG candidate time	minimal $(t_{\pi^0} - t_{KTAG})$	not used
GTK candidate quality	$\chi^2 \leq 50$	not used
GTK candidate in time with KTAG candidate	< 0.7 ns	not used
GTK candidate time	minimal $(t_{GTK} - t_{KTAG})$	not used
Z position of the π^0 vertex	(105, 175) m	(105, 165) m

Table 3.1.1: Summary of π^0 selection conditions used in the Spectrometer efficiency measurement and in the study of $K_{2\pi}$ kinematic tails in Chapter 4.

3.2 Spectrometer track reconstruction efficiency

Both the online (trigger) and the offline selections of data samples used for the evaluation of the STRAW track reconstruction efficiency clearly cannot use the information provided by the STRAW sub-detector. Therefore, the data recorded using a minimum-bias trigger (subsection 2.2.2) is used for this purpose. Three offline selection procedures are developed to select $K_{2\pi}$, $K_{\mu 3}$, and K_{e3} events without using STRAW information; their descriptions are given in the following sections. Each selection algorithm produces a pointer representing the predicted position and momentum of the positively charged track (either π^+, μ^+, or e^+). The algorithms are available in the NA62 software framework (subsection 2.3.3) in the form of analyzers, named `K2piSelectionNoSpectrometer`, `Kmu3SelectionNoSpectrometer`, and `Ke3SelectionNoSpectrometer`. Each

selection analyzer has five variables in the output: a boolean variable indicating if the event has passed the selection, the event time, the four-momentum of the pointer, the decay vertex position and ID of the GTK candidate selected in the event (if no GTK candidate is selected, a run dependent mean beam momentum is used and a default ID value is given in the output).

The position and the momentum of the pointer from the selected event are the inputs to the efficiency evaluation algorithm. The pointer is propagated from the vertex position downstream in the magnetic fields of the Blue Tube and the MNP33 magnet. Events that enter the evaluation of the STRAW track reconstruction efficiency are required to have their pointer in the geometrical acceptance of all four STRAW chambers; the distance from the beam axis is required to be above 10 cm. For each reference pointer in the geometrical acceptance of the STRAW, a STRAW candidate compatible with the pointer is looked for. The pointer position and its momentum are compared to reconstructed STRAW candidates at the $Z = 180\,\mathrm{m}$ plane, i.e. the candidate reference position before the MNP33 magnet. It is required that the momentum difference between the pointer and a STRAW candidate is less than 5 GeV/c (10 GeV/c) for π^+ and e^+ (μ^+) pointers. Furthermore, a momentum dependent cut is imposed on the distance between the pointer and a STRAW candidate:

$$\begin{aligned} &\Delta p < 5\,\mathrm{GeV}/c\,(10\,\mathrm{GeV}/c)\,, \\ &\Delta D < \left(-0.0025\frac{p_{pointer}}{\mathrm{MeV}/c} + 212.5\right)\mathrm{mm}. \end{aligned} \tag{3.2.1}$$

If a matching candidate is found, the event is considered efficient and enters the numerator of the efficiency.

The track reconstruction efficiency in a run is calculated as a ratio of the number of efficient events and the number of all events with a pointer in the geometrical acceptance of four STRAW chambers:

$$\varepsilon = \frac{\text{N efficient events}}{\text{N events with good pointer}} \tag{3.2.2}$$

and in the following sections it is displayed with 95 % CL error bars. The efficiency dependence on the pointer momentum, position before magnet at $Z = 180\,\mathrm{m}$, distance from beam axis and the instantaneous beam intensity is calculated as well.

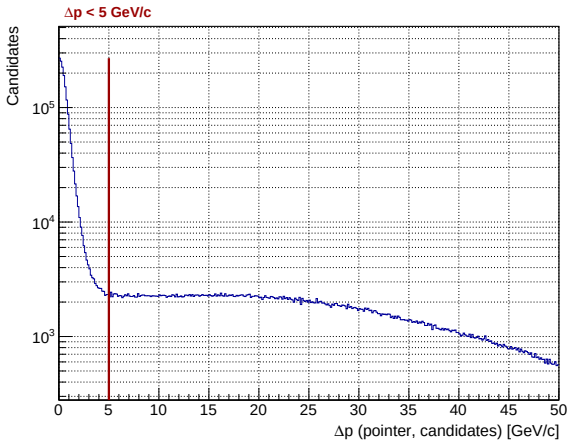

(a) $K_{2\pi}$ events

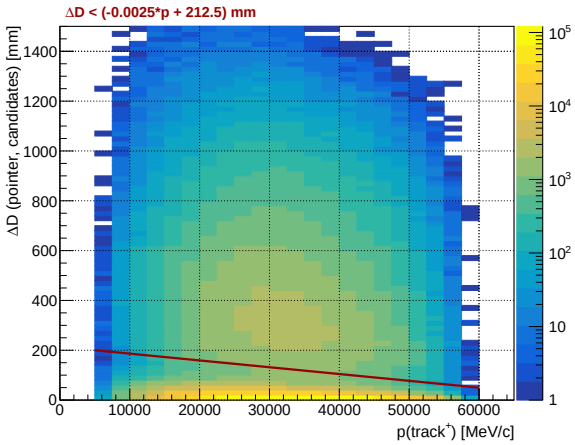

(b) $K_{2\pi}$ events

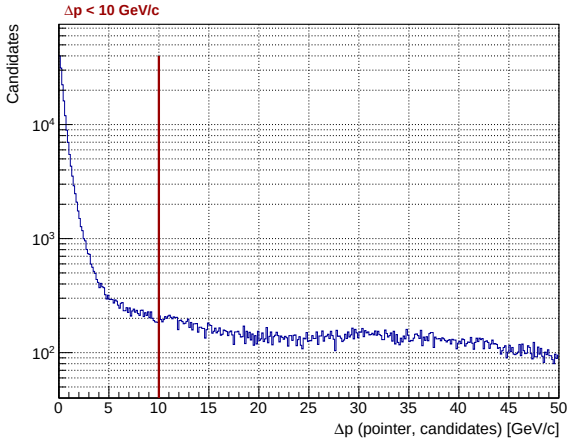

(c) $K_{\mu 3}$ events

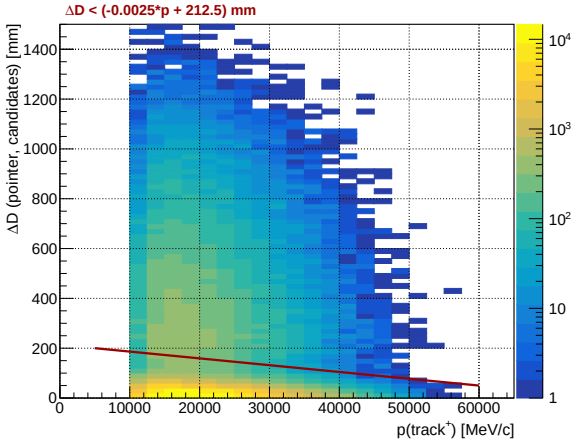

(d) $K_{\mu 3}$ events

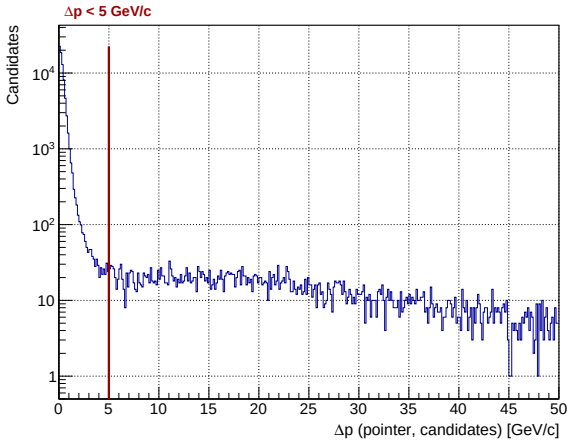

(e) K_{e3} events

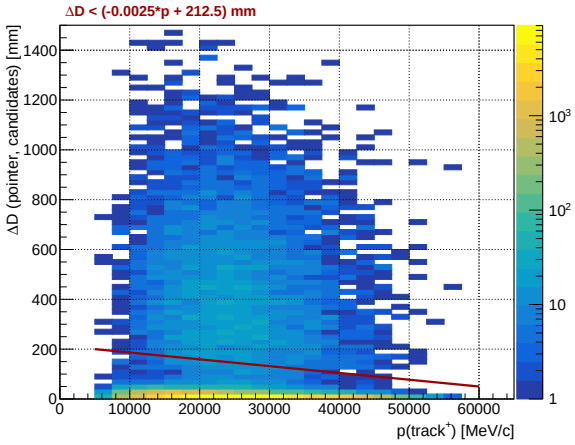

(f) K_{e3} events

Figure 3.2.1: Example plots for pointer and STRAW candidate matching. (a), (c), (e) Momentum difference between the pointer and a STRAW candidate. Red line indicates the cut used in the efficiency evaluation. (b), (d), (f) Position difference between the pointer and a STRAW candidate as a function of the pointer momentum. Red line indicates the 2D cut used in the efficiency evaluation. Data sample: 2017(A-D), control trigger.

The STRAW reconstruction algorithm produces two types of candidates (tracks). The candidates of the first type are reconstructed using hit information from all four STRAW chambers, while the candidates of the second type miss information from one of the chambers. The momentum and slope measurement resolution are worse for the latter type. Therefore, some of the NA62 analyses, including the main $K^+ \to \pi^+\nu\bar{\nu}$ analysis, do not use the 3-chamber tracks. Track reconstruction efficiency presented in this thesis is evaluated by considering both types of candidates and then separately by considering only the 4-chamber tracks.

Two classes of inefficient events are identified:

- events with no STRAW candidate reconstructed in the event,
- events with STRAW candidate(s) reconstructed, but no candidate satisfies the position and momentum criteria (Equation (3.2.1)).

In subsections 3.3.2, 3.4.2 and 3.5.2 the general results for all data sets (2016, 2017, 2018) and specific results for 2017 data set are shown alongside with the results for the Monte Carlo samples. For each data sample, a comparison of the results evaluated with both types of the STRAW candidates and with 4-chamber candidates only is shown.

3.3 Measurement of the π^+ reconstruction efficiency with $K^+ \to \pi^+\pi^0$ decay

The track reconstruction efficiency for π^+ tracks is evaluated using the $K^+ \to \pi^+\pi^0$ decay. The $K_{2\pi}$ event selection is based on the π^0 selection (see Section 3.1), the identification of π^+ using calorimeters, and the background suppression using muon and photon vetoes. Finally, a cut on the π^+ invariant mass variable is applied to select a clean $K_{2\pi}$ sample.

3.3.1 $K_{2\pi}$ selection

Events with exactly one reconstructed π^0 candidate enter the selection. The π^+ pointer four-momentum is computed using the assumption that the event is $K_{2\pi}$: $P_{\pi^+} = (P_K - P_{\pi^0})$. A muon veto condition is applied by requiring that no MUV3 candidates closer than 5 ns from the π^0 time are present in the event; the condition mainly suppresses the $K_{\mu 3}$ background. Precisely one additional LKr candidate is required to be reconstructed less than 100 mm from the pointer and in time (5 ns) with the π^0 time. This cut rejects various background processes, see Figure 3.3.3.

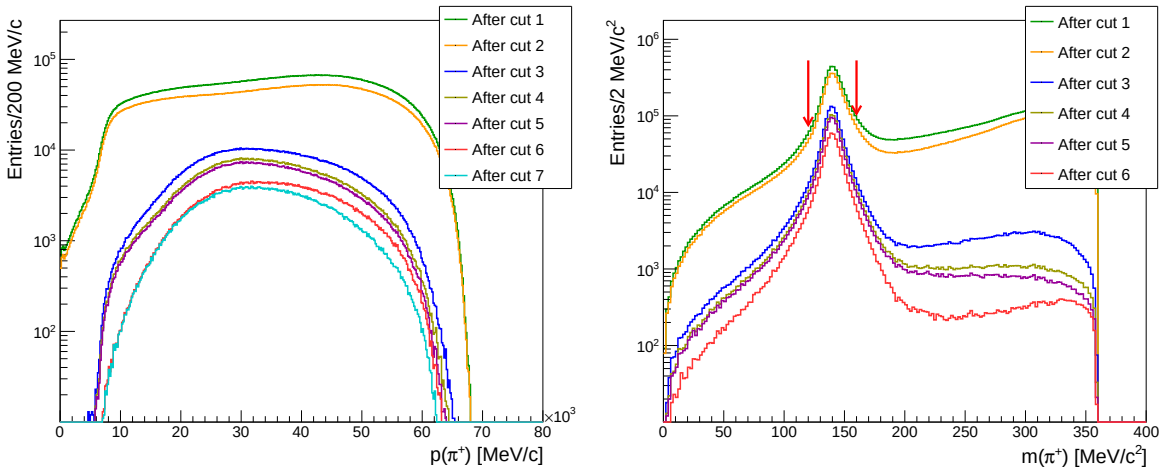

(a) (b)

Figure 3.3.1: (a) Momentum distribution of the π^+ pointer after the $K_{2\pi}$ event selection cuts. (b) π^+ mass distribution after the $K_{2\pi}$ event selection cuts. Red arrows indicate the final cut. Data sample: 2017A, control trigger.

To suppress backgrounds with photons in the final state, events with a matching in LAV (5 ns), SAC (10 ns) or IRC (10 ns) are rejected. The suppression of the K_{e3} background is achieved by requiring at least 15 in-time MUV1+MUV2 hits with the energy of more than 100 MeV, see Figure 3.3.4. Finally, a strict cut on the reconstructed π^+ mass is made to select a sample of $K_{2\pi}$ events with well reconstructed π^+ pointers. All the cuts are summarized in Table 3.3.1. In the following stack plots, only MC samples of kaon decays contributing to the integral in the selected range by more than 0.05 % are included.

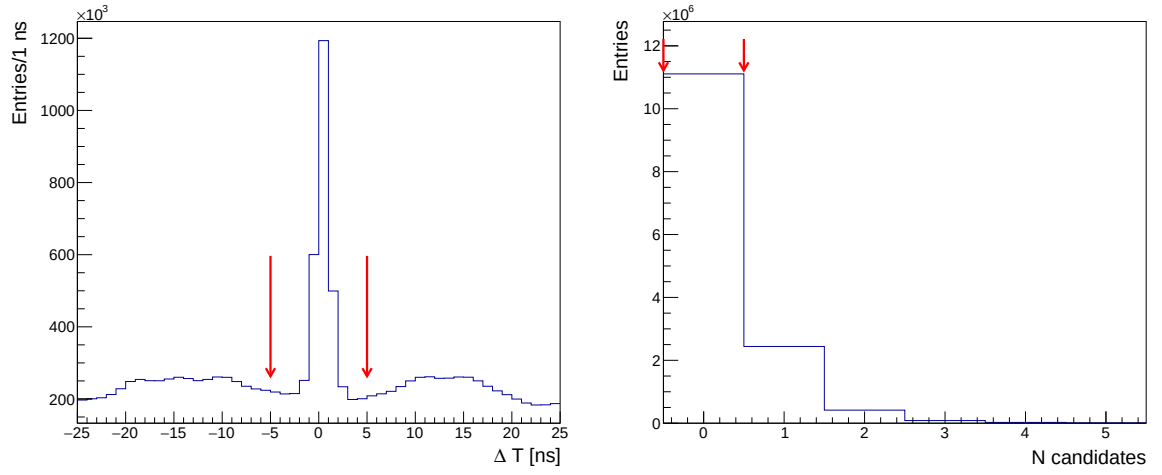

(a) (b)

Figure 3.3.2: Cut 2: (a) Time difference between π^0 and MUV3 candidates. Red arrows indicate the cut used in $K_{2\pi}$ event selection. (b) Number of MUV3 candidates in time with π^0 time. Red arrows indicate the cut values used in the $K_{2\pi}$ event selection. Data sample: 2017A, control trigger.

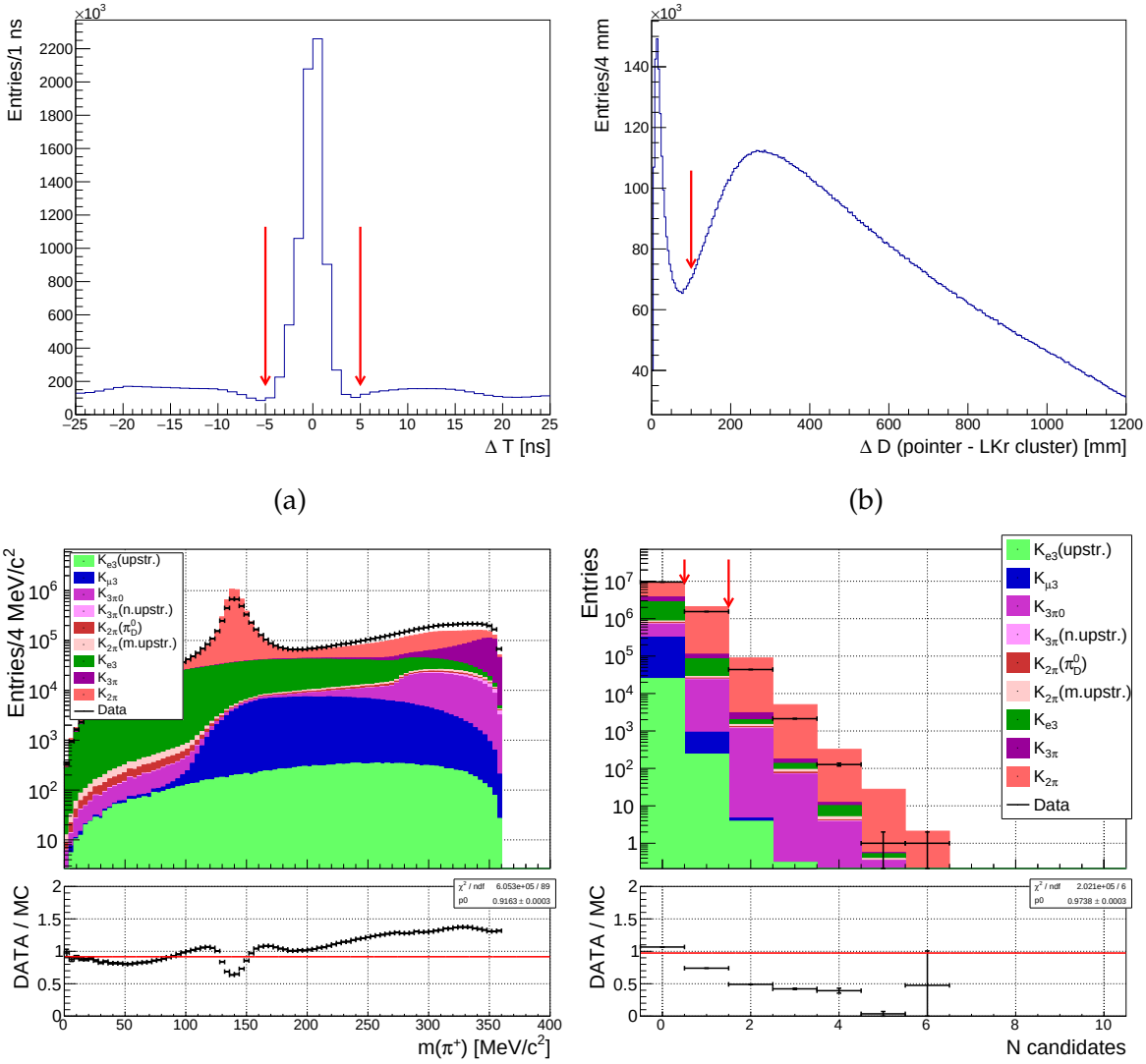

Figure 3.3.3: Cut 3 (additional LKr candidates): (a) Time difference between π^0 and additional LKr candidates. (b) Distance between the LKr candidates and the π^+ pointer. (c) Pion mass distribution before the cut. (d) Number of additional LKr candidates in time with π^0 and close to π^+ pointer. Red arrows indicate cuts used in the $K_{2\pi}$ event selection. Data sample: 2017A, control trigger.

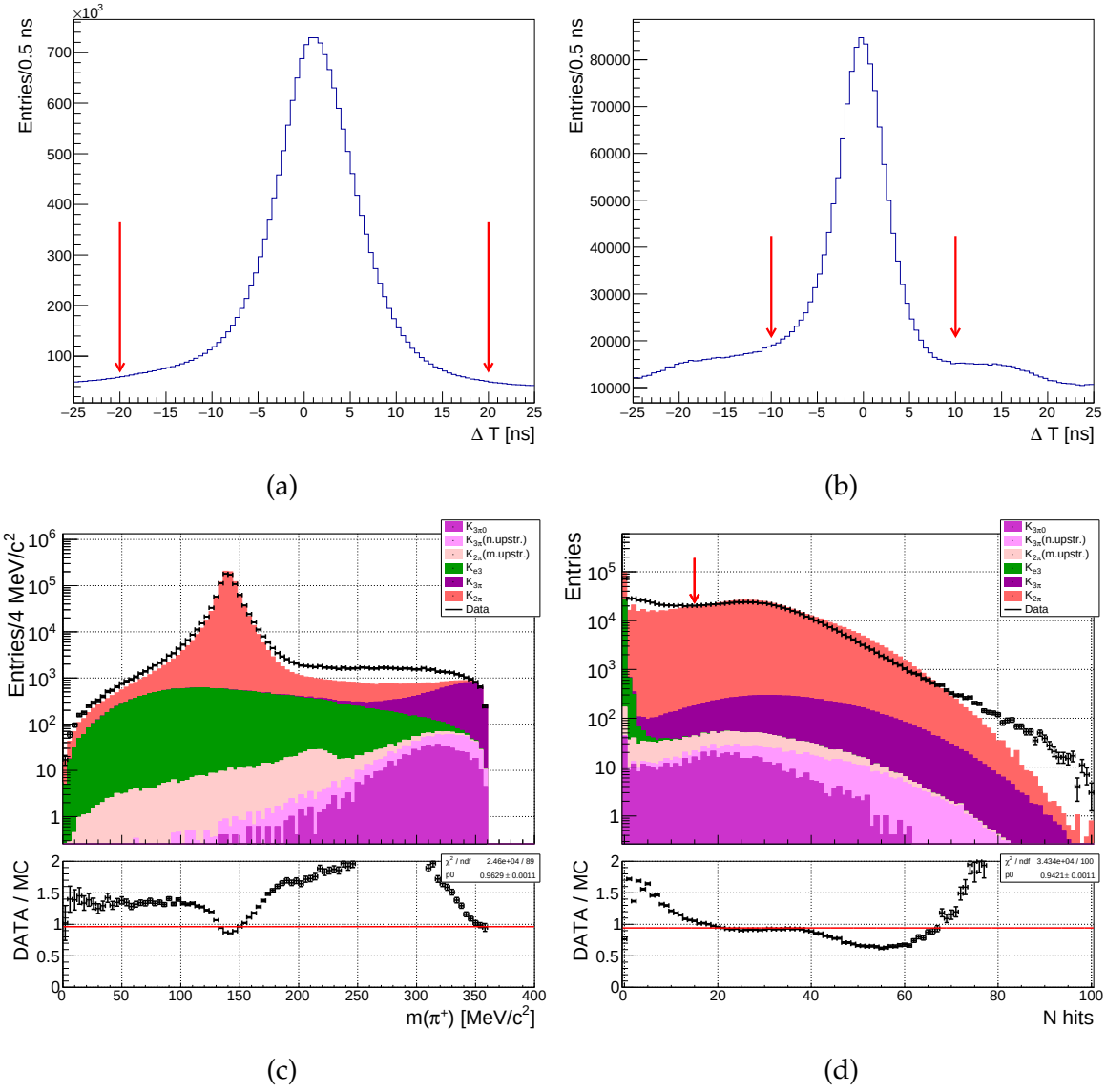

Figure 3.3.4: Cut 6 (MUV1, MUV2 hits): (a) Time difference between π^0 and MUV1 hits. (b) Time difference between π^0 and MUV2 hits. (c) Pion mass distribution before the cut. (d) Total number of in-time MUV1 and MUV2 hits with energy above 100 MeV. Red arrows indicate the cut values used in the $K_{2\pi}$ event selection. Data sample: 2017A, control trigger.

Cut 1	π^0 selected	1
Cut 2	No MUV3 candidate in time with π^0	< 5 ns
Cut 3	Additional LKr candidate in time with π^0 Additional LKr candidate close to π^+ pointer Number of additional LKr candidates	< 5 ns < 100 mm 1
Cut 4	LAV matching - half time window Number of LAV in-time matches	5 ns 0
Cut 5	IRC and SAC matching - half time window Number of IRC and SAC in-time matches	10 ns 0
Cut 6	MUV1 hit in time with π^0 MUV2 hit in time with π^0 Energy of MUV1 and MUV2 hit Total number of in-time MUV1 and MUV2 hits	< 20 ns < 10 ns > 100 MeV ≤ 15
Cut 7	$m(\pi^+)$	(120, 160) MeV/c

Table 3.3.1: $K_{2\pi}$ event selection summary.

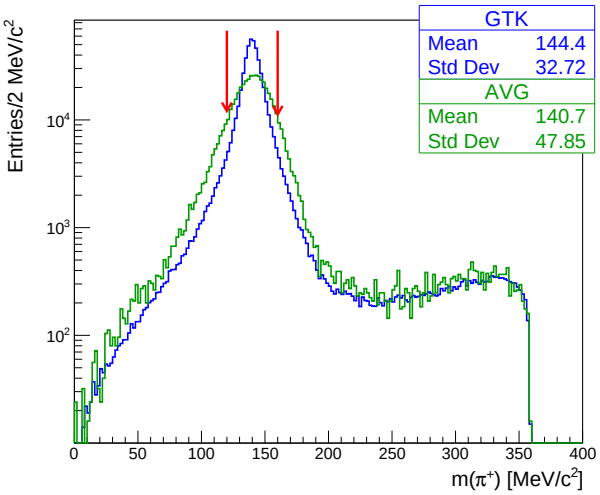

Figure 3.3.5: Comparison of the reconstructed pion mass before the final cut for events with a GTK candidate matched to the π^0 and for events in which the average kaon momentum was used. The resolution of the pion mass peak is measured to be (7.71 ± 0.01) MeV/c^2 with the GTK candidate and (14.38 ± 0.13) MeV/c^2 with the average kaon momentum. Data sample: 2017A, control trigger.

3.3.2 Results

The described $K_{2\pi}$ selection is very restrictive as the main goal is to select very clean samples of $K_{2\pi}$ decays for the π^+ track reconstruction efficiency measurement. The

$K_{2\pi}$ acceptance ($Z_{vtx}(true) \in$ (102.425, 180) m) is 3.74 % with a negligible uncertainty. The main background contribution to the $K_{2\pi}$ sample comes from $K_{3\pi}$ events with the acceptance of 1.2×10^{-5}, resulting in the $O(10^{-4})$ background contamination. Therefore, the background has a negligible effect on the π^+ track reconstruction efficiency measurement.

The π^+ track reconstruction efficiency is evaluated for all 2016, 2017 and 2018 data samples and for the $K_{2\pi}$ Monte Carlo events. The results are presented in the following pages, a summary table with efficiency values for all studied samples is in Appendix E.

A difference between the 2016 data sample and the 2017+2018 data samples is observed; the efficiency is lower by about 3 % in 2016. This is caused by events with zero candidates reconstructed by the STRAW, see Figure 3.3.10. The efficiency increase at the beginning of 2017 was most probably achieved thanks to an upgrade of the STRAW readout firmware, although no particular bug was identified in the 2016 firmware version.

To estimate how the results are sensitive to the π^+ pointer misreconstruction, two tests are performed. First, the efficiency in the 2017 data sample is evaluated using the same selection but with the final cut symmetrically extended to (100, 180) MeV/c^2, resulting in a shift of $\Delta\varepsilon = -0.14\,\%$ ($-0.25\,\%$ in 4CH case). In the second test, only events with a GTK candidate matched to the π^0 are considered. This results in $\Delta\varepsilon = 0.13\,\%$ ($0.29\,\%$ in 4CH case).

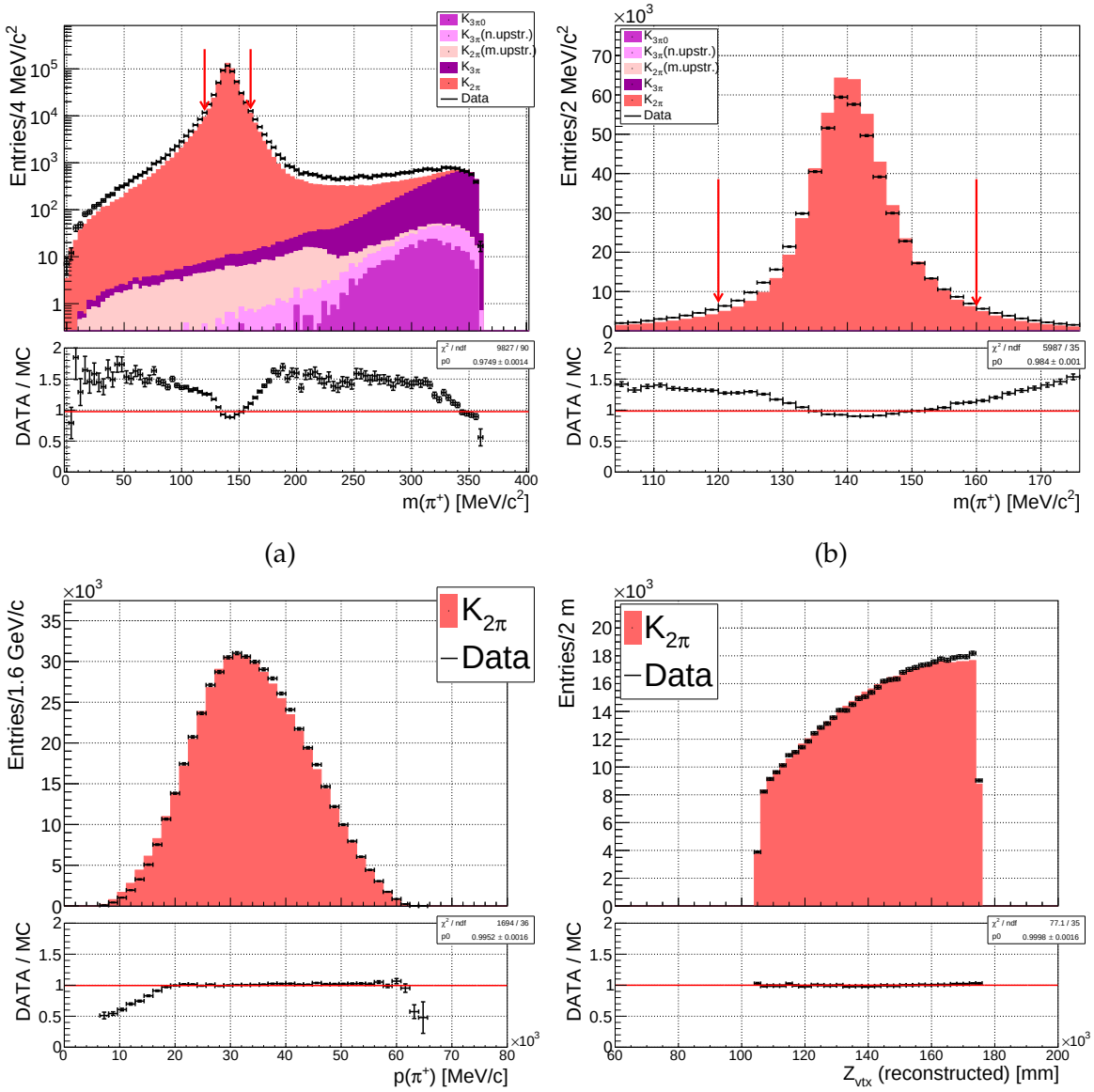

Figure 3.3.6: (a), (b) Reconstructed π^+ mass before the final cut. (c), (d) Distributions of π^+ momentum and Z_{vtx} after the final cut. Data sample: 2017A, control trigger.

3.3.2.1 Efficiency in data

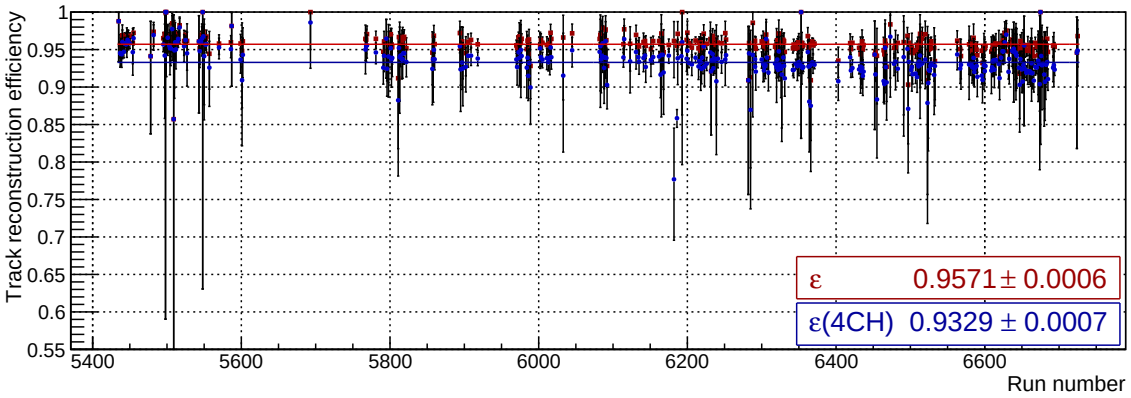

(a) 2016(A-B)

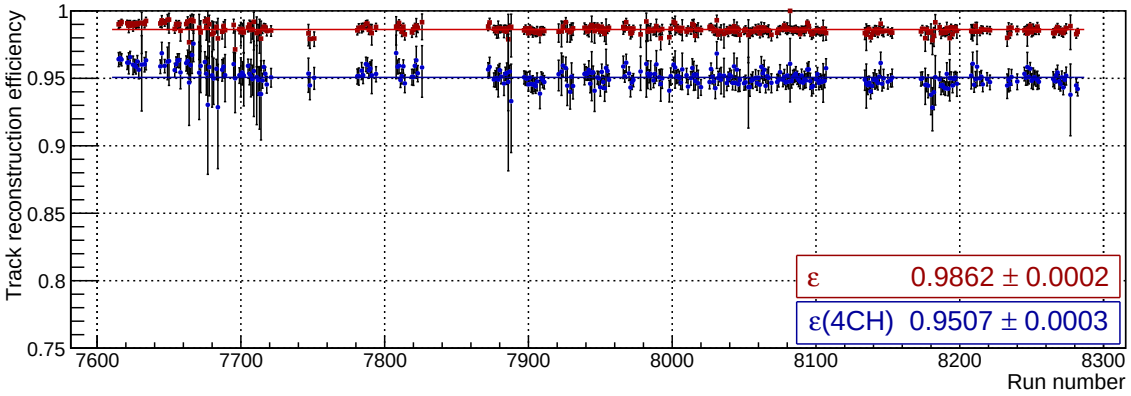

(b) 2017(A-D)

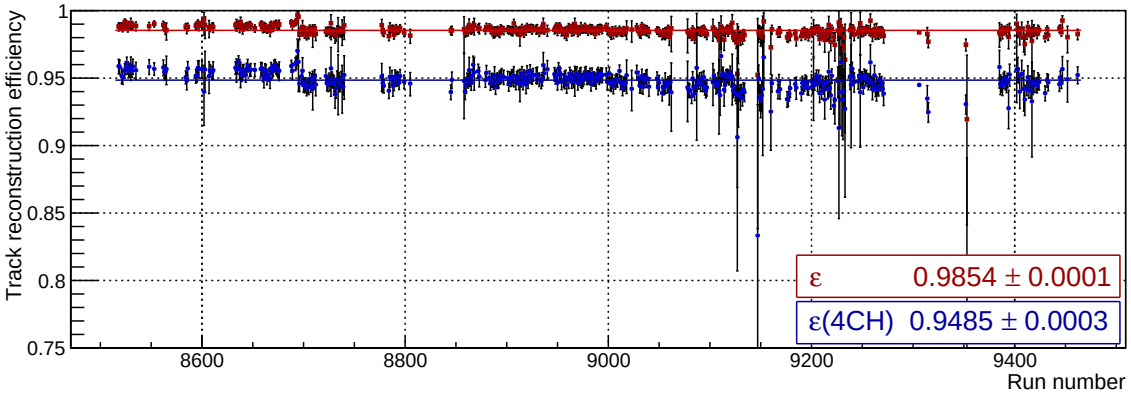

(c) 2018(A-H)

Figure 3.3.7: π^+ track reconstruction efficiency in all 2016, 2017 and 2018 runs. An increase of about 3 % in efficiency, related to readout, is visible in 2017 and 2018 runs with respect to 2016 runs.

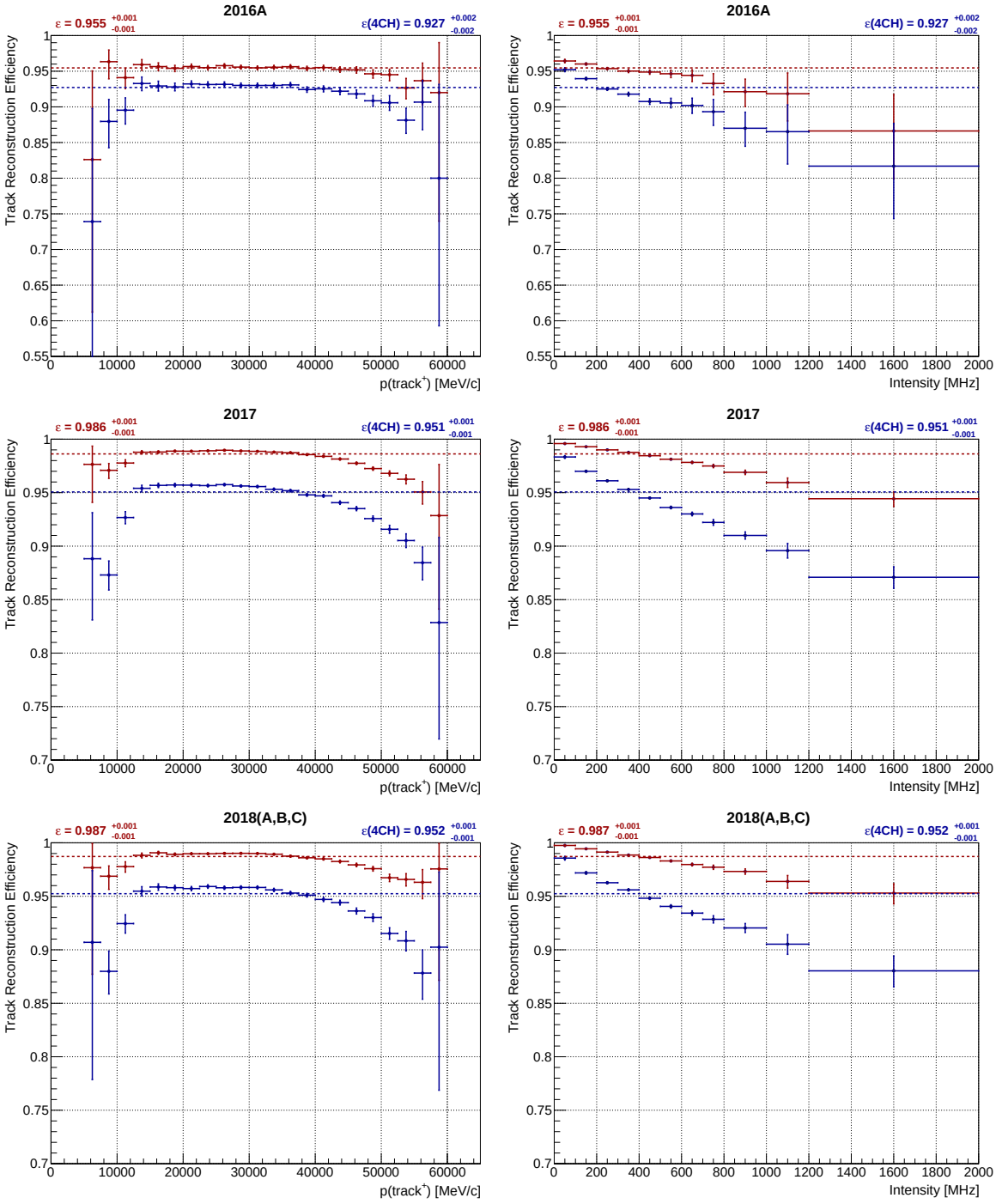

Figure 3.3.8: π^+ track reconstruction efficiency as a function of the momentum of the reconstructed π^+ pointer (left), and as a function of the instantaneous beam intensity (right). Data sample: 2016A, 2017, 2018(A-C), control trigger.

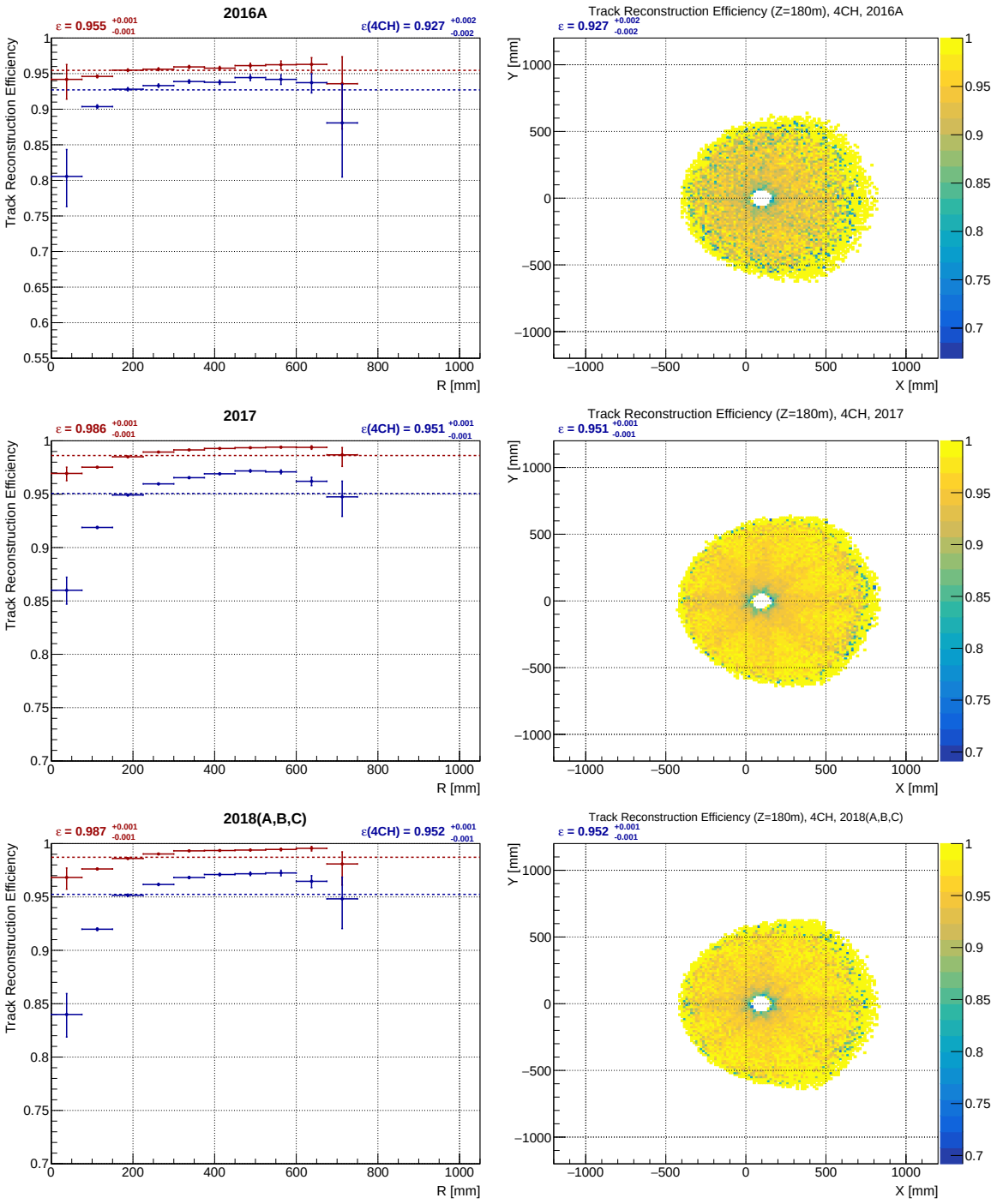

Figure 3.3.9: π^+ track reconstruction efficiency as a function of the distance from the beam axis (left), and as a function of the reconstructed π^+ pointer position before magnet at $Z = 180\,\mathrm{m}$ (right). Only candidates reconstructed from hits in all four chambers are used for the latter. Data sample: 2016A, 2017, 2018(A-C), control trigger.

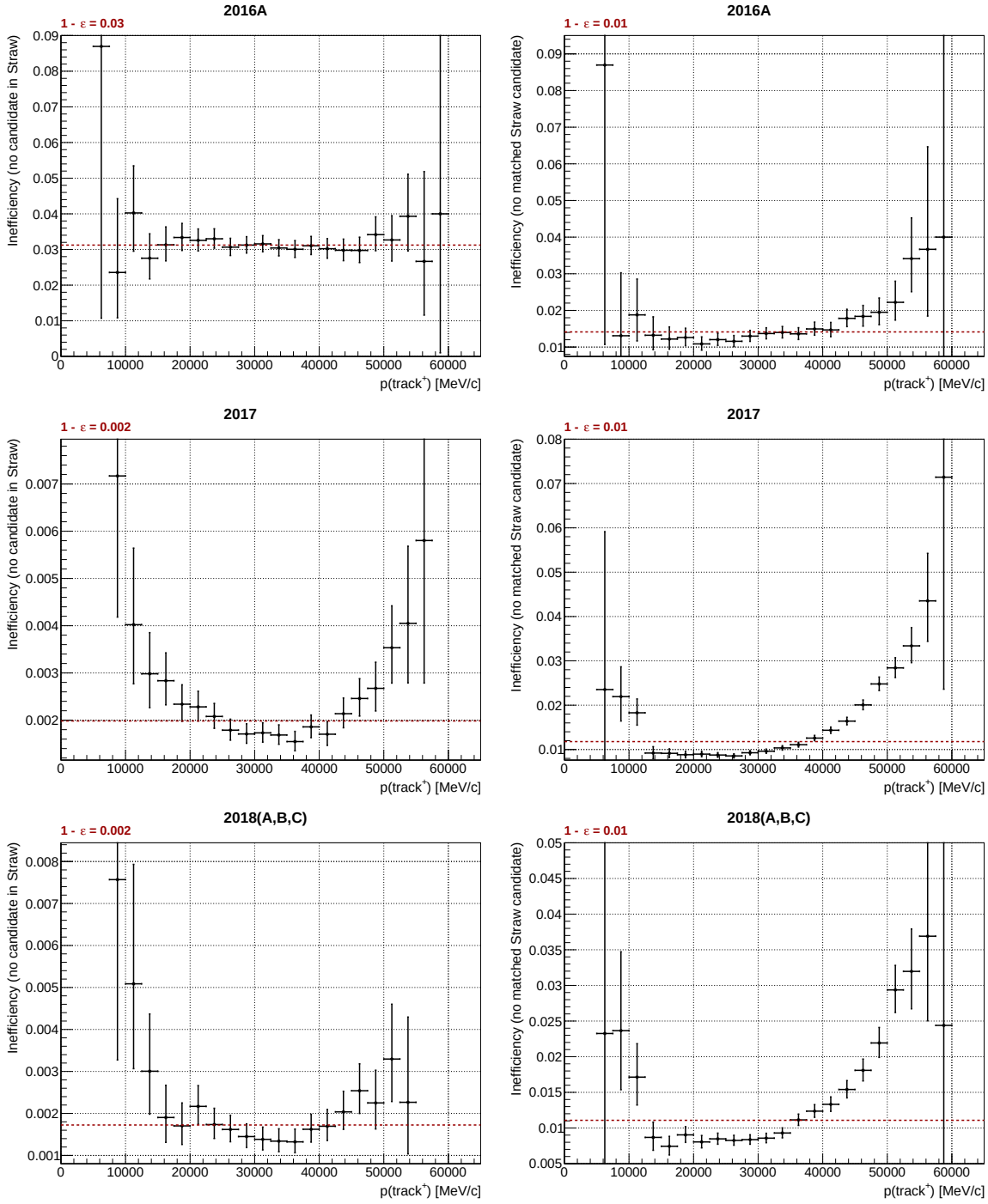

Figure 3.3.10: π^+ track reconstruction inefficiency as a function of the reconstructed π^+ momentum: the inefficiency caused by no STRAW candidate present in the event (left), the inefficiency due to no STRAW candidate compatible with the π^+ pointer found in the event (right). The compatibility criteria are based on the momentum and position difference between the pointer and a STRAW candidate and are summarized in Section 3.2. Data sample: 2016A, 2017, 2018(A-C), control trigger.

3.3.2.2 Efficiency in MC

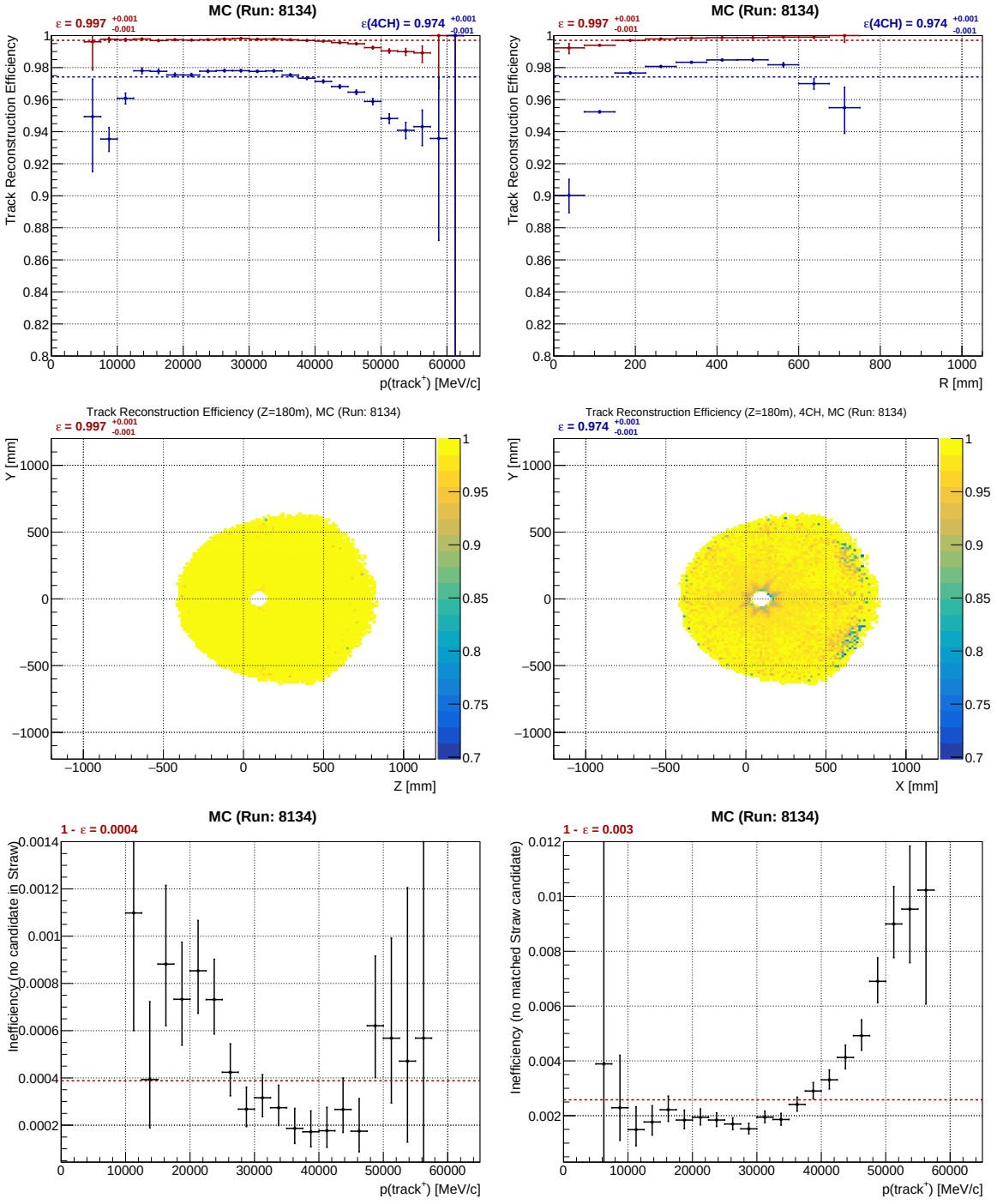

Figure 3.3.11: π^+ track reconstruction efficiency as a function of the reconstructed π^+ pointer momentum (top left), the distance from the beam axis (top right) and the π^+ pointer position before magnet ($Z = 180\,\mathrm{m}$): all STRAW candidates (middle left), only 4 chamber candidates (middle right). π^+ track reconstruction inefficiency as a function of the π^+ pointer momentum. Two classes of events are considered: events inefficient due to no candidate reconstructed in the STRAW (bottom left) and due to no STRAW candidate matched to the pointer (bottom right). MC sample: $K_{2\pi}$ events with upstream and downstream pile-up (subsection 2.3.3).

3.4 Measurement of the μ^+ reconstruction efficiency with $K^+ \to \pi^0\mu^+\nu_\mu$ decay

The track reconstruction efficiency for muons is evaluated using the $K^+ \to \pi^0\mu^+\nu_\mu$ decay. The $K_{\mu 3}$ selection is based on the π^0 selection (see Section 3.1), the muon pointer reconstruction using information from the RICH, the muon identification in the MUV3, and photon rejection using the LAV and the SAV. In the end, a cut on a squared missing mass variable is applied to select the sample entering the efficiency evaluation.

3.4.1 $K_{\mu 3}$ selection

Only events with exactly one reconstructed π^0 candidate enter the $K_{\mu 3}$ selection. Exactly one RICH ring candidate in time with the π^0 time is required. The muon pointer momentum is calculated from the ring radius:

$$p(\mu^+) = \left| \frac{\frac{1}{n\cos\left(\frac{R}{l_f}\right)} M_\mu}{\sqrt{1 - \frac{1}{n^2\cos^2\left(\frac{R}{l_f}\right)}}} \right|, \tag{3.4.1}$$

where $n = 1.000062$ is the RICH gas refractive index, $l_f = 17.020\,\mathrm{m}$ is the RICH focal length, R is the RICH candidate ring radius in mm, M_μ is the nominal muon mass. The pointer direction after the STRAW magnet is then calculated using the momentum and the ring center:

$$\begin{aligned} p_x &= \frac{R_x}{|R_y|} \frac{p(\mu^+)}{\sqrt{1 + \left(\frac{R_x^2}{R_y^2}\right) + \left(\frac{l_f^2}{R_y^2}\right)}} \\ p_y &= \frac{R_y}{|R_y|} \frac{p(\mu^+)}{\sqrt{1 + \left(\frac{R_x^2}{R_y^2}\right) + \left(\frac{l_f^2}{R_y^2}\right)}} \\ p_z &= \frac{l_f}{|R_y|} \frac{p(\mu^+)}{\sqrt{1 + \left(\frac{R_x^2}{R_y^2}\right) + \left(\frac{l_f^2}{R_y^2}\right)}}, \end{aligned} \tag{3.4.2}$$

where R_x and R_y are the RICH candidate ring center coordinates, and p_x, p_y and p_z are components of the muon momentum vector after the STRAW magnet.

The pointer four-momentum P_{μ^+} at the vertex is defined after extrapolating the muon momentum vector before the STRAW magnet. The reconstructed squared missing mass variable is computed under the assumption that the event is $K_{\mu 3}$: $m^2_{miss} = (P_K - P_{\pi^0} - P_{\mu^+})^2$.

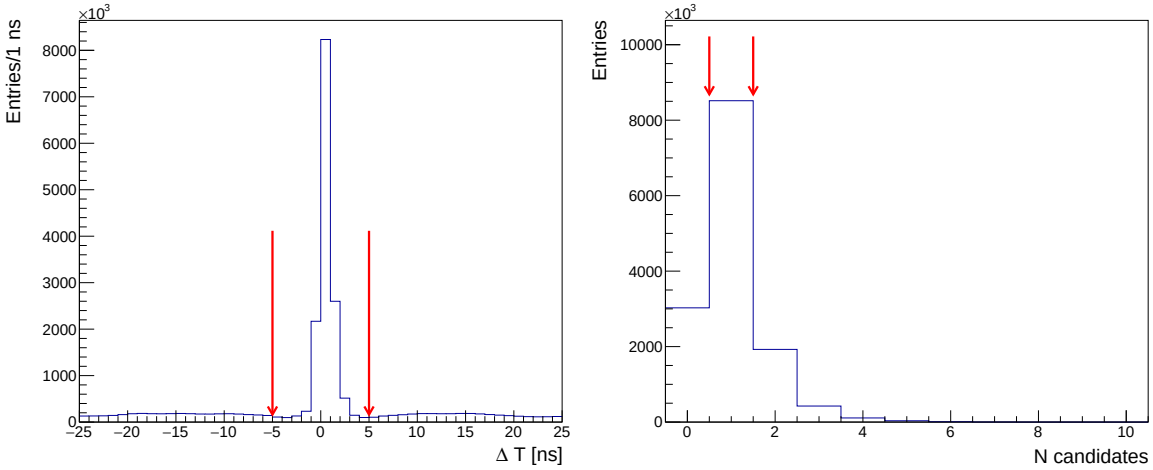

(a) (b)

Figure 3.4.1: Cut 2: (a) Time difference between π^0 and RICH candidates. (b) Number of RICH candidates in time with π^0. Red arrows indicate cut used in the $K_{\mu 3}$ event selection. Data sample: 2017A, control trigger.

The pointer is required to be in the MUV3 geometric acceptance. A MUV3 candidate in time (10 ns) with the π^0 time is then looked for. The candidate must be reconstructed close to the projected position of the pointer in the MUV3 plane using the momentum-dependent search radius:

$$\left|\vec{r}_{candidate} - \vec{r}_{pointer}\right| < \left(\frac{4 \cdot 530\,000\,\mathrm{MeV}/c}{p(\mu^+)}\right) \mathrm{mm}. \tag{3.4.3}$$

The search radius formula takes into account multiple scattering in the material between RICH and MUV3 and was obtained from a Monte Carlo study. If no MUV3 candidate is matched to the pointer, the event is rejected. The effect of this muon identification is illustrated in Figure 3.4.3; the cut rejects a large fraction of $K_{2\pi}$, $K_{3\pi}$ and K_{e3} events.

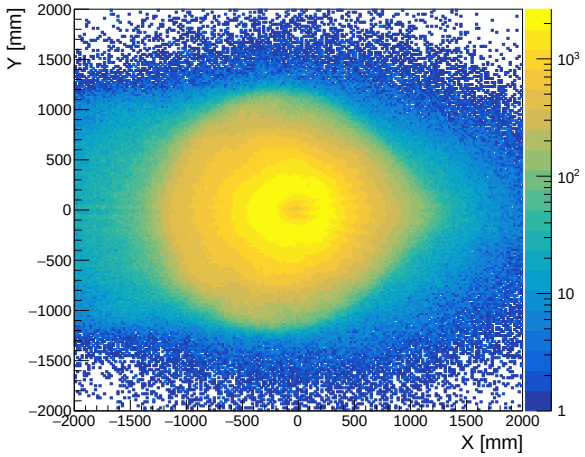

Figure 3.4.2: Cut 3: Pointer position at MUV3 plane.

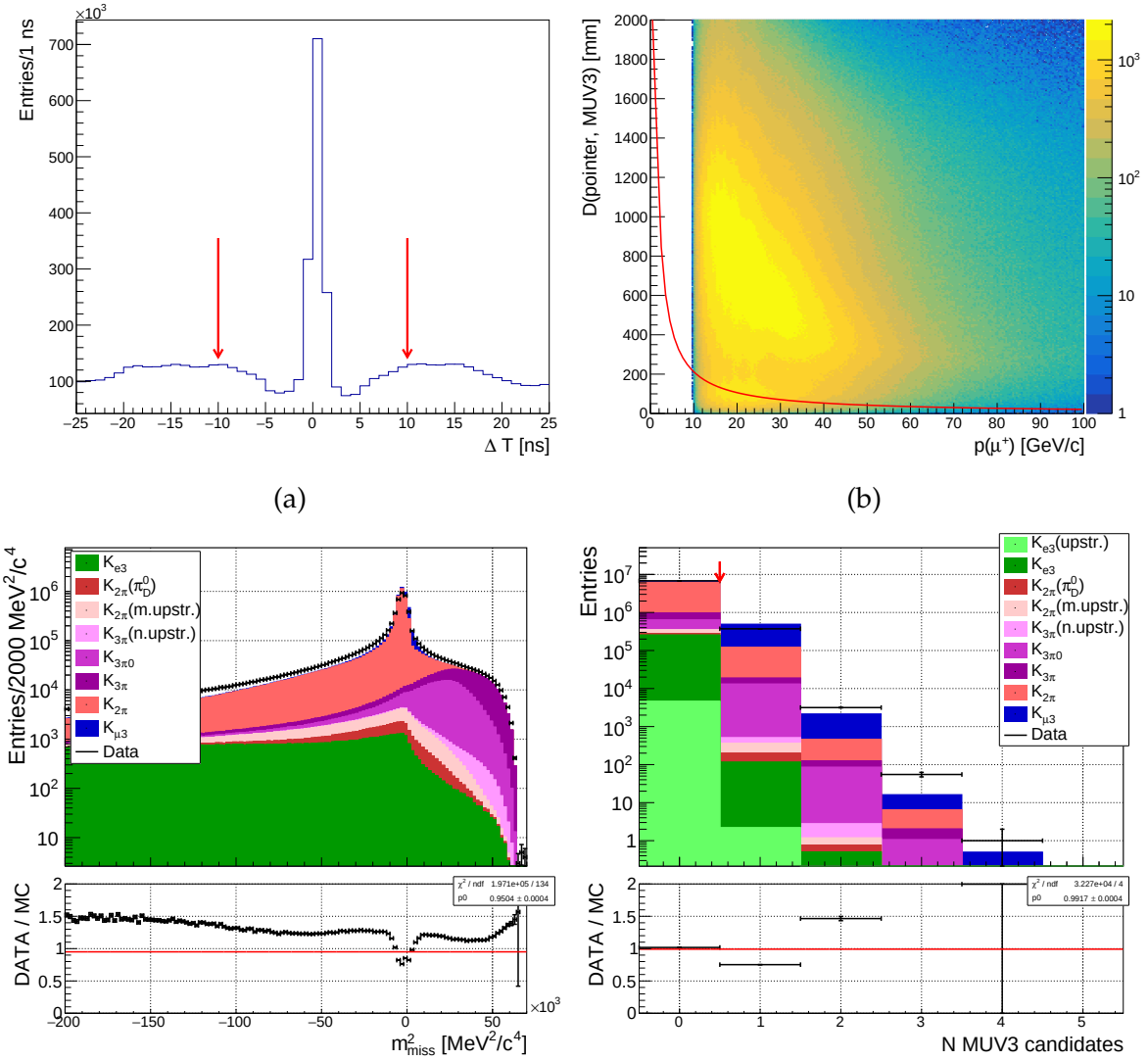

Figure 3.4.3: Cut 4 (MUV3 matching): (a) Time difference between π^0 and MUV3 candidates. Red arrows indicate the used time window. (b) Distance between the pointer and position of the MUV3 candidate as a function of the pointer momentum. Red line indicates the momentum-dependent search radius. (c) Squared missing mass after cut 2. (d) Number of MUV3 candidates matched in time with π^0 and close to the pointer position at MUV3 plane. At least one matched MUV3 candidate is required in the $K_{\mu 3}$ event selection. Data sample: 2017A, control trigger.

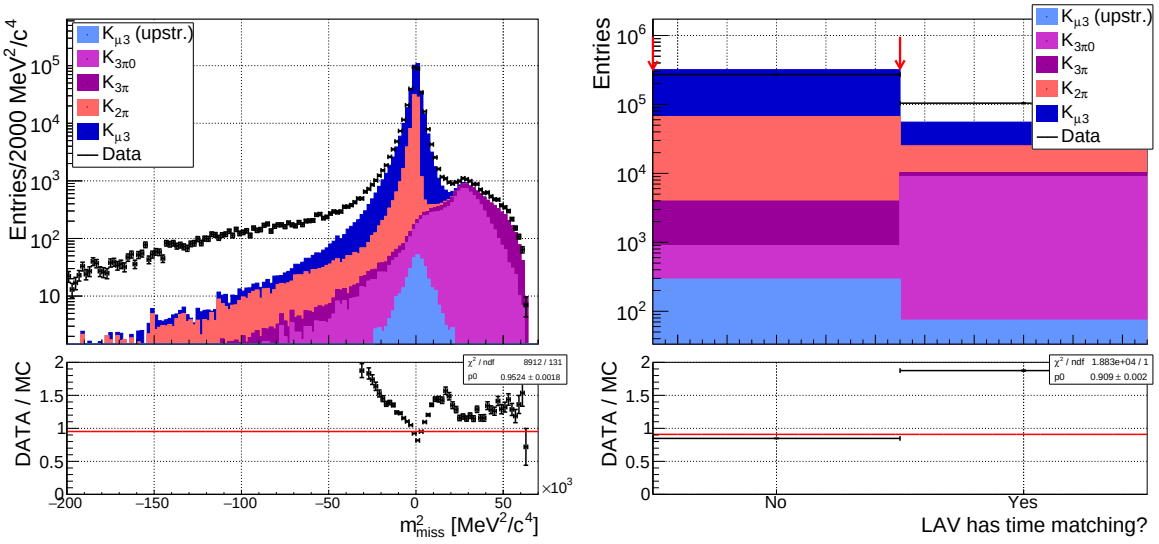

(a) (b)

Figure 3.4.4: Cut 5 (LAV veto): (a) Squared missing mass before the cut. (b) LAV time matching. Data sample: 2017A, control trigger.

The LAV, IRC, and SAC sub-detectors are used to veto $K^+ \to \pi^+\pi^0\pi^0$ events with a charged pion decay and events in which an accidental LKr cluster is used for the π^0 reconstruction, see Figure 3.4.4. At this point, about 26 % of events in the final signal region defined in Table 3.4.1 are $K_{2\pi}$ events with a μ^+ produced in the π^+ decay. In more than 53 % of these events the true Z coordinate of the π^+ decay vertex lies before the first STRAW chamber. Furthermore, in most of these decays, the momentum carried by muon does not differ from the pion momentum by more than 5 GeV/c with the difference mostly in p_z component. However, taking advantage of the fact that in the kaon rest frame, the momentum of the π^0 from the $K_{2\pi}$ decay is known (since it is a two-body decay), a cut on the π^0 momentum in the kaon rest frame (190 MeV/c) is used to reject most of the $K_{2\pi}$ background, see Figure 3.4.5.

If a GTK candidate is found in the π^0 selection, it is then used to calculate the squared missing mass. Otherwise, the average beam kaon momentum is used. The squared missing mass in a $K_{\mu 3}$ event is expected to peak around zero since it corresponds to the squared mass of a neutrino. A strict final cut at 2000 MeV$^2/c^4$ is imposed on this variable. All cuts used to select the $K_{\mu 3}$ events are summarized in Table 3.4.1. In the stack plots, only MC samples of kaon decays contributing to the integral in selected range by more than 0.05 % are included.

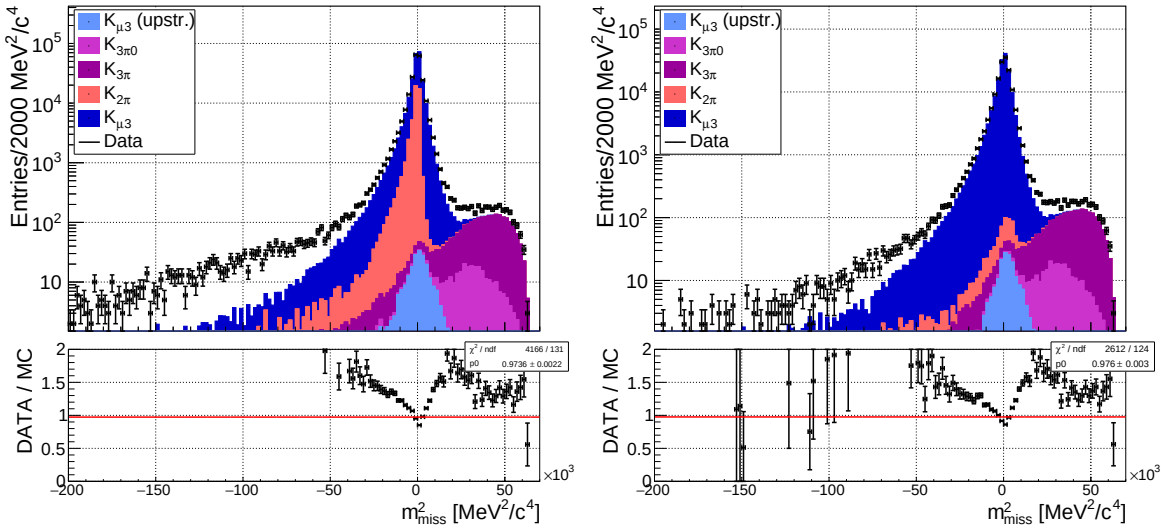

(a) (b)

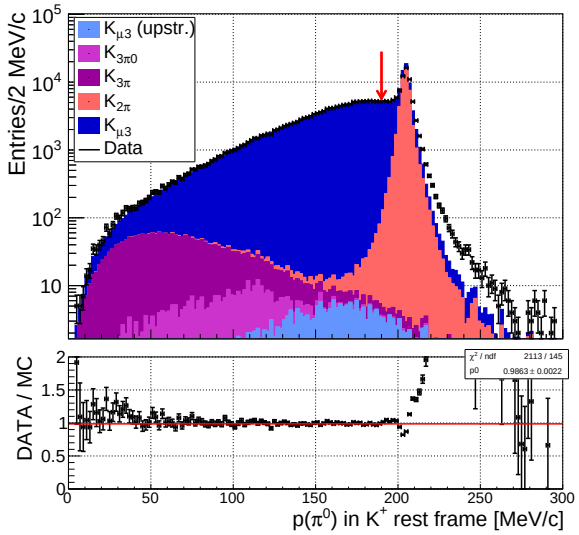

(c)

Figure 3.4.5: Cut 7 (π^0 momentum in K^+ rest frame): (a) Squared missing mass before the cut. (b) Squared missing mass after the cut. (c) π^0 momentum in K^+ rest frame. Red arrow indicates the cut used to reject $K_{2\pi}$ background. Data sample: 2017A, control trigger.

Cut 1	π^0 selected	1
Cut 2	One RICH candidate in time with π^0	< 5 ns
Cut 3	Pointer in MUV3 acceptance	
Cut 4	MUV3 candidate in time with π^0 MUV3 candidate close to the pointer Number of MUV3 candidates in time and close to π^0	< 10 ns Equation (3.4.3) ≥ 1
Cut 5	LAV matching - half time window Number of LAV in-time matches	5 ns 0
Cut 6	IRC and SAC matching - half time window Number of IRC and SAC in-time matches	10 ns 0
Cut 7	$p(\pi^0)$ in K^+ rest frame	< 190 MeV/c
Cut 8	$\lvert m^2_{miss} \rvert$	< 2000 MeV$^2/c^4$

Table 3.4.1: $K_{\mu 3}$ event selection summary.

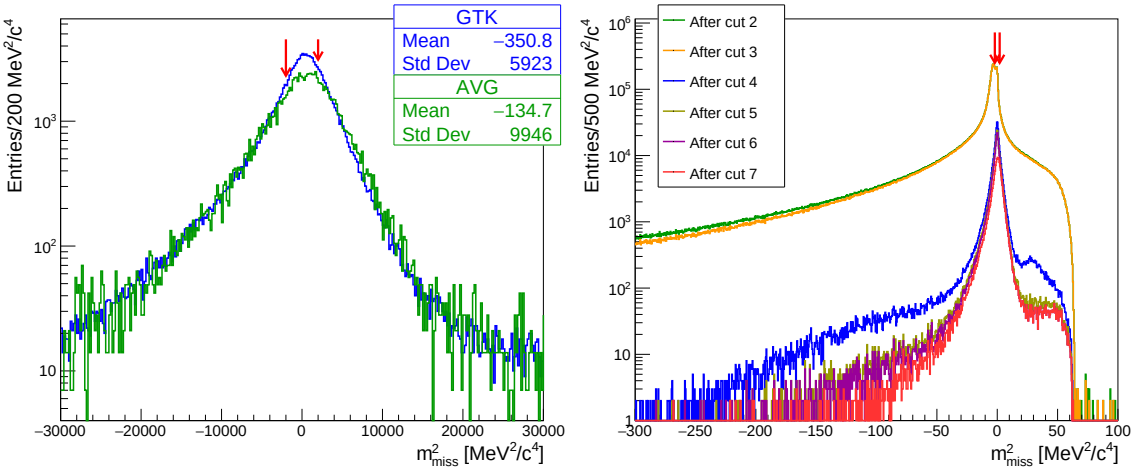

(a) (b)

Figure 3.4.6: (a) Comparison of reconstructed m^2_{miss} before the final cut for events with a GTK candidate matched to the π^0 and for events in which the average kaon momentum was used. The resolution of the squared missing mass peak was measured to be (1378.7 ± 7.9) MeV$^2/c^4$ with the GTK candidate and (1792.3 ± 48.1) MeV$^2/c^4$ with the average kaon momentum.(b) m^2_{miss} distribution after cuts of the $K_{\mu 3}$ event selection. Red arrows indicate the final cut. Data sample: 2017A, control trigger.

3.4.2 Results

Distributions of several important observable quantities, obtained after applying the $K_{\mu 3}$ selection are presented in the following figures.

The $K_{\mu 3}$ acceptance ($z_{vtx,true} \in (102\,425,\ 180\,000)$ mm) is 3.0 % while the $K_{2\pi}$ accept-

ance is 6.6×10^{-6}, both with negligible uncertainties. The acceptance of $K_{\mu 3}$ decays occurring upstream of the decay region is $4.2(2) \times 10^{-5}$.

To estimate how the results are sensitive to the μ^+ pointer misreconstruction, two tests are performed. First, the efficiency in the 2017 data sample is evaluated using the same selection but with the final cut symmetrically extended to (−5000, 5000) MeV$^2/c^4$, resulting in a shift of $\Delta\varepsilon = -0.11\,\%$ (−0.25 % in 4CH case). In the second test, only events with a GTK candidate matched to the π^0 are considered. This results in $\Delta\varepsilon = 0.11\,\%$ (0.27 % in 4CH case).

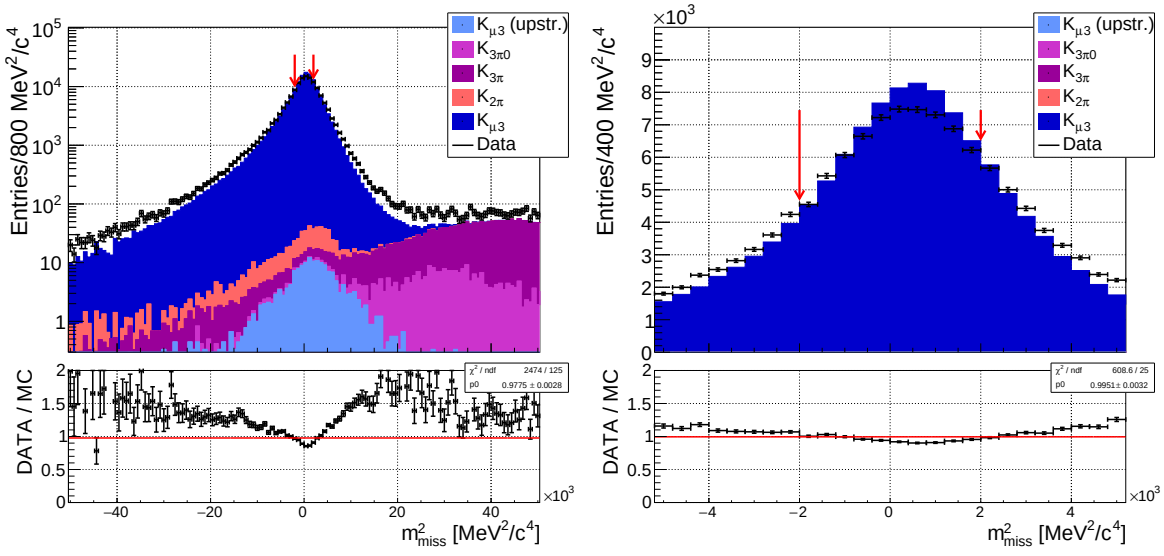

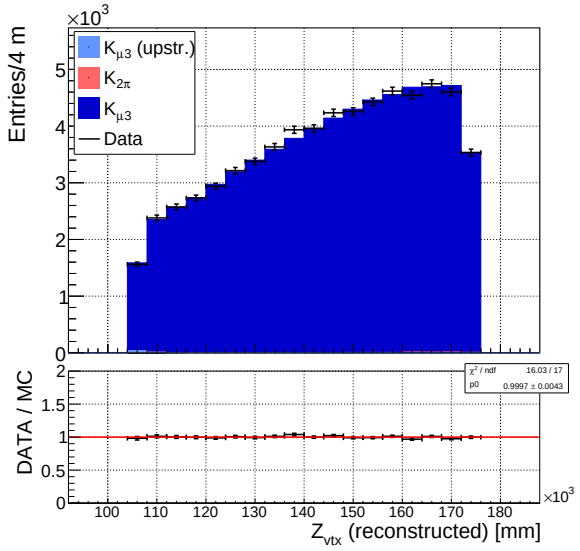

Figure 3.4.7: (a), (b) Reconstructed squared missing mass before the final cut. (c) Final distribution of z_{vtx}. Data sample: 2017A, control trigger.

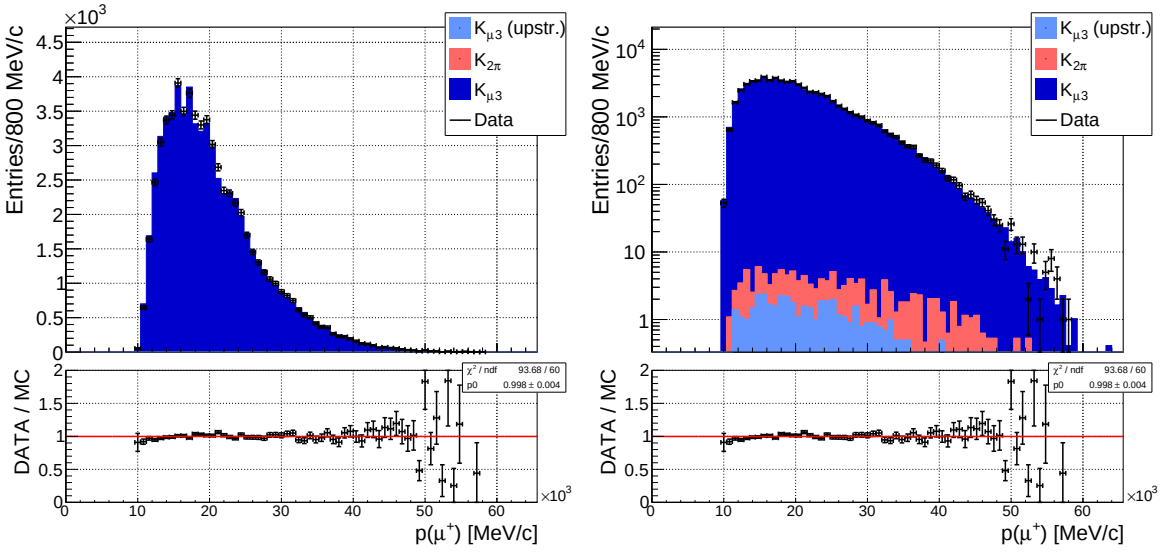

(a) (b)

Figure 3.4.8: (a), (b) Final reconstructed muon momentum distribution. Data sample: 2017A, control trigger.

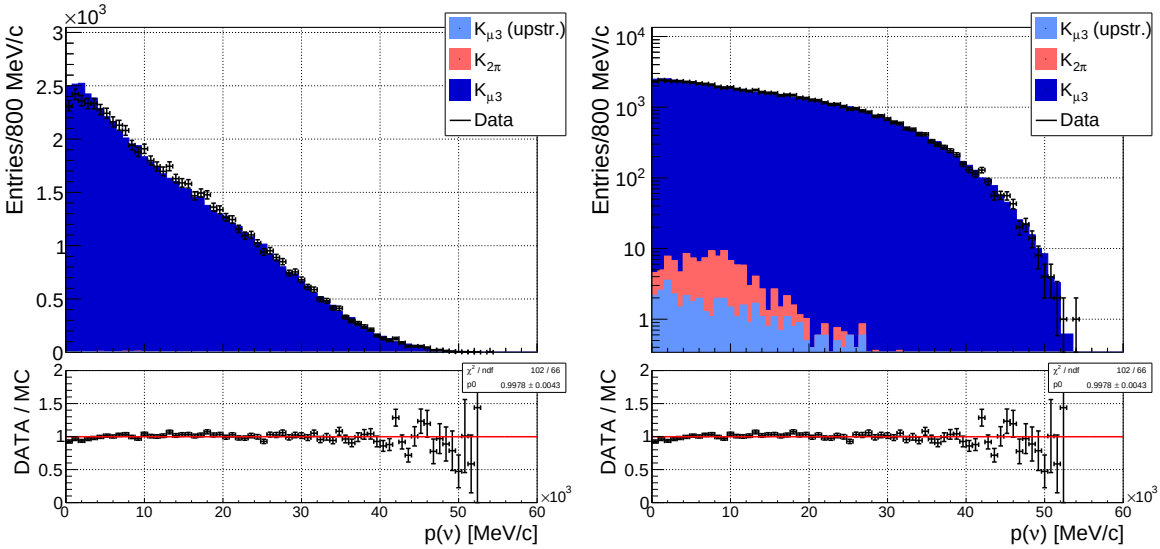

(a) (b)

Figure 3.4.9: (a), (b) Final missing momentum. Data sample: 2017A, control trigger.

The μ^+ track reconstruction efficiency is evaluated for all 2016, 2017 and 2018 data samples and for the $K_{\mu 3}$ Monte Carlo events. The results are presented in subsections 3.4.2.1 and 3.4.2.2, a summary table with efficiency values for all studied samples is in Appendix E. The difference of about 3 % between the 2016 data sample with respect to the 2017+2018 data samples, discussed for $K_{2\pi}$ in subsection 3.3.2, is also observed for $K_{\mu 3}$.

3.4.2.1 Efficiency in data

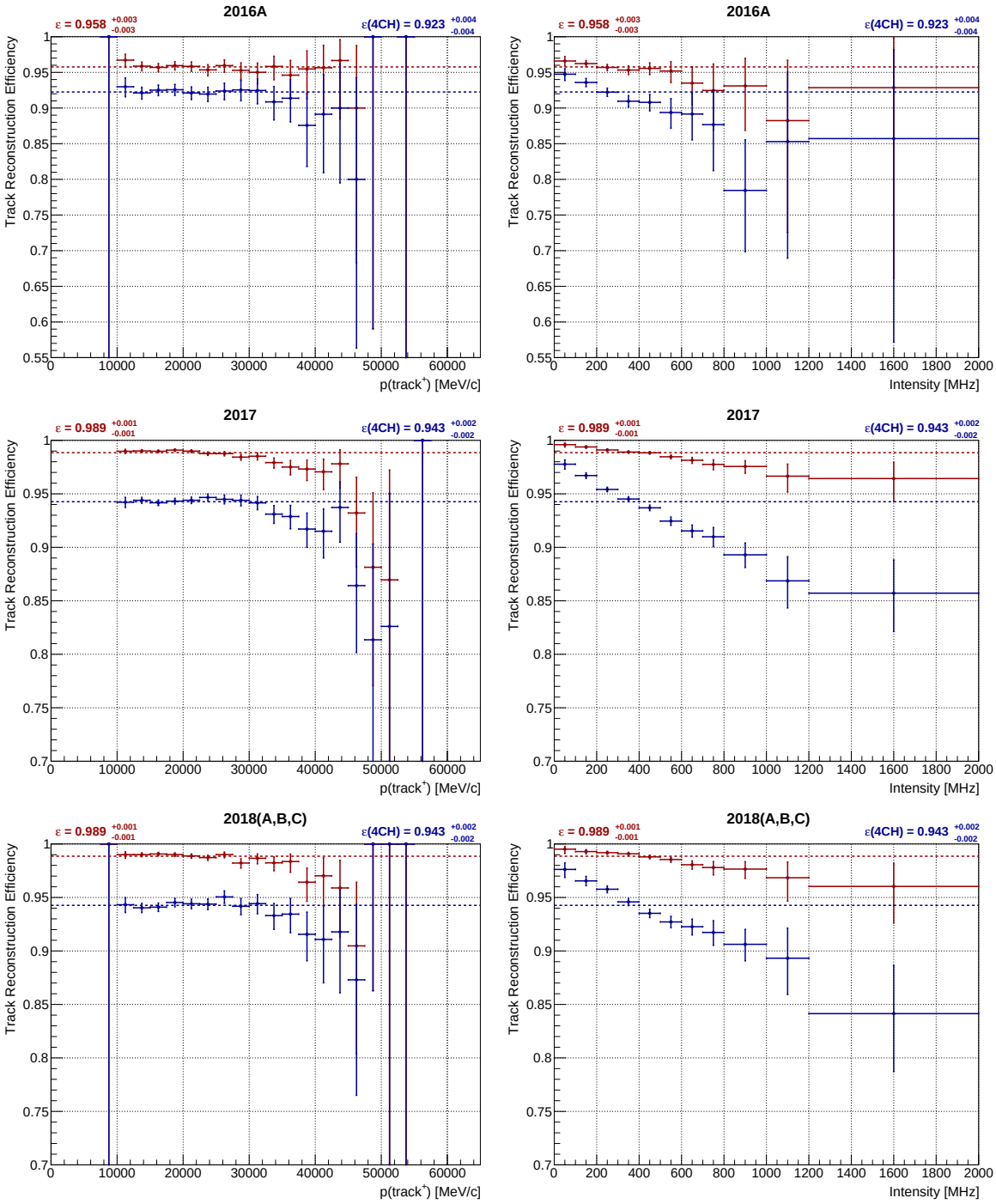

Figure 3.4.10: μ^+ track reconstruction efficiency as a function of the momentum of the reconstructed μ^+ pointer (left), and as a function of the instantaneous beam intensity (right). Data sample: 2016A, 2017, 2018(A-C), control trigger.

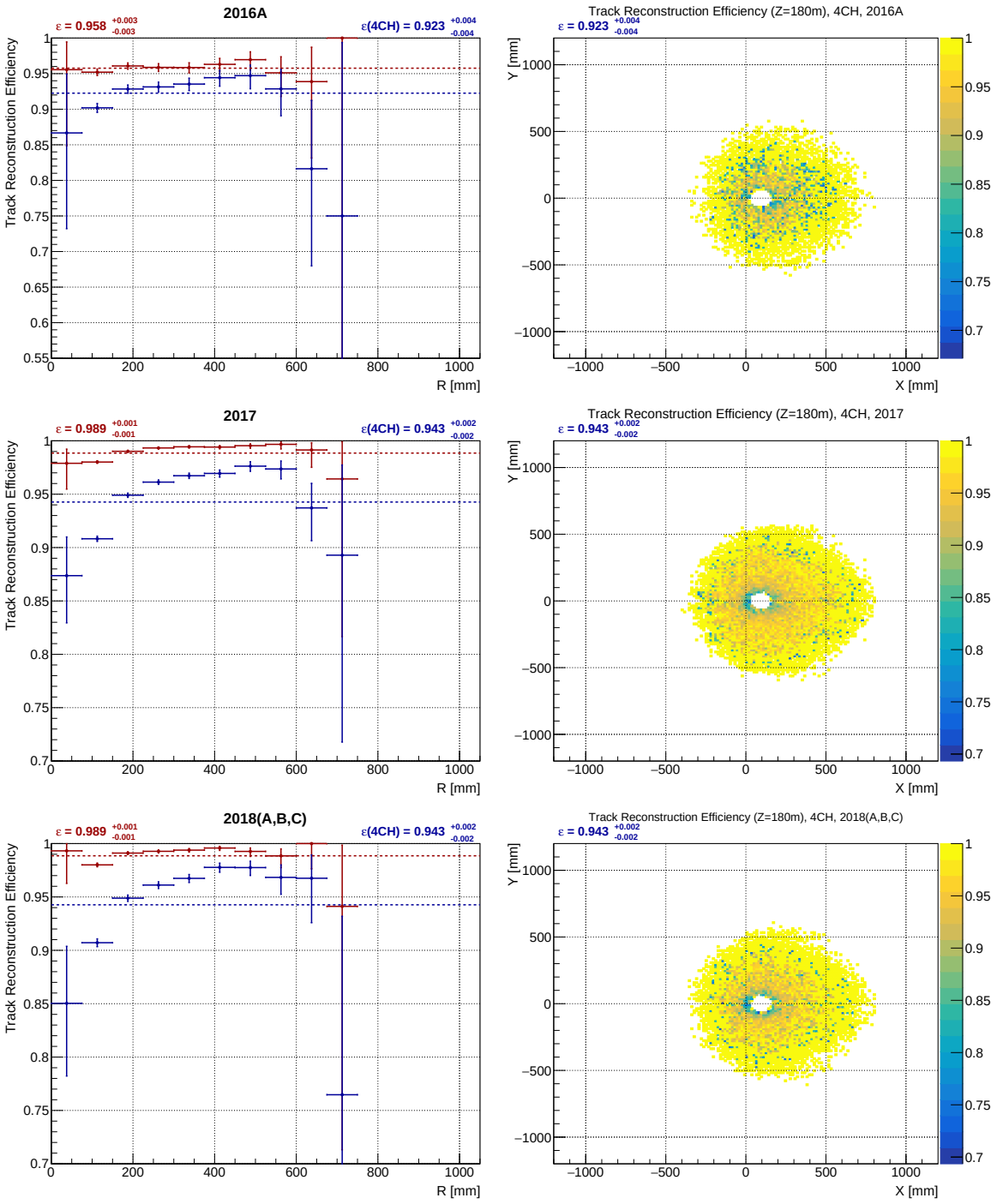

Figure 3.4.11: μ^+ track reconstruction efficiency as a function of the distance from the beam axis - (left), and as a function of the reconstructed μ^+ pointer position before magnet at $z = 180\,\mathrm{m}$ (only candidates reconstructed from hits in all four chambers are used) - (right). Data sample: 2016A, 2017, 2018(A-C), control trigger.

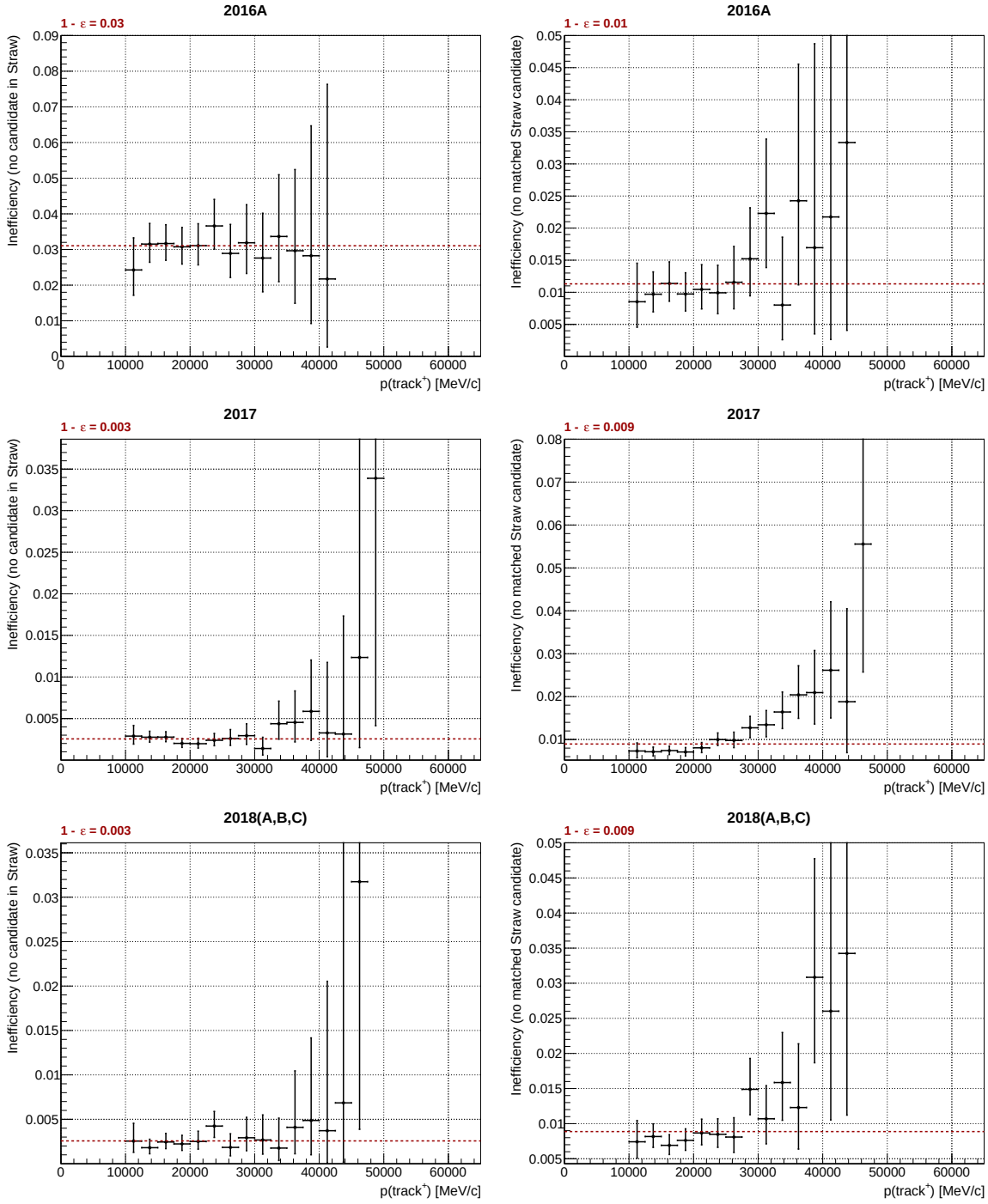

Figure 3.4.12: μ^+ track reconstruction inefficiency as a function of the reconstructed μ^+ momentum: the inefficiency caused by no STRAW candidate present in the event (left), the inefficiency due to no STRAW candidate compatible with the μ^+ pointer found in the event (right). The compatibility criteria are based on the momentum and position difference between the pointer and a STRAW candidate and are summarized in Section 3.2. Data sample: 2016A, 2017, 2018(A-C), control trigger.

3.4.2.2 Efficiency in MC

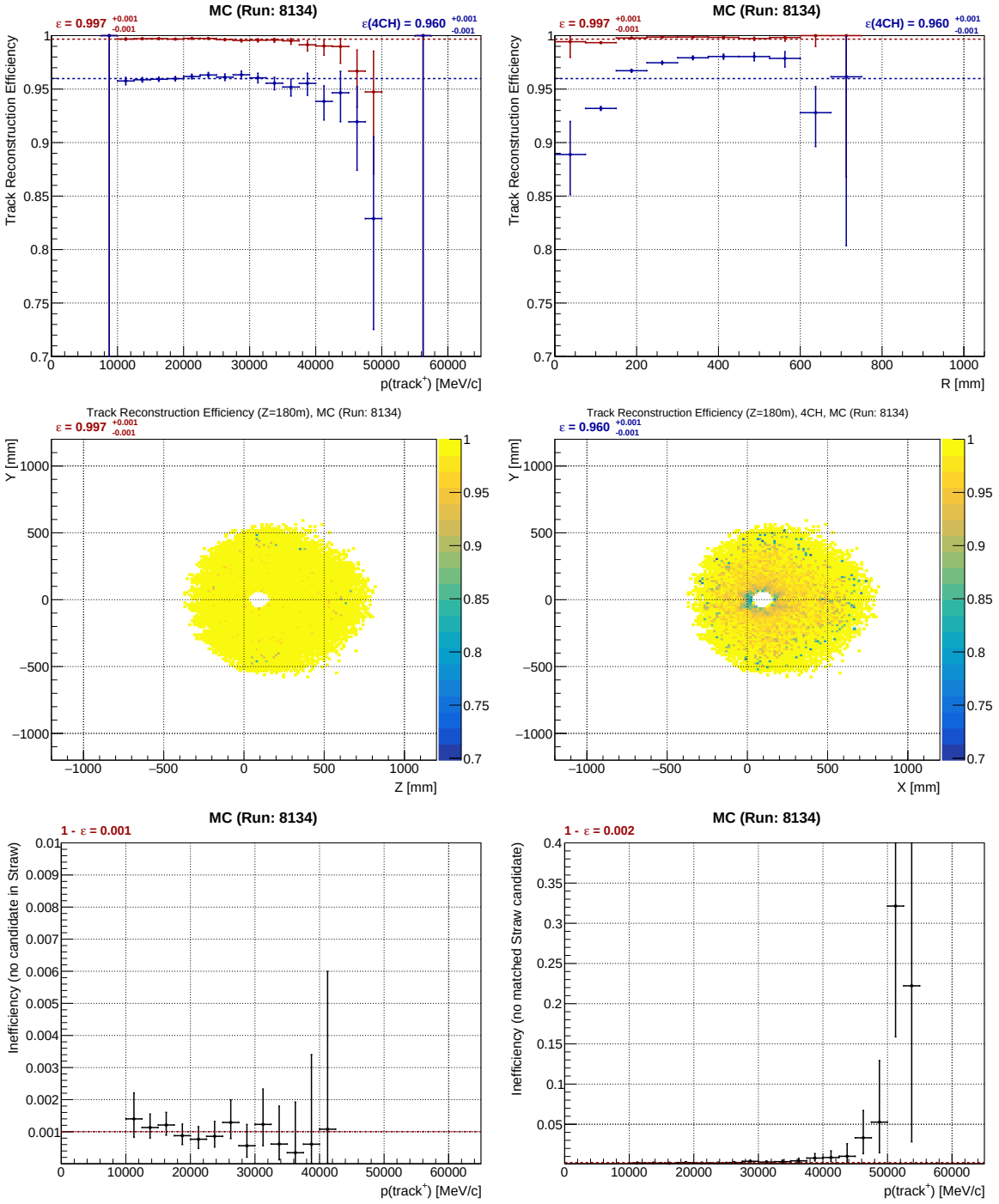

Figure 3.4.13: μ^+ track reconstruction efficiency as a function of the reconstructed μ^+ pointer momentum (top left), the distance from the beam axis (top right) and the μ^+ pointer position before magnet ($z = 180\,\mathrm{m}$): all STRAW candidates (middle left), only 4 chamber candidates (middle right). μ^+ track reconstruction inefficiency as a function of the μ^+ pointer momentum. Two classes of events are considered: events inefficient due to no candidate reconstructed in the STRAW (bottom left) and due to no STRAW candidate matched to the pointer (bottom right). MC sample: $K_{\mu 3}$ events with upstream and downstream pile-up (subsection 2.3.3).

3.5 Measurement of the e^+ reconstruction efficiency with $K^+ \to \pi^0 e^+ \nu_e$ decay

The efficiency of the STRAW e^+ track reconstruction is evaluated using the $K^+ \to \pi^0 e^+ \nu_e$ decay. In the K_{e3} selection the LKr information is used to reconstruct the e^+ pointer energy, while the radius and the position of the corresponding RICH ring are used for positron identification.

3.5.1 K_{e3} selection

Only events with exactly one reconstructed π^0 candidate enter the K_{e3} selection.

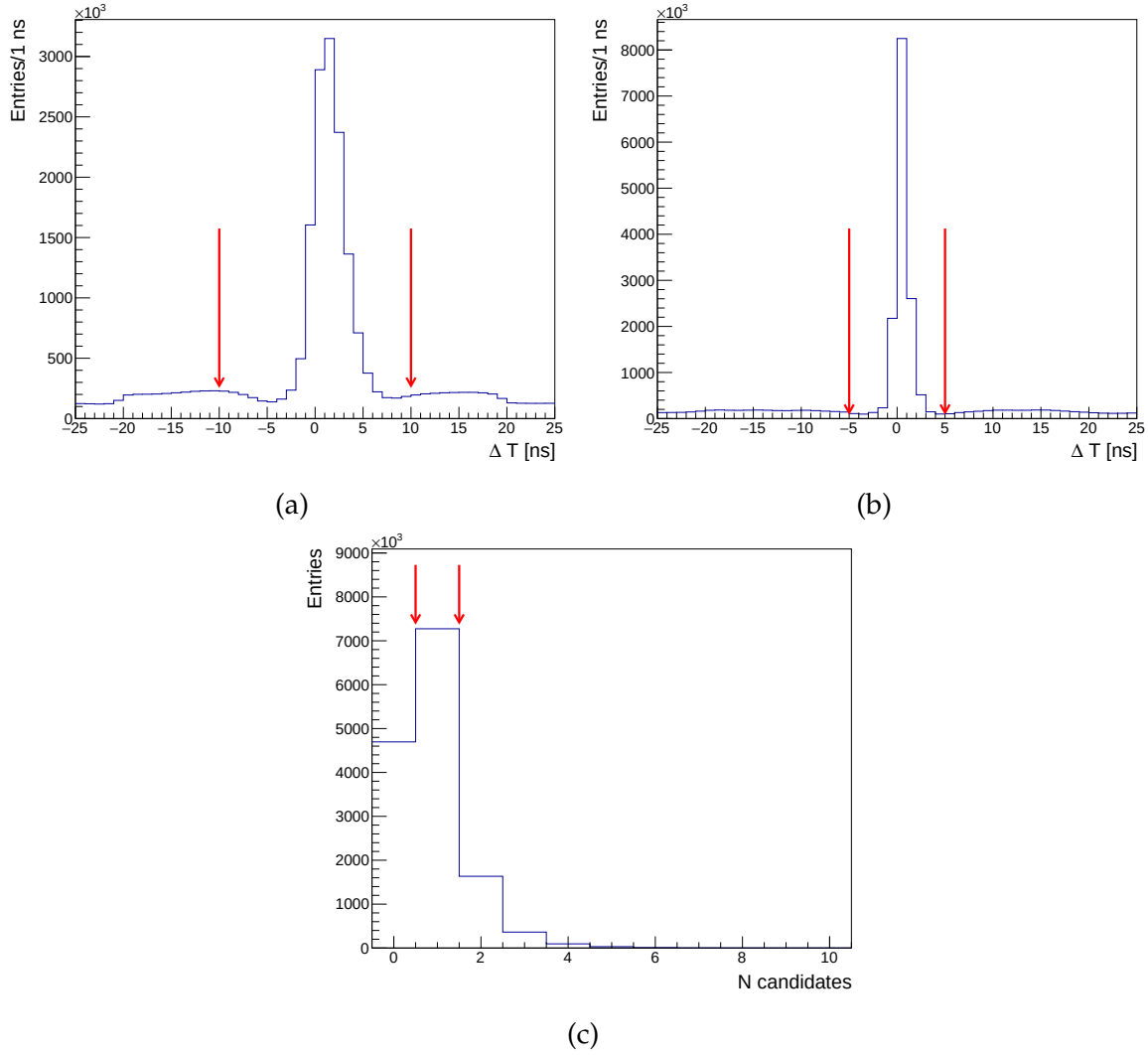

Figure 3.5.1: Cut 2: (a) Time difference between the trigger and RICH candidates. (b) Time difference between the π^0 and RICH candidates. (c) Number of in-time RICH candidates. Red arrows indicate the cut values used in the K_{e3} event selection. Data sample: 2017A, control trigger.

Precisely one RICH ring candidate in time with the trigger time (10 ns) and the

π^0 time (5 ns) is required, see Figure 3.5.1. The ring radius of the RICH candidate has to be larger than the run-dependent electron radius R_e to be identified as a positron.

One additional cluster in time with the π^0 time (10 ns) is then required to be found in the LKr. For this cluster, a positron hypothesis is considered and a momentum of the e^+ pointer is calculated from the neutral vertex position, the cluster position and the cluster energy, taking into account the MNP33 magnet with a momentum kick of 270 MeV/c in the negative X direction.

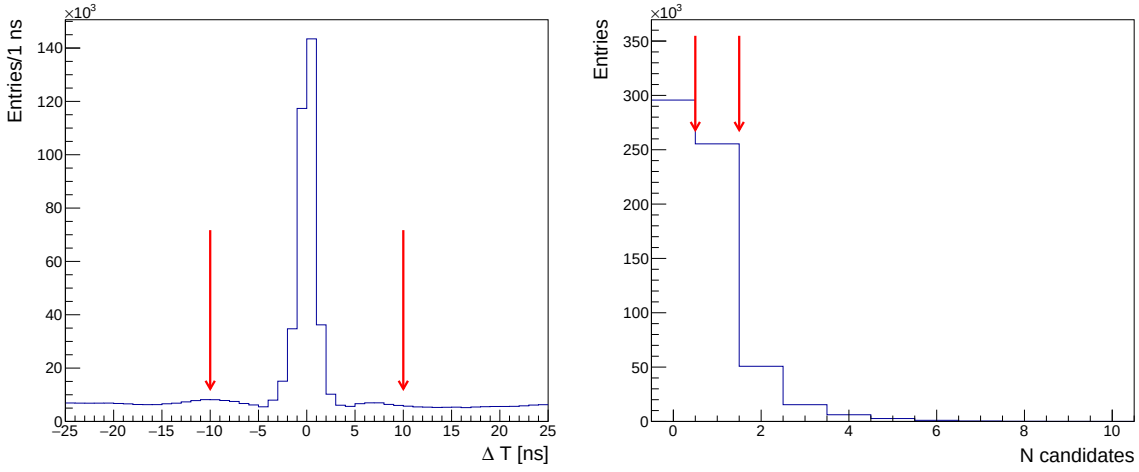

(a) (b)

Figure 3.5.2: Cut 4: (a) Time difference between π^0 and additional LKr candidates. (b) Number of additional LKr candidates in time with π^0 time. Red arrows indicate the cut values used in the K_{e3} selection. Data sample: 2017A, control trigger.

The expected ring radius and ring center in RICH corresponding to the positron can be computed from e^+ momentum after the MNP33 magnet, $\vec{p} = (p_x, p_y, p_z)$, in the following way:

$$R_{e^+} = l_f \arccos\left(\frac{\sqrt{M_e^2 + |\vec{p}|^2}}{n|\vec{p}|}\right), \tag{3.5.1}$$

$$\vec{r}_{RC} = \left(l_f \frac{p_x}{p_z}, l_f \frac{p_y}{p_z}, Z_{RICH}\right), \tag{3.5.2}$$

where $l_f = 17\,020$ mm is the RICH focal length, $n = 1.000062$ is the RICH gas refractive index, and M_e is the nominal positron mass. For positive positron identification it is then required that the difference between the expected positron radius and the RICH ring radius is smaller than 4 mm. To further suppress background, ring centers are compared as well: a maximum 20 mm cut is imposed on the distance between the expected positron ring center and the ring center of the RICH candidate, see Figure 3.5.3.

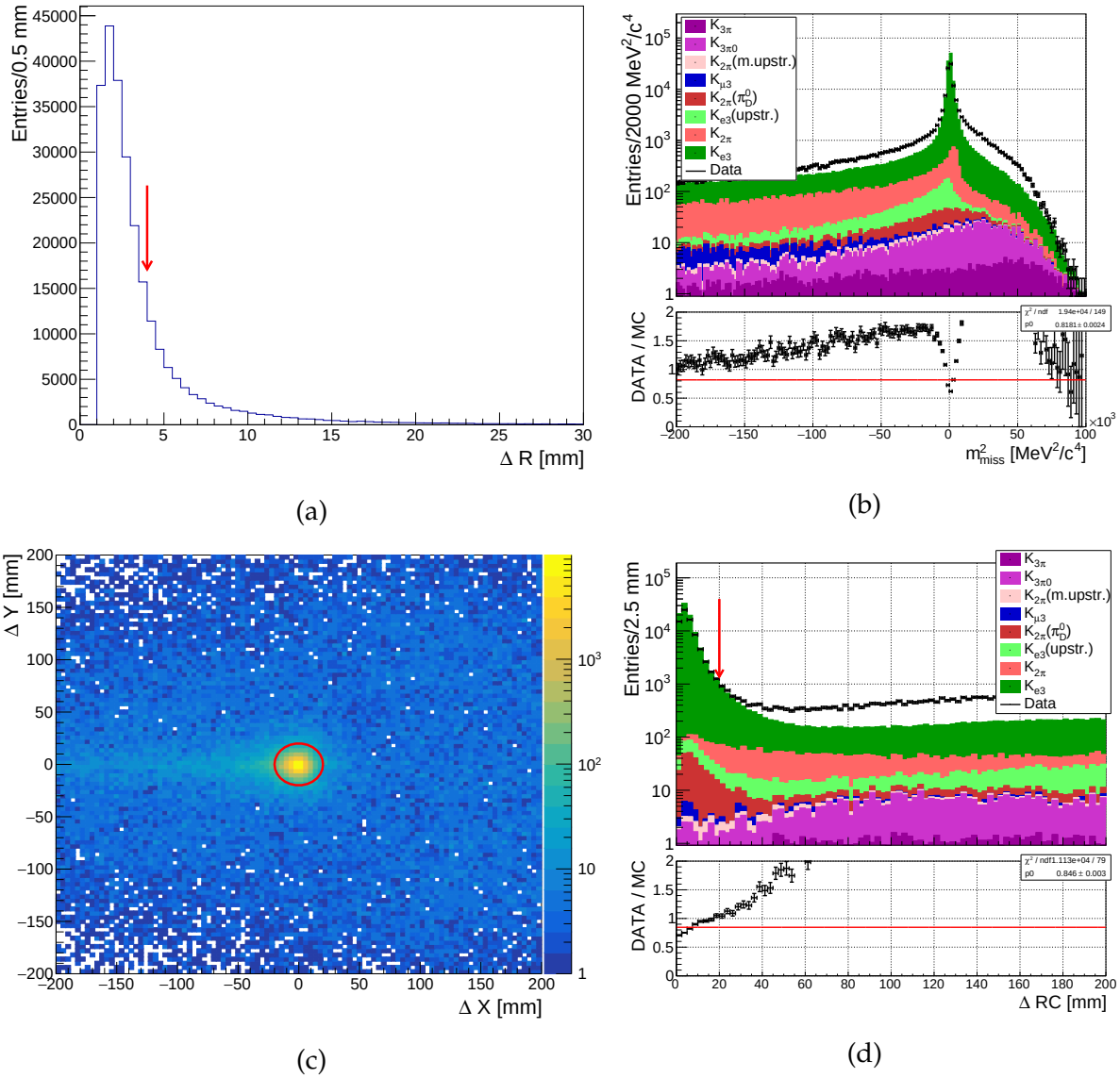

Figure 3.5.3: Cuts 5+6 (RICH e^+ ID): (a) Difference between the expected ring radius and the ring radius of RICH candidates. Red arrow indicates a cut used in the K_{e3} event selection. (b) Squared missing mass after cut 5. (c) X and Y coordinate difference between the expected positron ring center and the ring center of RICH candidates. Red circle indicates a cut used in the K_{e3} event selection. (d) Ring center difference. Data sample: 2017A, control trigger.

A MUV3 veto condition is applied and events with MUV3 candidates in time (15 ns) with the π^0 time are rejected to suppress the $K_{\mu 3}$ and $K_{\mu 2}$ backgrounds. Photon veto using LAV, IRC, and SAC sub-detectors is then used to reject events in which an accidental LKr cluster was used for the π^0 reconstruction, as well as events with radiative photons. Next, only events with no MUV1 candidates and no MUV1 hits in time with the π^0 time (15 ns) are kept, which suppresses π^+ backgrounds, see Figures 3.5.4 and 3.5.5.

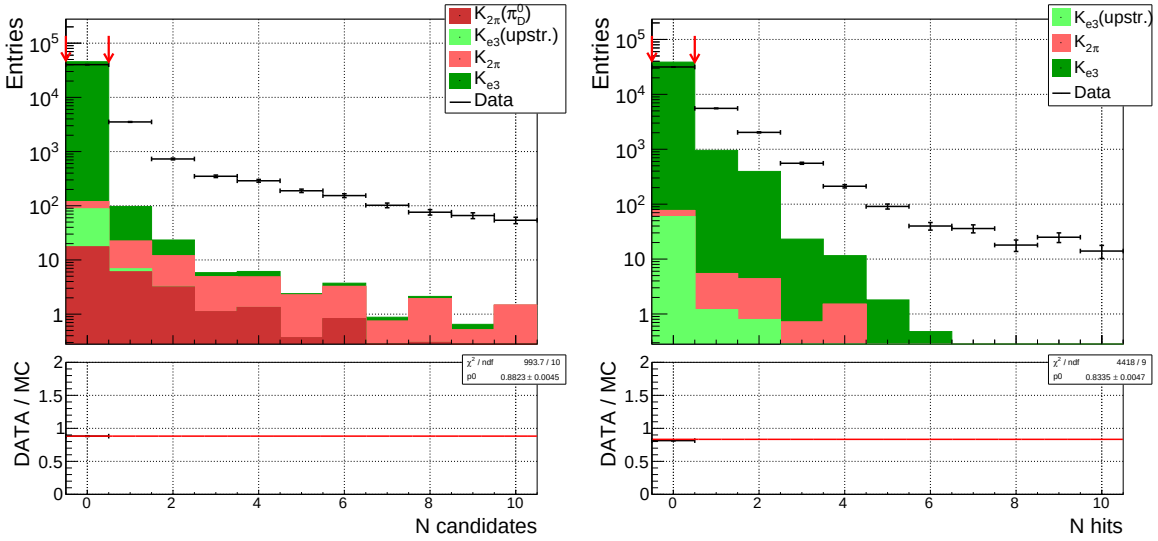

(a) (b)

Figure 3.5.4: (a) Cut 10: Number of MUV1 candidates in time with π^0. (b) Cut 11: Number of MUV1 hits in time with π^0. Red arrows indicate cuts used in the K_{e3} event selection. Data sample: 2017A, control trigger.

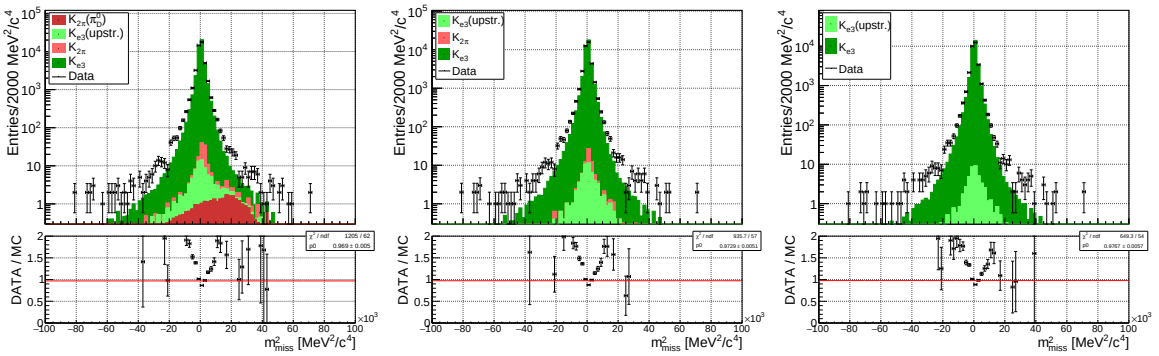

(a) (b) (c)

Figure 3.5.5: (a) Squared missing mass after cut 9. (b) Squared missing mass after cut 10. (c) Squared missing mass after cut 11. Data sample: 2017A, control trigger.

If available, the GTK candidate found in the π^0 selection is then used to calculate the squared missing mass. Otherwise, the average beam momentum is used. The squared missing mass in a K_{e3} event, calculated from kaon, pion and positron four-momenta as $m^2_{miss} = (P_{K^+} - P_{\pi^0} - P_{e^+})^2$, is expected to peak around zero since it corresponds to squared mass of the neutrino. Therefore a strict final cut at 2000 MeV$^2/c^4$ is imposed on this variable to select the final $K_{\mu 3}$ sample.

All cuts used to select K_{e3} events are summarized in Table 3.5.1. In the stack plots, only MC samples of kaon decays contributing to the integral in selected range by more than 0.05 % are included.

Cut 1	π^0 selected	1
Cut 2	RICH ring candidate in time with trigger RICH ring candidate in time with π^0 N RICH ring candidates in time with trigger and π^0	< 10 ns < 5 ns 1
Cut 3	RICH ring radius	$> R_e$ (run dep.)
Cut 4	One additional LKr cluster in time with π^0	< 10 ns
Cut 5	Difference between expected and found RICH ring radius	< 4 mm
Cut 6	Distance between expected and found RICH ring center	< 20 mm
Cut 7	No MUV3 candidate in time with π^0	< 15 ns
Cut 8	LAV matching - half time window Number of LAV in-time matches	5 ns 0
Cut 9	IRC and SAC matching - half time window Number of IRC and SAC in-time matches	10 ns 0
Cut 10	No MUV1 candidate in time with π^0	< 20 ns
Cut 11	No MUV1 hit in time with π^0	< 20 ns
Cut 12	$\lvert m^2_{miss}\rvert$	$< 2000\,\mathrm{MeV}^2/c^4$

Table 3.5.1: K_{e3} event selection summary.

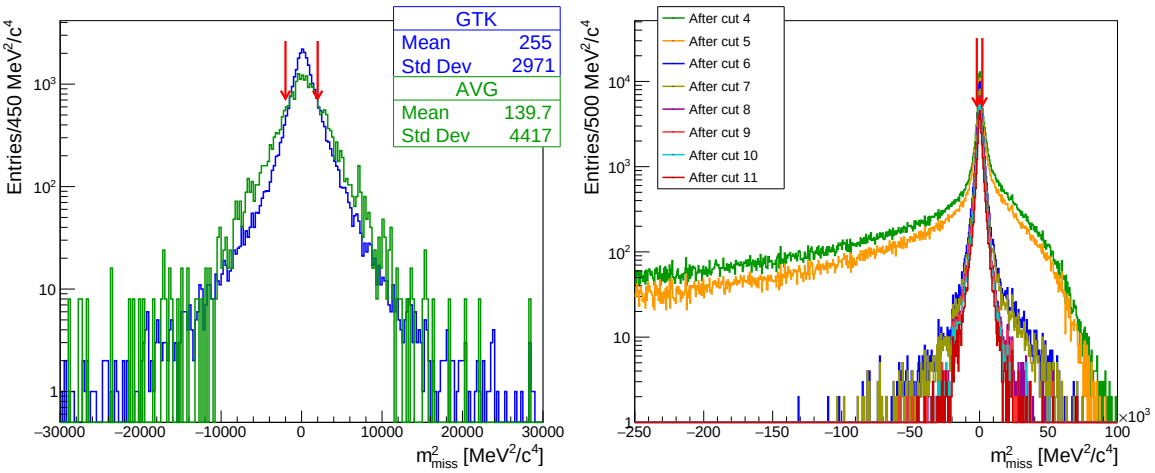

(a) (b)

Figure 3.5.6: (a) Comparison of reconstructed m^2_{miss} before the final cut for events with a GTK candidate matched to the π^0 and for events in which the average kaon momentum was used. The resolution of the squared missing mass peak is measured to be $(1139.9 \pm 11.7)\,\mathrm{MeV}^2/c^4$ with the GTK candidate and $(1716.4 \pm 111.1)\,\mathrm{MeV}^2/c^4$ with the average kaon momentum. (b) m^2_{miss} distribution after cuts of K_{e3} event selection. Red arrows indicate the final cut. Data sample: 2017A, control trigger.

3.5.2 Results

Since the K_{e3} selection is very strict, the selected samples contain only negligible amount of background events. Therefore, the effect of other kaon decays on the efficiency measurement can be neglected. The K_{e3} acceptance ($Z_{vtx}(true) \in (102.425,\ 180)\,\mathrm{m}$) is 0.973(1) %, while the acceptance of K_{e3} decays occurring upstream of the decay region is $1.5(1) \times 10^{-5}$.

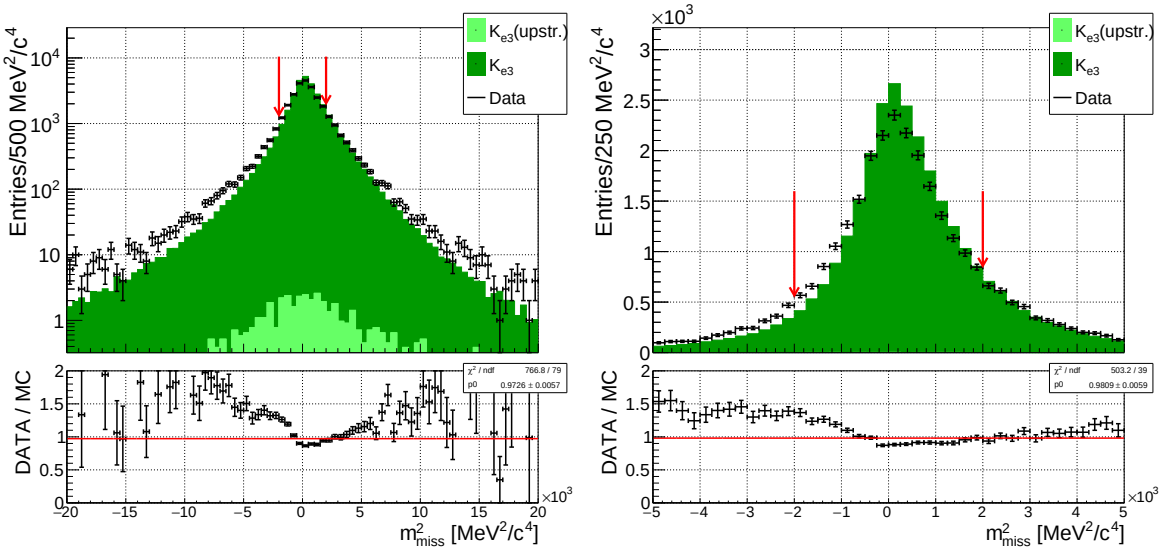

(a) (b)

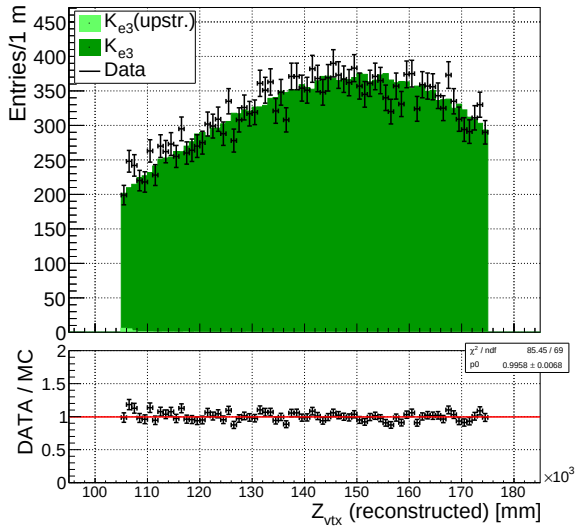

(c)

Figure 3.5.7: (a), (b) Squared missing mass before final cut. (c) Final distribution of Z_{vtx}. Data sample: 2017A, control trigger.

To estimate the result sensitivity to the e^+ pointer misreconstruction, two tests are performed. First, the efficiency in the 2017 data sample is evaluated using the same selection but with the final cut symmetrically extended to $(-5000, 5000)\,\mathrm{MeV}^2/c^4$, resulting in a shift of $\Delta\varepsilon = -0.07\,\%$ ($-0.20\,\%$ in 4CH case). In the second test, only events with a GTK candidate matched to the π^0 are considered. This resulted in

$\Delta\varepsilon = 0.01\,\%$ ($-0.01\,\%$ in 4CH case).

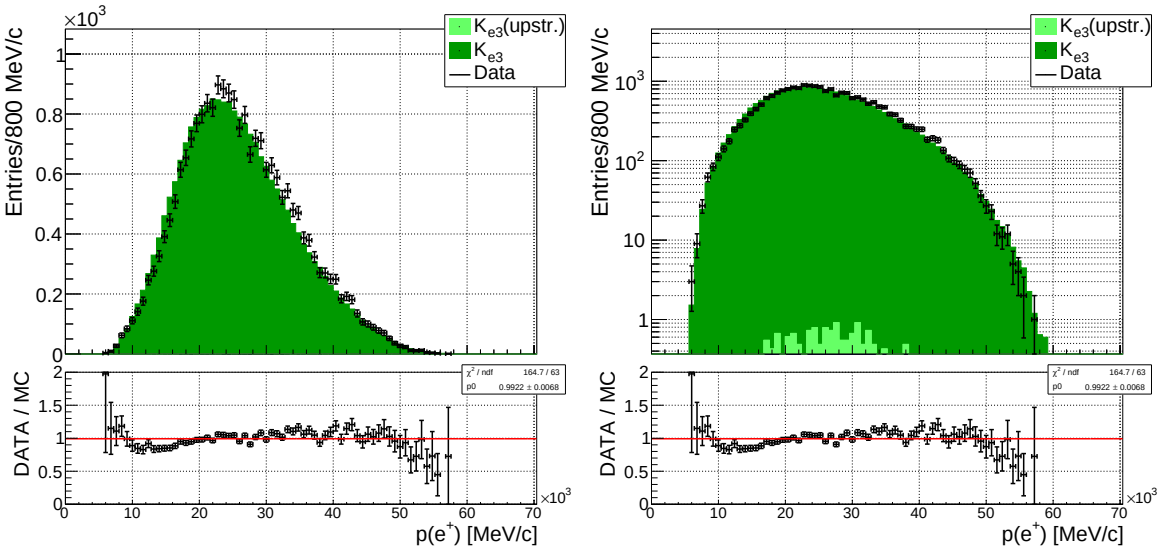

(a) (b)

Figure 3.5.8: (a), (b) Positron momentum distribution. Data sample: 2017A, control trigger.

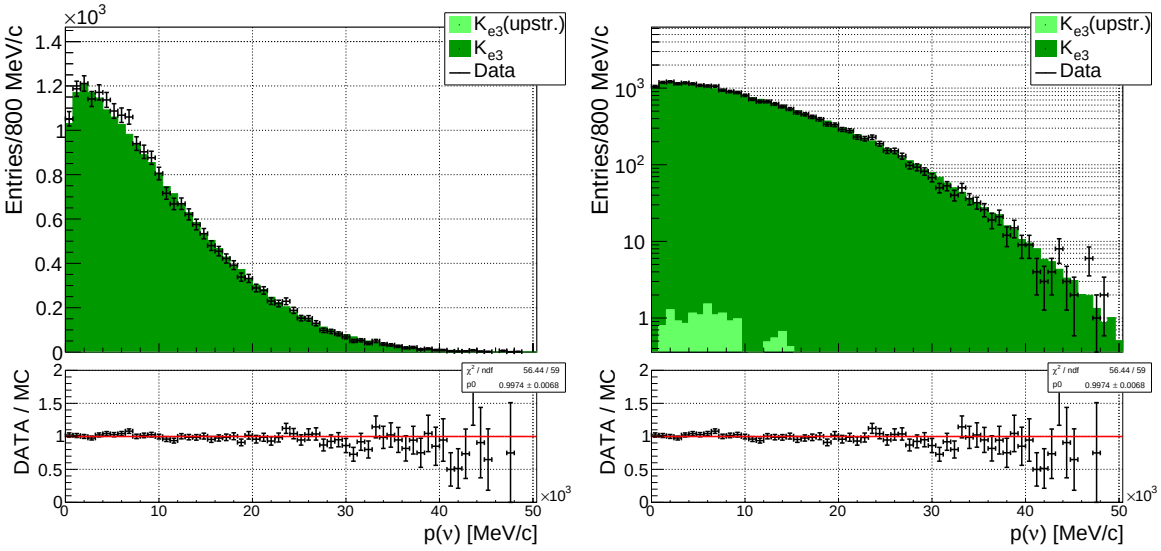

(a) (b)

Figure 3.5.9: (a), (b) Missing momentum distribution. Data sample: 2017A, control trigger.

The e^+ track reconstruction efficiency is evaluated for all 2016, 2017 and 2018 data samples and for the K_{e3} Monte Carlo events. The results are presented in the following pages, a summary table with efficiency values for all studied samples is in Appendix E. The $\sim$3 % difference between the 2016 data sample with respect to the 2017+2018 data samples, discussed already in subsection 3.3.2, is also observed in case of K_{e3}.

3.5.2.1 Efficiency in data

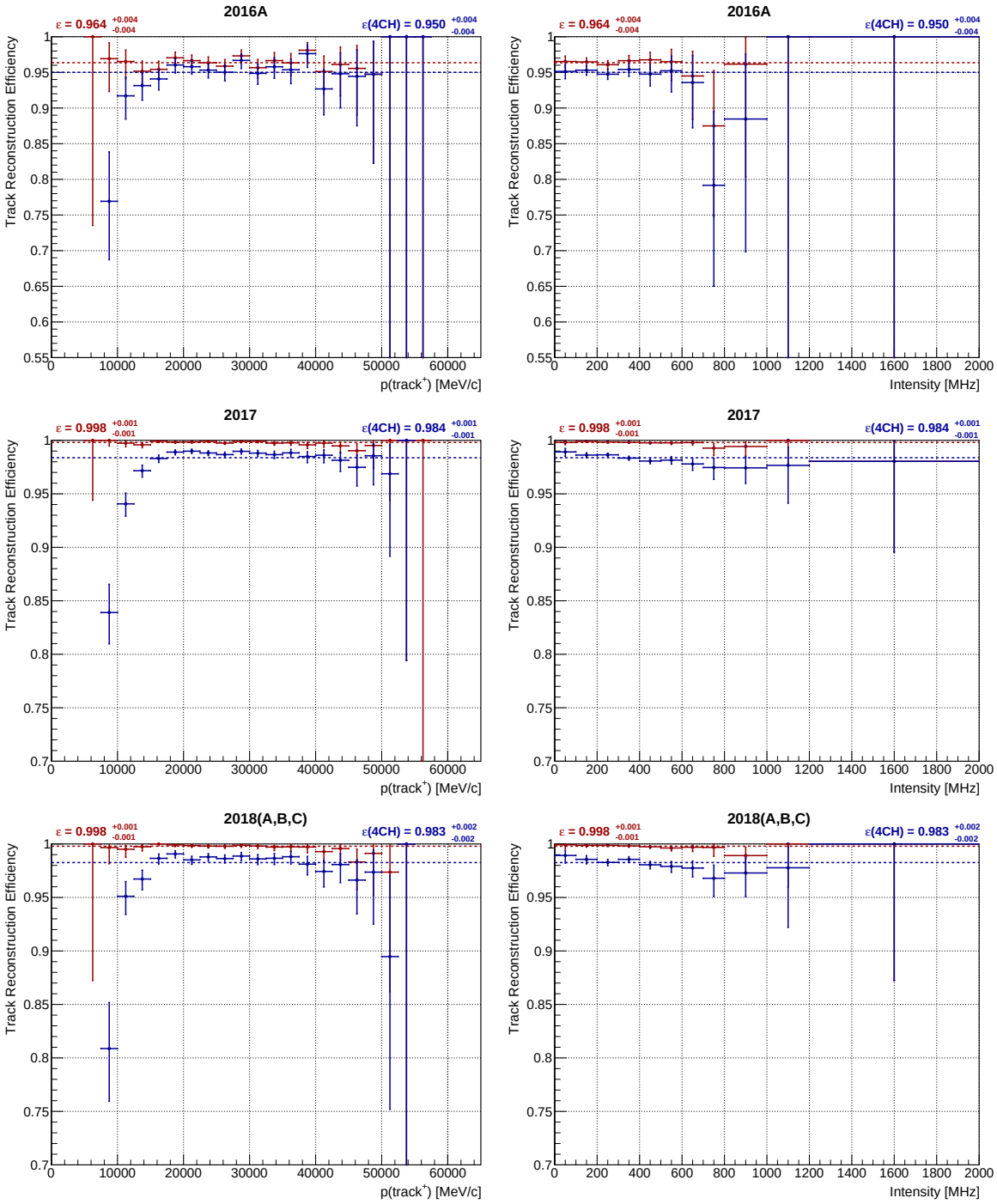

Figure 3.5.10: e^+ track reconstruction efficiency as a function of the momentum of the reconstructed e^+ pointer (left), and as a function of the instantaneous beam intensity (right). Data sample: 2016A, 2017, 2018(A-C), control trigger.

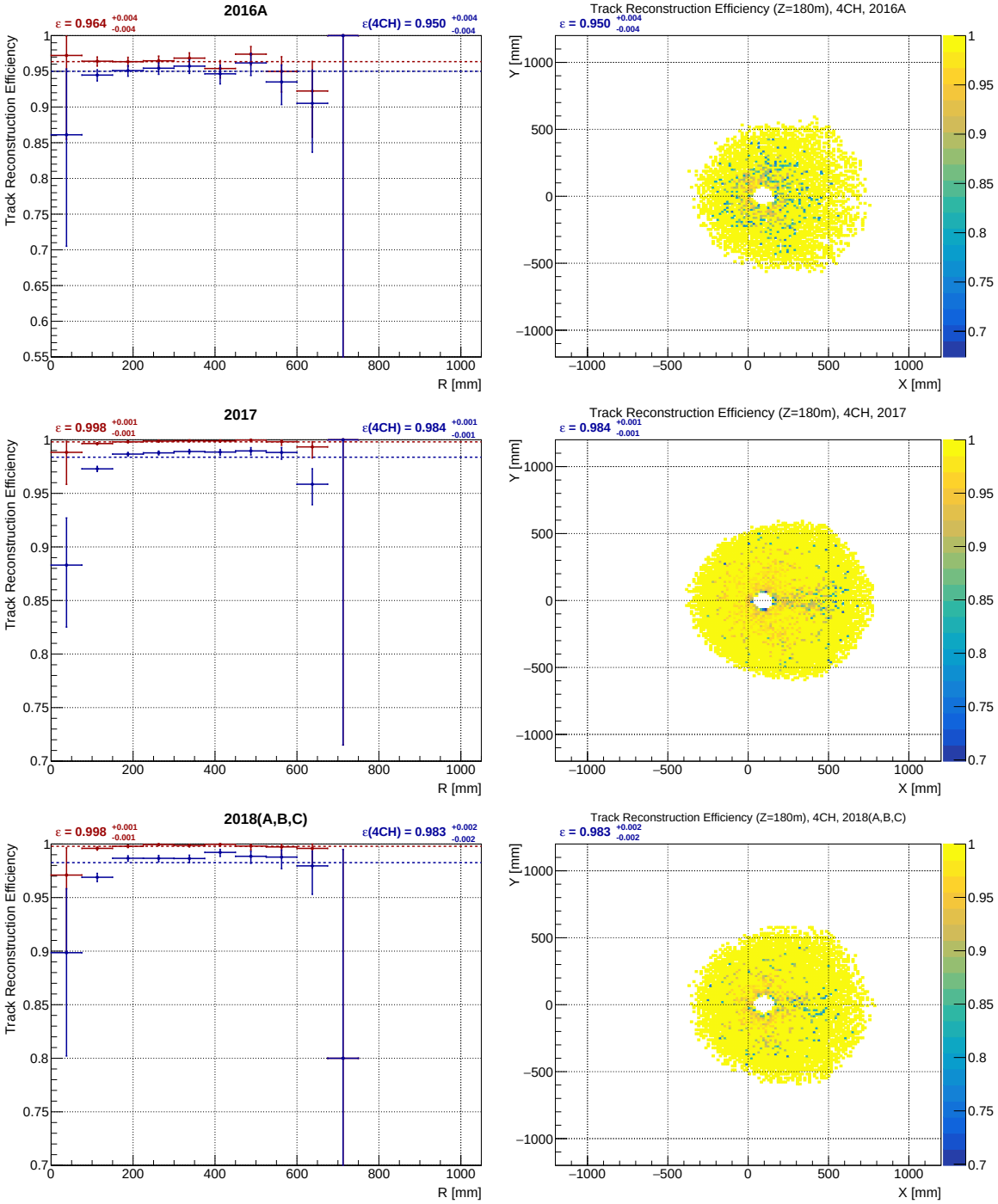

Figure 3.5.11: e^+ track reconstruction efficiency as a function of the distance from the beam axis (left), and as a function of the reconstructed e^+ pointer position before magnet ($Z = 180\,\mathrm{m}$) (right). Only candidates reconstructed from hits in all four chambers are used for the latter. Data sample: 2016A, 2017, 2018(A-C), control trigger.

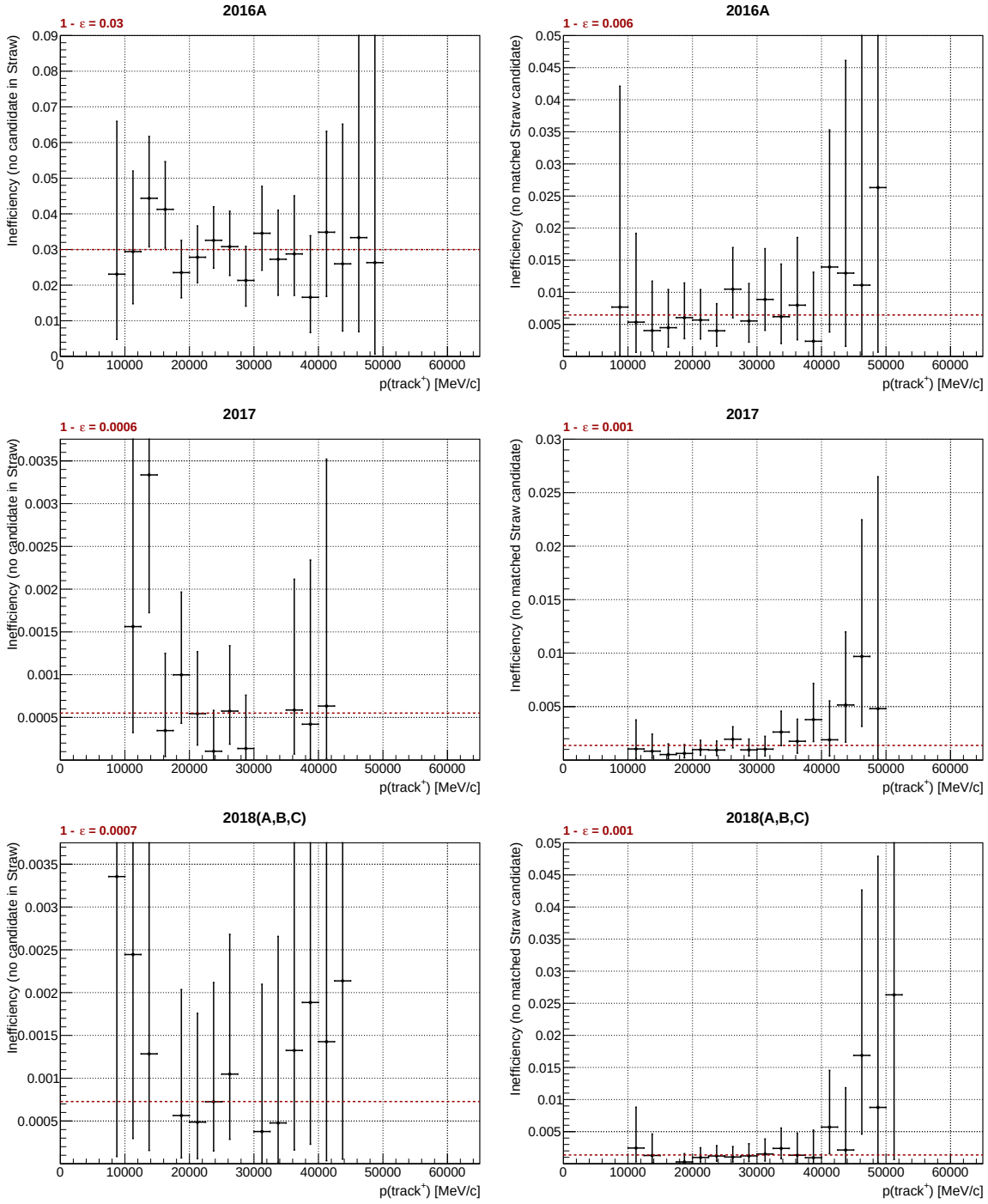

Figure 3.5.12: e^+ track reconstruction inefficiency as a function of the reconstructed e^+ momentum: the inefficiency caused by no STRAW candidate present in the event (left), the inefficiency due to no STRAW candidate compatible with the e^+ pointer found in the event (right). The compatibility criteria are based on the momentum and position difference between the pointer and a STRAW candidate and are summarized in Section 3.2. Data sample: 2016A, 2017, 2018(A-C), control trigger.

3.5.2.2 Efficiency in MC

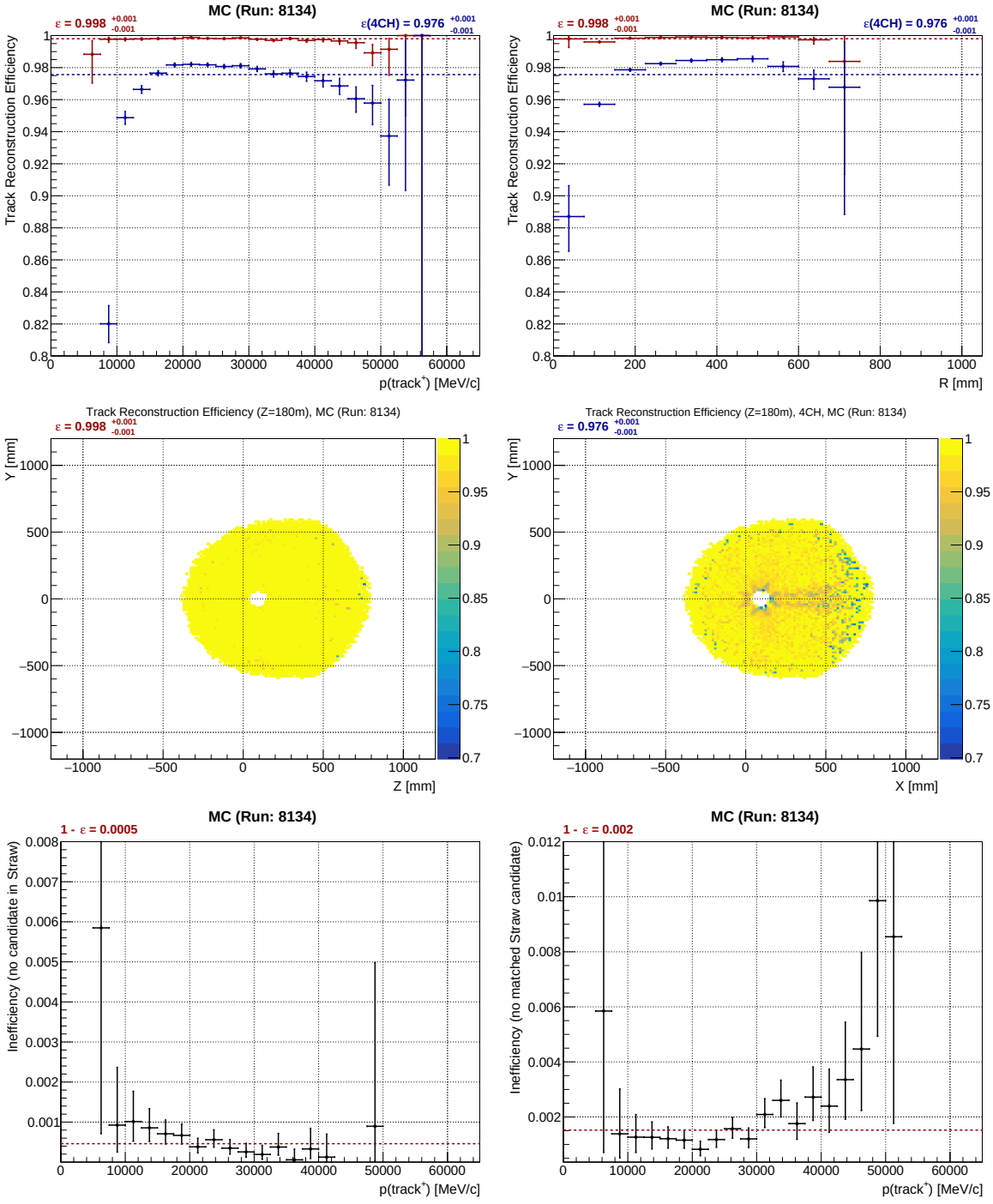

Figure 3.5.13: e^+ track reconstruction efficiency as a function of the reconstructed e^+ pointer momentum (top left), the distance from the beam axis (top right) and the e^+ pointer position before magnet ($Z = 180\,\mathrm{m}$): all STRAW candidates (middle left), only 4 chamber candidates (middle right). e^+ track reconstruction inefficiency as a function of the e^+ pointer momentum. Two classes of events are considered: events inefficient due to no candidate reconstructed in the STRAW (bottom left) and due to no STRAW candidate matched to the pointer (bottom right). MC sample: K_{e3} events with upstream and downstream pile-up (subsection 2.3.3).

3.6 Spectrometer track reconstruction efficiency using MC truth

In this section, a study carried out with the standard MC samples without upstream or downstream pile-up is described. The goal of this study is to evaluate the intrinsic inefficiency of the Spectrometer candidate reconstruction, as well as to estimate the effect of particle decay and interaction on the candidate reconstruction efficiency. MC truth information is used to select events in the denominator of the efficiency and the true charged track is used as the pointer for the efficiency evaluation. A reconstructed candidate with momentum within 1 GeV/c from the pointer momentum and with a distance from the pointer position in any STRAW chamber smaller than 25 mm is looked for. Events, in which at least one such candidate is found, enter the numerator of the efficiency.

We only consider events in which the charged particle reaches the first STRAW chamber and its position is in the acceptance of all four STRAW chambers. In case the particle decays or interacts inelastically before passing through the fourth chamber, the position is obtained by extrapolation from the latest available MC checkpoint. The fractions of such events are given in Table 3.6.1.

Decay	Reach end of CH4	Decay in CH1-4	Inelastic[1] interaction in CH1-4
$K_{2\pi}$	97.32%	2.20%	0.48%
$K_{\mu 3}$	99.97%	0.03%	0.00%
K_{e3}	99.95%	0.00%	0.05%

Table 3.6.1: Probabilities for the charged particle entering the STRAW (in acceptance of all chambers) to reach the end of STRAW CH4, to decay and to interact inellastically.

First, the track reconstruction efficiency is evaluated for particles that reach the end of STRAW CH4. The results in Table 3.6.2 show that the reconstruction efficiency is lower (especially for K_{e3}) than the efficiency obtained using the standard procedure in Table 3.7.1. To explain this discrepancy, we evaluated the efficiency using the algorithm described above on MC events passing the selections described in Sections 3.3 to 3.5. Results are given in the second row of Table 3.6.2 and show that for those events, the MC truth efficiency is compatible with the standard results. This can be explained by the fact that the inefficiency in the first MC truth sample is caused by events in which the charged tracks lost significant fraction of their energy or scattered in the STRAW chambers. As a result, they do not pass the selection criteria, especially the kinematic constraints on $m(\pi^+)$ or m^2_{miss}.

[1] Inelastic, Scintillation, Annihilation processes in GEANT4.

	π^+		μ^+		e^+	
	ε [%]	ε(4CH) [%]	ε [%]	ε(4CH) [%]	ε [%]	ε(4CH) [%]
All events	98.84%	96.03%	99.35%	94.91%	95.95%	89.04%
Selected events	99.68%	98.82%	99.88%	97.96%	99.65%	97.91%

Table 3.6.2: Spectrometer reconstruction efficiency with MC truth.

3.7 Results

The results of the Straw spectrometer reconstruction efficiency measurement are summarized for single track kaon decay events, see Table 3.7.1. The efficiency is evaluated separately for all tracks ($\geq$3 CH) and for four-chamber tracks (4 CH).

	π^+		μ^+		e^+	
	$\geq$3 CH	4 CH	$\geq$3 CH	4 CH	$\geq$3 CH	4 CH
2016 data	95.7 %	93.3 %	95.8 %	92.8 %	96.5 %	95.2 %
2017 data	98.6 %	95.1 %	98.9 %	94.3 %	99.8 %	98.4 %
2018 data	98.5 %	94.9 %	98.8 %	94.0 %	99.7 %	98.2 %
$K_{2\pi}$ MC	99.7 %	97.4 %				
$K_{\mu 3}$ MC			99.7 %	96.0 %		
K_{e3} MC					99.8 %	97.6 %

Table 3.7.1: Summary of the Spectrometer track reconstruction efficiency measurement for data and MC. The statistical uncertainties of the presented central values are at the level of 0.2 % or smaller. Results are stable within 0.2 % (0.3 % in 4 CH case) under variation of selection cuts.

We observe a difference between the 2016 data sample and the 2017+2018 data samples; the efficiency is lower by about 3 % in 2016. The efficiency improvement at the beginning of 2017 was most probably achieved thanks to an upgrade of the STRAW readout firmware. Otherwise, the reconstruction efficiency was stable for all 3 types of studied tracks during the whole data taking period.

The measured efficiency values in 2017–2018 are above 98 % for all three studied charged particles. The standard efficiency measurement does not take into account events in which a charged particle is lost either due to its decay before or between the STRAW chambers or due to an interaction with the material of the spectrometer, since such events generally do not pass the selections described in this thesis and thus do not enter the denominator of the efficiency computation as discussed in Section 3.6.

4 Kinematic studies for the $K^+ \to \pi^+ \nu\bar{\nu}$ measurement

The second goal of this thesis is to develop a new algorithm for matching single STRAW candidates with GTK candidates. The aim is to improve the performance of the existing algorithm in the $K_{\pi\nu\nu}$ analysis on the 2017 data set with regards to $K_{2\pi}$ and $K_{\mu 2}$ backgrounds. For this project, four event selections ($K_{\pi\nu\nu}$, $K_{2\pi}$ for normalization, $K_{2\pi}$, $K_{\mu 2}$) as well as the standard matching algorithm were implemented independently of the main analysis, but using same selection criteria [81]. Event-by-event comparison of the independent analyses proved to be useful to debug the main 2017 $K_{\pi\nu\nu}$ analysis before opening control and signal regions.

Performance of the STRAW–GTK matching algorithm in the $K_{\pi\nu\nu}$ analysis can be judged by multiple criteria. The focus of this work is on the $K_{2\pi}$ and $K_{\mu 2}$ backgrounds from non–gaussian reconstruction and radiative tails of the corresponding m^2_{miss} distributions, which span across the $K_{\pi\nu\nu}$ signal regions. Backgrounds result from $K_{2\pi}(\gamma)$ and $K_{\mu 2}(\gamma)$ events which pass the $K_{\pi\nu\nu}$ event selection and are reconstructed in the $K_{\pi\nu\nu}$ signal regions (see subsection 4.1.7). This only occurs when all photons (from π^0 decay and radiative) remain undetected, and in case of $K_{\mu 2}$, the muon is wrongly identified as a pion. Such events enter the signal regions due to misreconstruction of m^2_{miss} mainly caused by multiple scattering or pattern recognition error in the reconstruction procedures in GTK or STRAW, or by an incorrect STRAW–GTK matching (addressed in this thesis).

The backgrounds are estimated with two dedicated event selections applied on data. While the estimation of $K_{\mu 2}$ tails includes both components, the radiative part in $K_{2\pi}$ event selection is strongly suppressed by π^0 identification and a two-body decay kinematics requirement. Consequently, the effect of the remaining radiative component of $K_{2\pi}$ tails is measured separately in the main $K_{\pi\nu\nu}$ analysis.

$K_{2\pi}$ and $K_{\mu 2}$ kinematic tail fractions, computed from m^2_{miss} distributions in the corresponding event selections, are used to estimate the number of expected background events in the $K_{\pi\nu\nu}$ signal regions passing the $K_{\pi\nu\nu}$ event selection (more details in subsection 4.1.8). In case of the $K_{2\pi}$ background, this approach is valid

due to the fact that the requirements for suppression of $K_{2\pi}$ events with radiative photon do not bias the reconstruction tails [81]. In case of the $K_{\mu 2}$ background, the conditions for particle identification are different compared to the $K_{\pi\nu\nu}$ event selection, since a positive muon identification is required. This introduces bias to the $K_{\mu 2}$ tails measurement, which is estimated to be $\sim$5 % for the 2017 data analysis [81] and a corresponding systematic uncertainty is assigned to the result in the main $K_{\pi\nu\nu}$ analysis.

Events from other kaon decays, mainly $K_{3\pi}$, K_{e4}, semi–leptonic decays $K^+ \to \pi^0\mu^+\nu$ and $K^+ \to \pi^0 e^+\nu$ and $K^+ \to \pi^+\gamma\gamma$, enter the $K_{\pi\nu\nu}$ signal regions as well. Estimation of the expected background relies both on data (for $K_{3\pi}$) and simulation (the rest).

However, as mentioned in Appendix A, kaon decays occurring in the decay region are not the biggest source of background for the $K_{\pi\nu\nu}$ measurement. With the beam intensity of 2017 and 2018 data, the dominant background contribution comes from upstream events, which include early kaon decays and events with beam particle interactions in material upstream of the decay region.

Although the upstream background is impacted by the STRAW–GTK matching algorithm, evaluation of its contribution to the total background for the $K_{\pi\nu\nu}$ measurement is not one of the objectives of this work. Nevertheless it is briefly addressed in subsection 4.2.3.

In Section 4.1, a part of the $K_{\pi\nu\nu}$ analysis needed for this project is summarized. Most of the procedures and algorithms are shared among the four event selections. Events passing each of the selections are categorized into regions based on kinematic variable m^2_{miss} and momentum of the pion candidate.

In Section 4.2, first the standard STRAW–GTK matching algorithm currently used in the main $K_{\pi\nu\nu}$ analysis is reviewed. Then a procedure of three steps leading to a new matching algorithm is explained and a performance comparison with the standard matching algorithm, measured on $K_{3\pi}$ events, is given. Finally, results of the measurement of the kinematic tails, single event sensitivity and $K_{\pi\nu\nu}$ events in the full 2017 data set, obtained with both the standard and the new matching algorithms are presented in Section 4.3.

4.1 Event selection

As mentioned before, four event selections are used for this analysis. In sections subsections 4.1.1 and 4.1.2, procedures common for all the selections are described. De-

tails of the individual event selections are summarized in subsections 4.1.3 to 4.1.6. The selections differ mainly in particle identification requirements. Moreover, the $K_{2\pi}$ selection for kinematic tails measurement includes additional set of conditions for π^0 identification and suppression of the radiative decay component.

Only events with the downstream track momentum between 15 GeV/c and 35 GeV/c are considered in this analysis. The lower bound is given by the Cherenkov threshold of the RICH sub-detector, which limits the acceptance of π^+ with momentum below 13 GeV/c. The upper cut is motivated by $K_{\mu 2}$ kinematics and by the requirement for the energy of π^0 from $K_{2\pi}$ decays to be at least 40 GeV, thus allowing for more efficient suppression of the background in the $K_{\pi\nu\nu}$ analysis.

The $K_{\pi\nu\nu}$ analysis is performed in nine regions defined in variable $m^2_{miss} = \left(P_{K^+} - P_{\pi^+}\right)^2$ (see subsection 4.1.7). These include two signal regions for $K_{\pi\nu\nu}$ measurement, and three peak and four control regions for background estimation. To reduce the probability of wrongly reconstructing m^2_{miss} due to misreconstruction of kaon or pion momenta, two additional variables, $m^2_{miss}(RICH)$ and $m^2_{miss}(beam)$, are computed and further constrain mainly the signal regions. For evaluation of $m^2_{miss}(RICH)$, the track momentum in P_{π^+}, measured by STRAW, is replaced with the momentum measured in RICH while keeping the original direction. In $m^2_{miss}(beam)$, the GTK momentum in P_{K^+} is replaced with the run-dependent mean beam momentum measured with $K_{3\pi}$ events.

Additionally, each region is divided into four momentum bins: (15–20) GeV/c, (20–25) GeV/c, (25–30) GeV/c and (30–35) GeV/c.

4.1.1 Selection of a kaon decay event

Only events in which the signal in all sub-detectors is properly reconstructed and sub-detector efficiencies in the corresponding run or burst are above a predefined threshold. The common part of the event selections, in which pion and kaon candidates are identified, is explained in this section. First, trigger conditions and several basic quality cuts are applied. Then only STRAW tracks of good quality and in geometrical acceptance of the downstream sub-detectors are considered. Geometrical and time associations to the STRAW tracks are looked for in downstream sub-detectors as well as in the KTAG and the GTK. The algorithm for matching GTK candidates to preselected STRAW tracks is one of the objectives of the presented thesis. The standard algorithm, used in the main $K_{\pi\nu\nu}$ analysis, is reviewed in subsection 4.2.1, while the new algorithm developed in this work is described in subsection 4.2.2. One of the last steps of the kaon decay event selection is the choice of the single STRAW track, defined as the one for which all sub-detector associations are the closest to the trigger time.

4.1.1.1 Preselection

Two trigger streams, described in detail in subsection 2.3.3, are used in the $K_{\pi\nu\nu}$ analysis. Kinematic tail fractions of $K_{2\pi}$ and $K_{\mu 2}$ decays are computed from events passing the minimum bias (control) trigger stream, downscaled by a factor 400 in 2017 data set. Similarly, $K_{2\pi}$ decay events used for normalization in the $K_{\pi\nu\nu}$ analysis are selected from the control data as well, while the PNN trigger stream, which is not downscaled, is used for the $K_{\pi\nu\nu}$ event selection. Basic conditions applied in the preselection of events are summarized in Table 4.1.1.

Trigger	Control ($K_{2\pi}$, $K_{\mu 2}$, $K_{2\pi}$ for normalization) PNN ($K_{\pi\nu\nu}$)
Number of NA48-CHOD hits	> 0
Number of LKr hits	(0, 2000]
Number of STRAW candidates	(0, 10]
Number of pairs of horizontal and vertical NA48-CHOD hits in the same quadrant	> 0

Table 4.1.1: Summary of conditions applied at the preselection stage of pion candidate selection.

4.1.1.2 Pion candidate

STRAW candidates corresponding to positively charged tracks reconstructed from hits in all four STRAW chambers and fulfilling reconstruction quality criteria summarized in the first part of Table 4.1.2 are considered. Extrapolation to downstream sub-detectors determines the reference positions for matching sub-detector signals to the STRAW candidate. The reference positions in each sub-detector must lie in its geometrical acceptance defined in Table 4.1.3. Furthermore, a corresponding *kaon candidate*, defined by signals in KTAG and GTK, is associated to the STRAW track by the algorithm described in Section 4.2.

Signals associated to the track in downstream sub-detectors are later used for particle identification, photon rejection and to reject multi-track kaon decays with only one fully reconstructed STRAW track. The STRAW candidate satisfying the quality criteria, with associations in the upstream and downstream sub-detectors, is referred to as the *pion candidate*. All conditions defining a pion candidate are listed in Table 4.1.2, while procedures used for associating sub-detector signals to STRAW candidates are explained in the paragraphs below.

In case multiple pion candidates are found in one event, the following proced-

Track charge: +1
Reconstructed using hits from all 4 STRAW chambers
Reconstructed from at least 15 and not more than 42 hits
Hough quality [91] from the STRAW pattern recognition algorithm ≤ 4
Fit $\chi^2 \leq 20$
Momentum difference before and after fit $\leq 20\,\mathrm{GeV}/c$
Slope difference before and after fit: $\Delta S_x < 0.0003$ and $\Delta S_y < 0.001$
Not fake (subsection 4.1.2.1)
In geometrical acceptance of four STRAW chambers, RICH, NA48-CHOD, CHOD, LKr, MUV1, MUV2, MUV3
Inside the area given by the inner radius of LAV12 ring
Outside the geometrical acceptance of IRC
Associations in NA48-CHOD, CHOD, LKr, RICH, KTAG, GTK

Table 4.1.2: Summary of conditions defining a pion candidate.

ure is applied. For each sub-detector separately, the association closest to the trigger time is found among all associations corresponding to any pion candidate. If the closest associations in each sub-detector do not correspond to the same pion candidate, the event is rejected.

Finally, the pion candidate with all sub-detector associations closest to the trigger is selected and the kaon–pion pair is used to compute the main kinematic variable determining the $K_{\pi\nu\nu}$ signal, m^2_{miss}. In case of the $K_{2\pi}$ and $K_{\mu 2}$ selections for kinematic tails measurement and the $K_{\pi\nu\nu}$ selection, additional rules apply:

- not more than two STRAW candidates in the event,
- if there are two STRAW candidates, both have to be positive,
- if both STRAW candidates are also pion candidates, their distance at the point of closest approach is calculated and must be greater than 30 mm.

Since the time resolution of the STRAW sub-detector (subsection 2.1.5) is insufficient for the needs of the $K_{\pi\nu\nu}$ analysis, pion candidate time is computed as weighted average of t_{STRAW} and time of the NA48-CHOD ($t_{NA48\text{-}CHOD}$) and RICH single-ring (t_{RICH}) associations to the STRAW track:

- If RICH single-ring association is present:

$$t_{track} = \frac{\dfrac{t_{NA48\text{-}CHOD}}{(0.5\,\mathrm{ns})^2} + \dfrac{t_{RICH}}{(0.2\,\mathrm{ns})^2} + \dfrac{t_{STRAW}}{(10\,\mathrm{ns})^2}}{\dfrac{1}{(0.5\,\mathrm{ns})^2} + \dfrac{1}{(0.2\,\mathrm{ns})^2} + \dfrac{1}{(10\,\mathrm{ns})^2}}, \tag{4.1.1}$$

- If RICH single-ring association is not present:

$$t_{track} = \frac{\dfrac{t_{NA48\text{-}CHOD}}{(0.5\,\mathrm{ns})^2} + \dfrac{t_{STRAW}}{(10\,\mathrm{ns})^2}}{\dfrac{1}{(0.5\,\mathrm{ns})^2} + \dfrac{1}{(10\,\mathrm{ns})^2}}. \tag{4.1.2}$$

The weighting factors are related to the sub-detector time resolutions.

Geometrical acceptance

The STRAW track extrapolated to the Z plane of a given sub-detector is in its geometrical acceptance if the track position lies inside the range given by the inner and outer radii listed in Table 4.1.3. Track position at both front and back RICH planes is checked. The track also must be in the region with at least two STRAW views at all four STRAW chamber planes. Finally, the track must not pass through the active area of the LAV12 station and the IRC sub-detector.

Sub-detector	Inner radius	Outer radius
STRAW	63.8 mm	1000 mm
RICH	101 mm	1100 mm
NA48-CHOD	125 mm	1100 mm
CHOD	140 mm	1070 mm
LKr	150 mm	1130 mm
MUV1	130 mm	1100 mm
MUV2	130 mm	1100 mm
MUV3	130 mm	1200 mm
LAV12	1070 mm	1440 mm
IRC	60 mm	145 mm

Table 4.1.3: Definition of geometrical acceptance of downstream sub-detectors.

NA48-CHOD association

NA48-CHOD candidate is defined as a pair of hits in horizontal and vertical slabs in the same quadrant. Procedure to associate a pair of NA48-CHOD hits to the STRAW track is described in subsection 4.1.2.6 and is used with $\sigma_R = 23\,\mathrm{mm}$, $\sigma_{\Delta T} = 21\,\mathrm{ns}$ and $\sigma_T = 9\,\mathrm{ns}$. Position of the STRAW track extrapolated to NA48-CHOD and t_{STRAW} are used as reference. The hit pair selected by the procedure is associated to the track if additional conditions summarized in Table 4.1.4 are met.

CHOD association

The standard tool `SpectrometerNewCHODAssociation` is used to find a CHOD

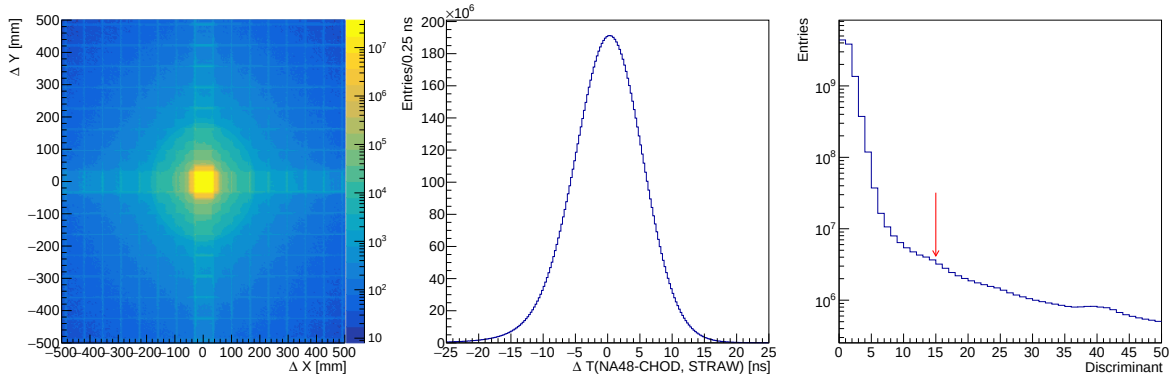

(a) (b) (c)

Figure 4.1.1: NA48-CHOD association: (a) X and Y position difference between NA48-CHOD candidates and STRAW tracks extrapolated to the NA48-CHOD plane; (b) time difference between NA48-CHOD candidates and t_{STRAW} of STRAW tracks; (c) discriminant used for matching NA48-CHOD candidates to STRAW tracks. Red arrow indicates cut used to find NA48-CHOD candidate associated to the track.

hit geometrically associated to the track. The tool uses the position of the STRAW track extrapolated to the CHOD plane as the center of a search circle with radius inversely proportional to the track momentum. A discriminant is built for the hit closest to the track impact point within the search radius. Track-hit distance, as well as time difference between hit time t_{CHOD} and t_{STRAW} are considered. The association is successful if conditions summarized in table Table 4.1.4 are met.

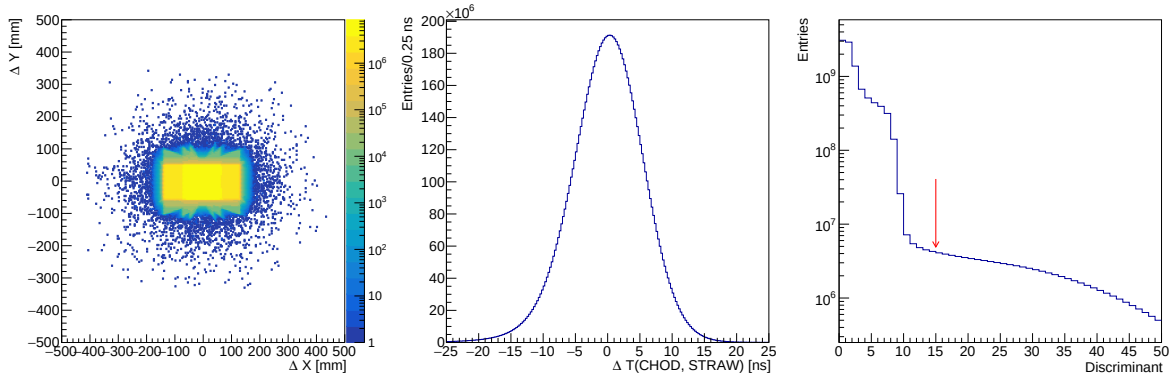

(a) (b) (c)

Figure 4.1.2: CHOD association: (a) X and Y position difference between CHOD candidates and STRAW tracks extrapolated to the CHOD plane; (b) time difference between CHOD candidates and t_{STRAW} of STRAW tracks; (c) discriminant used for matching CHOD candidates to STRAW tracks. Red arrow indicates cut used to select a CHOD association to the track.

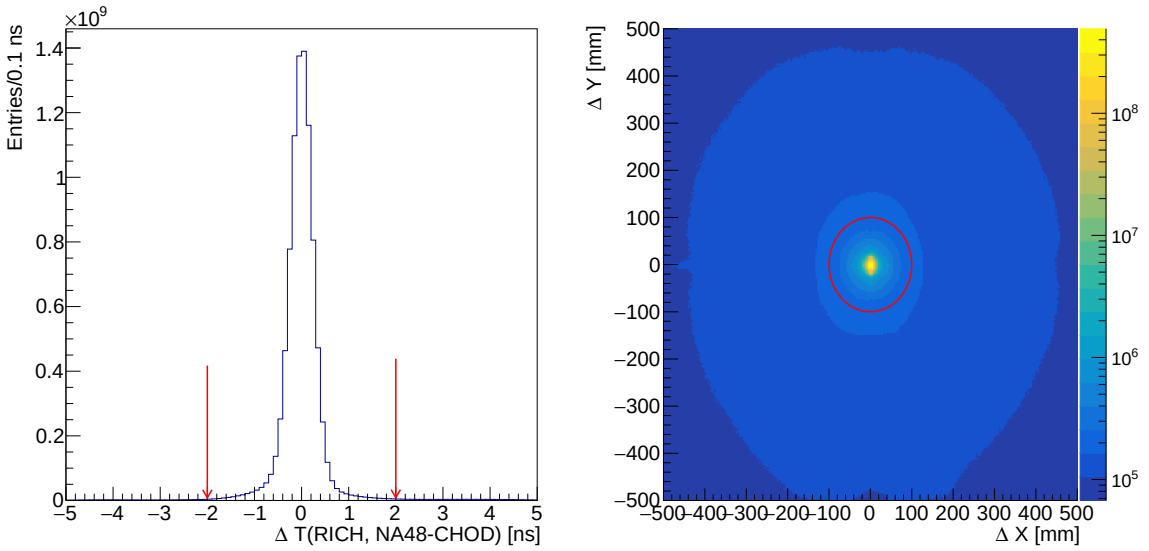

(a) (b)

Figure 4.1.3: (a) RICH single-ring association: time difference between RICH single-ring and NA48-CHOD associations to the STRAW track. (b) LKr association: cluster distance from the track position in the LKr. Red arrows and circle indicate cuts used in the preselection of the $K_{\pi\nu\nu}$ analysis.

RICH association

At least 1 RICH hit must be present in the event. A single-ring fit is performed on groups of RICH hits close in time, the ring time is defined as average of the hit times. Standard tool `SpectrometerRICHAssociationSingleRing` is then used to find a single-ring candidate in time and geometrically compatible with the STRAW track extrapolated to the RICH. Compatibility is tested with a discriminant D built from the time difference between the single-ring and the NA48-CHOD association to the track, and the distance between the fitted and expected (track based) single-ring center position. Additionally, a p-value of the single-ring χ^2-fit is computed. The best single-ring candidate is associated to the track if conditions summarized in table Table 4.1.4 are met. The single-ring time defines t_{RICH} of the pion candidate and is used for the t_{track} computation.

LKr association

Three procedures are used to reconstruct LKr clusters and associate them to the STRAW track. In the first procedure (referred to as the *standard* association), standard LKr candidates reconstructed from groups of in-time LKr hits without any input from other sub-detectors are used. The LKr candidate closest to the track extrapolated to the LKr plane is selected if the distance to the track position is less than 150 mm and the candidate is within 30 ns from t_{STRAW}.

In the second procedure (referred to as the *hit* association), the position of the

STRAW track extrapolated to the LKr is used as a reference for clusterization of LKr hits. Clusters are built from hits within 100 mm from the track impact point that are in time with t_{STRAW} (<20 ns). Cluster is created only if energy of the seed (the most energetic hit in the cluster) is greater than 40 MeV.

The third algorithm (referred to as the *calorimetric* association) is implemented in the standard tool `SpectrometerCalorimetersAssociation`, which provides association between STRAW tracks and energy deposits in LKr, MUV1 and MUV2 calorimeters based on the track position in each of these sub-detectors. If no match is found among the standard LKr candidates, a new candidate is reconstructed from hits in time (20 ns) with t_{STRAW} and close (100 mm) to the position of the STRAW track extrapolated to LKr.

Existence of hit and calorimetric associations is required for each pion candidate. If a standard association is available, it defines the time, position and energy of track–LKr association. Otherwise, the hit cluster parameters are used. Time of the association, t_{LKr}, is defined by the cluster seed while position is computed as a center of energy. The LKr association must be in time with t_{STRAW} (20 ns) and $t_{NA48\text{-}CHOD}$ (6 ns). Moreover, it must be closer than 100 mm to the track position in LKr.

KTAG association

Association between the STRAW track and a KTAG candidate reconstructed from hits in at least five sectors is based on the time difference with respect to t_{track}. KTAG candidate with time t_{KTAG} closest to t_{track} is matched to the STRAW candidate if the time difference is less than 1 ns (Table 4.1.4).

GTK association

At least one GTK candidate (with t_{GTK}) must be associated to the track by STRAW–GTK matching algorithm described in Section 4.2. Good quality of the matching is required.

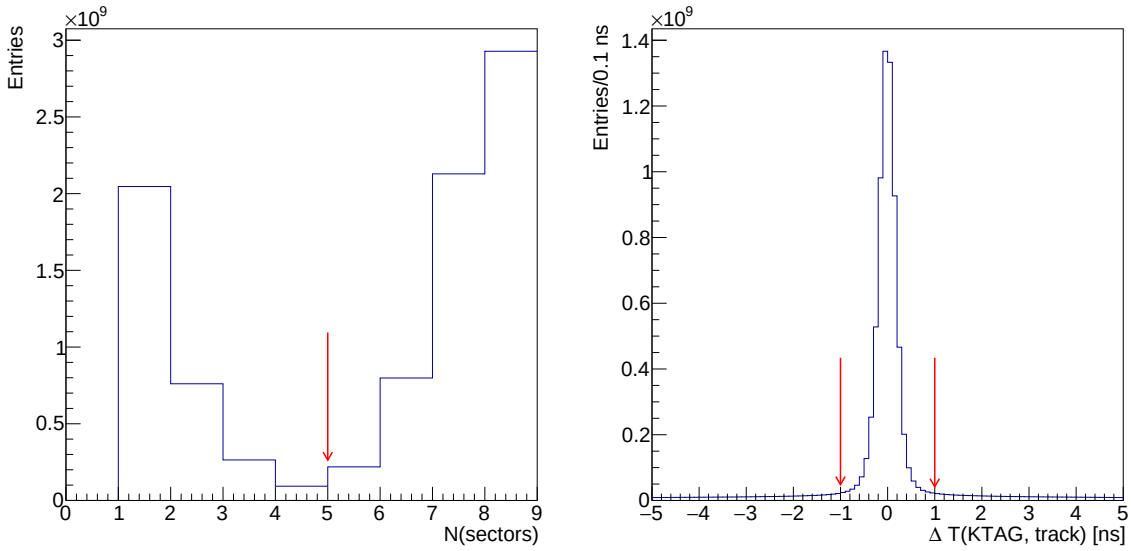

(a) (b)

Figure 4.1.4: KTAG association: (a) number of hit KTAG sectors used to reconstruct a KTAG candidate. (b) time difference between a KTAG candidate and the track time, t_{track} (Equation (4.1.1) or Equation (4.1.2)).Red arrows indicate cuts used to select KTAG association to the track.

NA48-CHOD	Discriminant < 15 $\|\Delta T(NA48\text{-}CHOD, trigger)\| \leq 25$ ns	
CHOD	Discriminant < 15 $\|\Delta T(CHOD, NA48\text{-}CHOD)\| \leq 5$ ns	
RICH	RICH hits	N $\geq$ 1
	RICH single ring	D $\leq$ 50 p-value > 0.01 $\|\Delta T(RICH, NA48\text{-}CHOD)\| \leq 2$ ns
LKr	Cluster distance from track in LKr $\leq$ 100 mm $\|\Delta T(LKr, STRAW)\| \leq 20$ ns $\|\Delta T(LKr, NA48\text{-}CHOD)\| \leq 6$ ns	
KTAG	N sectors $\geq$ 5 $\|\Delta T(KTAG, track)\|$ < 1 ns (Data) or 2 ns (MC)	
GTK	Section 4.2	

Table 4.1.4: Summary of conditions for sub-detector associations to a pion candidate.

4.1.2 Algorithms

Event selections used in this work consist of multiple sets of conditions applied on events with one pair of matching kaon and pion candidates selected in subsec-

tion 4.1.1.2. Based on their purpose, the conditions are divided into several categories including particle identification (subsection 4.1.2.8), photon rejection (subsections 4.1.2.4 and 4.1.2.5), multiplicity rejection (subsection 4.1.2.6), upstream background rejection (subsection 4.1.2.3), parameters of the STRAW candidates (subsection 4.1.2.1), parameters of the kaon candidate and the kaon decay event (subsection 4.1.2.2).

Sets of conditions from each algorithm applied in the event selections are specified in the corresponding sections (subsections 4.1.3 to 4.1.6).

Sub-detector associations to the pion candidate (in STRAW, NA48-CHOD, CHOD, RICH, LKr) and to the matched kaon candidate (in KTAG, GTK), together with their respective times (t_{STRAW}, $t_{NA48\text{-}CHOD}$, t_{CHOD}, t_{RICH}, t_{LKr}, t_{KTAG}, t_{GTK}), weighted time t_{track} of the pion candidate and the kaon–pion vertex position are used in the algorithms.

4.1.2.1 Fake track identification

Among STRAW tracks reconstructed from hits in less than four STRAW chambers, the ones with the fit χ^2 over 30 or with at least one hit in common with another STRAW track are considered fake. Only non-fake tracks are used in the analysis to increase precision of the track momentum reconstruction.

4.1.2.2 Parameters of kaon candidate and kaon decay event

First part of Table 4.1.5 summarizes additional conditions imposed on the kaon candidate selected in subsection 4.1.1.2. These include cuts on momentum magnitude $p(GTK)$ and momentum slopes S_x, S_y measured by GTK, as well as a check of compatibility with the mean beam parameters before TRIM5 magnet (subsection 2.1.2). The latter is tested by imposing a cut on variable θ defined as follows:

$$\theta = \sqrt{(S_x - \theta_{TRIM5} - \mu_{S_x})^2 + (S_y - \mu_{S_y})^2}, \tag{4.1.3}$$

where $\theta_{TRIM5} = 0.00120$ is the average deflection angle introduced by momentum kick in positive X direction provided by TRIM5, and $\mu_{S_x} = 0.00002$ and $\mu_{S_y} = 0.00002$ are mean beam momentum slopes before TRIM5.

The rest of the conditions in Table 4.1.5 concern the kaon–pion vertex position and ensure the vertex is reconstructed in the fiducial volume and is compatible with the beam profile. Vertex position used for evaluation of conditions 3, 4 and 5 is obtained from the STRAW–GTK matching algorithm in subsection 4.1.1.2.

1	GTK candidate quality	(a): 72 700 MeV/c < $p(GTK)$ < 77 200 MeV/c (b): $0.0009 < S_x < 0.0016$ and $-0.0003 < S_y < 0.0004$ (c): $\theta \leq$ 0.00035 (Equation (4.1.3))
2	$\lvert t_{GTK} - t_{NA48\text{-}CHOD} \rvert$	< 1.1 ns
3	Vertex Z	(a): $Z \geq 115$ m (b): $Z \leq 165$ m
4	Vertex X vs Z	$(0.00122 \cdot Z - 148.53\,\text{mm}) \leq$X$\leq (0.0012 \cdot Z - 93.9\,\text{mm})$
5	Vertex Y vs Z	$(-0.000099464 \cdot Z - 5.4\,\text{mm}) \leq$Y$\leq (0.000112 \cdot Z + 3.6\,\text{mm})$

Table 4.1.5: Kaon decay selection.

4.1.2.3 Upstream background rejection

The following conditions are used to suppress upstream events (see Appendix A) in which the kaon interacted with the material of GTK3 station (first part of Table 4.1.6), or events corresponding to early kaon decays or interactions of beam particles upstream of GTK3 (second part of Table 4.1.6). The position of the pion STRAW track extrapolated to the GTK3 plane is used in conditions 1 and 2 while for condition 6, the track was extrapolated to the plane of the TRIM5 magnet. R_{STRAW1} in condition 5 corresponds to the track distance from the center of the first STRAW chamber. Procedure to find extra GTK hits (condition 8) is explained below.

1	Track position at GTK3	$\lvert X_{track} \rvert > 30\,\text{mm}$ or $\lvert Y_{track} \rvert > 15\,\text{mm}$
2	Hits in GTK3	All hits at least 24 mm away from the track extrapolated to GTK3 plane
3	GTK hits with high ToT	No hits with ToT > 23 ns in time (1.2 ns) with t_{KTAG}
4	CHANTI	No CHANTI candidate in time (3 ns) with t_{KTAG}, t_{GTK} or t_{track}
5	Track radius in STRAW1 vs vertex Z position	(a): $R_{STRAW1} > -0.00436 \cdot Z + 830\,\text{mm}$ (b): $R_{STRAW1} > (-0.0625 \cdot Z + 7462.5\,\text{mm})$ and $R_{STRAW1} > (-0.004 \cdot Z + 735\,\text{mm})$ and $R_{STRAW1} < (-0.0098333 \cdot Z + 1812.5\,\text{mm})$
6	Position at TRIM5[1]	$\lvert X_{track} \rvert$ > 100 mm or $\lvert Y_{track} \rvert$ > 500 mm
7	Additional vertex	No vertex in range (100, 105) m between the pion candidate and any kaon candidate
8	No extra GTK hits	(a): t_{KTAG} used as reference (b): t_{RICH} used as reference

Table 4.1.6: Upstream background rejection.

Extra GTK hits

This procedure is used to check for GTK hits in time with the reference time, but not belonging to the GTK candidate associated to the pion candidate, nor close to it in any GTK station. In the analysis, t_{KTAG} and t_{RICH} associated to the pion candidate are used as reference times. Extra GTK hits in time with the pion candidate point to an upstream event of the second type, in which an accidental beam particle was reconstructed as a kaon candidate while the original kaon decayed inside the GTK sub-detector.

Looping over all GTK hits, an extra hit is found if all of the following conditions are fulfilled:

- the hit does not belong to the GTK candidate associated to the pion candidate,
- the hit time is within 0.4 ns from the reference time,
- the hit is farther away than 0.5 mm in both X and Y directions from the position of the associated GTK candidate in the corresponding GTK station.

4.1.2.4 Photon rejection in LKr

Two types of LKr clusters, referred to as standard and auxiliary, are used to reject photons in the $K_{\pi\nu\nu}$ analysis. The standard clusters, also called LKr candidates, are reconstructed by the standard LKr reconstruction algorithm, while the auxiliary clusters are reconstructed with a tool `LKrAuxClusterReco` providing higher efficiency for low energy clusters. The auxiliary reconstruction uses t_{track} as reference and the clusters are reconstructed only for data events. Fulfilling all conditions with either a standard or an auxiliary cluster is enough to find a photon in LKr and reject the event:

- the cluster is at least 100 mm away from the LKr association to the pion candidate,
- the cluster is at least 100 mm away from the position of the pion candidate in LKr.
- only for auxiliary clusters: $E_{clus} \geq 1\,\mathrm{GeV}$,

[1] This cut covers region of the central aperture of the last dipole magnet before GTK3. This area is weakly shielded against particles from upstream events. In the $K_{\pi\nu\nu}$ analysis of 2018 data, collected after installation of additional shielding in the magnet aperture, the cut is reduced to increase signal acceptance.

- only for data: the cluster is in time with t_{track}. The cut values depend on cluster energy and are summarized in Table 4.1.7. Variable σ is defined as follows: $\sigma = 0.56 + \frac{1.53\,\text{GeV}}{E} - \sqrt{\frac{0.233^2\,\text{GeV}}{E}}$ and $\Delta T \equiv (t_{LKr} - t_{ref})$.

$E < 1\,\text{GeV}$	$\lvert\Delta T\rvert < 5\,\text{ns}$
$1\,\text{GeV} \leq E < 2\,\text{GeV}$	$\lvert\Delta T\rvert < 5\sigma\text{ns}$
$2\,\text{GeV} \leq E < 15\,\text{GeV}$	$\lvert\Delta T\rvert < 15\sigma\text{ns}$
$E \geq 15\,\text{GeV}$	$\lvert\Delta T\rvert < 70\sigma\text{ns}$
$E > 10\,\text{GeV}$	$\lvert\Delta T - 25\,\text{ns}\rvert < 2.5\,\text{ns}$ or $\lvert\Delta T + 25\,\text{ns}\rvert < 2.5\,\text{ns}$

Table 4.1.7: Timing conditions for LKr clusters.

4.1.2.5 Photon rejection in other sub-detectors

In addition to LKr, three photon veto sub-detectors are used to reject events with photons: LAV, IRC and SAC (the last two called collectively SAV). Several procedures to find signal in time with t_{track} are used. Fulfilling all conditions in any one of the methods is enough to find a photon.

- LAV: standard algorithm `LAVMatching` is used. A photon is found in LAV if a well-defined signal in time (3 ns) with t_{track} is detected in at least one LAV block.

- SAV: standard algorithm `SAVMatching` checking both IRC and SAC at the same time is used alongside with another algorithm dealing with reconstructed SAV hits.

  - ⋆ A photon is found by `SAVMatching` if a well-defined signal in time (7 ns) with t_{track} is detected in at least one block of IRC or SAC.

  - ⋆ Hits closest to t_{track} and with the largest energy are found among those corresponding to IRC and SAC separately, if available. If either one of them has $E > 1\,\text{GeV}$ and is within 7 ns from t_{track}, it is considered to be caused by a photon.

- IRC: Based on the time-over-threshold (ToT) of each hit, a hit closest in time to t_{track} is found among all IRC hits corresponding to a well-defined signal. A photon is found by this procedure if any of the conditions summarized in Table 4.1.8 is met.

- SAC: Based on the time-over-threshold of each hit (in ns), the one closest in time to t_{track} is found among all SAC hits corresponding to a well defined signal. A photon is found by this procedure if any of the conditions summarized in table Table 4.1.8 is met.

	ToT range	Timing cut
IRC	$ToT < 2\,\text{ns}$	$\lvert t_{IRC} - t_{ref}\rvert < 7\,\text{ns}$ or $\lvert t_{IRC} - t_{ref} - 7\,\text{ns}\rvert < 7\,\text{ns}$
	$ToT \geq 2\,\text{ns}$	$-7\,\text{ns} < t_{IRC} - t_{ref} < 10\,\text{ns}$
SAC	$ToT < 2\,\text{ns}$	$7\,\text{ns} < t_{SAC} - t_{ref} < 10\,\text{ns}$
	$2\,\text{ns} \leq ToT < 25\,\text{ns}$	$\lvert t_{SAC} - t_{ref}\rvert < 7\,\text{ns}$ or $\lvert t_{SAC} - t_{ref} + 11.3524\,\text{ns} - 0.2105 \cdot ToT\rvert < 3\,\text{ns}$
	$ToT \geq 25\,\text{ns}$	$-7\,\text{ns} < t_{SAC} - t_{ref} < 4\,\text{ns}$

Table 4.1.8: Timing conditions based on the time-over-threshold of IRC and SAC signal.

4.1.2.6 Multiplicity rejection

The conditions listed below use hits in downstream sub-detectors to identify additional charged particles corresponding to the same event as the pion candidate, but not fully reconstructed in STRAW. In the event selections, this algorithm is used to reject kaon decay events with multiple charged particles in the final state or events with photon interactions with material before reaching photon veto sub-detectors.

Procedures to find an NA48-CHOD candidate, extra activity hits in LKr and CHOD, and STRAW segments are explained in the paragraphs below. The NA48-CHOD candidates related to extra activity hits in LKr and CHOD are selected using hit position and time as reference. On the other hand, conditions 7, 8 and 9 use the STRAW track corresponding to the pion candidate selected in subsection 4.1.1.2 as reference.

If any of the conditions is fulfilled, the event is flagged as containing an extra charged particle and thus rejected.

1. MC: at least one HAC hit present in the event. Data: at least one HAC hit in time (3 ns) with $t_{NA48\text{-}CHOD}$.

2. MC: at least one MUV0 hit present in the event. Data: at least one MUV0 hit in time with $t_{NA48\text{-}CHOD}$: $-10\,\text{ns} < \Delta T(NA48\text{-}CHOD, MUV0) < 8\,\text{ns}$.

3. At least 4 extra NA48-CHOD hits (in addition to the pair associated to the pion candidate) within 7 ns from $t_{NA48\text{-}CHOD}$.

4. NA48-CHOD candidate related to the LKr extra activity hit is found within 15 ns and less than 130 mm from the LKr hit. Additionally, at least one of the hits forming the NA48-CHOD candidate is not associated to the pion candidate.

5. At least one pair of extra activity hits in LKr and CHOD are closer than 250 mm in X direction and 140 mm in Y direction.

6. At least one CHOD extra activity hit and the related NA48-CHOD candidate are within 15 ns, 250 mm in X direction and 140 mm in Y direction at the same time. Additionally, at least one of the hits forming the NA48-CHOD candidate is not associated to the pion candidate.

7. An extra standard LKr cluster (in addition to the one associated to the pion candidate, if available) is found between 40 mm and 100 mm away from the reference track position in LKr and within 6 ns from $t_{NA48\text{-}CHOD}$.

8. Distance at the point of closest approach (CDA) between the reference track and at least one other non-fake track must be smaller than 60 mm.

9. A STRAW segment is reconstructed by the procedure described below with t_{GTK}, kaon–pion vertex position and the STRAW track corresponding to the pion candidate used as input.

In points 4 and 6, the NA48-CHOD candidate is selected using the method `NA48-CHOD candidate` described below with $\sigma_R = \sqrt{6} \cdot 16\,\text{mm}$, $\sigma_{\Delta T} = \sqrt{3} \cdot 7\,\text{ns}$ and $\sigma_T = 18\,\text{ns}$.

NA48-CHOD candidate

This function is used to find NA48-CHOD candidate, consisting of a pair of horizontal (H) and vertical (V) NA48-CHOD hits in the same quadrant, associated to the reference position R_{ref} and reference time t_{ref}. For each pair of H and V hits in the same quadrant, time of the pair is computed as a mean time of the two hits: $t_{HV} = \dfrac{t_H + t_V}{2}$. Then a discriminant D is constructed based on distance of the hit pair from the reference position and time difference with respect to the reference time:

$$D = \frac{\left(R_{NA48\text{-}CHOD} - R_{ref}\right)^2}{\sigma_R^2} + \frac{\left(t_{HV} - t_{ref}\right)^2}{\sigma_{\Delta T}^2} + \frac{\left(t_V - t_H\right)^2}{\sigma_T^2} \tag{4.1.4}$$

The values of σ_R, $\sigma_{\Delta T}$ and σ_T depend on the context in which this function is used.

The NA48-CHOD hit pair with the smallest discriminant is associated to the reference time and reference position.

Extra activity hit in LKr

Any hit in the LKr with energy $E > 50\,\mathrm{MeV}$, at least 100 mm away from the position of the pion candidate extrapolated to LKr, and fulfilling one of the conditions in table Table 4.1.9, is considered an extra activity hit.

$E < 300\,\mathrm{MeV}$	$\lvert t_{NA48\text{-}CHOD} - t_{LKr}\rvert < 4\,\mathrm{ns}$
$300\,\mathrm{MeV} < E < 2\,\mathrm{GeV}$	$-7\,\mathrm{ns} < (t_{NA48\text{-}CHOD} - t_{LKr}) < 10\,\mathrm{ns}$
$E > 2\,\mathrm{GeV}$	$\lvert t_{NA48\text{-}CHOD} - t_{LKr}\rvert < 10\,\mathrm{ns}$

Table 4.1.9: Extra activity in LKr: timing conditions based on the energy of the LKr hit.

Extra activity in CHOD

Any hit in the CHOD not associated to the pion candidate (subsection 4.1.1.2) is considered as extra activity if it is within 5 ns from $t_{NA48\text{-}CHOD}$.

STRAW segments

A tool `StrawSegmentAlgorithm` is used to further suppress multi-track events in which only one track was reconstructed by the standard Spectrometer reconstruction. Input to this tool includes the reference STRAW candidate, reference time and vertex position. STRAW hits not corresponding to the reference track are first grouped to doublets or triplets in each view and then combined to clusters in each chamber. Finally, chamber clusters are combined into track segments before and after the STRAW magnet. If possible, the segments are combined to form a simple track, which is then extrapolated to the vertex. If they are compatible (based on the distance from the vertex and time difference of the simple track with respect to the reference time), the event is flagged as a multi-track event candidate.

If it is not possible to create a simple track, two or more reconstructed clusters and the vertex are fitted with a straight line and a χ^2 test with distance from the line and time difference between the clusters and the reference time is performed. If the resulting χ^2 is smaller than a predefined threshold, the event is flagged.

4.1.2.7 Track - calorimetric energy association

The energy deposited in the LKr, MUV1 and MUV2 sub-detectors is associated to the STRAW track corresponding to the pion candidate via a multi-variate analysis (MVA) implemented in class `SpectrometerCalorimeterAssociation`. The following variables are provided and are used in this analysis:

- $Prob(\pi^+)$, $Prob(\mu^+)$ - probabilities that the clusters associated to the track corresponds to a pion or a muon,

- E_{MUV1}, E_{MUV2}, E_{LKr} - energy collected by MUV1, MUV2 and LKr sub-detectors associated to the track, respectively,

- E_{calo} - total calorimetric energy associated to the track given by sum of associated energies in MUV1, MUV2 and LKr sub-detectors,

- R_1, R_2 - fractions of the total calorimetric energy deposited in MUV1 and MUV2 sub-detectors,

- $E_{MUV1,extra}$, $E_{MUV2,extra}$ - energy deposited in MUV1 and MUV2 not spatially associated to the track, but within 10 ns from the energy associated to the track,

- A MIP signal discriminant $D_{MIP} = \frac{\sqrt{D_{LKr}^2+D_{MUV1}^2+D_{MUV2}^2}}{N_{assocDet}}$, where $N_{assocDet} = 1, 2$ or 3 is the number of sub-detectors (out of LKr, MUV1 and MUV2), in which a non-zero energy has been associated to the track. Partial discriminants are computed as follows:

  ⋆ $D_{LKr} = \frac{E_{LKr} - 600\,\mathrm{MeV}}{120\,\mathrm{MeV}}$, or 0 if E_{LKr} has not been associated,

  ⋆ $D_{MUV1} = \frac{E_{MUV1} - 1380\,\mathrm{MeV}}{330\,\mathrm{MeV}}$, or 0 if E_{MUV1} has not been associated,

  ⋆ $D_{MUV2} = \frac{E_{MUV2} - 1250\,\mathrm{MeV}}{360\,\mathrm{MeV}}$, or 0 if E_{MUV2} has not been associated.

4.1.2.8 Particle identification

Information combined from multiple sub-detectors is used for particle identification. In this analysis, positive pion identification is required in $K_{\pi\nu\nu}$, $K_{2\pi}$ and $K_{2\pi}$ normalization selections, while positive muon identification is required in $K_{\mu 2}$ event selection.

The particle identification is applied for the pion candidate selected in subsection 4.1.1.2 (here referred to as *track* to avoid confusion). Sub-detector associations to the pion candidate defined in sections subsection 4.1.1.2 and subsection 4.1.2.7 are used.

List below summarizes all conditions for particle identification in the presented analysis. Combinations of these conditions resulting in positive pion or muon identification, are specified below the list.

1. A RICH single ring association to the track (subsection 4.1.1.2) is required. Both of the following conditions have to be satisfied:

   - RICH single ring mass between 125 MeV/c^2 and 200 MeV/c^2,

- RICH single ring likelihood computed under any of kaon, pion, positron or muon hypotheses has to be always ≤ 0.12.

2. Track pion probability $Prob(\pi^+)$ given in subsection 4.1.2.7 must be greater than a limit computed as

$$\max\left(0.7, 0.98 - 0.4596 \cdot \exp\left\{-\frac{p - 11.44\,\text{GeV}/c}{5.27\,\text{GeV}/c}\right\}\right),$$

where p is the track momentum.

3. Total calorimetric energy E_{calo} associated to the track (subsection 4.1.2.7) must be below limit computed as $p \cdot 1.2\,c$, where p is the track momentum.

4. The LKr cluster associated to the track (4.1.1.2) is described by total cluster energy E_{LKr}, number of LKr cells N_{cells} contributing to the LKr cluster by non-zero energy, and seed energy $E_{LKr,seed}$ defined by the most energetic hit in the cluster. Additionally, two ratios, $R_S = \dfrac{E_{LKr,seed}}{E_{LKr}}$ and $R_C = \dfrac{N_{cells} \cdot \text{MeV}}{E_{LKr}}$, are computed, where R_S is the largest fraction of the associated LKr energy measured in one cell, and R_C is an inverse mean LKr energy per hit. Variables E_{MUV1} and E_{MUV2} are defined in subsection 4.1.2.7. None of the conditions below can be fulfilled:

   - $R_1 < 0.01$ and $R_2 < 0.01$ and any of the following:
     - $R_S < 0.05$
     - $R_S \leq 0.2$ and $R_C < 0.0018$
     - $R_S > 0.2$ and $R_C \leq 0.003$
     - $R_S > 0.35$
   - $0 < R_S < 0.8$ and $R_C < 0.0014$
   - $E_{MUV1} = 0$ and $E_{MUV2} > 0$

5. Sum of the extra energy in MUV1 and MUV2 (subsection 4.1.2.7), $E_{MUV1,extra} + E_{MUV2,extra}$, must be greater than 5 GeV.

6. Positron rejection: ratio between the LKr energy associated to the track (subsection 4.1.1.2) and its momentum, E/p, must be smaller than $0.8\,c$.

7. Muon probability $Prob(\mu^+)$, given in subsection 4.1.2.7, must be greater than 0.99.

8. A MIP signal discriminant D_{MIP}, given in subsection 4.1.2.7, must be smaller than 1.

9. At least one MUV3 candidate must be within 7 ns from the reference time (specified later).

10. At least one of the MUV3 candidates geometrically associated to the track by the tool `SpectrometerMUV3Association` must be within 7 ns from the reference time (specified later).

Pion identification

To identify a track as a pion, a positive outcome is required from conditions 1, 2, 3, 4 and 6 and negative outcome is required from conditions 5 and 9 listed above.

Muon identification

To identify a track as a muon, a positive outcome is required from conditions 6, 7, 8 and at least one of 9, 10 from the list above.

4.1.3 $K^+ \to \pi^+ \nu\bar{\nu}$ event selection

The $K_{\pi\nu\nu}$ signal selection is applied on data events passing the PNN trigger, or on the $K_{\pi\nu\nu}$ Monte Carlo sample. It starts with the preselection of kaon decay events containing a single pion candidate and a matching kaon candidate (subsection 4.1.1.2).

Since the $K_{\pi\nu\nu}$ decay is very rare (Table 1.2.1) and more abundant kaon decays enter the $K_{\pi\nu\nu}$ signal regions, strict background rejection and efficient particle identification criteria must be applied.

Kaon candidate and event quality (subsection 4.1.2.2) conditions allow to filter out events not compatible with beam kaon decays occurring inside the decay region.

As mentioned in Appendix A and in [81], the dominant background to the $K_{\pi\nu\nu}$ is caused by upstream kaon decays and interactions of beam particles upstream of the decay region. Multiple cuts defined in subsection 4.1.2.3 are applied to suppress these events.

Full photon rejection with LKr and photon veto detectors (summarized in subsections 4.1.2.4 and 4.1.2.5) is applied to reject $K_{2\pi}$ decays and other background events with photons. Events with additional charged particles produced by photon interactions with the material before reaching calorimeters, together with multi-track kaon decay events not fully reconstructed in the STRAW, are rejected by multiplicity conditions in subsection 4.1.2.6.

Information obtained from RICH, electromagnetic and hadronic calorimeters and MUV3 is combined to positively identify pions and to suppress muons and positrons (see subsection 4.1.2.8).

Kaon decay selection: conditions 1, 2, 3b, 4, 5	subsection 4.1.2.2
Upstream background rejection: all conditions	subsection 4.1.2.3
No photons found in LKr	subsection 4.1.2.4
No photons found in other photon veto detectors	subsection 4.1.2.5
No multiplicity	subsection 4.1.2.6
Positive π^+ identification with t_{track} used as the time reference	subsection 4.1.2.8
Suppression of μ^+ using negated condition 8	subsection 4.1.2.8

Table 4.1.10: Summary of the $K_{\pi\nu\nu}$ event selection.

4.1.4 $K^+ \to \pi^+\pi^0(\gamma)$ event selection for normalization

To compute the total number of kaon decays in the fiducial volume needed for normalization of the $K_{\pi\nu\nu}$ result, a dedicated $K_{2\pi}$ selection was developed. In order to not bias the measurement, criteria similar to the ones used in $K_{\pi\nu\nu}$ event selection are applied. Additionally, all non-crucial selection cuts not fully reproducible in the simulation, such as those affected by the pile-up in downstream sub-detectors, are omitted. Residual differences between data and simulation are taken into account in the main $K_{\pi\nu\nu}$ analysis in the evaluation of the systematic uncertainty.

The selection is applied on events passing the control trigger containing a pair of kaon and pion candidates. Positive π^+ identification is enforced by conditions defined in subsection 4.1.2.8. Strict cuts implemented in subsection 4.1.2.3 are used to reject upstream events, while multi-track events are suppressed by requiring no additional track forming a vertex with the pion candidate.

Kaon decay selection: conditions 1, 2, 3b, 4, 5	subsection 4.1.2.2
Upstream background rejection: conditions 1, 2, 3, 4, 5b, 6, 7, 8	subsection 4.1.2.3
Multi-track event rejection with condition 8	subsection 4.1.2.6
Positive π^+ identification with t_{track} used as the time reference	subsection 4.1.2.8

Table 4.1.11: Summary of the $K_{2\pi}$ event selection for normalization.

4.1.5 $K^+ \to \pi^+\pi^0$ event selection for kinematic tails evaluation

The following $K_{2\pi}$ event selection is used in the estimation of the non-radiative component of the $K_{2\pi}$ background in the $K_{\pi\nu\nu}$ signal regions.

All events passing the control trigger, in which a single kaon and pion candidate pair is selected (Table 4.1.2) are considered. In addition to the conditions summarized in the second half of Table 4.1.13, which are mostly common with other three

event selections, a robust π^0 identification and two-body kaon decay requirement are applied in this selection.

The `Pi0Selection` algorithm (Section 3.1) is used to select events with only one reconstructed π^0 candidate. In addition to the conditions specified in Table 3.1.1, the π^0 must be within 5 ns from $t_{NA48\text{-}CHOD}$. Moreover, the two photons from the π^0 candidate are required be in the RICH geometrical acceptance. To test this condition, two unit vectors are constructed, pointing from the reconstructed neutral vertex position towards the LKr clusters corresponding to the photons. They are propagated to the front and back planes of RICH, where the distances from the hole center are calculated. Both photons are in the RICH acceptance if they are at least 100 mm and 120 mm away from the hole center at the RICH front and back planes, respectively.

To suppress events with radiative photons and to ensure that the selected π^0 originates from a $K_{2\pi}$ decay, an expected π^+ four-momentum is computed from the selected π^0 and the run-dependent mean beam kaon four-momentum. The expected π^+ track is extrapolated to the STRAW, RICH, NA48-CHOD, LKr, MUV2 and MUV3 sub-detectors and it must fulfill all conditions listed in Table 4.1.12.

Expected π^+ momentum	(5, 80) GeV/c
Expected $m^2(\pi^+)$	(8000, 31 000) MeV^2/c^4
In acceptance of all STRAW stations	
In acceptance of NA48-CHOD	
In acceptance of RICH front and back plane	90 mm < D_{hole} < 1100 mm
In acceptance of MUV2	130 mm < D_{hole} < 1100 mm
In acceptance of MUV3	130 mm < D_{hole} < 1100 mm
Away from LKr clusters corresponding to photons from π^0	> 150 mm

Table 4.1.12: Summary of conditions for the expected π^+ in the $K_{2\pi}$ event selection.

Furthermore, either a standard LKr cluster or a hit cluster has to be associated to the expected π^+. A standard LKr candidate is associated to the expected π^+ if it is closer than 200 mm to the π^+ position in the LKr plane and within 5 ns from the π^0 time. If no such cluster is found among the LKr candidates, an attempt to reconstruct a hit cluster from LKr hits is made, similarly as in subsection 4.1.1.2. The hit cluster energy is summed up from all LKr hits within 100 mm from the π^+ position in the LKr and within 20 ns from the π^0 time. The hit with the highest energy, called seed, defines the cluster time. The association is successful if the energy of the seed is at least 40 MeV and the cluster time is within 8 ns from the π^0 time. All of the requirements explained above are summarized in the first half of Table 4.1.13.

Positive π^+ identification (subsection 4.1.2.8) with the same conditions as in the $K_{\pi\nu\nu}$ event selection is required. In addition to applying photon rejection criteria in LAV, IRC and SAC (subsection 4.1.2.5), the procedure to reject events with extra photons selected from the standard LKr candidates (subsection 4.1.2.4) is applied as well, excluding the LKr candidates corresponding to the two photons from π^0. Compatibility of the event with beam kaon decay inside the fiducial volume is ensured by cutting on the position of the reconstructed vertex (subsection 4.1.2.2). Moreover, upstream background (subsection 4.1.2.3) and multi-track kaon decays (subsection 4.1.2.6) are rejected.

One π^0 candidate	Section 3.1
Photons from π^0 in RICH acceptance	
Neutral vertex between 105 m and 165 m	
π^0 within 5 ns from $t_{NA48\text{-}CHOD}$	
Good expected π^+	Table 4.1.12
LKr cluster associated to the expected π^+	
Kaon decay selection: conditions 1, 3, 4, 5	subsection 4.1.2.2
Upstream background rejection: conditions 1, 2, 3, 4, 7, 8	subsection 4.1.2.3
No extra photon in LKr (standard candidates), the two LKr candidates corresponding to the two photons from π^0 are skipped over	subsection 4.1.2.4
No photons found in photon veto detectors	subsection 4.1.2.5
No multiplicity with 8, 9	subsection 4.1.2.6
Positive π^+ identification with t_{track} used as the time reference	subsection 4.1.2.8

Table 4.1.13: Summary of the $K_{2\pi}$ event selection.

4.1.6 $K^+ \to \mu^+\nu(\gamma)$ event selection for kinematic tails

The following $K_{\mu2}$ event selection is used in the estimation of the $K_{\mu2}$ background in the $K_{\pi\nu\nu}$ signal regions. $K_{\mu2}$ events pass the $K_{\pi\nu\nu}$ selection if the muon is misidentified as a pion. However, for statistical reasons, positive π^+ identification cannot be applied in this event selection. Instead, a positive μ^+ identification is required, exploiting conditions that minimally affect the shape of the final m^2_{miss} distribution (see details in subsection 4.1.7).

All events passing the control trigger are considered. A single pion candidate (in this case representing the $K_{\mu2}$ muon) and a matching kaon candidate, selected in subsection 4.1.1.2, are required. Events not compatible with beam kaon decays in fiducial volume are rejected by conditions defined in subsection 4.1.2.2. Addition-

ally, suppression of upstream background, multi-track kaon decays and events with photon interactions upstream of calorimeters is achieved by criteria listed in subsections 4.1.2.3 and 4.1.2.6. Similarly to the $K_{\pi\nu\nu}$ selection, events with photons found in LKr or photon veto detectors are rejected (subsections 4.1.2.4 and 4.1.2.5). Finally, positive μ^+ identification conditions are imposed combining information from LKr, hadronic calorimeters and MUV3 (subsection 4.1.2.8).

Kaon decay selection: conditions 1, 3, 4, 5	subsection 4.1.2.2
Upstream background rejection: conditions 1, 2, 3, 4, 5a, 7, 8	subsection 4.1.2.3
No photons found in LKr	subsection 4.1.2.4
No photons found in photon veto detectors	subsection 4.1.2.5
No multiplicity	subsection 4.1.2.6
Positive μ^+ identification with t_{track} used as the time reference	subsection 4.1.2.8

Table 4.1.14: Summary of the $K_{\mu 2}$ event selection.

4.1.7 Definition of regions

Events passing each of the selections are categorized into nine regions to allow for the observation of the $K_{\pi\nu\nu}$ signal event candidates and effective background estimation. The regions are defined by the kinematic variable m^2_{miss}:

$$m^2_{miss} = \left(P_{K^+} - P_{\pi^+}\right)^2, \tag{4.1.5}$$

in which P_{K^+} and P_{π^+} are the four-momenta of the selected kaon and pion candidates, respectively. The three-momenta are measured by the GTK and the STRAW and extrapolated to the decay vertex, while the last component of the four-momenta is computed using the assumption of K^+ and π^+ masses for the candidates. Note that for $K_{\mu 2}$ events the mass assignment is incorrect and thus the m^2_{miss} depends on the muon momentum, despite being a two-body decay.

Comparing distributions of this variable for the three most abundant kaon decays ($K_{\mu 2}$, $K_{2\pi}$, $K_{3\pi}$) with the one for the $K_{\pi\nu\nu}$ decay, two regions in which the contribution from the three common decays is the lowest, are identified. They are naturally placed between the peaks of $K_{\mu 2}$, $K_{2\pi}$ and $K_{3\pi}$ distributions (Figure 1.2.6) and are used as signal regions for the $K_{\pi\nu\nu}$ decay measurement. Both signal regions (denoted as SR1 and SR2) are blinded until the analysis is fully developed and all background estimations as well as evaluation of signal expectations are finalized.

Additionally, three background (peak) regions, covering the $K_{\mu 2}$, $K_{2\pi}$ and $K_{3\pi}$ peaks, are defined. Simulations show that events passing the $K_{\pi\nu\nu}$ event selection and populating these areas are predominantly $K_{\mu 2}$, $K_{2\pi}$ and $K_{3\pi}$ decay events, respectively, with only small contributions from other processes. Therefore the peak

regions are used for the evaluation of the expected background to $K_{\pi\nu\nu}$ in the signal regions through tail fraction comparison.

Finally, four control regions defined between the peak and the signal regions, dominated by background events, allow for a validation of the background estimation.

All regions are restricted to the pion candidate momentum range (15, 35) GeV/c and further divided into four momentum bins: (15, 20) GeV/c, (20, 25) GeV/c, (25, 30) GeV/c and (30, 35) GeV/c.

The region definition by m^2_{miss} is supplemented by additional momentum-dependent constraints expressed in terms of two kinematic variables $m^2_{miss}(RICH)$ and $m^2_{miss}(beam)$ defined similarly as m^2_{miss}, but:

- in $m^2_{miss}(RICH)$: P_{K^+} is the four-momentum of the selected kaon candidate with a mass of K^+ (as in the standard defition), while P_{π^+} is the four-momentum of the selected pion candidate with momentum slope measured by STRAW, the momentum magnitude measured by RICH and a mass of π^+,
- in $m^2_{miss}(beam)$: P_{K^+} is the four-momentum of a kaon candidate computed from a run-dependent mean beam momentum and a mass of K^+ and P_{π^+} is four-momentum of the selected pion candidate with momentum measured by STRAW and a mass of π^+ (as in the standard definition).

Full definition of all identified regions is given in Table 4.1.15. All control regions are masked until the background estimation is finalised. Both signal regions are masked until completion of the analysis.

Region		m^2_{miss} [GeV^2/c^4]	$m^2_{miss}(RICH)$ [GeV^2/c^4]	$m^2_{miss}(beam)$ [GeV^2/c^4]
$K_{\mu 2}$		(-0.05, $m^2_{kin} + 3\sigma$)		
CR($K_{\mu 2}$)		($m^2_{kin} + 3\sigma$, 0)		
SR1	p $\leq$ 20 GeV/c	(0, 0.01)	(0, 0.01)	(-0.005, 0.0135)
	p $\in$ (20, 25) GeV/c	(0, 0.01)	(0, 0.02)	(-0.005, 0.0135)
	p $\geq$ 25 GeV/c	(0, 0.01)	(-0.005, 0.02)	(0, 0.0135)
CR1($K_{2\pi}$)		(0.01, 0.015)		
$K_{2\pi}$		(0.015, 0.021)	(0, 0.07)	
CR2($K_{2\pi}$)		(0.021, 0.026)		
SR2		(0.026, 0.068)	(0.02, 0.07)	(0.024, 0.068)
CR($K_{3\pi}$)		(0.068, 0.072)		
$K_{3\pi}$		(0.072, 0.150)		

Table 4.1.15: Definition of regions.

Variable m^2_{kin}, which determines shape of the boundary between $K_{\mu 2}$ peak and control regions, is defined as large-momenta approximation of m^2_{miss} of $K_{\mu 2}$ events evaluated under the M_{π^+} hypothesis:

$$m^2_{kin} = \left(M^2_{\pi^+} - M^2_{\mu^+}\right) \cdot \left[1 - \frac{75\,\mathrm{GeV}/c}{p(\pi^+)}\right], \tag{4.1.6}$$

where $p(\pi^+)$ is the pion candidate momentum. Additionally, $\sigma = 1.2 \times 10^{-3}\,\mathrm{GeV}^2/c^4$ is the corresponding resolution. This definition copies the peak of the m^2_{miss} distribution (under M_{π^+} hypothesis) of the $K_{\mu 2}$ events across full muon momentum range.

Due to a correlation between π^+ identification with RICH and $m^2_{miss}(RICH)$, the signal region definition for events passing the $K_{\mu 2}$ selection includes only constraints on m^2_{miss} and $m^2_{miss}(beam)$. Alternatively, the RICH condition for positive π^+ identification, used in the $K_{\pi\nu\nu}$ selection, can be applied also to $K_{\mu 2}$ events and, subsequently, the full signal region definition can be used. Both approaches were exploited in the main $K_{\pi\nu\nu}$ analysis of 2018 data in estimation of the expected $K_{\mu 2}$ background contribution to signal regions after the $K_{\pi\nu\nu}$ selection, as well as to compute the corresponding systematic uncertainty caused by differences between $K_{\mu 2}$ and $K_{\pi\nu\nu}$ event selections.

4.1.8 Definitions of variables for the $K_{\pi\nu\nu}$ measurement

Quantities defined in this section are used to obtain the results of the $K_{\pi\nu\nu}$ measurement, as well as to compare the performance of the proposed STRAW–GTK matching algorithm in the $K_{\pi\nu\nu}$ analysis with respect to the standard algorithm.

Kinematic tails of $K_{2\pi}$ and $K_{\mu 2}$

The contribution of $K_{2\pi}$ and $K_{\mu 2}$ decay events to the background in the $K_{\pi\nu\nu}$ signal regions is estimated from minimum–bias data passing the $K_{2\pi}$ and $K_{\mu 2}$ event selections, combined with the PNN-triggered data passing the $K_{\pi\nu\nu}$ event selection. This method profits from the abundance of $K_{2\pi}$ and $K_{\mu 2}$ control events entering the $K_{\pi\nu\nu}$ signal regions owing to dedicated event selections, as well as from the benefits of data-driven background estimation. However, as the signal and background event selections differ in important details, such estimation is valid only if the selection criteria do not change the shapes of event distributions in the relevant regions (defined in subsection 4.1.7).

Important quantity obtained from the dedicated $K_{2\pi}$ and $K_{\mu 2}$ event selections is referred to as the *tail fraction* and is given by the ratio of the number of events in the tails to the number of events in the $K_{2\pi}$ and $K_{\mu 2}$ peaks of the m^2_{miss} distribution. To

account for potential track momentum dependency, tail fractions are estimated in four, $5\,\mathrm{GeV}/c$ - wide momentum bins.

The tail fraction of decay α ($K_{\mu 2}$ or $K_{2\pi}$) in region $\rho \in \{\mathrm{SR1}, \mathrm{SR2}\}$ and momentum bin $\eta \in \{1, 2, 3, 4\}$ is defined as:

$$f_{kin,\alpha}^{\rho,\eta} = \frac{N_{\alpha}^{\rho,\eta}}{N_{\alpha}^{R_\alpha,\eta}}, \tag{4.1.7}$$

where $N_{\alpha}^{\rho,\eta}$ ($N_{\alpha}^{R_\alpha,\eta}$) is the number of events of decay α passing the corresponding event selection and reconstructed in region ρ (peak region R_α) with the track momentum in range (2+η, 3+η) $\cdot\, 5\,\mathrm{GeV}/c$.

Expected background

Number of background events of decay α expected to occur in the $K_{\pi\nu\nu}$ signal region ρ after passing the $K_{\pi\nu\nu}$ event selection is computed from the tail fraction of decay α and $K_{\pi\nu\nu}$–selected data events reconstructed in peak region R_α:

$$N_{exp,\alpha}^{\rho} = \sum_{\eta=1}^{4} f_{kin,\alpha}^{\rho,\eta} \cdot N_{\pi\nu\nu}^{R_\alpha,\eta}, \tag{4.1.8}$$

where $N_{\pi\nu\nu}^{R_\alpha,\eta}$ is the number of events in peak region R_α with track momentum in bin η after the $K_{\pi\nu\nu}$ event selection.

Consequently, the total expected number of $K_{2\pi}$ and $K_{\mu 2}(\gamma)$ events passing the $K_{\pi\nu\nu}$ event selection, in both signal regions (SR1 and SR2) combined, is computed as follows:

$$N_{exp\ bg} = \sum_{\rho\in\{\mathrm{SR1,SR2}\}} \sum_{\eta=1}^{4} \left[f_{kin,2\pi}^{\rho,\eta} \cdot N_{\pi\nu\nu}^{R_{2\pi},\eta} + f_{kin,\mu\nu}^{\rho,\eta} \cdot N_{\pi\nu\nu}^{R_{\mu\nu},\eta} \right]. \tag{4.1.9}$$

This method relies on the assumption that after the $K_{\pi\nu\nu}$ selection, the peak regions R_α are populated predominantly by events of decay α, and that the number of events in R_α is not correlated with tail fraction of decay α. Inaccuracy of these assumptions results in a systematic uncertainty of the expected background estimate evaluated in the main $K_{\pi\nu\nu}$ analysis.

Acceptance

Signal and normalization acceptances are computed from simulated $K_{\pi\nu\nu}$ and $K_{2\pi}$ events, respectively. They account for geometrical and kinematic acceptance of the NA62 sub-detectors, signal reconstruction efficiency and the selection–specific criteria. The effect of random losses due to presence of accidental particles satisfying event veto conditions is quantified separately as it is independent from the kaon decay mode. Precision of the acceptance measurement depends on the level of accuracy to which the detector performance and physical processes (e.g. hadronic interactions) are reproduced in the simulation.

The acceptance is subject to the fiducial volume definition restricting the Z range of the generated kaon decay vertex positions considered in the analysis. We opted for region (105, 180) m denoted by FV in the following.

Acceptance of the $K_{\pi\nu\nu}$ event selection is defined as follows:

$$A(\pi\nu\nu) = \frac{1}{N^{FV}_{\pi\nu\nu}} \cdot \sum_{\rho\in\{SR1,SR2\}} N^{\rho}_{\pi\nu\nu}, \tag{4.1.10}$$

where $N^{\rho}_{\pi\nu\nu}$ is the total number of $K_{\pi\nu\nu}$ Monte Carlo events in region ρ after the $K_{\pi\nu\nu}$ event selection. The denominator, $N^{FV}_{\pi\nu\nu}$, stands for the number of generated $K_{\pi\nu\nu}$ Monte Carlo events decaying in the region FV.

Similarly, acceptance of the $K_{2\pi}$ normalization selection is defined as ratio:

$$A(2\pi N) = \frac{N^{R_{2\pi}}_{2\pi N}}{N^{FV}_{2\pi N}}, \tag{4.1.11}$$

where $N^{R_{2\pi}}_{2\pi N}$ is the number of $K_{2\pi}$ Monte Carlo events passing the normalization selection and reconstructed in the $K_{2\pi}$ peak region $R_{2\pi}$, while $N^{FV}_{2\pi N}$ is the number of $K_{2\pi}$ Monte Carlo events with the generated decay position in region FV.

Normalization

Minimum-bias $K_{2\pi}$ events selected with dedicated normalization selection described in subsection 4.1.4 are used for evaluation of the total number of kaon decays occurring in the fiducial volume:

$$\mathcal{N} = \frac{N^{R_{2\pi}}_{2\pi N}}{\mathcal{B}(K_{2\pi})\varepsilon_{2\pi N}} \frac{\mathcal{S}}{\varepsilon_{mb}}, \tag{4.1.12}$$

where $\mathcal{B}(K_{2\pi}) = 0.2067$ is the branching fraction of $K_{2\pi}$ decay (Table 1.2.1) and factor $\varepsilon_{2\pi N}$ includes the Monte Carlo acceptance of the normalization selection, $A(2\pi N)$, as well as a factor quantifying random rejection of events due to accidental particles. $\mathcal{S} = 400$ and ε_{mb} correspond to the scaling factor and efficiency of the minimum-bias trigger, respectively.

Single event sensitivity

Single event sensitivity (SES) of the $K_{\pi\nu\nu}$ analysis is given by the total number $\mathcal{N}$ of kaon decays in the fiducial volume, mean efficiency $\varepsilon_{pnn} = 0.87 \pm 0.03$ of the PNN trigger used for collecting data for the $K_{\pi\nu\nu}$ measurement, and efficiency $\varepsilon_{\pi\nu\nu}$ of the $K_{\pi\nu\nu}$ event selection representing both the Monte Carlo acceptance and the effect of random event veto:

$$SES = \frac{1}{\mathcal{N}\varepsilon_{\pi\nu\nu}\varepsilon_{pnn}}. \tag{4.1.13}$$

Expansion of $\mathcal{N}$ using equation Equation (4.1.12) reveals that SES depends on the ratio of the selection efficiencies. Thanks to the similarities between the signal and normalization selections, part of the random veto effect cancels out. The remaining effect is quantified in a single variable $\varepsilon_{RV} = 0.638 \pm 0.014$. Mean values of ε_{pnn} and ε_{RV}, averaged over track momentum and beam intensity, are obtained from the main $K_{\pi\nu\nu}$ analysis. The control trigger is used as a reference for the measurement of ε_{pnn}, therefore its efficiency is considered to be 1. This results in the following definition:

$$SES = \frac{\mathcal{B}(K_{2\pi})}{N_{2\pi N}^{R_{2\pi}}} \frac{A(2\pi N)}{A(\pi\nu\nu)} \frac{1}{\mathcal{S}\varepsilon_{RV}\varepsilon_{pnn}}. \tag{4.1.14}$$

Expected signal

Total number of Standard Model $K^+ \to \pi^+\nu\overline{\nu}$ decay events expected in the signal regions is obtained from SES and theoretical prediction of the $K_{\pi\nu\nu}$ branching fraction $\mathcal{B}(K_{\pi\nu\nu})$ (Table 1.2.1):

$$N_{exp\,\pi\nu\nu} = \frac{\mathcal{B}(\pi\nu\nu)}{SES}. \tag{4.1.15}$$

4.2 STRAW–GTK matching algorithm

As discussed before, the main kinematic variable used to identify the $K^+ \to \pi^+\nu\overline{\nu}$ decays and to suppress background processes is the squared missing mass:

$$m_{miss}^2 = \left(P_{K^+} - P_{\pi^+}\right)^2, \tag{4.2.1}$$

computed from the four-momenta P_{K^+} and P_{π^+} of the kaon and pion candidates, respectively. This shows that correctly matching the kaon candidate in GTK to the corresponding pion track in STRAW is crucial for the $K_{\pi\nu\nu}$ measurement. However, since rate of particles in both spectrometers is high (up to 750 MHz in GTK and 10 MHz in STRAW at nominal beam intensity), it is not sufficient to use only the reconstructed times for the matching, even though the time measurement of both mesons is very precise (better than 200 ps). A more sophisticated algorithm, employing times, positions and trajectories of the kaon and pion candidates has to be used.

The standard algorithm for matching a STRAW track with a GTK candidate, used in the main $K_{\pi\nu\nu}$ analysis, is summarized in subsection 4.2.1. Then the strategy to develop a new matching algorithm is discussed in detail in subsection 4.2.2, following three steps:

- Use $K_{3\pi}$ decay events, in which full kinematic information (momenta and positions of all the decay products) is available, to find the correct GTK candidate (subsection 4.2.2.1).

- Propose an algorithm to match individual pion tracks to GTK candidates. Use events from the previous step to prepare test distributions for the algorithm (subsection 4.2.2.2).

- Define matching quality cuts for the algorithm to achieve the best performance in the full $K_{\pi\nu\nu}$ analysis (subsection 4.2.2.3).

Finally, the performance of the new matching algorithm on $K_{3\pi}$ events is compared with the reference results obtained with the standard matching algorithm in subsection 4.2.3.

In all presented algorithms, reconstruction quality of GTK candidates, as well as their compatibility with the average beam is tested by the following conditions:

- χ^2 of the candidate fit from the GTK reconstruction: $\chi^2_{candidate} < 50$,

- $\chi^2_{event} < 20$.

Compatibility with the beam is tested with a χ^2_{event} variable, which takes into account the momentum $p(GTK)$ and slopes S_X and S_Y of the GTK candidate and is defined as follows:

$$\chi^2_{event} = \left(\frac{p(GTK) - p(beam)}{\sigma_p}\right)^2 + \left(\frac{S_x - S_x(beam)}{\sigma_{S_x}}\right)^2 + \left(\frac{S_y - S_y(beam)}{\sigma_{S_y}}\right)^2, \quad (4.2.2)$$

where $p(beam) = 74\,900$ MeV/c, $\sigma_p = 900$ MeV/c, $S_x(beam) = 0.00122$, $\sigma_{S_x} = 0.00012$, $S_y(beam) = 0.00002$, $\sigma_{S_y} = 0.00010$ are mean beam parameters and resolutions.

4.2.1 The standard STRAW–GTK matching algorithm

The standard STRAW–GTK matching procedure was developed and tuned for the main $K_{\pi\nu\nu}$ analysis, but is used in multiple other physics analyses at NA62.

Input to this algorithm consists of a STRAW candidate, time of a RICH association (t_{RICH}) and time of a KTAG association (t_{KTAG}) to the candidate, and all GTK candidates reconstructed in that event. In the $K_{\pi\nu\nu}$ analysis, the STRAW candidate corresponds to a single π^+ track and is selected in subsection 4.1.1.2, together with the RICH and KTAG associations, while the standard GTK reconstruction algorithm (subsection 2.3.3) is used to reconstruct new GTK candidates with t_{KTAG} used as the time reference.

A GTK candidate must be in time with t_{KTAG} (0.6 ns) and must meet the conditions defined in Section 4.2 ($\chi^2_{candidate}$, χ^2_{event}) to be considered in the matching. A three step procedure is used to compute position of the vertex between the STRAW

and GTK candidates. Starting with the STRAW track direction and position before the STRAW magnet and the direction and position of the GTK candidate in the last GTK station, a Z position of the point of closest approach is found assuming straight-line trajectories. The track and GTK candidate are then extrapolated through the magnetic field of the Blue Tube to the Z plane of the point of closest approach from the previous step and their momenta in this position, corrected for the Blue Tube field, are computed. The corrected momenta of the track and GTK candidate define new particle directions at their initial positions (before the STRAW magnet and in the last GTK station, respectively). Finally, position of a new point of closest approach, computed with the corrected particle directions, is used to define the final vertex position. Additionally, distance between the track and GTK candidate at the point of the closest approach (CDA) is computed and is used in the matching algorithm.

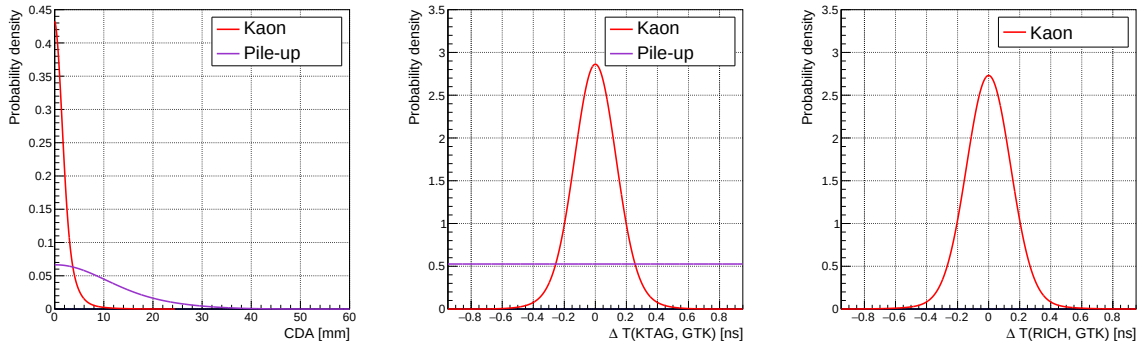

Figure 4.2.1: PDF distributions of CDA, $\Delta T(KTAG, GTK)$ and $\Delta T(RICH, GTK)$ used in the standard STRAW–GTK matching algorithm. The red set of functions (denoted "Kaon") is used to compute D_{KTAG} and D_{RICH}. The violet set of functions (denoted "Pile-up") in used to test hypothesis that the GTK candidate corresponds to an accidental beam particle (D_p).

For each pair of a STRAW track and a GTK candidate, the quality of the matching is assessed by a discriminant D_{KTAG} defined as a product of p-values computed from PDF distributions of $\Delta T(KTAG, GTK)$ and CDA shown in Figure 4.2.1 in red. The distributions were obtained from $K_{3\pi}$ events by a procedure similar to the one described in subsection 4.2.2.1.

All GTK candidates considered in an event are sorted by the largest discriminant D_{KTAG} with the first one being potentially matched to the π^+ track. To avoid mismatch between two similar GTK candidates and to ensure good quality of the matching, several additional conditions are applied. If at least three GTK candidates are considered in an event and the best two have similar discriminants (ΔD_{KTAG} < 0.3), a procedure testing hypotheses that the two candidates correspond to accidental beam particles takes place. First a new discriminant D_p is defined as a

product of p-values computed from the second set of PDF distributions shown in Figure 4.2.1 in violet, using $\Delta T(KTAG, GTK)$ and CDA of the relevant track-GTK candidate pair. These distributions were produced from $K_{3\pi}$ events with out-of-time GTK candidates representing pile-up particles not corresponding to the selected $K_{3\pi}$ decays. All GTK candidates with $\Delta D_{KTAG} < 0.3$ with respect to the best GTK candidate are sorted by the largest D_p. If the GTK candidate with the largest D_{KTAG} is not the candidate with the largest D_p, the event is rejected and no matching GTK candidate is found for the STRAW track. Otherwise, the first two GTK candidates in ordering by D_p are compared. For each of the two GTK candidates a ratio of their respective p-values of CDA and $\Delta T(KTAG, GTK)$ present in D_{KTAG} and D_p is computed: $R^1_{\Delta T}$ and R^1_{CDA} for the GTK candidate with the largest D_p and $R^2_{\Delta T}$ and R^2_{CDA} for the other GTK candidate. Then the two GTK candidates are compared by computing new ratios separately for timing and CDA, $R_{\Delta T} = R^1_{\Delta T}/R^2_{\Delta T}$ and $R_{CDA} = R^1_{CDA}/R^2_{CDA}$, and by imposing a cut on $R_{\Delta T}$ and R_{CDA}. If either one of these ratios is smaller than 1.5, the two GTK candidates are considered too similar and no matching GTK candidate is found for the STRAW track in this event.

Lastly, a third discriminant D_{RICH} is defined as a product of p-values computed from the PDF distributions (shown in Figure 4.2.1 in red) using $\Delta T(RICH, GTK)$ and CDA of this track-GTK candidate pair. The following conditions have to be met for the best GTK candidate to be successfully matched to the π^+ track:

- no more than 5 GTK candidates can be considered in an event (in time with t_{KTAG} and good $\chi^2_{candidate}$ and χ^2_{event}),
- at least one of the discriminants (D_{KTAG}, D_{RICH}) must be larger than 0.03,
- both discriminants (D_{KTAG}, D_{RICH}) must be larger than 0.005.

Output of this algorithm consists of the vertex position and STRAW and GTK candidate momenta computed at the vertex.

4.2.2 Development of a new matching algorithm

As explained before, the GTK sub-detector provides momentum and position measurement of all beam particles, including kaons, pions and protons. The reconstruction output is an upstream particle candidate with the momentum vector and the position measured at the last GTK station, and time t_{GTK} computed from hit times in all three GTK stations. Equivalently, hits in the STRAW sub-detector produced by charged kaon decay products in geometrical acceptance of STRAW chambers are used to reconstruct STRAW tracks. These downstream tracks contain information

about positions and momenta of the registered particles. In order to find the correct pair of upstream and downstream tracks, the matching algorithm has to rely on their time, position and direction measurements.

In the $K_{\pi\nu\nu}$ analysis, two times associated to the track are used for the STRAW-GTK matching: t_{RICH} of the RICH association and t_{KTAG} of the KTAG candidate associated to the track (subsection 4.1.1.2). For each GTK candidate, t_{GTK} is provided. Since the simple time differences $\Delta T(KTAG, GTK)$ and $\Delta T(RICH, GTK)$ are correlated, linear combinations are used instead for the new matching algorithm[2]:

$$\Delta T_+ = \frac{1}{\sqrt{2}} \left[\Delta T(KTAG, GTK) + \Delta T(RICH, GTK)\right] = \frac{1}{\sqrt{2}} \left[t_{KTAG} + t_{RICH} - 2t_{GTK}\right], \tag{4.2.3}$$

$$\Delta T_- = \frac{1}{\sqrt{2}} \left[\Delta T(KTAG, GTK) - \Delta T(RICH, GTK)\right] = \frac{1}{\sqrt{2}} \left[t_{KTAG} - t_{RICH}\right]. \tag{4.2.4}$$

For a pair of a downstream particle and a GTK candidate, the vertex position is found by extrapolating the momentum of the GTK candidate from the last GTK station and the momentum of the STRAW candidate from the first STRAW station into the decay region, where the directions of particles are affected by the magnetic field inside the Blue Tube (subsection 2.1.4). The vertex position is computed iteratively by repeating the following two steps until the GTK candidate and the downstream track are less than 5 m apart:

1. Find Z position of the point of closest approach by assuming straight-line crossing between the GTK candidate and the downstream track.

2. Propagate both the GTK candidate and the downstream track along the Z-axis to a half of the distance between their current position and the Z position found in the previous step. Provide the new momenta in their final positions corrected for the magnetic field.

Once the distance between the GTK candidate and the downstream track after the second step is less than 5 m, the first step is repeated for the last time and the final Z_{vtx} is found. Finally, both GTK candidate and the downstream track are propagated to Z_{vtxx} and their momenta in the vertex are computed, as well as the distance between their positions in the vertex plane, D_{vtx}.

The proposed matching algorithm checks compatibility of the reference downstream track with a subset of reconstructed GTK tracks. Each track-GTK candidate

[2]Given all time shifts between RICH, KTAG and GTK sub-detectors are removed fine time corrections applied in the analysis, ΔT_+ and ΔT_- are to a good degree uncorrelated thanks to similar time resolutions of RICH and KTAG.

pair is characterized by a set of three values: D_{vtx}, ΔT_+ and ΔT_-. Based on these values, two hypotheses are tested:

$H_0 \equiv$ The GTK candidate is the correct one and corresponds to the reference downstream track (*kaon* hypothesis).

$H_1 \equiv$ The GTK candidate is a pile-up particle and does not correspond to the reference downstream track (*pile-up* hypothesis).

For each hypothesis, probability density functions of D_{vtx}, ΔT_+ and ΔT_- are provided by fitting the relevant distributions obtained from data events in which the GTK candidate corresponding to a single STRAW track is known (see subsection 4.2.2.1).

$K^+ \to \pi^+\pi^+\pi^-$ decay events are the most suitable for obtaining these distributions due to their abundance [28] and the fact that all the decay products are detected and their positions and momenta are available using information only from the STRAW spectrometer. The tool `K3piStrictSelection` is used to produce a very clean $K_{3\pi}$ event sample from 2017A data set. Momenta, positions and time of all three pions together provide enough information to find (if reconstructed) the correct GTK candidate for the $K_{3\pi}$ event. The algorithm developed to match a GTK candidate to a kaon candidate in $K_{3\pi}$ events is described in subsection 4.2.2.1.

4.2.2.1 $K_{3\pi}$– GTK matching algorithm

A GTK candidate matching the $K_{3\pi}$ event is looked for using the $K_{3\pi}$ vertex position fitted from the three STRAW tracks, vertex time computed as a weighted mean of the times of NA48-CHOD and CHOD associations to the three pion candidates, and the kaon candidate momentum obtained from the `K3piStrictSelection` from the combined information of the three pion tracks.

At first a preselection is done on the previously filtered $K_{3\pi}$ control events requiring

- at least one KTAG candidate in the event, and
- $K_{3\pi}$ kaon candidate extrapolated back to the GTK3 plane to be in the geometrical acceptance of the GTK3 station ($|X| < 30$ mm and $|Y| < 15$ mm).

Since GTK detects all charged upstream particles, the KTAG sub-detector is used to distinguish kaons from other beam particles. The $K_{3\pi}$ kaon candidate is matched to a KTAG candidate reconstructed in at least five sectors, closest in time to the $K_{3\pi}$ vertex time with $\Delta T(K_{3\pi}, KTAG) < 1$ ns. Time of this KTAG candidate is used as the reference for the reconstruction of GTK candidates in this event (subsection 2.3.3).

To provide extra timing information for the matching, RICH associations to the three pions are found using the tool `SpectrometerRICHAssociation`. Mean time of the positive tracks is computed and defines t_{RICH} of the kaon candidate. Since the two available ΔT variables, $\Delta T(KTAG, GTK)$ and $\Delta T(RICH, GTK)$, are correlated, a linear combination, ΔT_+ (same definition as Equation (4.2.3)) is used for the matching instead.

The best GTK candidate for the kaon candidate is found among the ones for which $|\Delta T_+| < 0.8\,\text{ns}$, which are properly reconstructed and are compatible with the nominal beam ($\chi^2_{candidate}$ and χ^2_{event} conditions in Section 4.2).

For each GTK candidate tested in the matching, position and momentum at the $K_{3\pi}$ vertex plane are obtained by extrapolation of the GTK candidate from the last GTK station while accounting for the magnetic field inside the Blue Tube. To evaluate the geometrical and kinematic compatibility of a GTK candidate with the kaon candidate from the $K_{3\pi}$ event, a discriminant is built from the momentum difference between the kaon candidate and the GTK candidate, and the position difference between the $K_{3\pi}$ vertex and the GTK candidate extrapolated to the vertex plane:

$$D_{3\pi} = \frac{(p_x(kaon) - p_x(GTK))^2}{s(\Delta p_x)^2} + \frac{(p_y(kaon) - p_y(GTK))^2}{s(\Delta p_y)^2} + \frac{(p_z(kaon) - p_z(GTK))^2}{s(\Delta p_z)^2} + \\ + \frac{(X(kaon) - X(GTK))^2}{s(\Delta X)^2} + \frac{(Y(kaon) - Y(GTK))^2}{s(\Delta Y)^2}. \tag{4.2.5}$$

Values of standard deviation s used in the discriminant are listed in the Table 4.2.1.

$s(\Delta p_x)$	$s(\Delta p_y)$	$s(\Delta p_z)$	$s(\Delta X)$	$s(\Delta Y)$
1.9 MeV/c	1.9 MeV/c	275 MeV/c	1.2 mm	1.2 mm

Table 4.2.1: Summary of standard deviations s of variables used for evaluation of discriminant $D_{3\pi}$ (Equation (4.2.5)). Values are obtained from $K_{3\pi}$ data events.

GTK candidate with the smallest discriminant $D_{3\pi}$ is matched to the $K_{3\pi}$ event if the discriminant value is less than 20 and conditions 1 in subsection 4.1.2.2, ensuring that the reconstructed momentum and direction of the GTK candidate are compatible with the kaon beam, are met.

The GTK candidate matched to the $K_{3\pi}$ event is used to prepare PDF distributions (referred to as *kaon* distributions, Figure 4.2.3a) of D_{vtx}, ΔT_+ and ΔT_- for the new STRAW-GTK matching algorithm. One of the two positive pions is chosen randomly in each $K_{3\pi}$ event and t_{KTAG} and t_{RICH} are found in the same way as for the $K_{3\pi}$ kaon candidate. The iterative procedure described in subsection 4.2.2 is

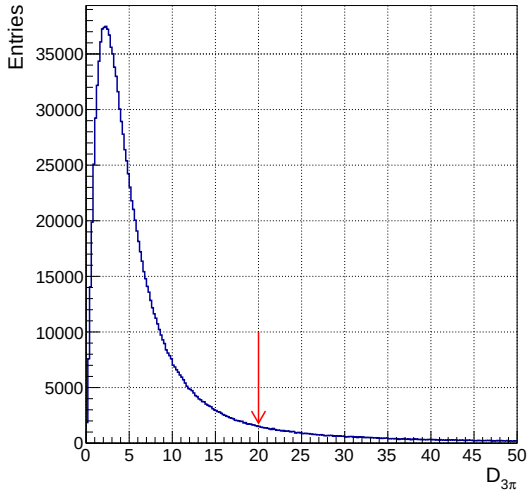

Figure 4.2.2: $D_{3\pi}$ of the best GTK candidate before application of final cuts. Red arrow indicates the cut used in the $K_{3\pi}-$ GTK candidate matching.

used to find the $K^+ - \pi^+$ vertex between the GTK candidate and the chosen π^+ and compute D_{vtx}. Time differences ΔT_+ and ΔT_- are obtained from t_{KTAG} and t_{RICH} associated to the π^+ track and t_{GTK} of the GTK candidate. Distributions of D_{vtx}, ΔT_+ and ΔT_-, obtained from the whole data sample, are fitted with combination of gaussian, exponential and linear functions and the normalized fit results are used as PDF distributions in the new matching algorithm.

Furthermore, events passing the $K_{3\pi}$ selection are categorized based on the number N of reconstructed GTK candidates with good quality and compatible with the kaon beam, and a probability of finding (reconstructing and selecting) a matching GTK candidate in a $K_{3\pi}$ event is computed (Figure 4.2.4). The results are used as marginal probabilities in the Bayes' theorem (subsection 4.2.2.2) employed in the new STRAW-GTK matching algorithm.

A second set of the PDF distributions (Figure 4.2.3b) is obtained from GTK candidates reconstructed from hits at least 15 ns away from the original reference time (time of the KTAG candidate associated to the $K_{3\pi}$ kaon candidate). In this case, all reconstructed GTK candidates are used for the distributions. Similarly as before, a vertex between each GTK candidate and one of the positive pions is found and D_{vtx}, ΔT_+ and ΔT_- distributions are prepared. They are then fitted by two gaussian functions (in the case of D_{vtx}, ΔT_-) and a constant (for ΔT_+) and the fit results are referred to as *pile-up* PDF distributions in the new STRAW-GTK matching algorithm.

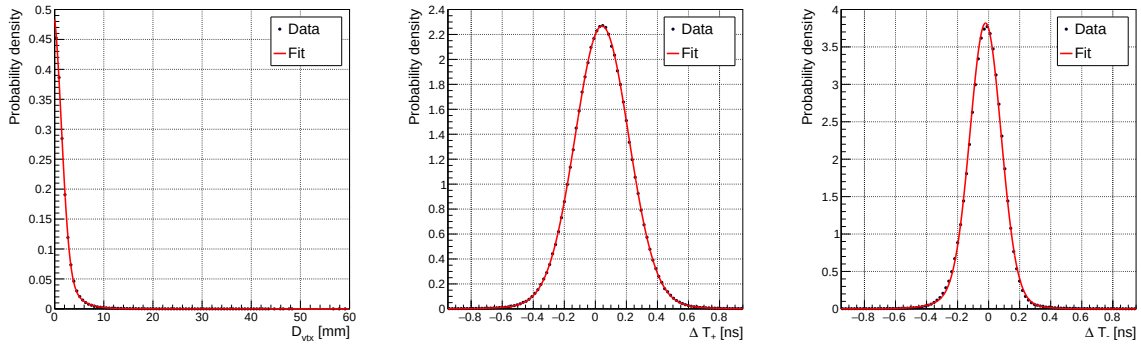

(a) *Kaon* PDF functions obtained from $K_{3\pi}$ events by fitting corresponding data distributions.

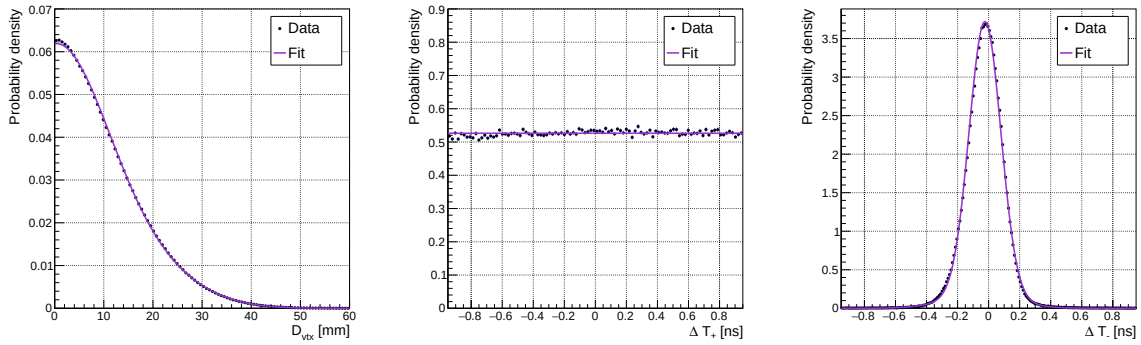

(b) *Pile-up* PDF functions obtained from $K_{3\pi}$ events with GTK candidates reconstructed from out-of-time hits by fitting corresponding data distributions.

Figure 4.2.3: PDF distributions of D_{vtx}, ΔT_+ and ΔT_-. Timing distributions are centered at zero before they are used in the STRAW–GTK matching algorithm, since additional fine time corrections are applied in the $K_{\pi\nu\nu}$ analysis to account for all residual time shifts between sub-detectors.

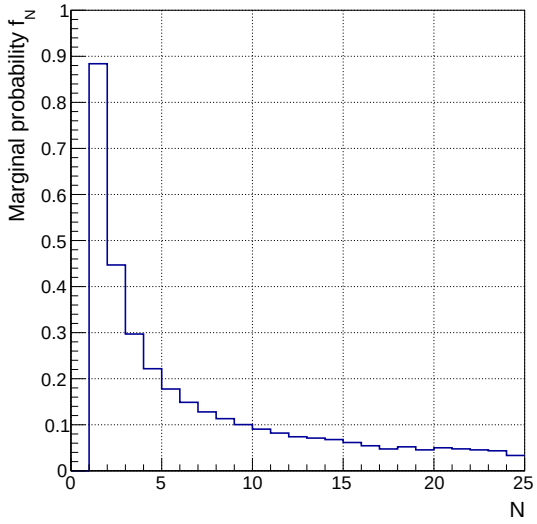

Figure 4.2.4: Distribution of marginal probability f_N for event categories denoted by N. Constant value of $f_N = 0.025$ is used for $N > 25$.

4.2.2.2 The Likelihood matching

The goal of the proposed algorithm is to match a single STRAW track with a GTK candidate based on their distance at the vertex and timing. Input to this algorithm includes the STRAW track, t_{RICH} and t_{KTAG} of the corresponding associations to the track and all GTK candidates in the event reconstructed by the standard GTK reconstruction algorithm with t_{KTAG} used as a reference time. The new matching algorithm is based on standard statistical classification methods involving Bayes' theorem and likelihood-ratio hypothesis testing [94].

First the event category N is determined by counting the number of GTK candidates of good quality which are compatible with the kaon beam ($\chi^2_{candidate}$ and χ^2_{event} conditions in Section 4.2) and are in time with the STRAW track ($|\Delta T_+| < 0.8$ ns). For evaluation of the χ^2_{event} condition, we use the run dependent mean beam parameters obtained with $K_{3\pi}$ events in each data run.

Given the category N, the probability f_N of reconstructing and randomly selecting the correct GTK candidate in an event with N good GTK candidates in time with the track is obtained from Figure 4.2.4. For each pair of track-GTK candidates, a vertex is found using the algorithm described in subsection 4.2.2 and the distance between the track and the GTK candidate in the vertex plane D_{vtx} is computed. Therefore, each track-GTK candidate pair is characterized by a set of values $\gamma = \{D_{vtx}, \Delta T_+, \Delta T_-\}$. The probability density functions of these variables for both *kaon* (H_0) and *pile-up* (H_1) hypotheses obtained in subsection 4.2.2.1 and shown in Figure 4.2.3 are normalized in the range (0, 60) mm, (−0.8, 0.8) ns and (−0.95, 0.95) ns, respectively.

Bayes' theorem is then used to compute the probability of the GTK candidate being the correct kaon candidate corresponding to the reference STRAW track given the observed γ:

$$P\left(H_0|\gamma\right) = \frac{P\left(\gamma|H_0\right) P\left(H_0\right)}{P\left(\gamma|H_0\right) P\left(H_0\right) + P\left(\gamma|H_1\right) P\left(H_1\right)}. \tag{4.2.6}$$

For a particular set of observed values γ, the probabilities $P(\gamma|H_0)$ and $P(\gamma|H_1)$ of obtaining γ under the two hypotheses can be replaced by likelihood functions:

- $\mathcal{L}\left(\gamma|H_0\right) = f^0_D(D_{vtx}) \cdot f^0_+(\Delta T_+) \cdot f^0_-(\Delta T_-)$,
- $\mathcal{L}\left(\gamma|H_1\right) = f^1_D(D_{vtx}) \cdot f^1_+(\Delta T_+) \cdot f^1_-(\Delta T_-)$,

where f^i_X is a probability density function of variable X in hypothesis H_i and D_{vtx}, ΔT_+ and ΔT_- form the set γ of measured values. The marginal probabilities are given by the event category:

- $P\left(H_0\right) = f_N$,

- $P(H_1) = (1 - f_N)$.

Therefore, the probability that the tested GTK candidate is in fact the correct one corresponding to the reference track is computed as follows:

$$P(H_0|\gamma) = \frac{\mathcal{L}(\gamma|H_0) \cdot f_N}{\mathcal{L}(\gamma|H_0) \cdot f_N + \mathcal{L}(\gamma|H_1) \cdot (1 - f_N)}. \tag{4.2.7}$$

All GTK candidates considered for the reference STRAW track are sorted by decreasing probability, with the best candidate being the one with the largest $P(H_0|\gamma)$. The best GTK candidate is matched to the reference track if the probability is greater than a predefined threshold.

However, in event categories with more than one GTK candidate considered in matching to the reference track (i.e. $N > 1$), the two best GTK candidates are compared using likelihood ratio test defined below, and thresholds for the likelihood ratio and the probability of the best GTK candidate are set. For these cases two hypotheses are tested with the best two GTK candidates, c_1 and c_2:

$H_A \equiv$ The best GTK candidate is the correct one and the second best GTK candidate is a pile-up candidate.

$H_B \equiv$ The second best GTK candidate is the correct one and the best GTK candidate is the pile-up kaon candidate.

The likelihood ratio test is therefore:

$$\Lambda(\Gamma) = \frac{\mathcal{L}(\Gamma|H_A)}{\mathcal{L}(\Gamma|H_B)}, \tag{4.2.8}$$

in which $\Gamma = \{\gamma_{c_1}, \gamma_{c_2}\}$ is a set of values obtained by two independent measurements for GTK candidates c_1 and c_2, respectively. Therefore both numerator and denominator can be replaced by a product of the previously calculated likelihoods:

$$\Lambda(\Gamma) = \frac{\mathcal{L}(\gamma_{c_1}|H_0) \cdot \mathcal{L}(\gamma_{c_2}|H_1)}{\mathcal{L}(\gamma_{c_2}|H_0) \cdot \mathcal{L}(\gamma_{c_1}|H_1)}, \tag{4.2.9}$$

or, via equation Equation (4.2.7), $\Lambda(\Gamma)$ can be expressed in terms of probabilities:

$$\Lambda(\Gamma) = \frac{P(H_0|\gamma_{c_1}) \cdot P(H_1|\gamma_{c_2})}{P(H_0|\gamma_{c_2}) \cdot P(H_1|\gamma_{c_1})}. \tag{4.2.10}$$

The last step is not necessary since all likelihoods are available, however it is taken in the matching algorithm for the reasons of convenience and consistency with the first event category ($N = 1$). For the same reasons, instead of using $\Lambda(\Gamma)$, which is unbounded from above and always equal to or greater than 1, a new function is defined with the same monotonicity and codomain equal to interval [0, 1):

$$\mathcal{F}(\Gamma) = \frac{\Lambda(\Gamma) - 1}{\Lambda(\Gamma)}. \tag{4.2.11}$$

The procedure of selecting the threshold values is described in subsection 4.2.2.3.

4.2.2.3 Scanning procedure

The goal of the new STRAW–GTK matching algorithm is to reduce the background contribution to the signal regions in the $K_{\pi\nu\nu}$ analysis (defined in subsection 4.1.7) from kinematic tails of $K_{2\pi}$ and $K_{\mu 2}$ events without degrading SES. For this purpose two variables of interest (defined in subsection 4.1.8) are identified: the total number of expected $K_{2\pi}$ and $K_{\mu 2}$ events in the $K_{\pi\nu\nu}$ signal regions, $N_{exp\,bg}$ (Equation (4.1.9)), and the number of $K_{2\pi}$ normalization events in the $K_{2\pi}$ peak region, $N_{2\pi N}$. Values obtained from the full $K_{\pi\nu\nu}$ analysis with the standard matching algorithm (subsection 4.2.1) are considered as the reference. The variables of interest are evaluated from the full $K_{\pi\nu\nu}$ analysis and two ratios are defined:

- $R_{bg} = \left(N_{exp\,bg}(likelihood)\right) / \left(N_{exp\,bg}(standard)\right)$,
- $R_{2\pi N} = \left(N_{2\pi N}(likelihood)\right) / \left(N_{2\pi N}(standard)\right)$.

Since both results are obtained from the same data sets and are used in ratios, no scaling or normalization is needed.

In the likelihood matching algorithm, the matching decision about the best GTK candidate is made in a different way for two event types:

- Events with a single good GTK candidate (event category $N = 1$): a cut on the probability $P\left(H_0|\gamma\right)$ (Equation (4.2.7)) of the best GTK candidate is made.
- Events with at least two good GTK candidates (event categories $N > 1$): a cut on the function of the likelihood ratio of the two best GTK candidates, $\mathcal{F}\left(\Gamma\right)$ (Equation (4.2.11)), and on the probability $P\left(H_0|\gamma\right)$ of the best GTK candidate is made.

The cut values are determined by a scanning procedure described in the following text. A one-dimensional histogram of the probability $P\left(H_0|\gamma\right)$ of the best GTK candidate and two-dimensional histogram of $\mathcal{F}\left(\Gamma\right)$ as a function of the probability $P\left(H_0|\gamma\right)$ of the best GTK candidate are saved for events of the first and the second type, respectively (Figures 4.2.5 and 4.2.6). The histograms are saved only for events which pass the corresponding event selection before application of the matching quality cuts, and by the full region definition (subsection 4.1.7) fall into the $K_{2\pi}$ peak region ($K_{\pi\nu\nu}$, $K_{2\pi}$ and $K_{2\pi}$ normalization selections), $K_{\mu 2}$ peak region ($K_{\pi\nu\nu}$ and $K_{\mu 2}$ selections) or into the $K_{\pi\nu\nu}$ signal regions ($K_{2\pi}$ and $K_{\mu 2}$ selections). In every region, separate histograms are made for each momentum bin.

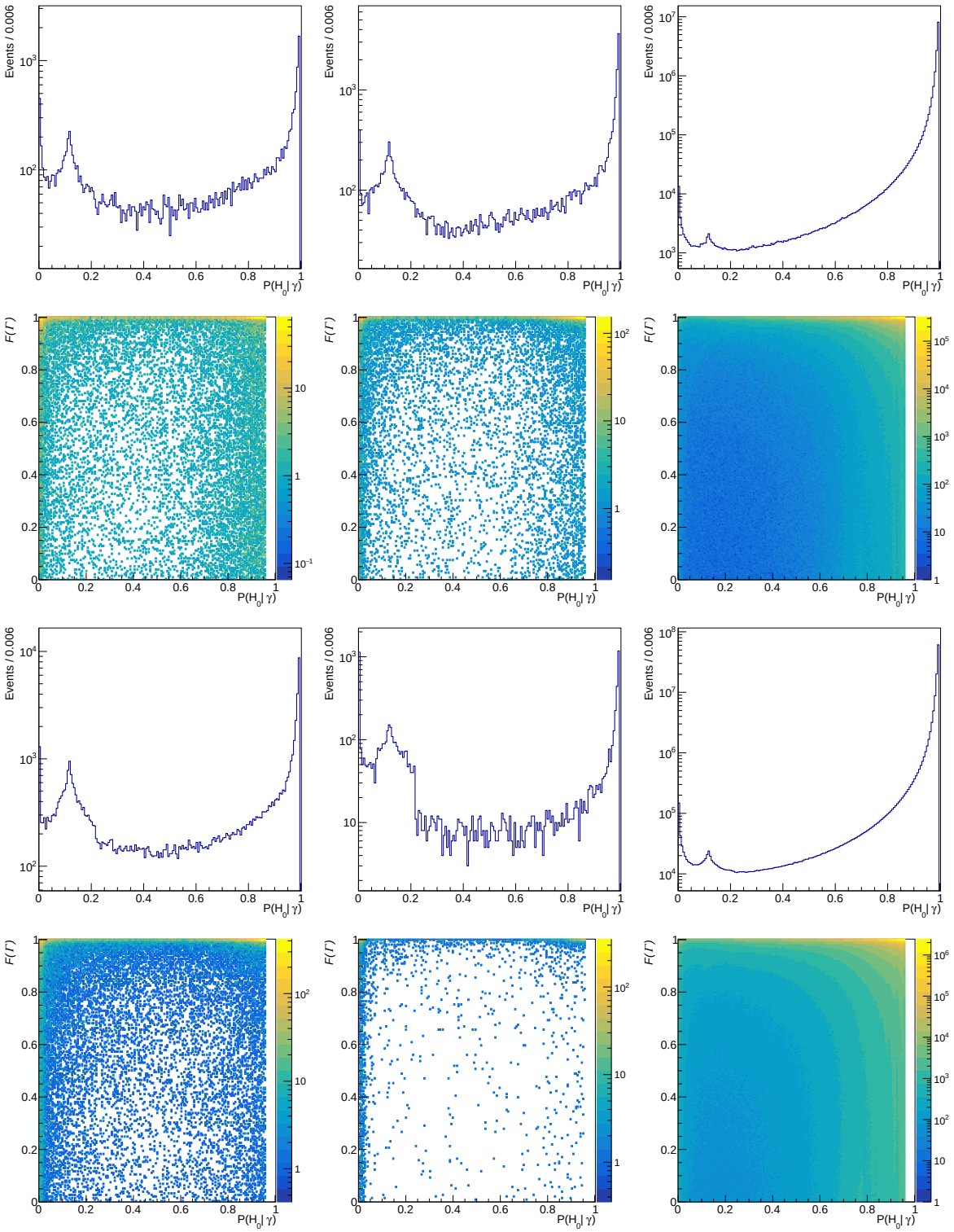

(a) Signal region 1. (b) Signal region 2. (c) Peak regions.

Figure 4.2.5: $K_{2\pi}$ (first two rows) and $K_{\mu 2}$ (second two rows) distributions of probability $P(H_0|\gamma)$ of the best GTK candidate for events in category $N = 1$ (top), and distributions of $\mathcal{F}(\Gamma)$ as a function of $P(H_0|\gamma)$ (bottom) for events in categories $N > 1$ in the $K_{\pi\nu\nu}$ signal regions (a, b) and in the peak regions (c). Distributions are shown for events in all momentum bins combined. Discontinuity in $K_{\mu 2}$ plot (b)-top is addressed in Appendix G.

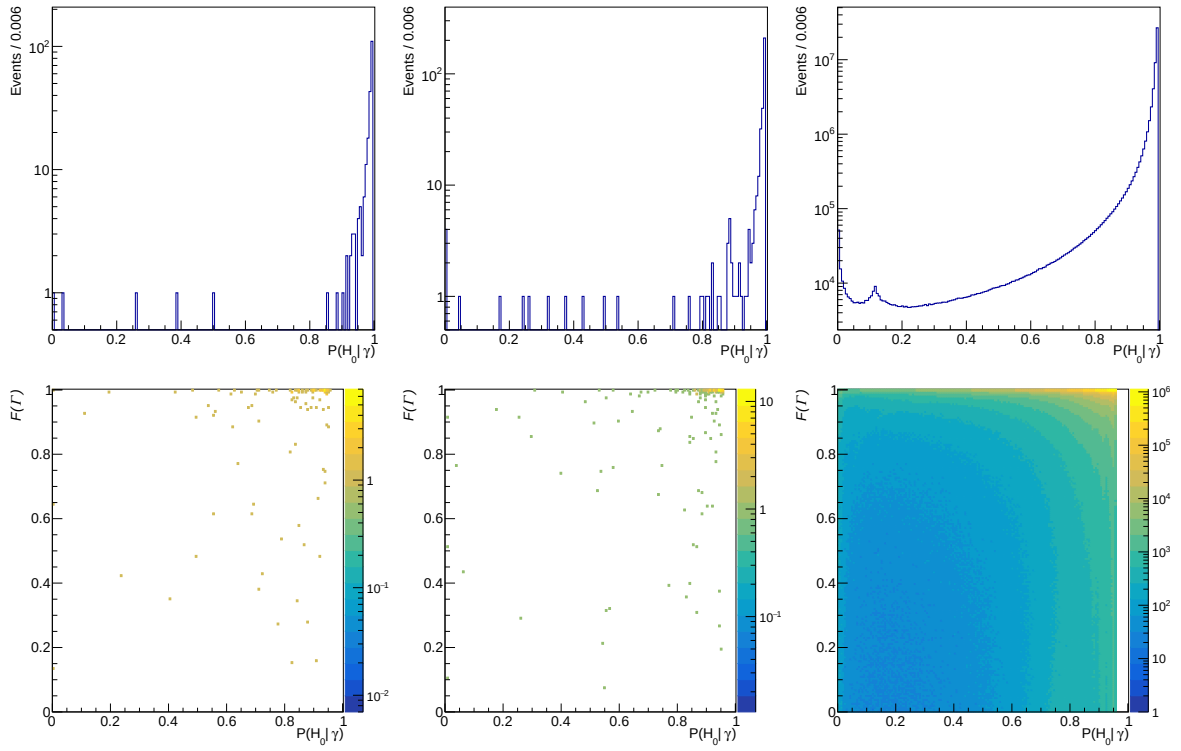

(a) $K_{2\pi}$ peak region. (b) $K_{\mu 2}$ peak region. (c) $K_{2\pi}$ peak region.

Figure 4.2.6: Distributions of probability $P(H_0|\gamma)$ of the best GTK candidate for events in category $N = 1$ (top), and two-dimensional distributions of $\mathcal{F}(\Gamma)$ as a function of $P(H_0|\gamma)$ (bottom) for $K_{\pi\nu\nu}$ events in the $K_{2\pi}$ peak region (a) and $K_{\mu 2}$ peak region (b), and for $K_{2\pi}$ normalization events in the $K_{2\pi}$ peak region (c). Final cuts on matching quality have not been applied. Distributions are shown for events in all momentum bins combined.

Each tested set of three threshold values is simultaneously applied on all saved histograms and the events remaining above the thresholds are counted for each decay in every region and momentum bin. Then the variables of interest are evaluated and the ratios R_{bg} and $R_{2\pi N}$ are computed (Figure 4.2.7). Sets of thresholds with best performance given by $R_{bg} \leq 1$ and $R_{2\pi N} \geq 1$ are selected and summarized in Table 4.2.2.

Alternatively, a similar scan can be performed to select a set of threshold values optimized for single-track analyses other than the $K_{\pi\nu\nu}$. In this case, only events selected by the $K_{2\pi}$ and $K_{\mu 2}$ event selections are needed. Variables of interest in this case would be the number of events in the peak and tail regions.

	$N = 1$	$N > 1$	
	$P\left(H_0\middle\vert\gamma\right)$	$\mathcal{F}\left(\Gamma\right)$	$P\left(H_0\middle\vert\gamma\right)$
SET 1	0.894	0.840	0.636
SET 2	0.952	0.360	0.660
SET 3	0.946	0.396	0.752
SET 4	0.936	0.810	0.714
SET 5	0.930	0.906	0.654

Table 4.2.2: Five sets of threshold values selected by the scanning procedure defining final quality cuts in the new matching algorithm.

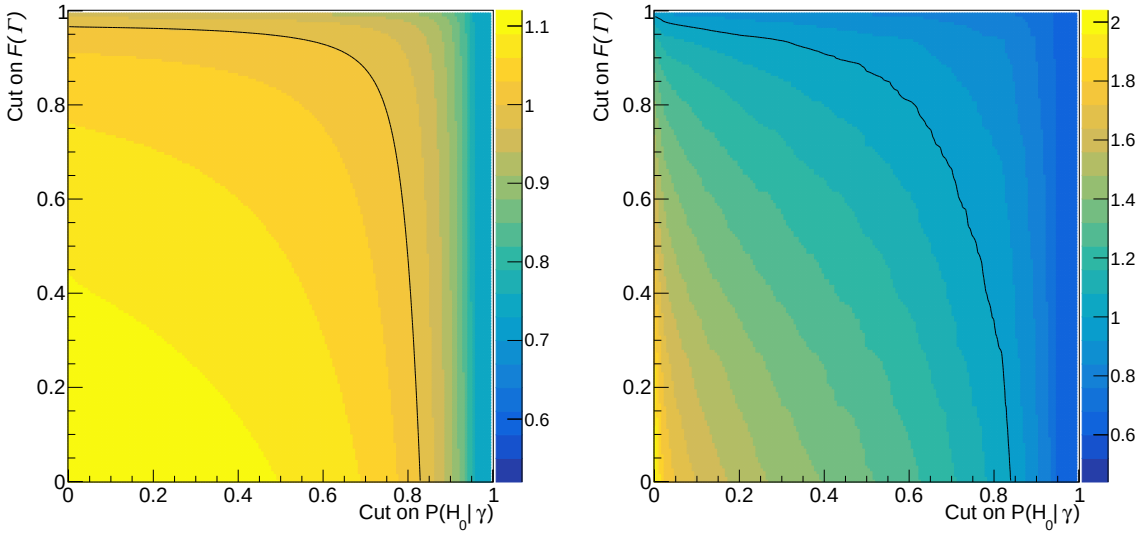

(a) Ratio $R_{2\pi N}$.

(b) Ratio R_{bg}.

Figure 4.2.7: Ratios of $K_{2\pi}$ events passing the normalization selection (a) and the total expected background (b). Number of events in numerator of each ratio at a given point is computed as a sum of events in category $N = 1$ with $P\left(H_0\middle\vert\gamma\right) > 0.93$, and events in categories $N > 1$ remaining after applying cuts determined by X and Y coordinates of the considered point. Desired values of $R_{2\pi N}$ (R_{bg}) are above (below) 1, indicated by black contours.

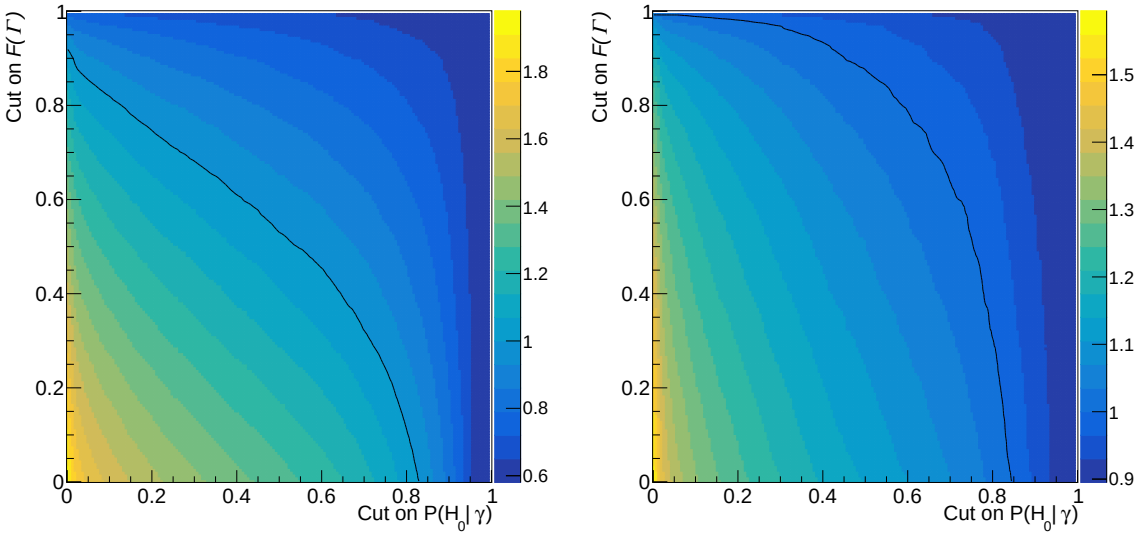

(a) $K_{2\pi}$ tails ratio in signal region 1.

(b) $K_{2\pi}$ tails ratio in signal region 2.

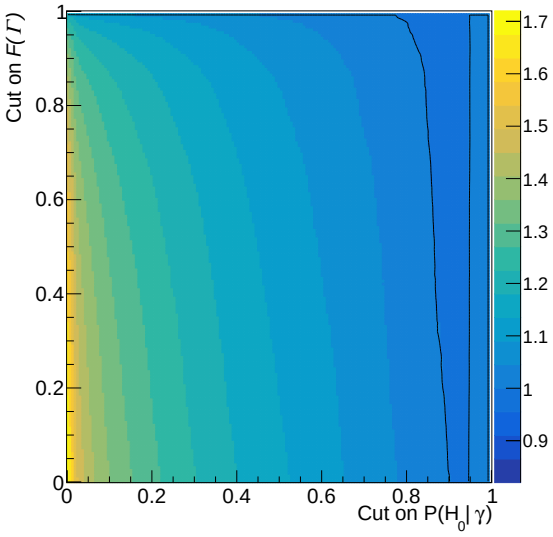

(c) $K_{\mu 2}$ tails ratio in signal region 1.

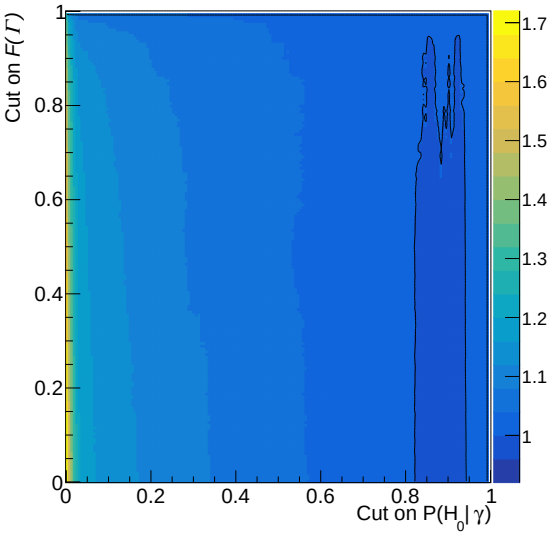

(d) $K_{\mu 2}$ tails ratio in signal region 2.

Figure 4.2.8: Ratio of $K_{2\pi}$ and $K_{\mu 2}$ kinematic tails computed with likelihood (numerator) and standard (denominator) matching algorithm. The numerator of the ratio at a given point is computed from events in category $N = 1$ that already passed $P(H_0|\gamma) > 0.93$ cut, and events in categories $N > 1$ remaining after applying cuts determined by X and Y coordinates of the considered point. Desired values of the ratio are below 1, indicated by black contours.

4.2.3 New algorithm performance for $K_{3\pi}$ events

Performance of the new matching algorithm is tested with $K_{3\pi}$ events selected from 2017A data set with the use of the `K3piStrictSelection`. For each selected event, a $K_{3\pi}$ kaon candidate is built from the three pion candidates. The standard GTK reconstruction algorithm with the reference time of the KTAG candidate asso-

ciated to the $K_{3\pi}$ kaon candidate is used to reconstruct GTK candidates in the $K_{3\pi}$ event. The correct GTK candidate is then selected by $K_{3\pi}$– GTK matching algorithm described in subsection 4.2.2.1. One of the two positive pions is randomly chosen and used as a reference track in the tested STRAW–GTK matching algorithm. Three variables are defined to evaluate the performance by comparing the GTK candidates selected by STRAW–GTK and $K_{3\pi}$– GTK matching algorithms:

A $\equiv$ Fraction of $K_{3\pi}$ events in which the correct GTK candidate is present and is also selected by the STRAW–GTK matching algorithm.

B $\equiv$ Fraction of $K_{3\pi}$ events in which the correct GTK candidate is present, but different GTK candidate is selected by the STRAW–GTK matching algorithm.

C $\equiv$ Fraction of $K_{3\pi}$ events in which a GTK candidate reconstructed from out-of-time hits is selected by the STRAW–GTK matching algorithm.

First two variables are used to assess the performance of the matching algorithm on events in which the correct GTK candidate is reconstructed. They estimate the rates of good match and mismatch, respectively. In the rest of the events, no GTK candidate is selected by the STRAW-GTK matching algorithm.

To evaluate the variable C, the GTK reconstruction algorithm is used to reconstruct GTK candidates from hits 15 ns away from the reference time. This is done to ensure that the correct GTK candidate is not reconstructed. Therefore, if a GTK candidate is selected by the STRAW-GTK matching algorithm, the match is fake. Variable C is used to estimate the rate of successful matching by the STRAW-GTK algorithm in events where the correct GTK candidate is not present. Therefore, it also gives an insight into the behavior of the matching algorithm when dealing with upstream events (Appendix A).

The overall goal is to keep the number of events with incorrectly selected GTK candidate (B and C) as low as possible while retaining the acceptance (given by the sum of events of types A and B) and high good-match rate (A). In the $K_{\pi\nu\nu}$ analysis, the incorrect matching between STRAW and GTK candidates leads to a wrong value of the reconstructed m^2_{miss}. This, in turn, leads to an enlarged background event rate in the signal regions and thus decreases the statistical power of the $K_{\pi\nu\nu}$ branching fraction measurement. Additionally, the acceptance of the matching algorithm is reflected in the overall acceptance of the $K_{\pi\nu\nu}$ event selection.

	A [%]	B [%]	C [%]
Standard	73.47	1.41	2.81
SET 1	79.20	0.44	3.36
SET 2	75.42	1.43	2.61
SET 3	74.19	1.12	2.52
SET 4	74.86	0.45	2.68
SET 5	75.45	0.28	2.81

Table 4.2.3: Comparison of the performance of the new and standard STRAW–GTK matching algorithms evaluated on the same sample of $K_{3\pi}$ events.

Comparison with the standard matching algorithm in Table 4.2.3 shows that the new algorithm can lower the mismatch rate (B) by up to 80 % (relative) and improve the good-match rate (A) by 1 % to 8 % at the same time. The rejection power of events in which the matched GTK candidate corresponds to a pile-up particle is estimated by the column C. The performance varies between different sets of cut values; from 20 % degradation in SET 1 to 10 % improvement in SET 3 with respect to the standard algorithm.

Since the $K_{\pi\nu\nu}$ analysis suffers from low signal acceptance due to strict selection criteria, a matching algorithm with an improved acceptance (and low mismatch rate) is desirable. As expected and also indicated by Table 4.2.3, a significant increase in good-match rate (A) in SET 1 results in substantially worsened fake-match rate (C). This could be an issue in the $K_{\pi\nu\nu}$ analysis where the fake-match rate directly affects the level of upstream background. Therefore, the performance of the new matching algorithm with various sets of final cut values needs to be carefully evaluated in connection to the upstream background. However, in future data taking at NA62, multiple changes in the experimental setup are planned, aiming at decreasing the upstream background level. These include installation of the fourth GTK station[3] and a new upstream veto counter [95]. Moreover, several passive components shielding the decay region from upstream events have already been installed in the GTK area and will remain in use during the next run. Thanks to the improved performance, the new matching algorithm is intended to replace the currently used one in the main analysis of future data.

[3]This will change the distributions of D_{vtx}, ΔT_+ and ΔT_- used in the likelihood matching algorithm. Consequently, a new set of threshold values defining the final matching cuts will have to be determined.

4.3 Results

Performances of the standard and likelihood matching algorithms in the $K_{\pi\nu\nu}$ analysis, discussed in this section, are compared via the m^2_{miss} distribution and quantities defined in subsection 4.1.8.

Four event selections described in subsections 4.1.3 to 4.1.6 with either the standard or the likelihood matching algorithm are applied on the full 2017 data set and the relevant Monte Carlo samples. The plots obtained using the likelihood matching were produced with the final quality cuts given by the SET 5 (see Table 4.2.2). Uncorrelated errors between the results obtained with the standard and likelihood matching algorithms are negligible and are not shown.

Figure 4.3.1 shows a comparison of the resulting m^2_{miss} distributions of $K_{2\pi}$ and $K_{\mu 2}$ data events obtained by applying the $K_{2\pi}$ and $K_{\mu 2}$ event selections with the standard or likelihood matching algorithms. Numbers of events in peak regions differ by less than 0.6 % in both $K_{2\pi}$ and $K_{\mu 2}$. Usage of the likelihood matching algorithm in the event selections results in narrower distributions, which is clearly visible in the areas between the peak and nearby signal regions. The most noticeable improvement can be seen in signal region 1 of the $K_{2\pi}$ distribution. This is reflected in the lower tail fraction (Table 4.3.1).

	$f^{\rho}_{kin,2\pi}$ [$\times 10^{-4}$]		$f^{\rho}_{kin,\mu\nu}$ [$\times 10^{-4}$]		$N_{exp\ bg}$
	SR1	SR2	SR1	SR2	
Standard	5.502	6.443	2.015	0.216	0.442
SET 1	4.533	6.651	2.265	0.230	0.457
SET 2	5.378	6.538	2.071	0.218	0.465
SET 3	4.946	6.375	2.034	0.216	0.434
SET 4	4.120	6.207	2.065	0.220	0.405
SET 5	3.957	6.206	2.099	0.222	0.405

Table 4.3.1: Summary of the obtained results: $K_{2\pi}$ and $K_{\mu 2}$ tail fractions in the $K_{\pi\nu\nu}$ signal regions (summed over momentum bins) and the total number of expected background events from kinematic tails of $K_{2\pi}$ and $K_{\mu 2}$ m^2_{miss} distributions in both signal regions after the $K_{\pi\nu\nu}$ selection.

Comparison of the $K_{2\pi}$ and $K_{\mu 2}$ m^2_{miss} distributions for data and Monte Carlo events is displayed in Figure 4.3.2. A discrepancy in the widths of data and Monte Carlo distributions is caused by the missing simulation of pile-up in the downstream sub-detectors. This leads to even narrower Monte Carlo distributions when the likelihood matching is used in the event selections.

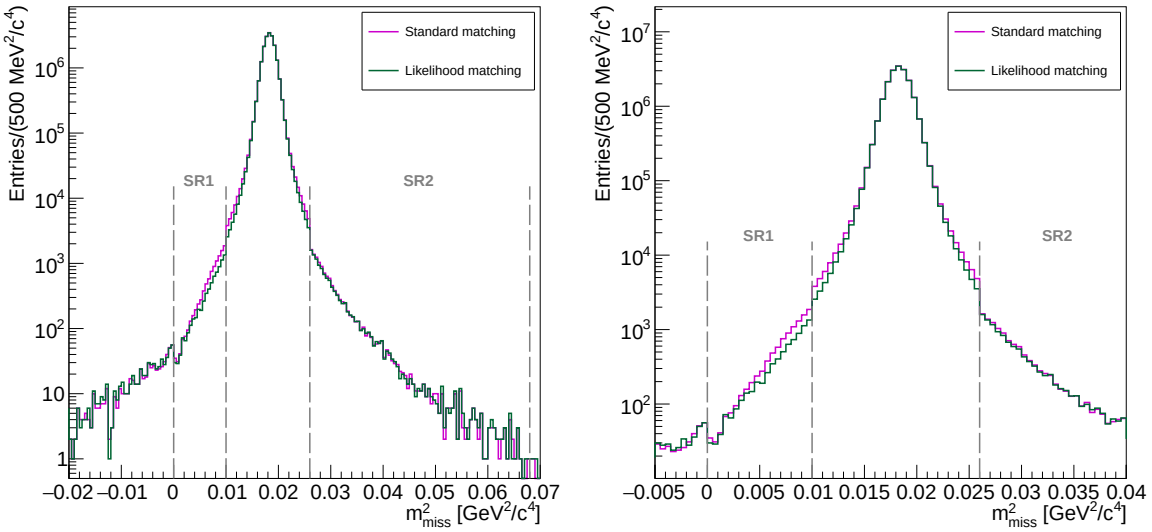

(a) Data events passing the $K_{2\pi}$ selection for kinematic tails measurement.

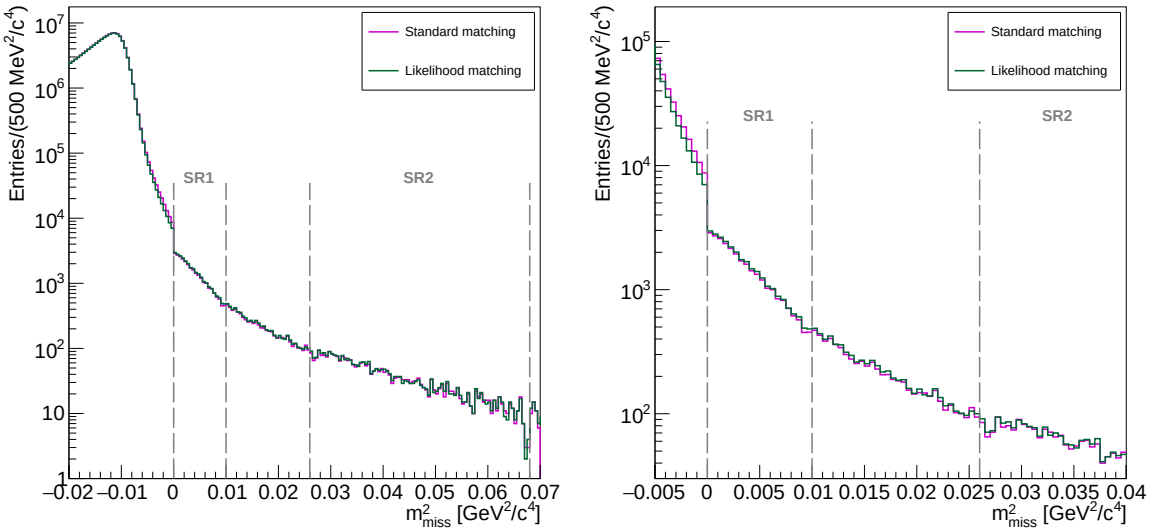

(b) Data events passing the $K_{\mu 2}$ selection for kinematic tails measurement.

Figure 4.3.1: m^2_{miss} distribution of $K_{2\pi}$ (a) and $K_{\mu 2}$ (b) events obtained from the $K_{2\pi}$ and $K_{\mu 2}$ event selections with the standard (magenta) and likelihood (green) matching algorithms, measured on the 2017 data sample. Only events occurring in one of the regions defined by all three m^2_{miss} variables (subsection 4.1.7) contribute to the distribution. The steps at signal region boundaries (shown as grey dashed lines), clearly visible in the zoomed plots on the right, are a consequence of extra restrictions ($m^2_{miss}(RICH)$, $m^2_{miss}(beam)$) imposed on events in signal regions. The final cuts of the likelihood matching algorithm are defined by threshold values of SET 5.

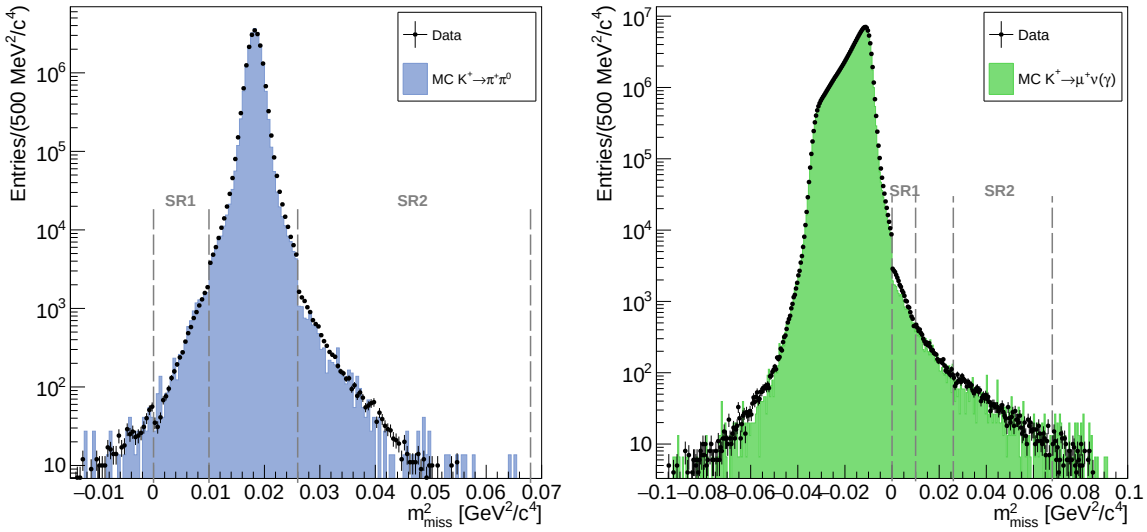

(a) Standard matching.

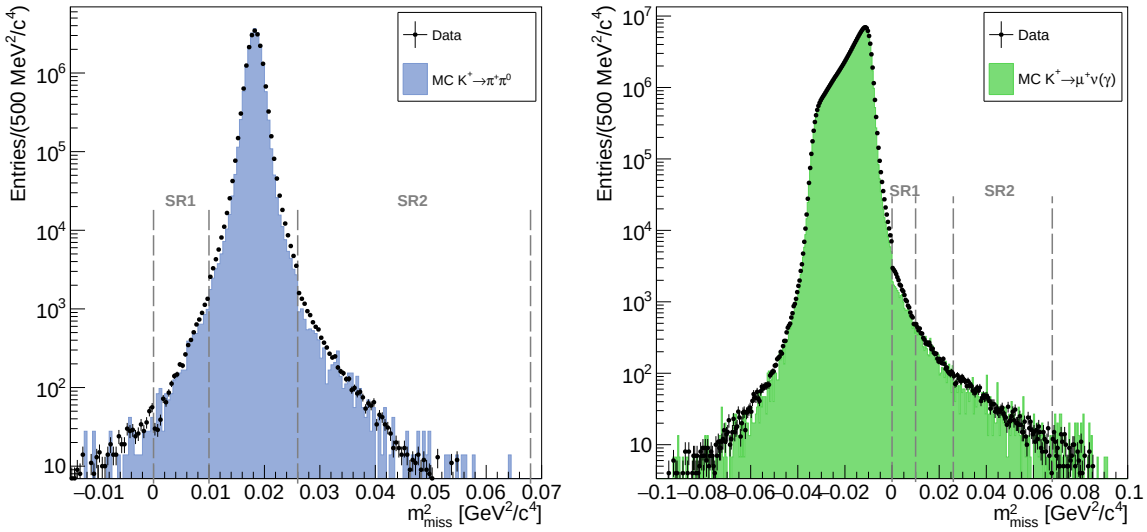

(b) Likelihood matching with threshold values of SET 5.

Figure 4.3.2: m^2_{miss} distributions of events selected by the $K_{2\pi}$ and $K_{\mu 2}$ event selections with the standard (a) and the likelihood (b) matching algorithm. Distributions obtained from the 2017 data set are compared with the corresponding distributions of Monte Carlo samples. Full region definition is applied resulting in steps in the m^2_{miss} distributions. Limits of signal regions are shown as grey dashed lines. The final cuts of the likelihood matching algorithm are defined by threshold values of SET 5.

The $K_{2\pi}$ and $K_{\mu 2}$ tail fractions measured on the full 2017 data set in four momentum bins are shown in Figures 4.3.3 and 4.3.4 and quantified in Table 4.3.1. Comparison of the $K_{2\pi}$ tail fraction in signal region 1, obtained with the standard and likelihood matching algorithms, reveals an improvement of up to 30 % in all momentum bins and a slight change in momentum dependency. Less dramatic im-

provement (up to 4 %) is observed for the $K_{2\pi}$ tail fraction in signal region 2 for three of the selected sets of thresholds for the likelihood matching algorithm. Up to 12 % (6 %) worsening is seen for the $K_{\mu 2}$ tail fraction in the signal region 1 (2), mainly in the high momentum bin. Nevertheless, lower $K_{2\pi}$ tail fraction in signal region 1 is enough to produce smaller (by more than 8 % at the best) total expected background for three of the five proposed sets. It is worth noticing that the $K_{\mu 2}$ tail fraction in the signal region 2 is by one order of magnitude smaller than the rest, which is expected as the signal region 2 is far away from the $K_{\mu 2}$ m^2_{miss} peak.

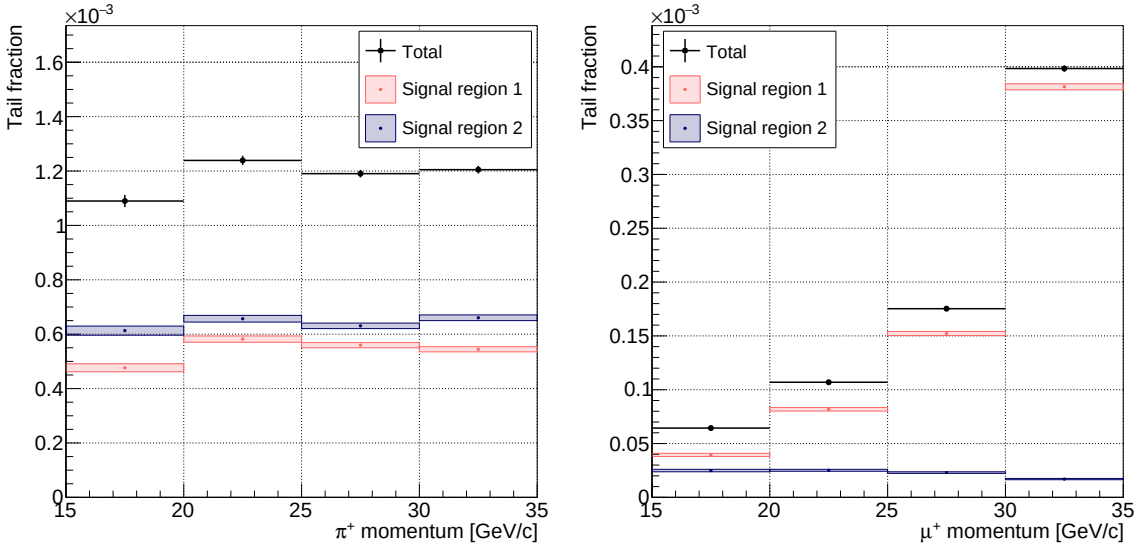

(a) Standard matching.

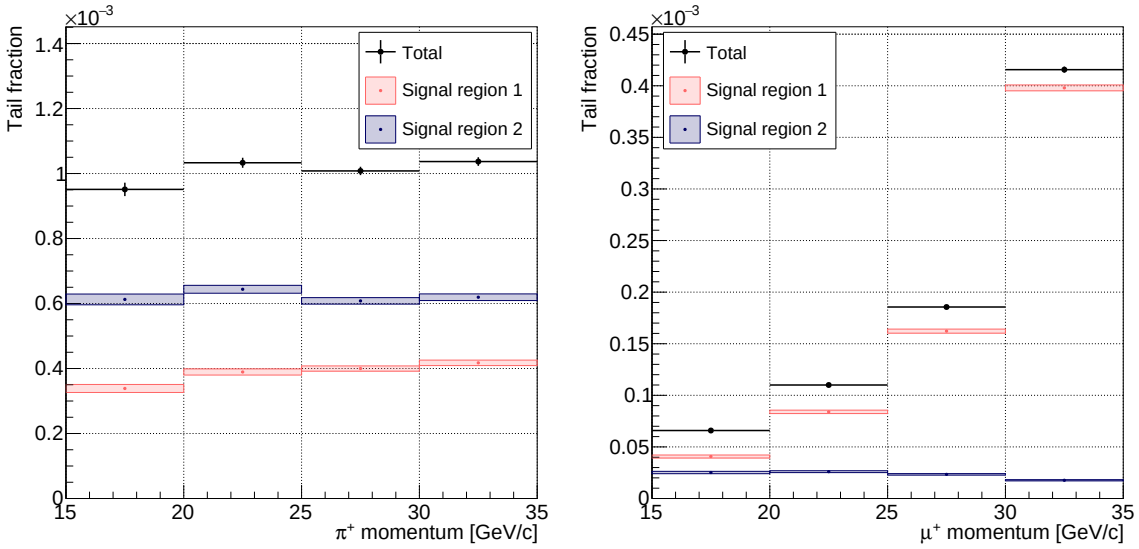

(b) Likelihood matching with threshold values of SET 5.

Figure 4.3.3: $K_{2\pi}$ and $K_{\mu 2}$ tail fractions in both $K_{\pi\nu\nu}$ signal regions measured with the standard (a) and the likelihood (b) matching algorithms on the full 2017 data set. Tail fractions are evaluated in four bins of the π^+ or μ^+ track momentum.

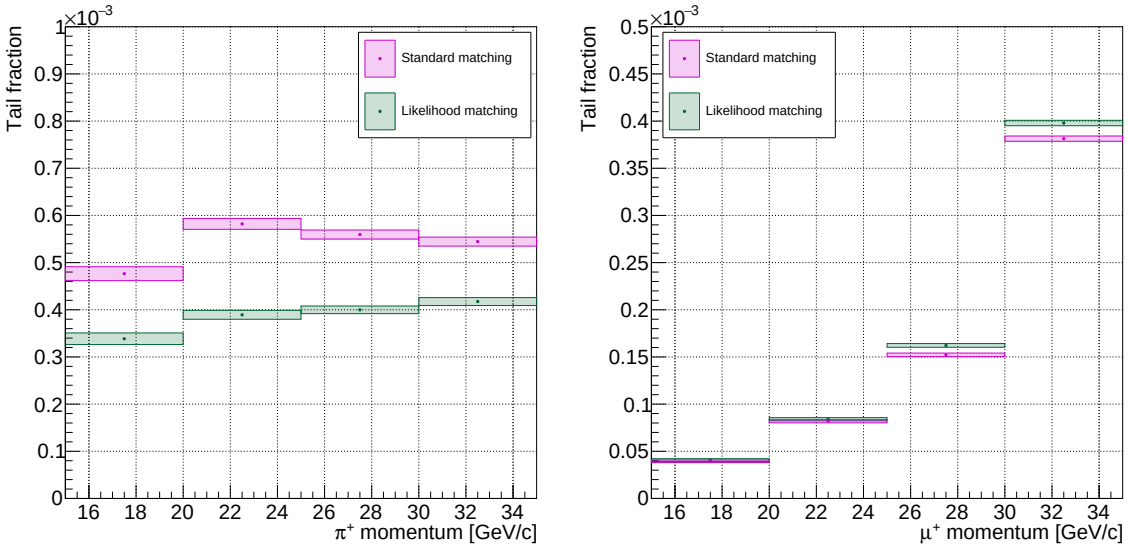

(a) Signal region 1.

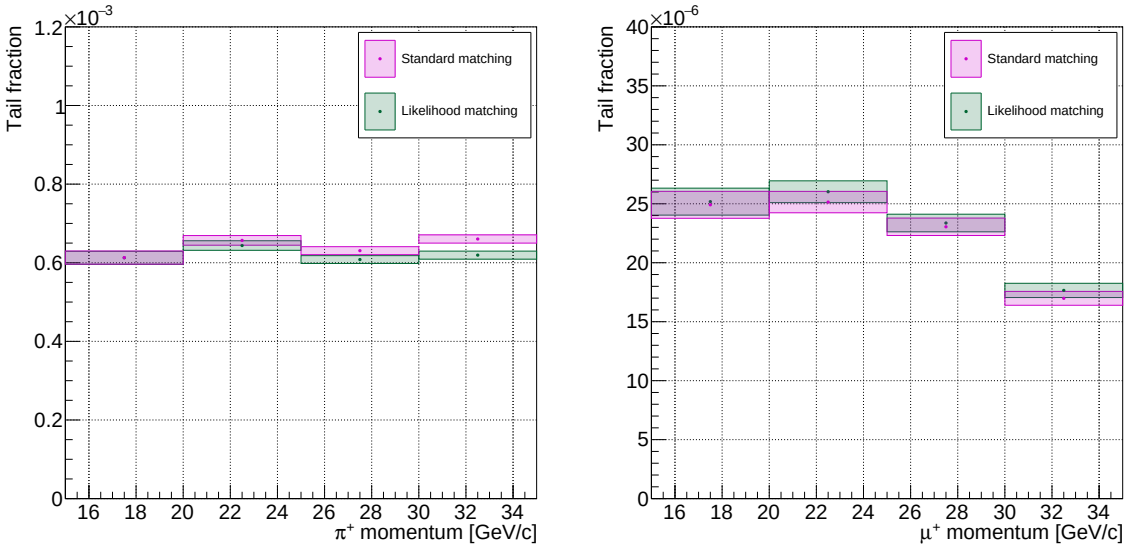

(b) Signal region 2.

Figure 4.3.4: Comparison of the $K_{2\pi}$ (left) and $K_{\mu 2}$ (right) tail fractions in the signal region 1 (a) and signal region 2 (b) measured on the full 2017 data set with the standard (magenta) and the likelihood (green) matching algorithms. The final cuts of the likelihood matching algorithm are defined by threshold values of SET 5.

The acceptance of the $K_{\pi\nu\nu}$ event selection with the likelihood matching algorithm, shown in Figure 4.3.5a as a function of the generated m^2_{miss}, varies for the proposed sets of threshold values between up to 1.2 % improvement and about 2.5 % loss with respect to the case with the standard matching. Similar results (up to 1.9 % improvement and less than 1.7 % loss) are observed for the acceptance of the $K_{2\pi}$ normalization selection (see Table 4.3.2). Both acceptances are used in evaluation of the single event sensitivity and the expected number of $K_{\pi\nu\nu}$ events to be observed in the $K_{\pi\nu\nu}$ signal regions combined, both varying between up to 1 % worsening

and up to 3 % improvement. The expected signal-over-background ratio, shown in the last column of Table 4.3.2, is higher by up to 8.4 %. The ratio is also plotted in Figure 4.3.5b as a function of the reconstructed m^2_{miss}, revealing that the major part of the improvement comes from the signal region 1 for m^2_{miss} in range (0.005, 0.01) GeV$^2/c^4$ dominated by the left tail of the $K_{2\pi}$ distribution. The plot is limited to the range of m^2_{miss} with non-negligible contribution of the $K_{2\pi}$ and $K_{\mu 2}$ backgrounds investigated in this thesis.

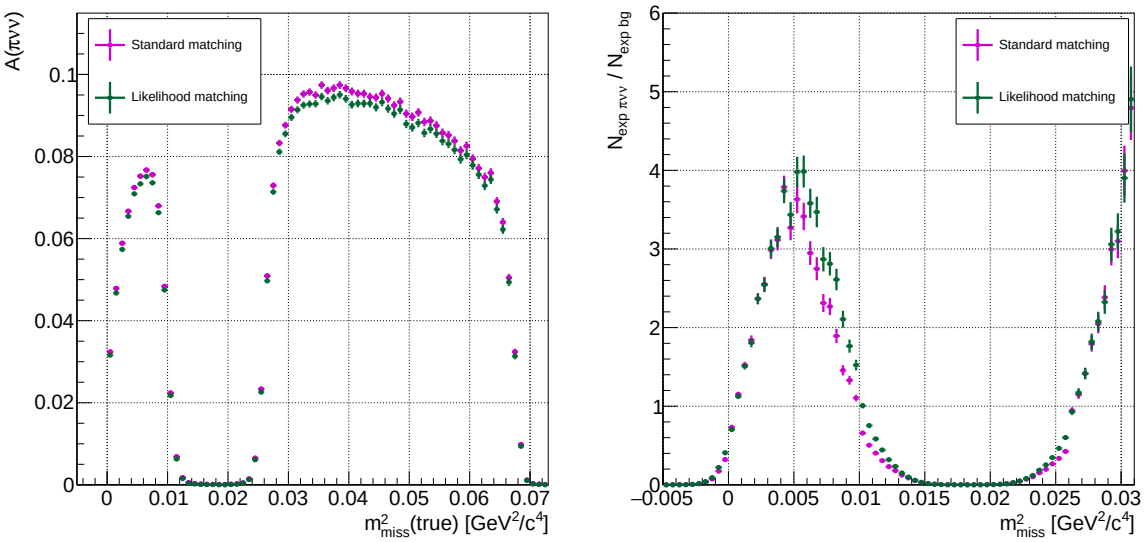

(a) (b)

Figure 4.3.5: (a) Comparison of the $K_{\pi\nu\nu}$ event selection acceptances measured on the $K_{\pi\nu\nu}$ Monte Carlo events with the standard (magenta) and the likelihood (green) matching algorithms. The acceptances are shown as functions of the $K_{\pi\nu\nu}$ event m^2_{miss} computed from the generated (true) momenta of events passing the $K_{\pi\nu\nu}$ selection and reconstructed in one of the signal regions. (b) Ratio of the scaled (using SES) m^2_{miss} distribution of the $K_{\pi\nu\nu}$ Monte Carlo events passing the $K_{\pi\nu\nu}$ selection to the combination of m^2_{miss} distributions of data events passing $K_{2\pi}$ and $K_{\mu 2}$ selections. Distributions in the denominator are normalized in each of the four momentum bins to have the same peak integrals as the similar $K_{\pi\nu\nu}$– selected data distribution. Only events reconstructed in one of the nine regions defined in Table 4.1.15 contribute to the ratio. Full region definitions are used in both figures. The final cuts of the likelihood matching algorithm are defined by threshold values of SET 5.

	$A(\pi\nu\nu)$ [%]	$A(2\pi N)$ [%]	SES [$\times 10^{-10}$]	$N_{exp\ \pi\nu\nu}$	$N_{exp\ \pi\nu\nu}/N_{exp\ bg}$
Standard	2.454	6.563	0.389	2.157	4.881
SET 1	2.481	6.687	0.379	2.218	4.853
SET 2	2.484	6.648	0.382	2.200	4.728
SET 3	2.429	6.507	0.388	2.164	4.988
SET 4	2.400	6.461	0.392	2.143	5.291
SET 5	2.392	6.453	0.393	2.139	5.282

Table 4.3.2: Summary of the obtained results: acceptances of the $K_{\pi\nu\nu}$ and $K_{2\pi}$ normalization selections computed from the $K_{\pi\nu\nu}$ and $K_{2\pi}$ Monte Carlo samples, respectively; single event sensitivity (SES) measured on the full 2017 data set; expectation for the number of $K_{\pi\nu\nu}$ events in both signal regions combined, computed from SES and the Standard Model branching fraction of $K^+ \to \pi^+\nu\overline{\nu}$ (Table 1.2.1). The expected signal-over-background ratio (accounting only for the $K_{\mu 2}(\gamma)$ and $K_{2\pi}$ background) in the last column is computed from unrounded numbers.

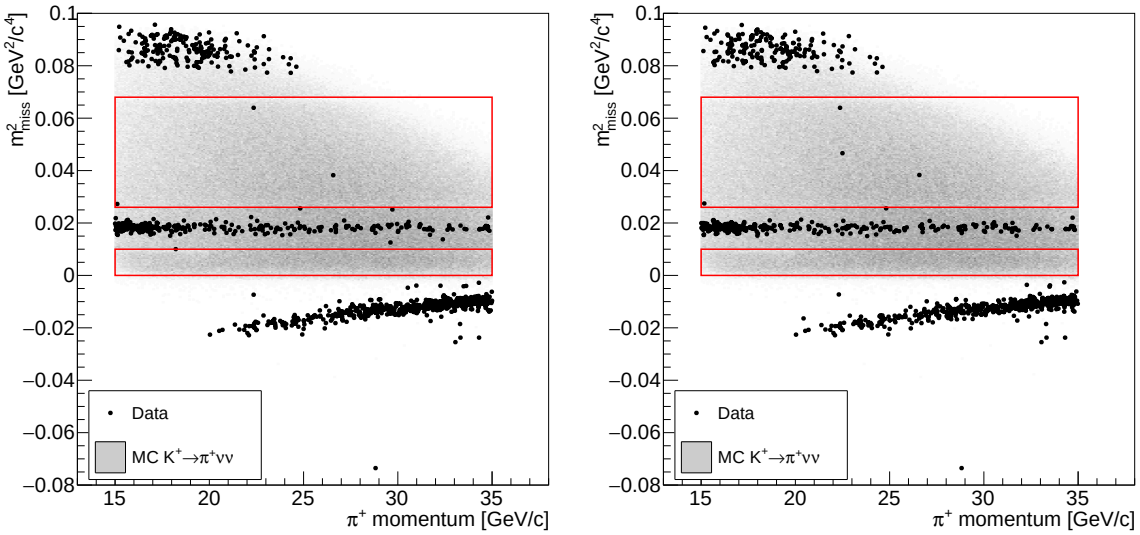

(a) Standard matching.

(b) Likelihood matching.

Figure 4.3.6: m^2_{miss} distribution of events passing the $K_{\pi\nu\nu}$ event selection with the standard (a) and the likelihood (b) matching algorithms, plotted as a function of the π^+ track momentum (to be compared with Figure 23 in [81]). Grey area corresponds to the $K_{\pi\nu\nu}$ Monte Carlo events, black dots are 2017 data events. Two red rectangles correspond to the $K_{\pi\nu\nu}$ signal regions. Only events reconstructed in one of the nine regions (subsection 4.1.7) with π^+ momentum in range (15, 35) GeV/c are shown. The final cuts of the likelihood matching algorithm are defined by threshold values of SET 5.

Figure 4.3.6 shows the 2017 data and $K_{\pi\nu\nu}$ Monte Carlo events passing the $K_{\pi\nu\nu}$

event selection. Three peak regions, corresponding to the three most abundant kaon decays, are recognized in data: $K_{\mu 2}$ at negative m^2_{miss}, $K_{2\pi}$ at $m^2(\pi^0)$ between the $K_{\pi\nu\nu}$ signal regions, and $K_{3\pi}$ at the top. The momentum dependence of the $K_{\mu 2}$ m^2_{miss} evaluated under the π^+ mass hypothesis causes increase of the $K_{\mu 2}$ tail fraction for higher track momenta, observed in Figure 4.3.3. Data points in the signal regions correspond to the observed $K_{\pi\nu\nu}$ event candidates and are summarized in Table 4.3.3. Zero $K_{\pi\nu\nu}$ event candidates are observed in the signal region 1, while three or four are observed in signal region 2, depending on the set of threshold values used in the likelihood matching algorithm. The $K_{\pi\nu\nu}$ event selection with the standard matching algorithm results in three $K_{\pi\nu\nu}$ event candidates, two of which (and only these two) are also observed by the main $K_{\pi\nu\nu}$ analysis [81]. Investigation of the third event (marked as N° 1) revealed that it was rejected by an older version of the `StrawSegmentAlgorithm` tool used in the main $K_{\pi\nu\nu}$ analysis.

Same three $K_{\pi\nu\nu}$ candidate events are observed also in cases with the likelihood matching algorithm used in the $K_{\pi\nu\nu}$ event selection, with an additional one selected with four out of the five proposed sets of final matching cuts.

N°	m^2_{miss} [GeV^2/c^4]	$p(\pi^+)$ [GeV/c]
1.	0.027	15.18
2.	0.064	22.39
3.	0.047	22.46
4.	0.038	26.53

	N observed	N°
Standard	3	1, 2, 4
SET 1	4	1, 2, 3, 4
SET 2	3	1, 2, 4
SET 3	4	1, 2, 3, 4
SET 4	4	1, 2, 3, 4
SET 5	4	1, 2, 3, 4

Table 4.3.3: Summary of the $K_{\pi\nu\nu}$ event candidates observed in the 2017 data set. Table on the right shows which candidates are selected by the $K_{\pi\nu\nu}$ event selection with the standard or likelihood matching algorithms.

The $K_{\pi\nu\nu}$ candidate events can be seen also in Figure 4.3.7 together with the expected signal and background contributions to the $K_{\pi\nu\nu}$ signal regions. Several components of the background not investigated in this work are missing, which causes the signal-over-background ratios shown in Table 4.3.2 to be larger than those observed in the main $K_{\pi\nu\nu}$ analysis with all backgrounds taken into account. These include $K^+ \to \pi^+\pi^+\pi^-$ and $K^+ \to \pi^+\pi^- e^+\nu$ decays filling mainly the peak in data at high m^2_{miss}, other kaon decays such as $K^+ \to \mu^+\nu(\mu^+ \to e^+)$ and $K^+ \to \pi^+\pi^0\gamma$ contributing to the right-hand sides of $K_{\mu 2}$ and $K_{2\pi}$ peaks, respectively, as well as the upstream background spanning across the full m^2_{miss} range and completely dominating the total background in the $K_{\pi\nu\nu}$ analysis [81].

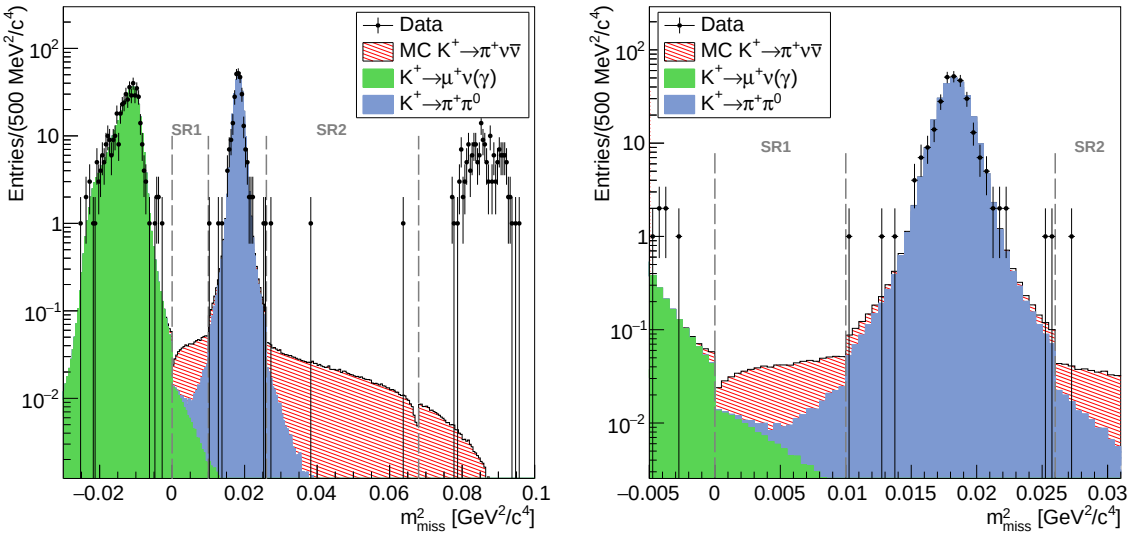

(a) Standard matching.

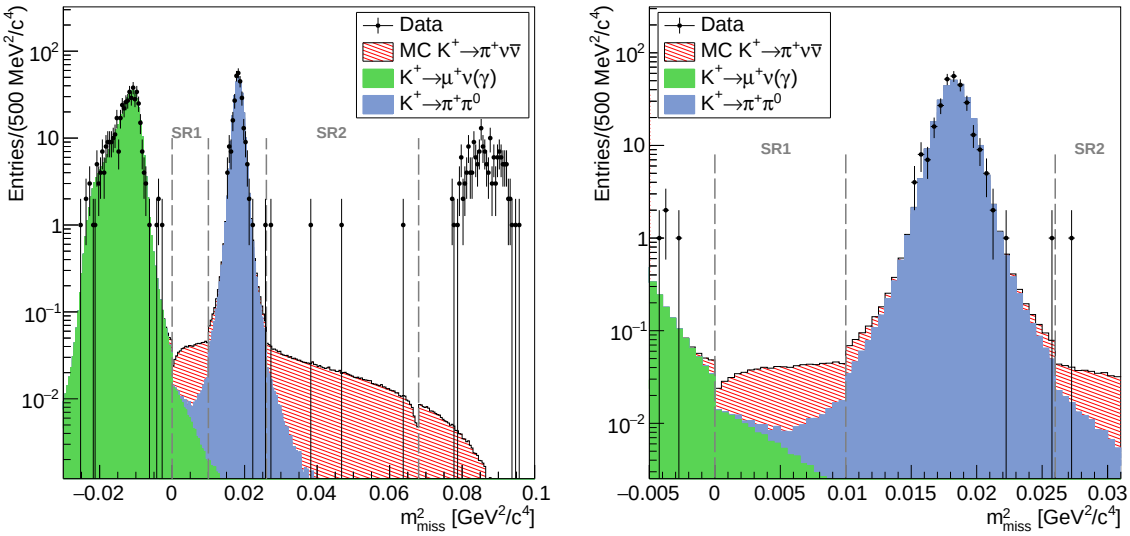

(b) Likelihood matching with threshold values of SET 5.

Figure 4.3.7: Stack plots obtained as a combination of the m^2_{miss} distribution of the $K_{\pi\nu\nu}$ Monte Carlo events passing the $K_{\pi\nu\nu}$ selection and two distributions of 2017 data events selected by the $K_{2\pi}$ and $K_{\mu 2}$ selections, overlaid with the $K_{\pi\nu\nu}$– selected data. Distributions are produced with the standard (a) and the likelihood (b) matching algorithms (to be compared with Figure 1.2.7b). The $K_{2\pi}$ and $K_{\mu 2}$ distributions are normalized in each of the four momentum bins to have the same peak integrals as the overlaid data distribution, while the $K_{\pi\nu\nu}$ Monte Carlo distribution is scaled according to the SES. Only events reconstructed in one of the nine regions defined in subsection 4.1.7 contribute to the plots. Contributions from upstream events, K_{e4}, $K_{3\pi}$, and other less abundant background components are missing. The steps in the distributions are caused by $m^2_{miss}(RICH)$ and $m^2_{miss}(beam)$ constraining the $K_{\pi\nu\nu}$ signal regions. Grey dashed lines indicate the two $K_{\pi\nu\nu}$ signal regions.

Conclusions

The presented thesis summarizes author's contribution to the current and future measurement of the rare kaon decay $K^+ \to \pi^+ \nu\overline{\nu}$ at the NA62 experiment at CERN.

In Chapter 1 we gave a brief overview of history of kaons and their contribution to our current understanding of weak interactions. We motivated the experimental efforts to measure the branching fractions of both neutral and charged modes of the $K \to \pi\nu\nu$ decay, and summarized the current experimental status with the emphasis on the charged decay mode measured by NA62.

We dedicated the Chapter 2 to the description of the NA62 detector system and software modules used for simulation, data processing and physics analyses.

In Section 3.2 we focused on the first objective of our work - measurement of the track reconstruction efficiency in the STRAW spectrometer. We developed three event selections of decays $K_{2\pi}$, $K_{\mu 3}$ and K_{e3} without using STRAW information to obtain samples of expected tracks (pointers) for three different positively charged particles: π^+, μ^+, and e^+. We evaluated the efficiency for all available 2016, 2017 and 2018 data sets, as well as for $K_{2\pi}$, $K_{\mu 3}$ and K_{e3} Monte Carlo samples. The measured efficiency for π^+ (μ^+, e^+) is above 93 % (92 %, 95 %) in 2016 data with up to 3 % improvement in the 2017 and 2018 data set thanks to an upgrade of the STRAW readout firmware. The π^+ track reconstruction efficiency in the pion momentum range (15, 35) GeV needed for the $K_{\pi\nu\nu}$ measurement was observed to depend only on the instantaneous beam intensity. This result was used in the main $K_{\pi\nu\nu}$ analysis of the 2017 data set [81].

The second goal of our work, discussed in Chapter 4, was to develop a new algorithm for matching the STRAW tracks with upstream kaon candidates reconstructed by the GTK in the $K_{\pi\nu\nu}$ analysis to reduce the $K_{2\pi}$ and $K_{\mu 2}$ background caused by kinematic tails of the corresponding m^2_{miss} distributions entering the $K_{\pi\nu\nu}$ signal regions.

We proposed a likelihood-based algorithm and derived the matching procedure with the final quality cuts performed in two event categories based on the number of reconstructed GTK candidates. We chose five sets of threshold values for the quality cuts and evaluated the matching performance on $K_{3\pi}$ events, where the correct kaon candidate is identified by a dedicated matching procedure. Compared to the results

obtained with the standard matching algorithm used in the main $K_{\pi\nu\nu}$ analysis, we obtained up to 80 % lower mismatch rate and an increased good-match rate by 1 % to 8 % relative. We also showed that an improvement of about 10 % can be achieved for the probability of tracks being matched to an accidental GTK candidate.

Moreover, performance of the new algorithm in the $K_{\pi\nu\nu}$ analysis of the 2017 data set was quantified by computing the $K_{2\pi}$ and $K_{\mu 2}$ tail fractions and the resulting expected background contributions, as well as the single event sensitivity and the expected number of $K_{\pi\nu\nu}$ events. A significant improvement was observed in the left tail of the $K_{2\pi}$ m^2_{miss} distribution contributing to the $K_{\pi\nu\nu}$ signal region 1, leading to up to 8 % decrease in the total number of expected $K_{2\pi}$ and $K_{\mu 2}$ events in both $K_{\pi\nu\nu}$ signal regions combined, and similar increase in the signal-over-background ratio (taking into account only $K_{\mu 2}$ and non-radiative part of $K_{2\pi}$ backgrounds). Finally, we were able to observe four $K_{\pi\nu\nu}$ event candidates with the likelihood matching algorithm and three of them also with the standard matching algorithm. This is to be compared with the main $K_{\pi\nu\nu}$ analysis observing two of them [81], while the third candidate was rejected by an older version of the selection software.

Before including the likelihood matching algorithm in the main $K_{\pi\nu\nu}$ analysis for the next run of data taking, it has to be tested against upstream events currently producing the dominant background contribution to the $K_{\pi\nu\nu}$ analysis.

Appendices

Appendix A

Note on the upstream background

The $K_{\pi\nu\nu}$ event selection requires presence of a charged particle reconstructed in STRAW identified as a pion and a beam particle reconstructed in GTK identified as a kaon by KTAG. Events with extra particles (charged leptons, photons) are rejected.

The $K_{\pi\nu\nu}$ analysis of NA62 data recorded in 2016–2018 revealed that the dominant background originates from upstream events in which beam particles either interacted or decayed upstream of the fiducial decay volume. There are two main types of upstream events producing background to $K_{\pi\nu\nu}$.

In upstream events of the first type, the kaon, detected by both KTAG and GTK, interacted inelastically in the last GTK station. As a result, a pion was produced (directly or via a decay of another particle), which then entered the decay volume and was detected in the STRAW.

The second type of the upstream background includes events in which a kaon, detected in KTAG, decays or inelastically interacts upstream of GTK3 producing a pion, which is then matched to an accidental GTK candidate (Figure A1). Additional particles produced in the decay or interaction are absorbed by material in the beam line. Monte Carlo simulations, as well as studies of data samples enriched with upstream events show, that pions produced in the second type of upstream events enter the decay region mostly through the beam hole of the final collimator or through the aperture of the last dipole magnet.

Several cuts suppressing upstream events at the analysis level are used, relying mainly on position of STRAW track extrapolated upstream of the decay volume. Although very effective, they result in substantial loss (more than 30 % [96]) of signal acceptance. Additionally, upstream events, in which the pion underwent large-angle scattering before entering the decay volume or in the first STRAW chamber, are not affected by these cuts and can be suppressed only by installation of new hardware components in the GTK area of the NA62 detector (see subsections 2.1.2 and 4.2.3, [95]).

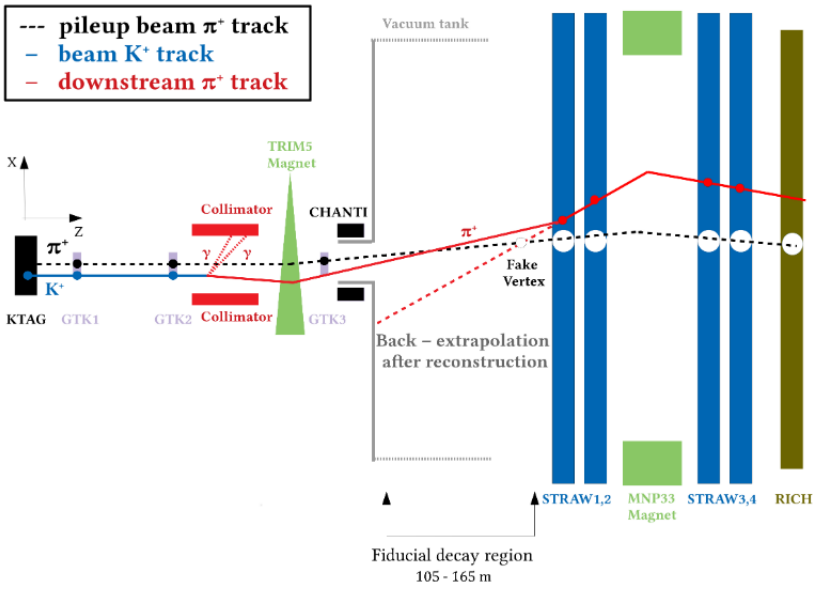

Figure A1: Sketch of an upstream event of the second type in the horizontal plane (not to scale) [81]. Three GTK stations are displayed together with the final collimator. The reconstructed π^+ undergoes large-angle scattering in the first STRAW chamber.

Appendix B

Monte Carlo samples

Based on the kaon decay position, two types of MC samples are produced:

- Kaon decays in the standard region (102.425, 180) m
- Kaon decays in one of the upstream regions:
  - ⋆ standard upstream (upstr.): (69.175, 102.425) m
  - ⋆ mid-upstream (m.upstr.): (92.310, 101.255) m
  - ⋆ near-upstream (n.upstr.): (96.950, 102.425) m.

In both cases, kaon can decay only in the given region. However, in the first case, kaon can interact anywhere up to 180 m, while in the second case, the interaction of kaon with detector or beam pipe material can occur only up to the upper range defining the region. To eliminate the double-counting of kaon interactions, the standard samples are restricted in the selections by a cut to contain only events, in which the kaon interaction or decay occur inside the standard decay region (102.425, 180) m.

Appendix C

Neutral vertex position formula

The neutral vertex position in kaon decays with neutral pion immediately decaying to two photons is derived. This is useful in cases when no downstream tracking information is available or it cannot be used. The derivation requires known positions and energies of the two photon candidates, as well as kaon candidates with known momenta and positions. The Z position of the vertex is found numerically. An approximate formula using the nominal kaon is also derived.
In this section a convention for speed of light $c = 1$ is adopted.

Let the unknown neutral vertex position be $\vec{r} = (X, Y, Z)$. For each pair of photon candidates their position and energy is measured in LKr:

photon	energy	position
γ_1	E_1	$\vec{r}_1 = (X_1, Y_1, Z_1)$
γ_2	E_2	$\vec{r}_2 = (X_2, Y_2, Z_2)$.

Assuming both photons come from the same neutral vertex, their momenta are

$$\vec{p}_1 = E_1 \left(\frac{\vec{r}_1 - \vec{r}}{|\vec{r}_1 - \vec{r}|} \right) \equiv E_1 \frac{\vec{u}_1}{|\vec{u}_1|} \qquad |\vec{p}_1| = E_1 \tag{C1}$$

$$\vec{p}_2 = E_2 \left(\frac{\vec{r}_2 - \vec{r}}{|\vec{r}_2 - \vec{r}|} \right) \equiv E_2 \frac{\vec{u}_2}{|\vec{u}_2|} \qquad |\vec{p}_2| = E_2. \tag{C2}$$

Therefore, the four-momenta of both photons are

$$\mathrm{P}_1 = (E_1, \vec{p}_1) \qquad m^2(\gamma_1) = \mathrm{P}_1^2 = 0 \tag{C3}$$

$$\mathrm{P}_2 = (E_2, \vec{p}_2) \qquad m^2(\gamma_2) = \mathrm{P}_2^2 = 0. \tag{C4}$$

If the photons come from a π^0 decay, using the four-momentum conservation and energy-mass relation we obtain:

$$(\mathrm{P}_1 + \mathrm{P}_2)^2 \stackrel{!}{=} m^2(\pi^0) \tag{C5}$$

$$= (E_1 + E_2, \vec{p}_1 + \vec{p}_2)^2 = (E_1 + E_2)^2 - (\vec{p}_1 + \vec{p}_2)^2 = \tag{C6}$$

$$= E_1^2 + 2E_1E_2 + E_2^2 - (\vec{p}_1)^2 - 2\vec{p}_1 \cdot \vec{p}_2 - (\vec{p}_2)^2 = \tag{C7}$$

$$= E_1^2 - (\vec{p}_1)^2 + E_2^2 - (\vec{p}_2)^2 + 2\left(E_1E_2 - \vec{p}_1 \cdot \vec{p}_2\right) = \tag{C8}$$

$$= m^2(\gamma_1) + m^2(\gamma_2) + 2E_1E_2 \left[1 - \frac{\vec{u}_1 \cdot \vec{u}_2}{|\vec{u}_1||\vec{u}_2|} \right] = \tag{C9}$$

$$= 2E_1E_2 \left[1 - \frac{\vec{u}_1 \cdot \vec{u}_2}{|\vec{u}_1||\vec{u}_2|} \right]. \tag{C10}$$

Therefore

$$m^2(\pi^0) = 2E_1E_2\left[1 - \frac{\vec{u}_1 \cdot \vec{u}_2}{|\vec{u}_1||\vec{u}_2|}\right]. \tag{C11}$$

Since π^0 decays almost immediately, the $\pi^0 \to \gamma\gamma$ vertex position is considered to be identical to the kaon decay vertex position.

GTK candidate or average beam momentum and position

The position and momentum of the GTK candidate are known at the GTK3 plane. That is true also for the run-dependent average beam momentum. Therefore the Z position of the vertex can be found numerically as a root of $f(Z)$ in the range (102.4, 180) mm:

$$f(Z) = m^2(\pi^0) - 2E_1E_2\left[1 - \frac{\vec{u}_1 \cdot \vec{u}_2}{|\vec{u}_1||\vec{u}_2|}\right] \tag{C12}$$

while using the following $\vec{r}$:

- if Z is inside the Blue Tube field region, the GTK candidate position $\vec{r}$ at given Z is corrected for the Blue Tube field
- if Z is outside the Blue Tube field region, a linear extrapolation of GTK candidate trajectory to the Z plane from candidate position and momentum at GTK3 is used as $\vec{r}$

The full vertex position is then given by GTK candidate position at the computed Z plane corrected for the Blue Tube field.

Nominal kaon

The position and momentum of the nominal kaon are known at any Z. Therefore an approximate formula can be derived from C11.

First noticing that the fraction in brackets is equal to cosine of the angle φ between the two photon momenta,

$$\frac{\vec{u}_1 \cdot \vec{u}_2}{|\vec{u}_1||\vec{u}_2|} = \cos\varphi, \tag{C13}$$

C11 can be rewritten as

$$m^2(\pi^0) = 2E_1E_2\left[2\sin^2\frac{\varphi}{2}\right], \tag{C14}$$

where a relation between trigonometric functions, $1 - \cos\varphi = 2\sin^2\frac{\varphi}{2}$, was used.

Assuming the angle φ is small and that the distance d_{12} between the photons in the LKr plane is much smaller than the distance R between the cluster positions in the LKr and the vertex plane, an approximation of $\sin^2\frac{\varphi}{2}$ by $\left(\frac{\varphi}{2}\right)^2$, and consequently $\varphi \doteq \frac{d_{12}}{R}$ can be done. Finally, R can be approximated by $Z_{LKr} - Z_{vtx}$, leading to the result

$$Z_{vtx} = \left(Z_{LKr} - \frac{\sqrt{E_1E_2}d_{12}}{m(\pi^0)}\right). \tag{C15}$$

At the GTK3, the position of the nominal kaon is $(0, 0, 102.4)$m and the direction of the nominal kaon momentum deviates from the Z direction by 1.2 mrad towards the positive X-axis. Therefore the X position of the nominal kaon at the Z_{vtx}-plane is found to be

$$X = (Z_{vtx} - 102.4\,\mathrm{m})\tan(0.0012). \tag{C16}$$

The full nominal kaon decay vertex position is then

$$\vec{r_v} = \left(\left[Z_{LKr} - \frac{\sqrt{E_1 E_2}d_{12}}{m(\pi^0)} - 102.4\,\mathrm{m}\right]\tan(0.0012), 0, Z_{LKr} - \frac{\sqrt{E_1 E_2}d_{12}}{m(\pi^0)}\right). \tag{C17}$$

Appendix D

MC-Data stack histograms

The following paragraphs contain a detailed description of the procedure how the Data/MC comparison histograms presented in Chapter 3 were obtained. The procedure consists of two steps: first a Monte Carlo stack histogram is produced, taking into account the branching fractions and lengths of decay regions. The reference decay ($K_{2\pi}$ for $K_{2\pi}$ selection, $K_{\mu 3}$ for $K_{\mu 3}$ selection and K_{e3} for K_{e3} selection) is used for normalization. Then the Monte Carlo stack histogram is scaled to have the same integral in the histogram range as data.

Preparing MC histograms

The following table summarizes the notation used in this paragraph.

	Reference decay	m-th decay
Initial number of MC events (Appendix B)	N_i	$M_{i,m}$, $\widetilde{M_{i,m}}$
Number of MC events after the selection	N_f	$M_{f,m}$, $\widetilde{M_{f,m}}$
Acceptance	$A_n = \frac{N_f}{N_i}$	$A_m = \frac{M_{f,m}}{M_{i,m}}$
Branching fraction	$B_n = \frac{\Gamma_n}{\Gamma_{\text{all}}}$	$B_m = \frac{\Gamma_m}{\Gamma_{\text{all}}}$

N_i and $M_{i,m}$ are the MC sample sizes as described in Appendix B ($Z_{end}(K)$ restricted to (102 425, 180 000) mm for standard samples). Since the upstream decay regions are shorter than the standard decay region, $M_{i,m}$ of the upstream Monte Carlo samples are multiplied (before computation of $\widetilde{M_{f,m}}$) by additional factors reflecting this fact: 2.12 for the standard upstream region, 8.02 for the mid-upstream region and 13.17 for the near-upstream region. These factors are derived from the exponential decay formula with $\tau_{K^+} = 1.238 \times 10^{-8}$s, $m_{K^+} = 493.677\,\text{MeV/c}^2$ and $P_{K^+} = 75\,\text{GeV/c}$. The definitions of the decay regions are given in Appendix B.
N_f and $M_{f,m}$ are the numbers of events passing the event selection. $\widetilde{M_{i,m}}$ $\left(\widetilde{M_{f,m}}\right)$ is the computed initial (final) number of events of the m–th decay after normalization to the initial number of events of the reference decay, N_i.

Scaling number of initial events by branching fraction:

	Number of initial events
All K decays	X
Reference decay	$N_i = XB_n$
m-th decay	$\widetilde{M_{i,m}} = XB_m = \frac{N_i}{B_n}B_m$

For N_i initial events of the reference decay, the expected number of initial events of the m-th decay is $\widetilde{M_i} = N_i \frac{B_m}{B_n}$.

Taking into consideration the acceptance of the m-th decay, the expected number of final events of the m-th decay, $\widetilde{M_{f,m}}$, is computed in the following way:

$$\widetilde{M_{f,m}} = A_m \widetilde{M_{i,m}} = \frac{M_{f,m}}{M_{i,m}} \widetilde{M_{i,m}} = M_{f,m} \underbrace{\frac{N_i}{M_{i,m}} \frac{B_m}{B_n}}_{F_m} . \tag{D1}$$

Stack histogram is produced by stacking the Monte Carlo histograms scaled by F_m on top of each other.

Scaling Stack MC histogram to data

Stack MC histogram is scaled by ratio $R = \frac{intD}{intMC}$.

	Number of final events
Data (integral of data histogram)	intD
MC (integral of Stack MC histogram)	intMC

Appendix E

Single track reconstruction efficiency summary

Track	Sample	ε [%]	ε(4CH) [%]
π^+	$K_{2\pi}$ (v1.1.4+5)	99.7±0.1	97.4±0.1
μ^+	$K_{\mu 3}$ (v1.1.4)	99.7±0.1	96.0±0.1
e^+	K_{e3} (v1.1.4+5)	99.8±0.1	97.6±0.1

Table E1: Track reconstruction efficiency in Monte Carlo.

	π^+	μ^+	e^+
Sample	ε [%]	ε [%]	ε [%]
2016A	95.46±0.09	95.76±0.25	96.40±0.33
2016B	95.96±0.08	95.93±0.24	96.62±0.31
2017A	98.53±0.04	98.81±0.10	99.80±0.07
2017B	98.59±0.03	98.81±0.07	99.81±0.05
2017C	98.71±0.07	98.98±0.19	99.84±0.14
2017D	98.91±0.05	99.03±0.14	99.79±0.12
2018A	98.89±0.07	99.06±0.22	99.80±0.20
2018B	98.73±0.03	98.84±0.09	99.78±0.07
2018C	98.52±0.08	98.74±0.24	99.79±0.20
2018D	98.58±0.03	98.81±0.09	99.73±0.08
2018E	98.56±0.04	98.80±0.11	99.74±0.09
2018F	98.36±0.04	98.67±0.12	99.73±0.10
2018G	98.38±0.04	98.66±0.10	99.72±0.09
2018H	98.39±0.06	98.63±0.16	99.80±0.12

Table E2: Track reconstruction efficiency in data computed using all reconstructed tracks.

	π^+	μ^+	e^+
Sample	ε(4CH) [%]	ε(4CH) [%]	ε(4CH) [%]
2016A	92.72±0.11	92.25±0.32	95.03±0.38
2016B	93.89±0.10	93.26±0.30	95.36±0.35
2017A	94.80±0.07	94.14±0.22	98.23±0.20
2017B	94.97±0.05	94.12±0.16	98.42±0.13
2017C	95.47±0.12	94.73±0.39	98.39±0.36
2017D	95.85±0.09	94.87±0.31	98.37±0.28
2018A	95.65±0.14	94.56±0.49	98.17±0.47
2018B	95.26±0.06	94.22±0.19	98.22±0.18
2018C	94.78±0.14	94.23±0.47	98.36±0.45
2018D	94.97±0.06	94.24±0.19	98.07±0.19
2018E	94.93±0.07	94.00±0.23	98.37±0.20
2018F	94.49±0.07	93.76±0.24	98.19±0.22
2018G	94.52±0.07	93.48±0.22	98.07±0.21
2018H	94.50±0.10	93.64±0.33	98.09±0.32

Table E3: Track reconstruction efficiency in data computed using only tracks reconstructed in all four STRAW chambers.

Appendix F

Likelihood matching performance scan

Figures F1 and F2 show the dependence of the likelihood matching performance in $K_{3\pi}$ events (selected from the 2017A data set) on the three matching parameters: $P(H_0|\gamma)$ in category $N = 1$ (one GTK candidate considered in the matching), and $\mathcal{F}(\Gamma)$ and $P(H_0|\gamma)$ in category $N > 1$.

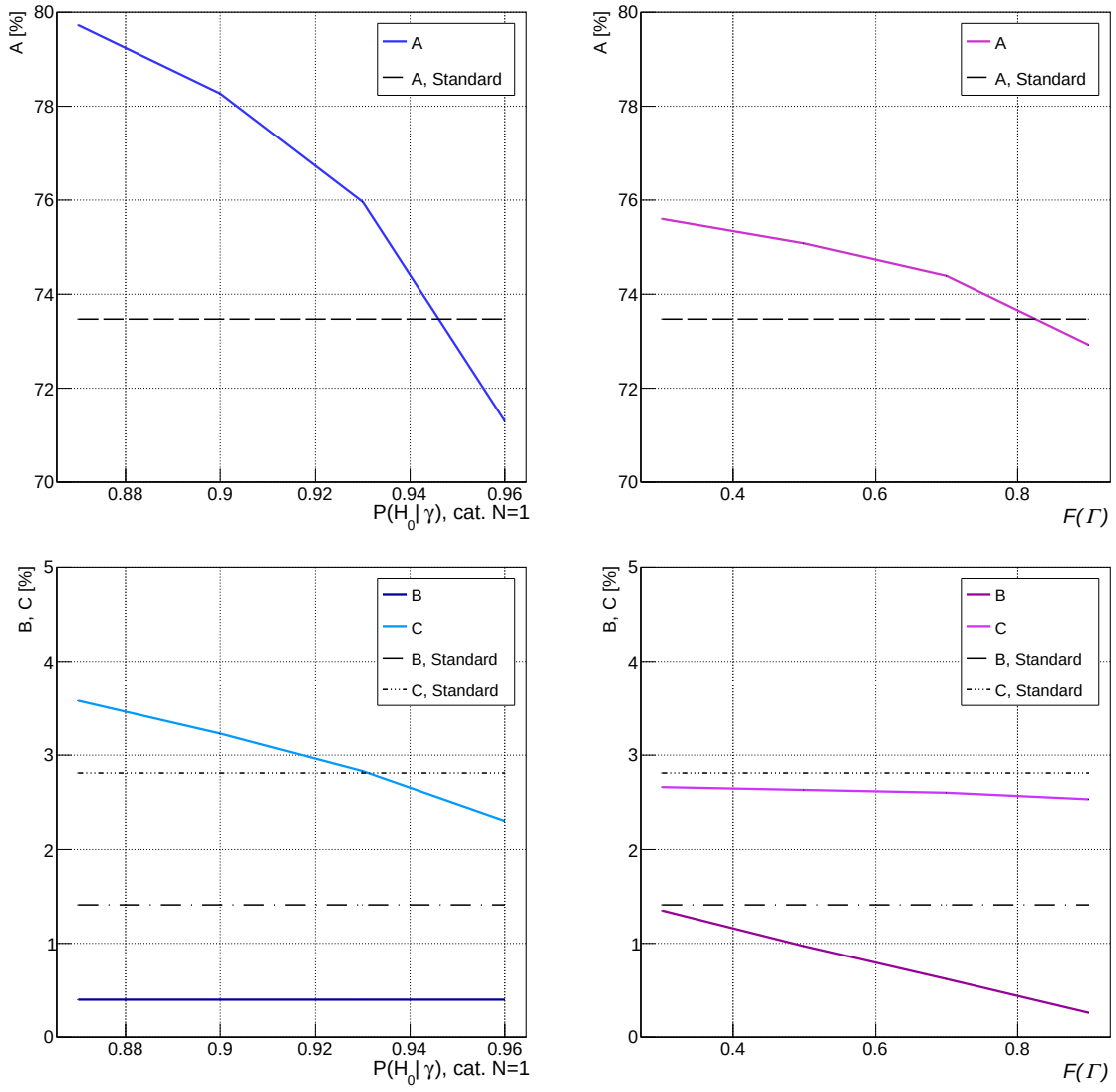

(a) Scan of $P(H_0|\gamma)$ (category $N = 1$)

(b) Scan of $\mathcal{F}(\Gamma)$ (category $N > 1$)

Figure F1: Constant threshold values used in the scan: (a) category $N > 1$: $P(H_0|\gamma) = 0.67$, $\mathcal{F}(\Gamma) = 0.85$; (b) category $N = 1$: $P(H_0|\gamma) = 0.94$, category $N > 1$: $P(H_0|\gamma) = 0.74$.

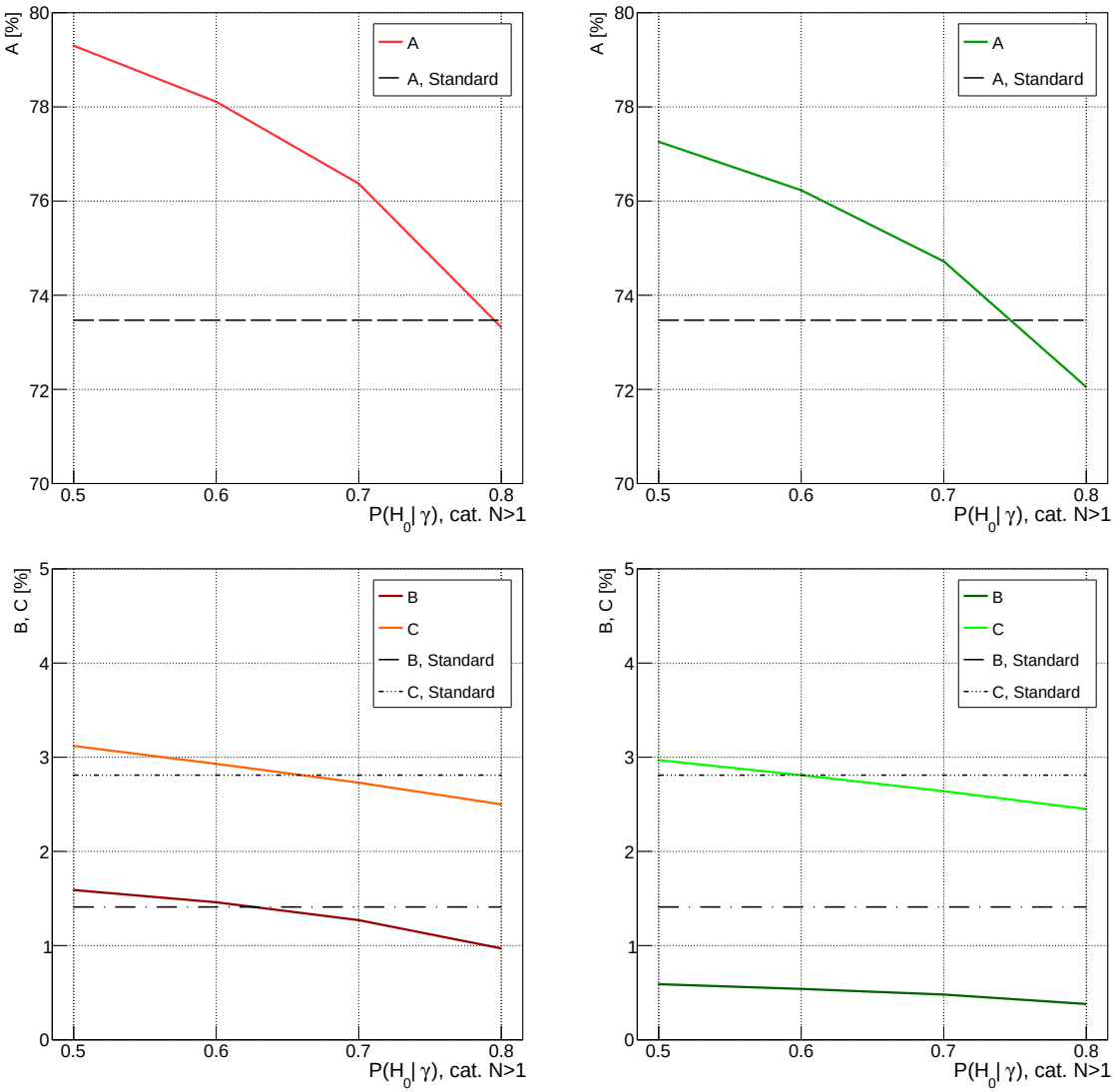

(a) Scan of $P(H_0|\gamma)$ (category $N > 1$)

(b) Scan of $P(H_0|\gamma)$ (category $N > 1$)

Figure F2: Constant threshold values used in the scan: (a) category $N = 1$: $P(H_0|\gamma) = 0.94$, category $N > 1$: $\mathcal{F}(\Gamma) = 0.39$; (b) category $N = 1$: $P(H_0|\gamma) = 0.94$, category $N > 1$: $\mathcal{F}(\Gamma) = 0.8$.

Variables A, B and C, defined in subsection 4.2.3, are used to assess the performance. Each pair of histograms shows the matching performance evaluated for four threshold values of one of the parameters, while keeping the other two parameters constant. The tested ranges of threshold values are selected such that the resulting performance is similar to the reference obtained with the standard matching algorithm and shown in the plots as black dashed and dash-dotted lines.

Appendix G

Note on the shape of the $P(H_0|\gamma)$ for $K_{\mu 2}$ events in the signal region 2

This appendix addresses the step observed in the distribution of $P(H_0|\gamma)$ in category $N = 1$ for $K_{\mu 2}$ events in the $K_{\pi\nu\nu}$ signal region 2 (Figure 4.2.5). One can see in Figure G3a that the step is related to the abundance of events in large D_{vtx} – low $P(H_0|\gamma)$ region. Additionally, the typical shape of the boundary of the D_{vtx}–$P(H_0|\gamma)$ distribution at $D_{vtx} \in (\sim 20, \sim 40)$ mm is a consequence of the fact that, as shown in Figure G1, the kaon distribution contributing to both numerator and denominator of $P(H_0|\gamma)$ is decreasing more slowly than the pile-up distribution contributing only to the denominator. This results in an increase of the maximum of $P(H_0|\gamma)$ when moving to the higher D_{vtx}. We show similar distributions for $K_{2\pi}$ and $K_{\mu 2}$ in both signal regions for comparison.

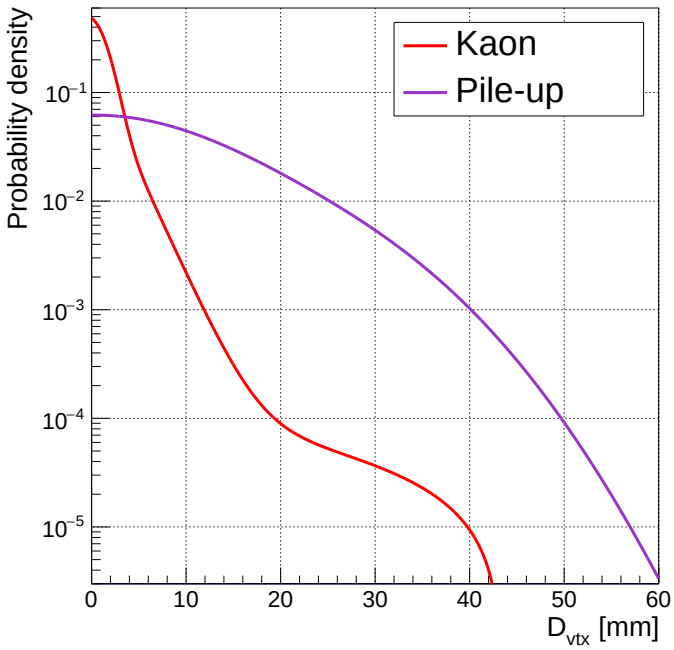

Figure G1: Kaon and pile-up probability density distributions as a function of D_{vtx} used in the likelihood matching algorithm (Figure 4.2.3).

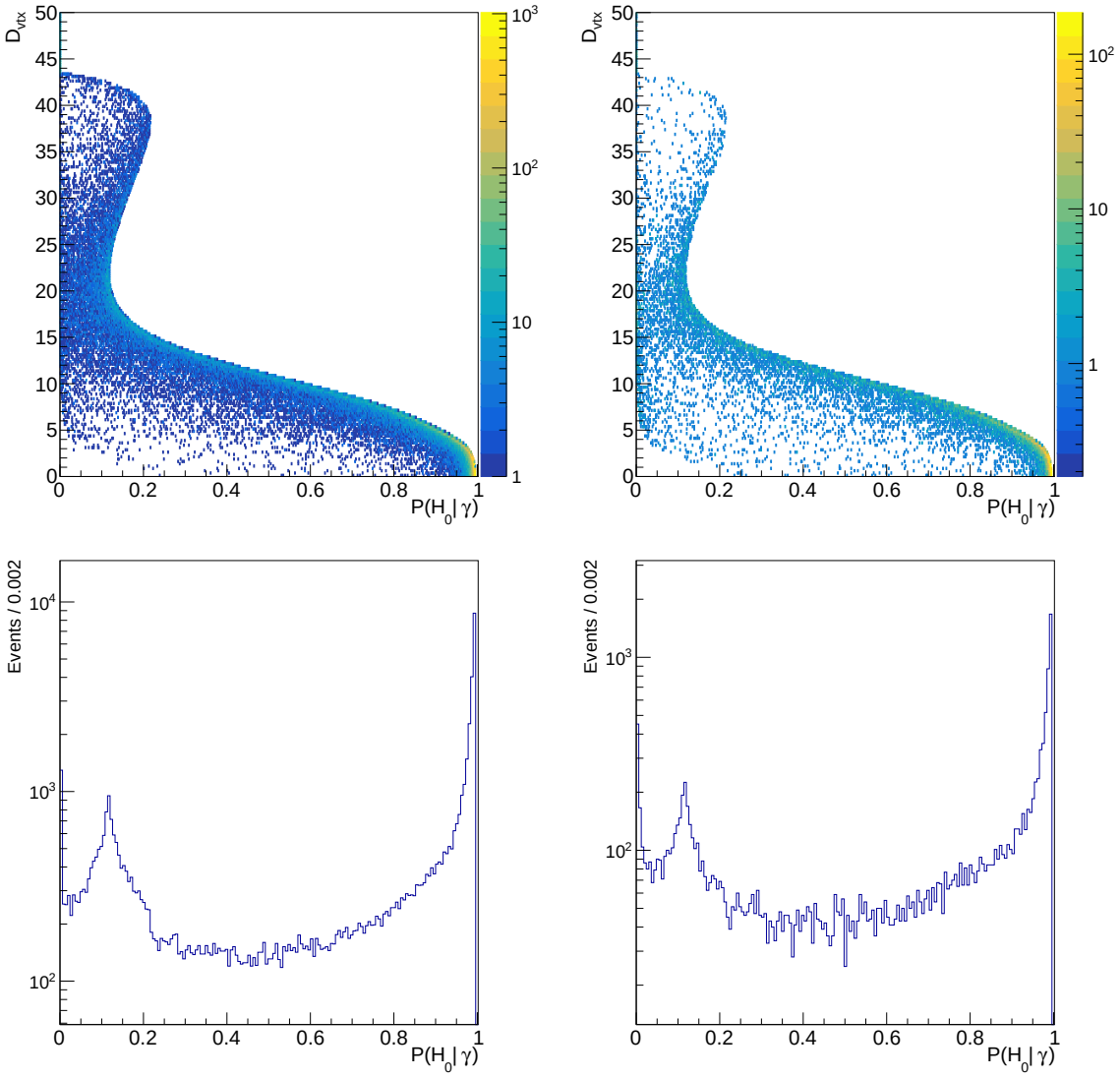

(a) $K_{\mu 2}$ (b) $K_{2\pi}$

Figure G2: D_{vtx} distributions as functions of $P(H_0|\gamma)$ in category $N = 1$ (top row), and projected $P(H_0|\gamma)$ (bottom row) for $K_{\mu 2}$ (a) and $K_{2\pi}$ (b) control events in the $K_{\pi\nu\nu}$ signal region 1.

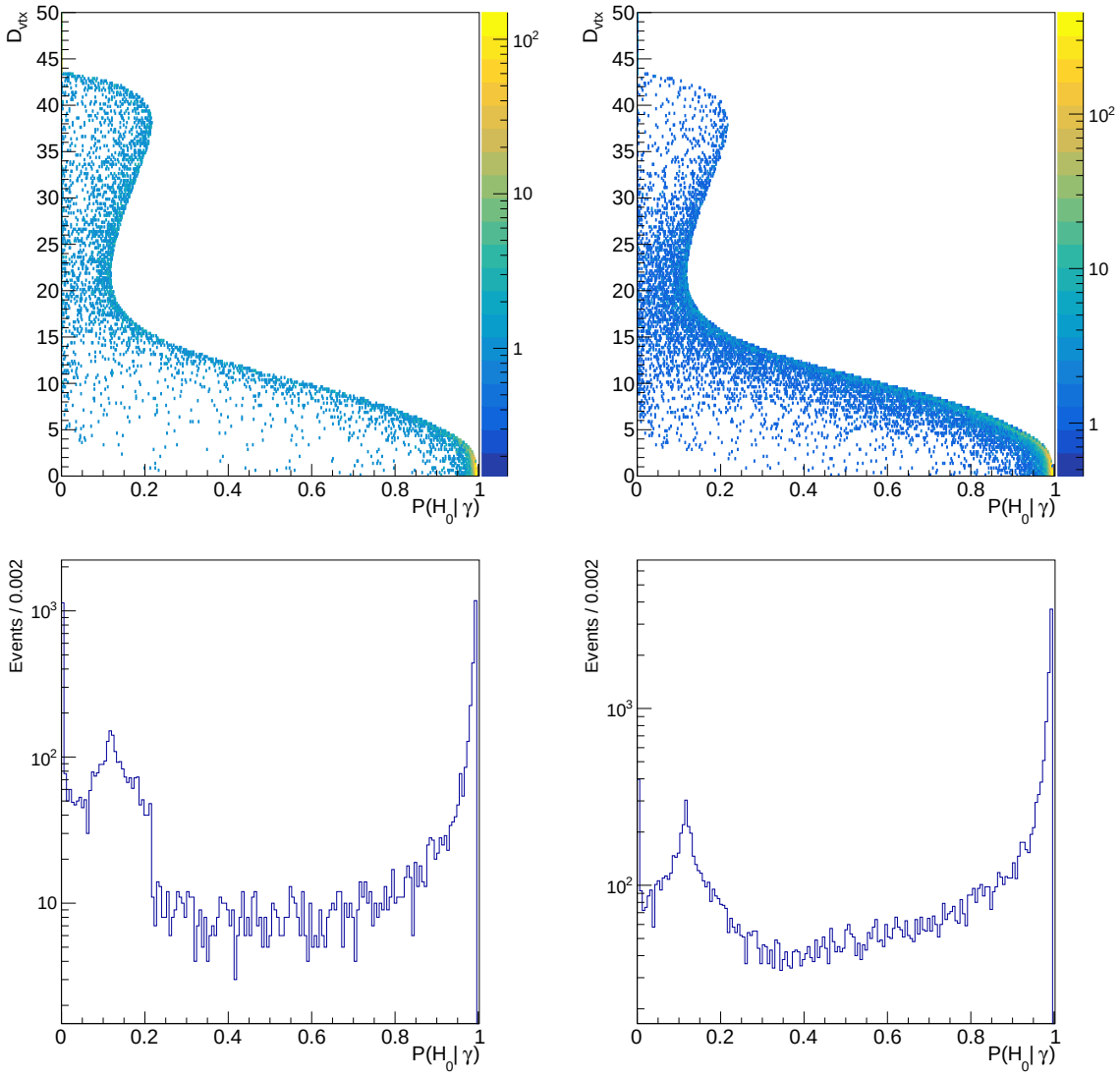

(a) $K_{\mu 2}$ (b) $K_{2\pi}$

Figure G3: D_{vtx} distributions as functions of $P(H_0|\gamma)$ in category $N = 1$ (top row), and projected $P(H_0|\gamma)$ (bottom row) for $K_{\mu 2}$ (a) and $K_{2\pi}$ (b) control events in the $K_{\pi\nu\nu}$ signal region 2.

Bibliography

[1] Sheldon L. Glashow. 'Partial-symmetries of weak interactions'. In: *Nuclear Physics* 22.4 (1961), pp. 579–588. ISSN: 0029-5582. DOI: 10.1016/0029-5582(61)90469-2.

[2] Steven Weinberg. 'A Model of Leptons'. In: *Phys. Rev. Lett.* 19 (21 Nov. 1967), pp. 1264–1266. DOI: 10.1103/PhysRevLett.19.1264.

[3] S. L. Glashow, J. Iliopoulos and L. Maiani. 'Weak Interactions with Lepton-Hadron Symmetry'. In: *Phys. Rev. D* 2 (7 Oct. 1970), pp. 1285–1292. DOI: 10.1103/PhysRevD.2.1285.

[4] H. Fritzsch, Murray Gell-Mann and H. Leutwyler. 'Advantages of the Color Octet Gluon Picture'. In: *Phys. Lett. B* 47 (1973), pp. 365–368. DOI: 10.1016/0370-2693(73)90625-4.

[5] F. Abe et al. 'Observation of Top Quark Production in $\overline{p}p$ Collisions with the Collider Detector at Fermilab'. In: *Phys. Rev. Lett.* 74 (14 Apr. 1995), pp. 2626–2631. DOI: 10.1103/PhysRevLett.74.2626.

[6] S. Abachi et al. 'Observation of the Top Quark'. In: *Phys. Rev. Lett.* 74 (14 Apr. 1995), pp. 2632–2637. DOI: 10.1103/PhysRevLett.74.2632.

[7] K. Kodama et al. 'Observation of tau neutrino interactions'. In: *Physics Letters B* 504.3 (Apr. 2001), pp. 218–224. ISSN: 0370-2693. DOI: 10.1016/s0370-2693(01)00307-0.

[8] G. Aad et al. 'Observation of a new particle in the search for the Standard Model Higgs boson with the ATLAS detector at the LHC'. In: *Physics Letters B* 716.1 (2012), pp. 1–29. ISSN: 0370-2693. DOI: 10.1016/j.physletb.2012.08.020.

[9] S. Chatrchyan et al. 'Observation of a new boson at a mass of 125 GeV with the CMS experiment at the LHC'. In: *Physics Letters B* 716.1 (2012), pp. 30–61. ISSN: 0370-2693. DOI: 10.1016/j.physletb.2012.08.021.

[10] G. Arnison et al. 'Experimental observation of isolated large transverse energy electrons with associated missing energy at s=540 GeV'. In: *Physics Letters B* 122.1 (1983), pp. 103–116. ISSN: 0370-2693. DOI: 10.1016/0370-2693(83)91177-2.

[11] M. Banner et al. 'Observation of single isolated electrons of high transverse momentum in events with missing transverse energy at the CERN pp collider'. In: *Physics Letters B* 122.5 (1983), pp. 476–485. ISSN: 0370-2693. DOI: 10.1016/0370-2693(83)91605-2.

[12] D.P. Barber et al. 'Discovery of Three Jet Events and a Test of Quantum Chromodynamics at PETRA Energies'. In: *Phys. Rev. Lett.* 43 (1979), p. 830. DOI: 10.1103/PhysRevLett.43.830.

[13] R. Brandelik et al. 'Evidence for Planar Events in e+ e- Annihilation at High-Energies'. In: *Phys. Lett. B* 86 (1979), pp. 243–249. DOI: 10.1016/0370-2693(79)90830-X.

[14] JAAN EINASTO, ANTS KAASIK and ENN SAAR. 'Dynamic evidence on massive coronas of galaxies'. In: *Nature* 250 (5464 1974), pp. 309–310. ISSN: 1476-4687. DOI: 10.1038/250309a0.

[15] Q. R. Ahmad et al. 'Direct Evidence for Neutrino Flavor Transformation from Neutral-Current Interactions in the Sudbury Neutrino Observatory'. In: *Phys. Rev. Lett.* 89 (1 June 2002), p. 011301. DOI: 10.1103/PhysRevLett.89.011301.

[16] Y. Fukuda et al. 'Evidence for Oscillation of Atmospheric Neutrinos'. In: *Phys. Rev. Lett.* 81 (8 Aug. 1998), pp. 1562–1567. DOI: 10.1103/PhysRevLett.81.1562.

[17] Q. R. Ahmad et al. 'Measurement of the Rate of $\nu_e + d \rightarrow p + p + e^-$ Interactions Produced by ^8B Solar Neutrinos at the Sudbury Neutrino Observatory'. In: *Phys. Rev. Lett.* 87 (7 July 2001), p. 071301. DOI: 10.1103/PhysRevLett.87.071301.

[18] NobelPrize.org. *Press release*. 6th Oct. 2015. URL: https://www.nobelprize.org/prizes/physics/2015/press-release/.

[19] *AMS-02: The Alpha Magnetic Spectrometer on the International Space Station*. URL: https://ams02.space/.

[20] *IceCube South Pole Neutrino Observatory*. URL: https://icecube.wisc.edu/.

[21] *Super-Kamiokande*. URL: http://www-sk.icrr.u-tokyo.ac.jp/sk/index-e.html.

[22] *ALICE: A Large Ion Collider Experiment*. URL: http://alice.web.cern.ch/.

[23] *CERN: European Council for Nuclear Research*. URL: https://home.cern/.

[24] *ATLAS Experiment*. URL: https://atlas.cern/.

[25] *CMS Experiment*. URL: https://cms.cern/.

[26] *NA62 Experiment*. URL: https://na62.web.cern.ch/.

[27] NA62 Collaboration. 'Proposal to Measure the Rare Decay $K^+ \to \pi^+ \nu\overline{\nu}$ at the CERN SPS'. 2005.

[28] Particle Data Group. 'Review of Particle Physics'. In: *Progress of Theoretical and Experimental Physics* 2020.8 (Aug. 2020). 083C01. ISSN: 2050-3911. DOI: 10.1093/ptep/ptaa104.

[29] Luciano Maiani. 'The GIM Mechanism: origin, predictions and recent uses'. In: *Proceedings, 48th Rencontres de Moriond on Electroweak Interactions and Unified Theories: La Thuile, Italy, March 2-9, 2013*. 2013, pp. 3–16. arXiv: 1303.6154 [hep-ph].

[30] D. Rochester and C. C. Butler. 'Evidence for the existence of new unstable elementary particles'. In: *Nature* 160 (1947), pp. 855–857.

[31] R. et al. Brown. 'Observations with electron-sensitive plates exposed to cosmic radiation'. In: *Nature* 163 (4133 1949), pp. 82–87.

[32] Jonathan L. Rosner and Bruce D. Winstein. *Kaon Physics*. University of Chicago Press, 2001.

[33] M. Gell-Mann. 'Isotopic Spin and New Unstable Particles'. In: *Phys. Rev.* 92 (3 Nov. 1953), pp. 833–834. DOI: 10.1103/PhysRev.92.833.

[34] Kazuhiko Nishijima. 'Charge Independence Theory of V Particles*'. In: *Progress of Theoretical Physics* 13.3 (Mar. 1955), pp. 285–304. ISSN: 0033-068X. DOI: 10.1143/PTP.13.285.

[35] Tadao Nakano and Kazuhiko Nishijima. 'Charge Independence for V-particles*'. In: *Progress of Theoretical Physics* 10.5 (Nov. 1953), pp. 581–582. ISSN: 0033-068X. DOI: 10.1143/PTP.10.581.

[36] A. Pais. 'Some Remarks on the V-Particles'. In: *Phys. Rev.* 86 (5 June 1952), pp. 663–672. DOI: 10.1103/PhysRev.86.663.

[37] T. D. Lee and C. N. Yang. 'Question of Parity Conservation in Weak Interactions'. In: *Phys. Rev.* 104 (1 Oct. 1956), pp. 254–258. DOI: 10.1103/PhysRev.104.254.

[38] C. S. Wu et al. 'Experimental Test of Parity Conservation in Beta Decay'. In: *Phys. Rev.* 105 (4 Feb. 1957), pp. 1413–1415. DOI: 10.1103/PhysRev.105.1413.

[39] Richard L. Garwin, Leon M. Lederman and Marcel Weinrich. 'Observations of the Failure of Conservation of Parity and Charge Conjugation in Meson Decays: the Magnetic Moment of the Free Muon'. In: *Phys. Rev.* 105 (4 Feb. 1957), pp. 1415–1417. DOI: 10.1103/PhysRev.105.1415.

[40] A. Pais and O. Piccioni. 'Note on the Decay and Absorption of the θ^0'. In: *Phys. Rev.* 100 (5 Dec. 1955), pp. 1487–1489. DOI: 10.1103/PhysRev.100.1487.

[41] J. H. Christenson et al. 'Evidence for the 2π Decay of the K_2^0 Meson'. In: *Phys. Rev. Lett.* 13 (4 July 1964), pp. 138–140. DOI: 10.1103/PhysRevLett.13.138.

[42] Andrzej Buras. 'Flavour Dynamics: CP Violation and Rare Decays'. In: *The Subnuclear Series*. Vol. 38. Mar. 2001. DOI: 10.1142/9789812778253_0005.

[43] H. Burkhardt et al. 'First evidence for direct CP violation'. In: *Physics Letters B* 206.1 (1988), pp. 169–176. ISSN: 0370-2693. DOI: 10.1016/0370-2693(88)91282-8.

[44] J.R Batley et al. 'A precision measurement of direct CP violation in the decay of neutral kaons into two pions'. In: *Physics Letters B* 544.1-2 (Sept. 2002), pp. 97–112. ISSN: 0370-2693. DOI: 10.1016/s0370-2693(02)02476-0.

[45] A. Alavi-Harati et al. 'Measurements of direct CP violation, CPT symmetry, and other parameters in the neutral kaon system'. In: *Phys. Rev. D* 67 (1 Jan. 2003), p. 012005. DOI: 10.1103/PhysRevD.67.012005.

[46] E. Abouzaid et al. 'Precise measurements of direct CP violation, CPT symmetry, and other parameters in the neutral kaon system'. In: *Phys. Rev. D* 83 (9 May 2011), p. 092001. DOI: 10.1103/PhysRevD.83.092001.

[47] Makoto Kobayashi and Toshihide Maskawa. 'CP-Violation in the Renormalizable Theory of Weak Interaction'. In: *Progress of Theoretical Physics* 49.2 (Feb. 1973), pp. 652–657. ISSN: 0033-068X. DOI: 10.1143/PTP.49.652.

[48] Nicola Cabibbo. 'Unitary Symmetry and Leptonic Decays'. In: *Phys. Rev. Lett.* 10 (12 June 1963), pp. 531–533. DOI: 10.1103/PhysRevLett.10.531.

[49] Jonathan M Flynn. 'The standard model calculation of $\epsilon\prime/\epsilon\prime\prime$'. In: *Nuclear Physics A* 527 (1991), pp. 735–738. ISSN: 0375-9474. DOI: 10.1016/0375-9474(91)90224-T.

[50] Ling-Lie Chau and Wai-Yee Keung. 'Comments on the Parametrization of the Kobayashi-Maskawa Matrix'. In: *Phys. Rev. Lett.* 53 (19 Nov. 1984), pp. 1802–1805. DOI: 10.1103/PhysRevLett.53.1802.

[51] Lincoln Wolfenstein. 'Parametrization of the Kobayashi-Maskawa Matrix'. In: *Phys. Rev. Lett.* 51 (21 Nov. 1983), pp. 1945–1947. DOI: 10.1103/PhysRevLett.51.1945.

[52] M. Schmidtler and K. R. Schubert. 'Experimental constraints on the phase in the Cabibbo-Kobayashi-Maskawa matrix'. In: *Zeitschrift fur Physik C Particles and Fields* 53 (2 1992), pp. 347–353. ISSN: 1431-5858. DOI: 10.1007/BF01597574.

[53] Andrzej J. Buras, Markus E. Lautenbacher and Gaby Ostermaier. 'Waiting for the top quark mass, $K^+ \to \pi^+\nu\overline{\nu}$, B_s^0-$\overline{B}_s^0$ mixing, and CP asymmetries in B decays'. In: *Physical Review D* 50.5 (Sept. 1994), pp. 3433–3446. ISSN: 0556-2821. DOI: 10.1103/physrevd.50.3433.

[54] Yuval Grossman and Yosef Nir. '$K_L \to \pi^0 \nu\bar{\nu}$ Beyond the Standard Model'. In: *Physics Letters B* 398.1-2 (Apr. 1997), pp. 163–168. ISSN: 0370-2693. DOI: 10.1016/s0370-2693(97)00210-4.

[55] S. Fajfer, N. Košnik and L. Vale Silva. 'Footprints of leptoquarks: from $R_{K^{(*)}}$ to $K \to \pi\nu\bar{\nu}$'. In: *Eur. Phys. J. C* 78.4 (2018), p. 275. DOI: 10.1140/epjc/s10052-018-5757-5.

[56] R. Aaij et al. 'Test of lepton universality with $B^0 \to K^{*0} l^+ l^-$ decays'. In: *Journal of High Energy Physics* 2017.8 (Aug. 2017). ISSN: 1029-8479. DOI: 10.1007/jhep08(2017)055.

[57] R. Aaij et al. 'Measurement of the Ratio of Branching Fractions $\mathcal{B}(B_c^+ \to J/\psi\tau^+\nu_\tau)/\mathcal{B}(B_c^+ \to J/\psi\mu^+\nu_\mu)$'. In: *Physical Review Letters* 120.12 (Mar. 2018). ISSN: 1079-7114. DOI: 10.1103/physrevlett.120.121801.

[58] Roel Aaij et al. 'Measurements of the S-wave fraction in $B^0 \to K^+\pi^-\mu^+\mu^-$ decays and the $B^0 \to K^*(892)^0\mu^+\mu^-$ differential branching fraction'. In: *JHEP* 11 (2016). [Erratum: JHEP 04, 142 (2017)], p. 047. DOI: 10.1007/JHEP11(2016)047. arXiv: 1606.04731 [hep-ex].

[59] Marzia Bordone et al. 'Probing lepton-flavour universality with $K \to \pi\nu\bar{\nu}$ decays'. In: *The European Physical Journal C* 77 (9 2017). ISSN: 1434-6052. DOI: 10.1140/epjc/s10052-017-5202-1.

[60] Monika Blanke, Andrzej J. Buras and Stefan Recksiegel. 'Quark flavour observables in the Littlest Higgs model with T-parity after LHC Run 1'. In: *The European Physical Journal C* 76.4 (Apr. 2016). ISSN: 1434-6052. DOI: 10.1140/epjc/s10052-016-4019-7.

[61] Andrzej J. Buras, Dario Buttazzo and Robert Knegjens. '$K \to \pi\nu\bar{\nu}$ and $\varepsilon\prime/\varepsilon$ in simplified new physics models'. In: *Journal of High Energy Physics* 2015 (11 2015). ISSN: 1029-8479. DOI: 10.1007/JHEP11(2015)166.

[62] Tomáš Blažek and Peter Maták. 'Left–left squark mixing, $K^+ \to \pi^+\nu\bar{\nu}$ and minimal supersymmetry with large tanβ'. In: *Int. J. Mod. Phys. A* 29.27 (2014), pp. 145–162. DOI: 10.1142/S0217751X14501620.

[63] Andrzej J. Buras et al. '$K^+ \to \pi^+\nu\bar{\nu}$ and $K_L \to \pi^0\nu\bar{\nu}$ in the Standard Model: status and perspectives'. In: *JHEP* 11 (2015), p. 033. DOI: 10.1007/JHEP11(2015)033.

[64] S Shinohara and. 'Search for the rare decay $K_L \to \pi^0\nu\bar{\nu}$ at J-PARC KOTO experiment'. In: *Journal of Physics: Conference Series* 1526 (Apr. 2020), p. 012002. DOI: 10.1088/1742-6596/1526/1/012002.

[65] M. Weaver et al. 'Limit on the Branching Ratio of $K_L \to \pi^0\nu\bar{\nu}$'. In: *Phys. Rev. Lett.* 72 (24 June 1994), pp. 3758–3761. DOI: 10.1103/PhysRevLett.72.3758.

[66] J. Adams et al. 'Search for the decay $K_L \to \pi^0\nu\nu$'. In: *Physics Letters B* 447.3 (1999), pp. 240–245. ISSN: 0370-2693. DOI: 10.1016/S0370-2693(98)01593-7.

[67] A. Alavi-Harati et al. 'Search for the decay $K_L \to \pi^0\nu\bar{\nu}$ using $\pi^0 \to e^+e^-\gamma$'. In: *Physical Review D* 61.7 (Mar. 2000). ISSN: 1089-4918. DOI: 10.1103/physrevd.61.072006.

[68] J. K. Ahn et al. 'Experimental study of the decay $K_L^0 \to \pi^0\nu\bar{\nu}$'. In: *Phys. Rev. D* 81 (7 Apr. 2010), p. 072004. DOI: 10.1103/PhysRevD.81.072004.

[69] *J-PARC E14 KOTO Experiment*. URL: http://koto.kek.jp/.

[70] J. K. Ahn et al. 'Search for $K_L \to \pi^0\nu\bar{\nu}$ and $K_L \to \pi^0 X^0$ Decays at the J-PARC KOTO Experiment'. In: *Phys. Rev. Lett.* 122 (2 Jan. 2019), p. 021802. DOI: 10.1103/PhysRevLett.122.021802.

[71] Shimizu Nobuhiro. 'Search for New Physics via the $K_L \to \pi^0\nu\bar{\nu}$ decay at the J-PARC KOTO experiment'. URL: https://indico.cern.ch/event/868940/contributions/3815582/.

[72] Andrzej J. Buras. 'Weak Hamiltonian, CP violation and rare decays'. In: *Les Houches Summer School in Theoretical Physics, Session 68: Probing the Standard Model of Particle Interactions*. June 1998, pp. 281–539. arXiv: hep-ph/9806471.

[73] U. Camerini et al. 'Experimental Search for Semileptonic Neutrino Neutral Currents'. In: *Phys. Rev. Lett.* 23 (6 Aug. 1969), pp. 326–329. DOI: 10.1103/PhysRevLett.23.326.

[74] D. Ljung and D. Cline. 'Experimental Study of the Rare K^+ Decay Modes: $K^+ \to \pi^+\pi^0\gamma$, $K^+ \to \mu^+\pi^0\nu\gamma$, $K^+ \to \pi^+\gamma\gamma$, $K^+ \to \pi^+\nu\bar{\nu}$, $K^+ \to \pi^0\pi^0 e^+\nu$, and $K^+ \to e^+\pi^0\nu\gamma$'. In: *Phys. Rev. D* 8 (5 Sept. 1973), pp. 1307–1330. DOI: 10.1103/PhysRevD.8.1307.

[75] G. D. Cable et al. 'Search for Rare K^+ Decays. II. $K^+ \to \pi^+\nu\bar{\nu}$'. In: *Phys. Rev. D* 8 (11 Dec. 1973), pp. 3807–3812. DOI: 10.1103/PhysRevD.8.3807.

[76] Y. Asano et al. 'Search for a rare decay mode $K^+ \to \pi^+\nu\nu$ and axion'. In: *Physics Letters B* 107.1 (1981), pp. 159–162. ISSN: 0370-2693. DOI: 10.1016/0370-2693(81)91172-2.

[77] S. Adler et al. 'Further Evidence for the Decay $K^+ \to \pi^+\nu\bar{\nu}$'. In: *Physical Review Letters* 88.4 (Jan. 2002). ISSN: 1079-7114. DOI: 10.1103/physrevlett.88.041803.

[78] E949 Collaboration. 'New measurement of the $K^+ \to \pi^+\nu\bar{\nu}$ branching ratio'. In: *Physical Review Letters* (2008). DOI: 10.1103/PhysRevLett.101.191802.

[79] A. V. Artamonov et al. 'Study of the decay $K^+ \to \pi^+ \nu\bar{\nu}$ in the momentum region $140 < P_\pi < 199$ MeV/c'. In: *Phys. Rev.* D79 (2009), p. 092004. DOI: 10.1103/PhysRevD.79.092004.

[80] E. Cortina Gil et al. 'First search for $K^+ \to \pi^+ \nu\bar{\nu}$ using the decay-in-flight technique'. In: *Physics Letters B* 791 (2019), pp. 156–166. ISSN: 0370-2693. DOI: 10.1016/j.physletb.2019.01.067.

[81] NA62 Collaboration. *An investigation of the very rare $K^+ \to \pi^+ \nu\bar{\nu}$ decay*. 2020. arXiv: 2007.08218 [hep-ex].

[82] Radoslav Marchevski. 'New result on the search for the $K^+ \to \pi^+ \nu\bar{\nu}$ decay at the NA62 experiment at CERN'. URL: https://indico.cern.ch/event/868940/contributions/3815641/.

[83] NA62 Collaboration. 'NA62 Technical Design Document'. NA62-10-27. 2010.

[84] E. Cortina Gil et al. 'The beam and detector of the NA62 experiment at CERN'. In: *Journal of Instrumentation* 12.05 (May 2017). DOI: 10.1088/1748-0221/12/05/p05025.

[85] *NA62 Software*. URL: https://na62-sw.web.cern.ch/software.

[86] CERN. *ROOT: A Data Analysis Framework*. URL: http://root.cern.ch/.

[87] Iselin Brown. *Decay TURTLE*. URL: https://sba.web.cern.ch/sba/Documentations/docs/turtle.pdf.

[88] S. Agostinelli et al. 'Geant4—a simulation toolkit'. In: *Nuclear Instruments and Methods in Physics Research Section A: Accelerators, Spectrometers, Detectors and Associated Equipment* 506.3 (2003), pp. 250–303. ISSN: 0168-9002. DOI: 10.1016/S0168-9002(03)01368-8.

[89] J. Allison et al. 'Geant4 developments and applications'. In: *IEEE Transactions on Nuclear Science* 53.1 (2006), pp. 270–278.

[90] J. Allison et al. 'Recent developments in Geant4'. In: *Nuclear Instruments and Methods in Physics Research Section A: Accelerators, Spectrometers, Detectors and Associated Equipment* 835 (2016), pp. 186–225. ISSN: 0168-9002. DOI: 10.1016/j.nima.2016.06.125.

[91] Richard O. Duda and Peter E. Hart. 'Use of the Hough Transformation to Detect Lines and Curves in Pictures'. In: *Commun. ACM* 15.1 (Jan. 1972), pp. 11–15. ISSN: 0001-0782. DOI: 10.1145/361237.361242.

[92] Rudolph Emil Kalman. 'A New Approach to Linear Filtering and Prediction Problems'. In: *Transactions of the ASME–Journal of Basic Engineering* 82.Series D (1960), pp. 35–45.

[93] Zuzana Kucerova and Michal Koval. 'Spectrometer reconstruction efficiency for single track events'. Internal note. 2020.

[94] Helge Voss. 'Classification'. In: *Data Analysis in High Energy Physics*. John Wiley & Sons, Ltd, 2013. Chap. 5, pp. 153–186. ISBN: 9783527653416. DOI: 10.1002/9783527653416.ch5.

[95] NA62 Collaboration. *ADDENDUM I TO P326 Continuation of the physics programme of the NA62 experiment*. Tech. rep. CERN-SPSC-2019-039. SPSC-P-326-ADD-1. Geneva: CERN, Oct. 2019. URL: https://cds.cern.ch/record/2691873.

[96] Radoslav Marchevski and Giuseppe Ruggiero. '$K^+ \to \pi^+ \nu\overline{\nu}$ selection'. Internal note. 2018.